Integrative Imaging and Electron Cryo-Tomography of Viral Transport Mechanisms



Michael Grange

St. Catherine's College

University of Oxford

A thesis submitted for the degree of

Doctor of Philosophy

Trinity 2016

Acknowledgements

During the course of my D. Phil, I have encountered numerous generous and kind people who have offered me advice and support. However, in particular I would like to thank Kay Grünewald, Daven Vasishtan, Lindsay Baker, C. Alistair Siebert, Ben Vollmer, Christoph Hagen, Pascale Schellenberger, Tzviya Zeev-Ben-Mordehai, Justin Demmerle, Sarah Finnegan, Sam Griffiths and Elizabeth Smethurst for their overwhelming friendship, advice and support.

Parts of this thesis have been published in peer reviewed journals for which I am a primary author, and . Specifically:

Christoph Hagen*, Kyle C. Dent*, Tzviya Zeev-Ben-Mordehai*, Michael Grange*, Jens B. Bosse*, Cathy Whittle, Barbara G. Klupp, C. Alistair Siebert, Daven Vasishtan, Felix J. B. Bäuerlein, Juliana Cheleski, Stephan Werner, Peter Guttmann, Stefan Rehbein, Katja Henzler, Justin Demmerle, Barbara Adler, Ulrich Koszinowski, Lothar Schermelleh, Gerd Schneider, Lynn W. Enquist, Jürgen M. Plitzko, Thomas C. Mettenleiter, Kay Grünewald. (2015). Structural basis of vesicle formation at the inner nuclear membrane. Cell, 163(7), pp.1692–1701. *equal contribution

Michael Grange, Daven Vasishtan & Kay Grünewald. (2016). Cellular electron cryo tomography and in situ sub-volume averaging reveal the context of microtubule-based processes. Journal of Structural Biology. (In Press). http://dx.doi.org/10.1016/j.jsb.2016.06.024

A copy of these papers are attached to the appendix for reference purposes.

Integrative Imaging and Electron Cryo-Tomography of Viral Transport Mechanisms

Michael Grange

St. Catherine's College, University of Oxford

Doctor of Philosophy, Trinity 2016

Abstract

To comprehensively understand a biological process or mechanism from molecule to cell it requires the combination of multiple techniques across a range of resolutions and scales. We currently rely on a variety of different approaches to highlight given aspects of biology that are then interlinked through interpretation. Intracellular transport is a process whereby vesicles and organelles are transported to different parts of cells with a precise spatial and temporal accuracy. This process is often hijacked by viruses, which utilize cellular machineries for active transport to and from the nucleus during their entry and egress. In this thesis I focus on the intracellular transport of adenoviruses, which are able to recruit and bind to the cytoskeletal motor, dynein, and use it to travel to the nucleus. I apply electron cryo-microscopy and fluorescence microscopy to elucidate the basis for this process, and link this to the behaviour of adenoviruses as they are recruited to microtubules. I then apply electron cryo-tomography to directly observe proteins in their native cellular environment. I discuss the ability of this technique to be utilized in the *in situ* determination of the structure of viruses as they infect a cell. I show that (i) in situ sub-volume averaging from single tomograms can guide and complement segmentation of biological features and (ii) that novel, transient processes can be imaged with high levels of detail. As a second example of transport in cells, I study the nuclear egress of herpesvirus capsids, utilizing a multi-modal approach in an attempt to characterize this process from cellular to molecular level, and ask how herpesviruses modulate the nuclear membrane during capsid egress into the cytosol. Finally, I discuss an emergent technique in the field of electron cryo-microscopy, the Volta phase plate, its potential application in molecular tomography, and how it may enhance our current ability to discern contextual molecular mechanism.

Contents

Common Abbreviations ix

1 Thesis Overview **1**

1.1 Rationale 1

1.2 Thesis Structure 4

2 Structural and temporal determination of dynein-engaged cargoes **7**

2.1 Introduction 7

2.1.1 Microtubule-based transport in cells 7

2.1.2 Dynein-based transport 9

2.1.3 Cytoskeletal transport of viruses 12

2.1.3.1 Herpes Simplex Virus 1 12

2.1.3.2 Adenovirus 14

2.1.4 Preparation of samples for electron cryo-microscopy studies . . 17

2.1.4.1 Purified or isolated macromolecules 18

2.1.4.2 Approaches to investigating macromolecular complexes and their interactions 19

2.1.4.3 Macromolecular interactions in their native cellular context 20

2.1.5 Introduction to electron microscopy 21

2.1.5.1 Electron sources and coherence 22

2.1.5.2 Image formation 23

2.1.5.3 Methods for data collection in electron cryo-microscopy 25

2.1.5.4 Electron detection and a push to increased resolution and signal-to-noise 29

2.2 Materials and Methods 31

2.2.1 Preparation of microtubules 31

2.2.2 Dynein-dependent recruitment of adenovirus to microtubules . 31
2.2.2.1 pH-treatment of adenovirus for dynein interaction studies . . . 32
2.2.2.2 Heat treatment of adenovirus for dynein interaction studies . . . 33
2.2.3 Investigation of dynein tail complex interaction with adenovirus 33
2.2.4 Plunge freezing . . . 34
2.2.5 Preparation of isolated herpesvirus capsids . . . 34
2.2.5.1 Virus purification and capsid isolation . . . 34
2.2.6 Total Internal Reflectance Fluorescence (TIRFM) motility assays 34
2.2.6.1 *In vitro* motility assays of herpesvirus capsids . . . 37
2.2.6.2 *In vitro* motility assays of adenovirus . . . 38
2.2.7 Data acquisition for electron cryo-tomography . . . 39
2.2.8 Data processing of electron cryo-tomograms . . . 39
2.2.9 Data collection for single particle analysis and 3D structure determination . . . 41
2.3 Results and Discussion . . . 42
2.3.1 TIRFM reveals the dynamics of viral trafficking *in vitro* . . . 42
2.3.1.1 Transport of herpesviruses reveals a minimalist cargo-recruitment machinery within the inner tegument layer 42
2.3.1.2 Recruitment of dynein to adenoviruses bound to microtubules is enhanced upon pH 5 treatment . . . 45
2.3.2 Structural determination of the adenoviral surface at pH 5 . . 47
2.3.2.1 Structure determination of a ΔpIX-adenovirus variant 47
2.3.2.2 The C-terminal coiled-coil of pIX is destabilized when exposed to low pH . . . 49
2.3.3 pH-dependency of dynein tail component binding to adenovirus 51
2.3.3.1 Localized classification of N-terminus of the dynein heavy chain . . . 51
2.3.3.2 Recruitment of the dynein tail is enhanced by pH treatment . . . 57
2.3.4 Electron cryo-tomography of dynein-mediated adenovirus trafficking on microtubules . . . 61

2.3.4.1 Heat-treatment of adenovirus results in collapse of the capsid and release of DNA . . . 61
2.3.4.2 pH 5-treated adenovirus can support the recruitment of multiple dynein bound to the microtubule . . . 62
2.3.4.3 Dynein-adenovirus-microtubule global architecture . 66
2.3.5 Viruses expose surface proteins that promote the recruitment of dynein during trafficking to the nucleus . . . 71
2.4 Concluding Remarks . . . 74

3 Towards visualization of virus transport *in situ* 76
3.1 Introduction . . . 76
3.1.1 Cellular electron cryo-tomography as a cell biological tool . . . 76
3.1.2 Emergent technologies that drive the field forward . . . 79
3.1.2.1 Sample thinning and targeting rare events . . . 79
3.1.2.2 Increasing contrast . . . 80
3.1.3 Perspectives in cryoET of cells . . . 82
3.1.4 *In situ* structure determination of macromolecules in their biological context . . . 84
3.2 Materials and Methods . . . 85
3.2.1 Cell culture and plunge freezing . . . 85
3.2.2 Electron microscopy . . . 86
3.2.3 Tomogram reconstruction, segmentation and sub-volume averaging . . . 86
3.3 Results and Discussion . . . 88
3.3.1 CryoET of the cellular periphery . . . 88
3.3.2 *In situ* sub-volume averaging from a single tomogram . . . 92
3.3.3 Back-plotting of sub-volume average structure into the tomogram results in a 3-dimensional context for structural interaction 97
3.3.4 Evaluation of CTF correction of tomograms for *in situ* sub-volume averaging . . . 99
3.3.5 Determination of virus structure *in situ* improves understanding of virus-host interaction . . . 105
3.4 Concluding Remarks . . . 106

4 Determination of the transport and membrane dynamics of herpesvirus capsids during nuclear egress 109
4.1 Introduction . . . 109
4.1.1 Herpesvirus life cycle . . . 109
4.1.2 Nuclear egress of herpesvirus capsids . . . 111
4.1.3 General introduction to fluorescence microscopy . . . 114
4.1.4 3-Dimensional structured illumination microscopy (3D-SIM) . 116
4.2 Materials and Methods . . . 120
4.2.1 3D-SIM imaging conditions . . . 120
4.2.2 Live-cell conditions: phase, oil and pitch calibrations . . . 122
4.2.3 Cell culture . . . 123
4.2.3.1 UL34-GFP/UL31-EFN cells (RIE3134-GFP) . . . 123
4.2.3.2 NIH-3T3-LBR-GFP and wild-type cells . . . 124
4.2.3.3 Rabbit kidney epithelial cells (RKLBR-GFP-GFP) . 125
4.2.3.4 Physiological imaging conditions . . . 126
4.2.4 Electron cryo-microscopy, focused ion beam milling and sub-volume averaging . . . 127
4.3 Results and Discussion . . . 127
4.3.1 Optimization of Live Cell 3D-SIM . . . 127
4.3.1.1 Initial testing of live-cell conditions: room temperature 127
4.3.1.2 Testing of live-cell conditions: 37°C . . . 128
4.3.2 3D-SIM of RIE3134-GFP cells . . . 130
4.3.3 Widefield Imaging of MCMV and PrV infection . . . 134
4.3.4 Electron cryo-tomography and focused ion beam milling of pUL31/34 peri-nuclear vesicles . . . 137
4.3.5 Sub-volume averaging of pUL31/34 peri-nuclear vesicles . . . 139
4.3.6 CryoET and FIBSEM reveal the NEC defines a precise vesicle geometry to accommodate capsids . . . 142
4.3.7 Integrative structural biology of nuclear egress . . . 145
4.4 Concluding Remarks . . . 146

5 Application of phase plates in molecular electron cryo-tomography 149
5.1 Introduction . . . 149
5.1.1 Principle of phase contrast microscopy . . . 149
5.1.2 Types of phase plates in electron microscopy . . . 154

5.1.2.1 Zernike phase plate 155
5.1.2.2 Volta phase plate 156
5.1.3 Biological applications of phase plates in electron microscopy . 157
5.2 Materials and Methods 161
5.2.1 Sample preparation 161
5.2.1.1 Dynein/Adenovirus 161
5.2.1.2 Glycoprotein B 162
5.2.2 Electron microscopy 162
5.3 Results and Discussion 163
5.3.1 Assessment of quality of data acquired with a Volta phase plate 163
5.3.1.1 Herpesvirus glycoprotein B 163
5.3.1.2 Dynein/Adenovirus 166
5.3.2 Factors affecting data quality 169
5.3.2.1 Lens normalization and beam shift pivot points . . . 171
5.3.2.2 Mechanical instability of the phase plate assembly . . 176
5.4 Concluding Remarks 177

6 Thesis Summary and Common Themes **180**

References **183**

A Extended Methods **212**
A.1 HSV1 purification and capsid isolation protocol 212
A.2 FSC curves for SPA experiments performed in Chapter 2 215
A.3 Table of parameters for tomograms used for analysis in Chapter 3 . . 217

B Published Works **219**

List of Figures

1.1 Overview of integrative imaging utilizing information from multiple techniques and resolution scales. 2

2.1 Schematic representation of the dynein motor and the bidirectional nature of cargo transport in cells 10
2.2 Adenovirus entry and trafficking to the nucleus 15
2.3 Schematic of a typical 2-condenser lens, field emission gun electron-cryo-microscope, equipped with post-column energy selecting filter . . 26
2.4 Virus preparation and isolation of capsids from cellular supernatant . 35
2.5 Total Internal Reflectance Fluorescence Microscopy (TIRFM) images and kymograph of a single movement along a microtubule 43
2.6 TIRFM of dynein-mediated adenovirus trafficking 46
2.7 Structural comparison of wildtype adenovirus and a ΔpIX variant. . . 48
2.8 Exposure to low pH results in the partial unfolding of surface protein pIX. 50
2.9 Structural comparison of wildtype adenovirus at pH 5 and pH 7. . . 52
2.10 Comparison of N-terminus of the dynein heavy chain (NHC) association with adenovirus under pH 7- and pH 5-treated conditions 54
2.11 Determination of viral hexons containing additional densities for the NHC construct 56
2.12 Association of the dynein tail complex with adenovirus in a pH-dependent manner 58
2.13 Electron cryo-tomogram of adenovirus interacting with the dynein tail complex viewed using a Volta phase plate 60
2.14 Electron cryo-tomography of heat-treated adenoviruses 63
2.15 Electron cryo-tomography of multiple dynein engaged with a single adenovirus 64

2.16 Assessment of the interaction between dynein, adenovirus and microtubules by electron cryo tomography 67
2.17 Segmentation of tomograms to isolate dynein transport events 69
2.18 Full segmentation of an individual dynein-recruitment event 70
2.19 A model for the pH dependent recruitment of the dynein tail to the adenovirus capsid 72
2.20 Schematic model of the putative dynein-adenovirus complex bound to a microtubule 73

3.1 Comparison of cellular electron cryo-tomograms from U87MG and U2OS cell lines 89
3.2 CryoET of a peripheral region of an adherent U87MG neuronal cell line imaged using direct electron detection 91
3.3 Structural context of Vault protein/dynein interaction 93
3.4 Sub-volume averaging of microtubules 96
3.5 Endosomal entry of Adenoviruses as a case for structure determination *in situ* 100
3.6 Model of the linear model used to determine the microtubule structure in Figure 3.5 101
3.7 Symmetrized structure of the Adenovirus in the U2OS tomogram . . 102
3.8 Sub-volume averaging *in situ* in a single tomogram is enough to correct for the CTF, and results in a corrected sub-volume averaged structure 104
3.9 Comparison of "gold standard" FSC curves for CTF and non-CTF determined structures 105
3.10 Comparison of sub-volume averaged microtubule structures with a PDB-generated "ideal" 13 protofilament model 107

4.1 Summary of the interaction network at the nuclear lamin of the inner nuclear membrane (INM) during egress 113
4.2 Summary of the optical setup, and beam conditions in 3D-SIM 117
4.3 Illustration of phase shift and angle change during acquisition of data for 3D-SIM 118
4.4 Diagram of the arrangement of coverslip and slide for live-cell imaging 125
4.5 Live cell 3D-SIM of RIE3134-GFP cells imaged at room temperature 129

4.6 Comparison of projection images of RIE3134-GFP nuclei taken from the same SIM stack and processed using widefield deconvolution and 3D-SIM reconstruction 131
4.7 Slices through a 3D volume of a porcine epithelial-like embryonic kidney cell determined by live-cell 3D-SIM at 37°C (~120 nm lateral resolution) 132
4.8 Projection images of widefield substacks taken from MCMV-infected NIH-3T3-LBRGFP cells PrV-infected and RKLBR-GFP cells 136
4.9 Slices and schematic of peri-nuclear vesicles within an electron cryotomogram of a cryoFIB lamella 138
4.10 Sub-tomogram average of a pUL31/34 perinuclear vesicle at 35 Å resolution 141
4.11 The model for the arrangement of the NEC coat 143
4.12 Schematic model of the NEC in peri-nuclear vesicles 144

5.1 Simplified schematic comparison of phase contrast methods employed in a phase contrast light micrograph and a single condenser electron microscope with a Zernike phase plate 151
5.2 Representation of the relationship between phase shift of the scattered and unscattered beams when considering weak phase objects 155
5.3 Schematic of two types of phase plate, the Zernike phase plate (ZPP) and the Volta phase plate (VPP) 158
5.4 Electron cryo-tomography of gB-enriched vesicles without a VPP . . 164
5.5 Electron cryo-tomography of gB-enriched vesicles with a VPP 167
5.6 Electron cryo-tomogram of adenovirus interacting with the dynein tail complex after treatment of the adenovirus to a pH 5 environment . . 168
5.7 Comparison of two images from an aligned tilt series acquired using the Volta phase plate with fall-off in contrast due to VPP/beam instabilities 170
5.8 Comparison of beam conditions in an electron microscope whereby "off-plane" imaging conditions may become evident using a VPP . . 174

A.1 Fourier shell correlation curves for adenovirus structures determined using SPA in this thesis. 216

Common Abbreviations

3D-SIM - 3-dimensional structured illumination microscopy

AAA+ - ATPase and associated activity

BicD - bicaudal D

CCD - charge coupled device

CEMOVIS - electron cryo microscopy of vitreous sections

cryoCLEM - correlative electron/light cryo microscopy

cryoEM - electron cryo microscopy

cryoET - electron cryo tomography

cryoFIBSEM - cryo focused ion beam/scanning electron microscopy

DED - direct electron detector

DPC - defocus phase contrast

DQE - detective quantum efficiency

Dynein - cytoplasmic dynein-1

EMDB - electron microscopy databank

FEG - field emission gun

FIBSEM - focused ion beam/scanning electron microscopy

FSC - Fourier shell correlation

GFP - green fluorescent protein

GIF - Gatan imaging filter

Hexon - adenovirus hexon protein

HSV1 - herpes simplex virus 1

INM - inner nuclear membrane

LBR - lamin B receptor

MAP - microtubule associated protein

MCMV - murine cytomegalovirus

MT - microtubule

MTOC - microtubule organization centre

NEC - nuclear egress complex

NR - nucleoplasic reticulum

ONM - outer nuclear membrane

OTF - optical transfer function

PALM - photoactivated light microscopy

pIX - adenovirus protein 9

PrV - pseudorabies virus

SPA - single particle analysis

STORM - stochastic optical reconstruction microscopy

TEM - transmission electron microscope

TIRFM - total internal reflectance fluorecence microscopy

VPP - Volta phase plate

WPA - weak phase approximation

ZPP - Zernike phase plate

1

Thesis Overview

1.1 Rationale

The ability to understand the mechanism of a cellular process in its entirety requires a holistic approach, that integrates information gained from atomic structure, three-dimensional conformation, binding partners and epitopes, protein localization and how the function of that protein impacts upon that organism. It is increasingly more important that the results be combined in ways that allow us to understand how a protein performs its function.

Recent advancements in fluorescence microscopy, and in particular, super-resolution microscopy (Schermelleh et al. (2010); Li and Betzig (2016); Sahl et al. (2016); Hoyer et al. (2016)) have re-defined the resolution limit to which we can image inside cells, both in fixed and live specimens. Super-resolution techniques such as photo-activated light microscopy (PALM) and stimulated-emission depletion microscopy (STED) are approaching resolutions as low as 5nm (Galbraith and Galbraith (2011))

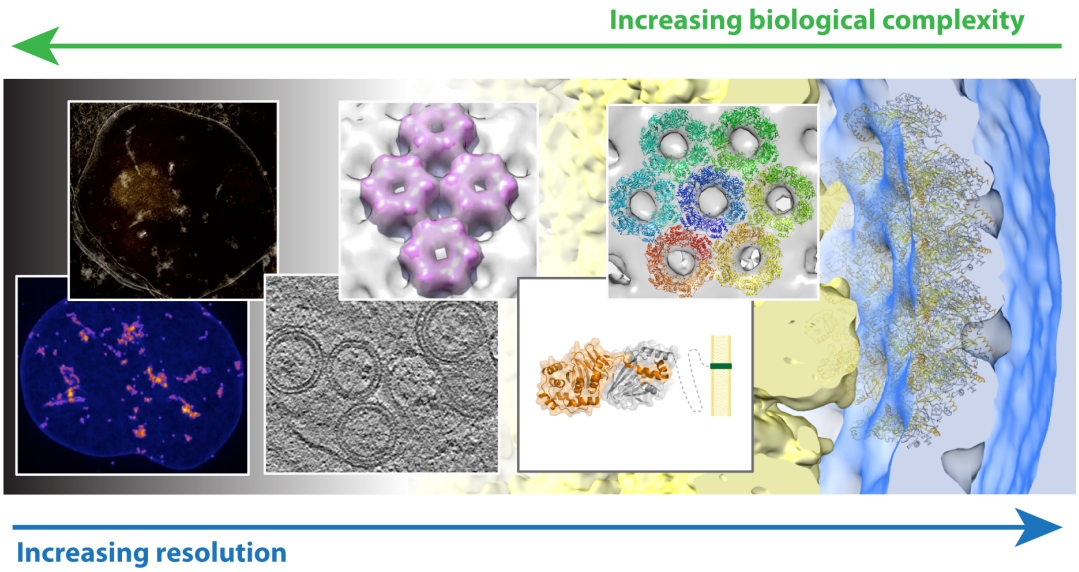

Figure 1.1 – Overview of integrative imaging utilizing information from multiple techniques and resolution scales. (Hagen et al. (2015); Zeev-Ben-Mordehai et al. (2015, 2014)).

and is now in the range of localization that can directly inform other techniques used in the structural biology field. Techniques such as cryo-correlative light and electron cryo-microscopy (cryoCLEM)(Schellenberger et al. (2014); Schorb and Briggs (2014)) and super-resolution cryo-microscopy techniques (Kaufmann et al. (2014); Liu et al. (2015); Chang et al. (2014)) combine fluorescence microscopy with electron cryo-microscopy and tomography (cryoEM/T) enabling the characterization of biological phenomena through multiple modes and resolutions. The combination of these approaches with live cell microscopy techniques (such as total internal reflectance microscopy, confocal microscopy and, at a more complex level, live cell super-resolution microscopy) also enable the assessment of dynamic features which can inform the above techniques. In combination, these approaches provide a very powerful method of determining the mechanism by which biological phenomena occur, and ultimately bridge the gap between high-resolution atomic and protein structure,

medium-resolution cellular organization and low-resolution dynamics.

Electron cryo-microscopy is another field that has recently entered a new era, recently reviewed in Nogales (2015). Direct electron detectors with a greater detective quantum efficiency (DQE) and increased frame rates now allow the collection of datasets as movies (Li et al. (2013)). Correction of beam-induced movement in the sample and the subsequent shifts between the individual frames of these movies results in more accurate determination of features within the corrected micrographs and hence contain a greater signal-to-noise ratio. This has led to an increase in the ability of cryoEM to produce atomic or pseudo-atomic structures of macromolecules. This has also led to an increase in the capabilities of cryoET, as a technique for determining the structure of irregular, pleomorphic objects (such as membrane bound organelles, or membrane proteins) that are analyzed *in situ* in their native environment (Schur et al. (2015); Bharat et al. (2015); Zeev-Ben-Mordehai et al. (2014)). Although informative, determining the structure of isolated molecules does not allow us to comprehensively explain a given process. In contrast, cryoET and its combination with other methods provide the means to dissect the biology in a cellular context and hence provide a more comprehensive picture of a biological process. The development of focussed ion beam milling-scanning electron cryo-microscopy (cryoFIB-SEM) now offers a means for the production of cellular samples in regions of cells that were hitherto inaccessible to cryoET (Marko et al. (2007); Rigort et al. (2012); Hagen et al. (2015); Mahamid et al. (2016)). Furthermore, the development of reliable phase plates that can be used routinely in an electron microscope, such as the Volta phase plate (VPP)(Danev et al. (2014); Fukuda et al. (2015); Danev and Baumeister (2016)), also

offer great potential in determination of the structural cellular context of biological processes.

1.2 Thesis Structure

In this thesis I use a combination of approaches, encompassing fluorescence microscopy, cryoEM, cryoET and cryoFIB/SEM, to investigate two crucial dynamic processes and understand their underlying molecular interactions; (i) the cytoskeletal trafficking of adenoviruses by the minus-end directed microtubule motor, dynein, and (ii) the egress of herpes virus capsids out of the nucleus across the inner nuclear membrane.

I discuss (Chapter 2) how adenoviruses recruit the cellular cytoskeletal motor, dynein, and how it mediates the interaction of adenovirus to the microtubule. The complicated nature of the dynein-cargo interaction mechanism makes it difficult to determine whether there is a direct interaction between adenovirus and dynein, or whether a cellular co-factor is required to mediate the process. I establish whether a direct interaction is possible and whether there is a pH-dependent effect on the interaction, and relate this to pH-dependent structural variations on the surface of the adenovirus. Investigation of the reconstituted dynein tail complex with the adenovirus then allows me to assess the ability of dynein to associate with an adenovirus. This led me to analyze the 3-dimensional organization of the full dynein complex while bound to the microtubule and adenovirus, and to propose a putative dynein tail binding region on the adenovirus capsid.

The interaction of the dynein complex with adenovirus and the microtubule, as viewed *in vitro*, allows the determination of the 3-dimensional organization in an isolated recombinant system. However, the process of adenovirus transport to the nucleus does not occur in isolation from other cellular factors. Hence, I next assess the ability of cellular cryo-electron tomography to unravel the organization of virus transport *in situ* (Chapter 3). I assess what can be revealed in cases of rare or unique events, and the level of structural information that can be dissected within cellular cryo-tomograms (Chapter 3). I discuss how this may bridge the knowledge between *in vitro* structure determination, *in situ* structure determination and cellular context and how the information that can be currently obtained on a biological process can be improved upon using cryoFIB/SEM (Chapter 4), cryoCLEM and phase plates (Chapter 5).

Super-resolution microscopy is a means of imaging of cells at sub-diffractive resolution, in both live and fixed specimens, in which the organization and localization of proteins can be viewed in the cellular context. I use the greater contextual information super-resolution microscopy provides, as well as widefield techniques, to view the egress of herpes virus capsids as they are transported across the inner nuclear membrane (Chapter 4). Integrating these methods with cryoET, cryoFIB/SEM and sub-volume averaging, I discuss the mechanism of a novel, herpes-specific means of nuclear-pore independent transport out of the nucleus, and discuss its potential as a potential cellular mechanism for nuclear escape of large cargoes.

Finally, lack of contrast in cryoET is a major limitation in our ability to discern structures both *in vitro and in vivo*. Recent developments in the production of more

stable and robust phase plates for electron microscopy are beginning to show potential in becoming a routine method of contrast enhancement in cryoET. I provide a discussion and examples of the application of Volta phase plates for in-focus molecular cryo-tomography (Chapter 5), and its implementation into current electron microscopes. I discuss the theoretical basis of the VPP and suggest ways to improve the stability and application of this technology in cryoET.

The examples highlighted in this thesis represent an attempt to use a wide range of techniques available to probe the structure and context of biological processes. Future application and combination of these techniques promises a revolution in the way that structural cellular biology is carried out, and provides a superior method for viewing the native context of biological processes to that traditionally used in classical electron microscopy.

2

Structural and temporal determination of dynein-engaged cargoes

2.1 Introduction

2.1.1 Microtubule-based transport in cells

The canonical single unit of life, the cell, is a complex multifunctional body containing a multitude of compartmentalized and non-compartmentalized organelles that perform an array of different functions essential for its overall propagation and survival. Prokaryotic cells, which include bacteria, and archea, are on the order of 2-20 µm in size, dependent on the organism. In contrast, eukaryotic cells, which make up the main unit in multicellular organisms, are typically much larger. Cells, and sub-

stituent organelles, must share, communicate and transport cellular factors in order to function. The size of a eukaryotic cell precludes the ability of the cell to rely on simple diffusion of material, as this is not efficient for regulated cellular functions. Eukaryotic cells rely on an intricate cytoskeletal network that maintains the overall structural integrity of the cell and allows intracellular transport of material. This cytoskeleton is made up of various polymeric filaments that perform different roles.

Components of the cytoskeleton include actin, which is involved in a number of essential cellular processes, including transport (via interaction with myosins), and is one of the main components involved in muscle contraction, and intermediate filaments, which serve as a major component of the structural framework of cells. Another component of the cytoskeleton, microtubules, are cylindrical polymers that are assembled from the approx. 50 kDa protein, tubulin. α- and β-heterodimers of tubulin are able to self assemble and polymerize from the microtubule-organizing centre (MTOC), located near the nucleus. Here, a molecular scaffold known as the γ-TuSC complex (Kollman et al. (2010, 2015)) nucleates the formation of the minus-end of a microtubule and serves as a template from which the microtubule can grow from towards the periphery of a cell at the microtubule's plus-end, which polymerizes at a faster rate than the minus end. Due to the arrangement of the γ-TuSC complex, microtubules contain 13 protofilaments *in vivo*. Microtubules serve as a cellular highway for the directed trafficking of cargoes around the cell (Figure 2.1). The inherent polarity of the microtubule means that motor proteins are able to molecularly sense the directionality of the tubulin α- and β-heterodimers, move in a defined direction and thus direct transport to and from the poles of the microtubule (Carter et al.

(2008); Shang et al. (2014); Woehlke et al. (1997)).

2.1.2 Dynein-based transport

Cytoskeletal trafficking of cargoes is an essential cellular process and involves the active transport of molecular entities, vesicles and organelles to the correct spatial and temporal locations within cells. These processes are performed through the action of the molecular motors myosin (actin), kinesin (microtubules) and dynein, which utilize the actin and microtubule cytoskeletons as molecular railroads (Hackney (1996); Mallik and Gross (2004); Kardon and Vale (2009)). Kinesins are responsible for the bulk of plus-end directed cargo trafficking (Kinesin-1) (although some kinesins are minus-end directed). Cytoplasmic dynein-1 (Dynein) is a minus end-directed microtubule associated protein (MAP) that is able to perform work to move along microtubules (Burgess et al. (2003); Schmidt et al. (2012); Kon et al. (2012); McKenney et al. (2014); Schlager et al. (2014)). Dynein is a large, multimeric complex of approximately 1.5 MDa, with an ATPase with associated activities (AAA+)-related motor domain of approximately 500 kDa that is responsible for force-generation (Kon et al. (2012); Schmidt et al. (2014, 2012)). The rest of the motor is made up of multiple light, light-intermediate and intermediate chains, as well as TCTEX1 and Roadblock 1 (RobI) (Schlager et al. (2014)). These domains are important in binding to cargoes, cargo-adaptor proteins such as NudE, Lis1, Hook3 and BicD, and to the processivity factor dynactin (Kardon and Vale (2009); Schroeder and Vale (2016)). The ability for dynein to bind to different cellular cargoes is obtained through these cargo-adaptor

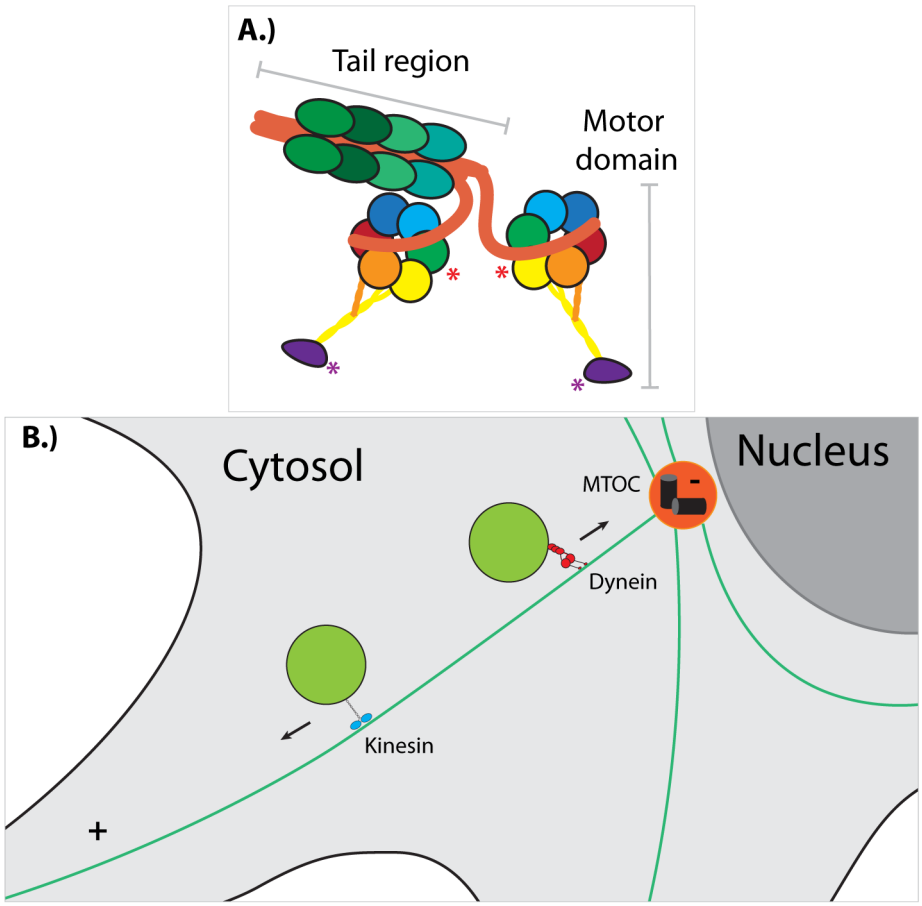

Figure 2.1 – Schematic representation of the dynein motor and the bidirectional nature of cargo transport in cells. A.) the full-length dynein dimer, highlighting the AAA+ motor domain (red asterisk) (with domain colouring taken from Schmidt et al. (2014)), the dynein tail region and microtubule binding region (purple asterisk). Orange shows the linker and tail-binding region of the heavy chain which is continuous with the AAA+ domain. B.) the bidirectional nature of cargo transport in cells. Vesicular (and organelle) cargoes are transported towards the minus end (MTOC) of cells via cytoplasmic dynein-1, facilitated by accessory co-factors, whereas peripheral transport of cargoes towards the plus end is directed by kinesins (such as kinesin-1).

proteins. This is in contrast to the plus-end directed motor, kinesin, which has many genetic isoforms that perform various roles in cells.

Dynactin is a 1.2 MDa protein that plays a key role in the processivity of the dynein motor during transport of cargoes, as well as other roles in eukaryotic cells such as centrosome tethering (Schroer (2004)). Dynactin is important in the transport of large cargoes such as vesicles, organelles and viruses, and down-regulation of dynactin via the over-expression of the dynactin sub-unit dynamitin in cells has been shown to abrogate herpes simplex-1 (HSV1) cytosolic trafficking (Radtke et al. (2010)). This capability of dynein/dynactin for ubiquitous cytoskeletal transport has been hijacked during the evolution of viruses, with a known interaction between the dynein motor and both adenovirus and HSV1 capsids (Dodding and Way (2011)), as well as a putative role for dynein in the transport of human immunodeficiency virus-1 (HIV1) (Lehmann et al. (2009); Dodding and Way (2011)). Reconstitution *in vitro* of cellular vesicle trafficking using cellular components has proven to be difficult. As such, a viral cargo, that contains the peripheral entities required for trafficking would prove to be a novel route to assess the dynein/cargo binding properties.

An important molecular determinant for which cargoes are recruited by dynein is the accessory cargo-adaptor protein that is associated with the cargo. Unlike the kinesin superfamily of plus-end directed motors, cytoplasmic dynein-1 is the only minus-end directed motor that is expressed and present in the cytosol of cells (cytoplasmic dynein-2 is a cilia transport effector). As such, dynein has evolved a molecular toolkit (Kardon and Vale (2009)) of accessory proteins that act in the transport of certain factors in cells e.g. organelles, vesicles or mRNA. Such accessory proteins, for

example BicD, facilitate the recruitment of dynactin to the dynein motor and thereby increase its processivity (Schlager et al. (2014); Urnavicius et al. (2015)). These accessory proteins typically form a coiled-coil motif, implicating coiled-coil proteins in transport as processivity factors for dynein. Viral subjugation of this aspect has been proposed as a potential method of efficient viral transport to the nucleus (Pasdeloup et al. (2013); Pitts et al. (2014)).

2.1.3 Cytoskeletal transport of viruses

2.1.3.1 Herpes Simplex Virus 1

Herpesvirales is an order of viruses that contain large DNA genomes, surrounded by a T=16 nucleocapsid of approximately 120 nm diameter (Cheng et al. (2002)) and a membranous outer envelope. In between the capsid and the membrane, there is a proteinaceous layer called the tegument (Grünewald et al. (2003)). The order are commonly grouped into three sub-families; alpha-, beta-, and gamma-herpesviruses. These three groups all contain high degrees of homology in terms of gene sequence as well as overall morphology (Mettenleiter et al. (2009)).

HSV1 is an alphaherpesvirus and human pathogen that has been characterized structurally using electron cryo-tomography (cryoET) (Grünewald et al. (2003)). It is a membrane enveloped virus approximately 200 nm in diameter coated with multiple glycoproteins that are essential in cellular fusion and entry (Maurer et al. (2013)). Inside the membrane is contained the tegument layer and the genome-encapsulating icosahedral capsid. The tegument is a proteinaceous layer associated with the capsid

and performs multiple functions in the life cycle of HSV1. An outer tegument remains with the cytoplasmic membrane during entry, and an inner portion remains associated with the capsid. This is important for trafficking to the nucleus and capsid docking with the nuclear pore complex (Pasdeloup et al. (2009, 2013); Dodding and Way (2011)). The herpesviral capsid has T=16 icosahedral symmetry, made up of VP5 (major capsid protein), VP26, VP23 and VP19C. The 12 vertices of the icosahedral capsid are occupied by 11 pentons units, with one vertex forming a portal for the packaging of viral DNA and potential release of DNA after docking with the nuclear pore complex (Bowman et al. (2003)).

Retrograde transport of the herpesvirus capsid, i.e. towards the nucleus, requires multiple components of the tegument. It has been shown that the tegument protein, pUL36, and the capsid protein, pUL25, are essential for the transport of the capsid toward the nucleus and for dynein/dynactin-mediated microtubule transport (Zaichick et al. (2013)). Interestingly, a recent study has suggested a key role for pUL37 in trafficking of the herpes capsid, with the crystal structure of the N-terminus of pUL37 having significant homology to multi-subunit tethering complexes that play significant roles in vesicle trafficking and membrane fusion (Whyte and Munro (2002); Bröcker et al. (2010); Pitts et al. (2014)). This suggests a viral hijacking of the mechanisms of vesicle trafficking in cells, and therefore research into the process of viral trafficking is not only relevant to the treatment of disease, but also to understanding of the global cellular process of cargo trafficking.

2.1.3.2 Adenovirus

Adenoviridae are a family of viruses that cause a widespread range of symptoms in humans and animals. Human adenovirus is a respiratory virus that can cause mild flu-like symptoms, or, in immuno-compromized individuals, life-threatening organ failure. Adenovirus is a non-enveloped virus, approximately 95 nm in diameter composed of a proteinaceous icosahedral capsid, inside which is contained the genetic material. Adenoviruses bind to cells via their penton fibre, contained on the 5-fold vertex of the icosahedral capsid. A penton knob structure on the end of the penton fibre binds directly to the Coxsackie-Adenovirus receptor (CAR) (Bewley et al. (1999)) and cells expressing the CAR receptor are susceptible to infection by Adenovirus. Interaction of the CAR-penton knob complex with β-integrin encourages clathrin-mediated internalization into an endosome (Wickham et al. (1993)). Once internalized, traditional models of adenovirus entry have suggested that the adenovirus begins to break down, and penton release occurs, as well as the release of pVI and its subsequent disruption of the endosomal membrane (Martinez et al. (2015)). Subsequently, the release of adenovirus into the cytosol and its trafficking to the nucleus are thought to be dependent on dynein (Scherer and Vallee (2015); Scherer et al. (2014); Bremner et al. (2009); Strunze et al. (2011)). A schematic model of adenovirus entry is shown in Figure 2.2.

The models for adenovirus trafficking have all relied on the ability of adenovirus to recruit dynein to the surface hexon protein of the icosahedral capsid, which is the main structural component (Scherer et al. (2014); Scherer and Vallee (2015)). The

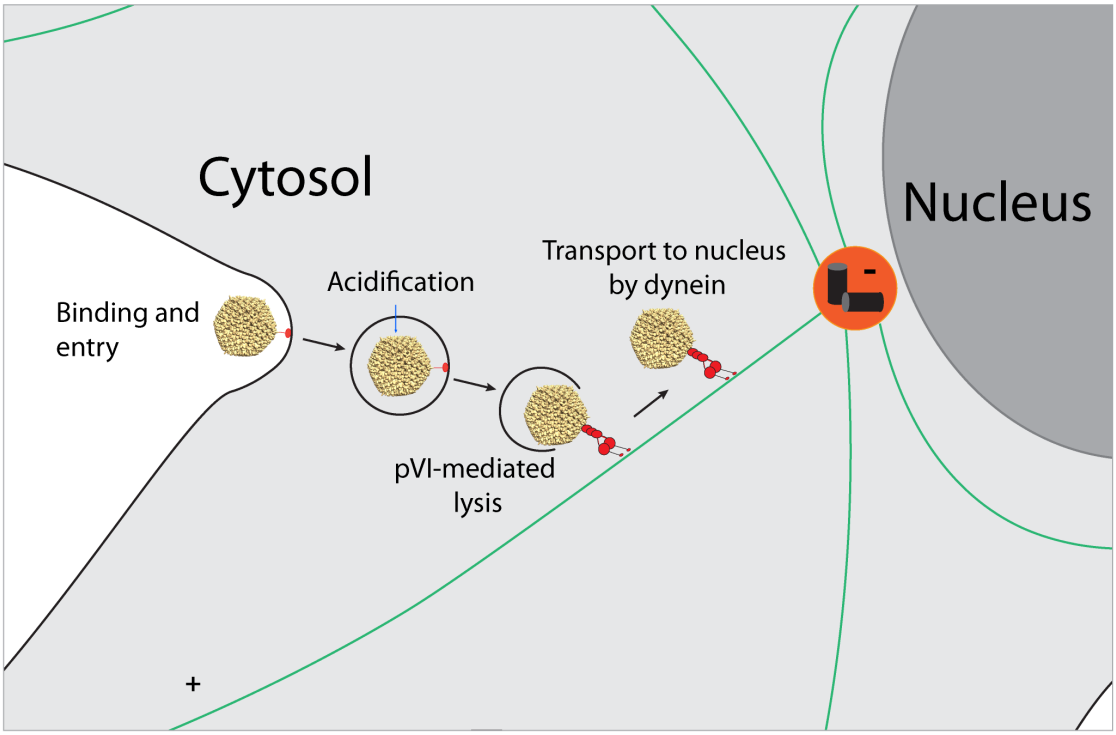

Figure 2.2 – Adenovirus entry and trafficking to the nucleus. Schematic representation of adenovirus entry into the cell, subsequent recruitment of dynein and transport to the nucleus.

recruitment of motor proteins has been suggested to play a role in the disruption the adenovirus particle at the nuclear pore, and have implicated other adenoviral proteins, for example protein pIX interaction with kinesin-1, to be important in this process. (Strunze et al. (2011)). It may well be feasible that other cellular co-factors as well as other components of adenovirus are important in the recruitment of adenoviruses, the determination of processivity and, potentially, the production of a kinesin-dynein transport holocomplex (Mallik et al. (2013)). The ability for dynein to associate as ensembles to cargo, thereby determining the direction of processivity as a function of tug-of-war is also an unknown quantity when considering viral transport (Rai et al. (2016)). These above aspects of adenovirus transport still remain ambiguous, and the precise role, interaction, stoichiometry and dynamics of dynein association with adenovirus, still remains to be fully elucidated.

Electron cryo-microscopy (cryoEM) and electron cryo–tomography (cryoET) allow the direct imaging of proteins and other macromolecules in their native, frozen-hydrated state, and their subsequent structure determination by sub-volume averaging or single particle analysis. CryoET, in particular, is a very useful technique for determining the 3-dimensional architecture of pleomorphic, non-uniform and transient structures. Here, I use cryoEM and cryoET, as well as fluorescence microscopy, to directly image and characterize the transport of dynein-engaged adenovirus along microtubules.

2.1.4 Preparation of samples for electron cryo-microscopy studies

Electron microscopes operate at high vacuum, in order to reduce scattering of the electron beam by air molecules. Historically, EM sample preparation techniques required the dehydration and staining of purified proteins onto EM grids in order to enable imaging (Radermacher et al. (1987)). This requirement lead to a very robust and clear way of viewing proteins as well as many complexes, that gave an insight into their low resolution organization (Chowdhury et al. (2015); Imai et al. (2014, 2015); Radermacher et al. (1986)). However, the contrast produced in the negative-stain images is a result of the scattering by the heavy metal atoms in the stain, and the resolution of the stained protein is limited to around 15-20 Å, due to the depth of penetration of the stain and the lack of fully 3-dimensional coverage of stain around the whole sample. Furthermore, the dehydration needed to prepare the samples alters them chemically, producing a structure of proteins or large macromolecular complexes (e.g. viruses) that is not native.

In order to solve these issues, attempts were made to move the sample conditions more to the native environment and preserve the hydrated state. However, liquid water would evaporate inside the high vacuum of the microscope. In a landmark study, Taylor and Glaeser were able to produce frozen-hydrated catalase crystals able to produce high-resolution diffraction patterns using EM (Taylor and Glaeser (1974)). However, the most crucial (and relevant) development toward viewing frozen-hydrated individual complexes using EM was devised by Jacques Dubochet in 1981 (Dubochet

and McDowall (1981)). This development allowed the vitrification of thin samples on electron microscopy grids that preserved the hydrated nature of the biological sample. The sample is applied to an electron microscopy grid held by tweezers in a hydraulic device above a dewar. Inside the dewar is a small cup, filled with ethane and cooled to near liquid nitrogen temperatures. This liquefies the ethane. The high specific heat capacity of ethane means that is has a large rate of change of temperature, and serves a better vitrification medium than liquid nitrogen. The sample is dropped into the cup of ethane after the sample has been wicked away to form a thin layer, typically between 50-300 nm, on the grid. The combined large specific heat capacity of ethane, high speed of plunging of the grid into the ethane and the large surface area of the sample result in a very large rate of change of temperature of the sample. This freezing is so quick (approx. $105 K/s^{-1}$) that water molecules are unable to nucleate and crystallize, and results in a disordered arrangement similar to the aqueous form.

Since this work by Jacques Dubochet and colleagues, there has been much progress in developing more complex means of preparing frozen-hydrated vitreous samples, from molecules to cells.

2.1.4.1 Purified or isolated macromolecules

The ability of the electron microscope to image molecules with a very small wavelength provides a means to determine high resolution atomic structures (Azubel et al. (2014)). In structural biology, the low scattering propensity of biological macromolecules due to the low molecular weight of carbon, oxygen and nitrogen (from which they are composed) means that extensive computational processing must be

utilized in order to recover the signal of the protein from the relatively high noise signal in the micrographs. This requires a large number of different views of the macromolecule and therefore a sample that is highly purified, ideally homogeneous, and well distributed across the grid. The ice thickness of the sample must be very thin, in order to achieve the greatest signal-to-noise possible and the concentration of particles must, in general, be high in order to acquire enough images with enough particles for downstream processing. In order to achieve the thin ice in a reproducible fashion, automated or semi-automated plunging apparatus are often used. These apparatus are able to regulate the humidity and environment of the sample while on the grid, in order to prevent evaporation. Further improvements can be made by utilizing emerging technologies, such as gold grids (Russo and Passmore (2014)), and by utilizing amphipols (Flötenmeyer et al. (2007)) which help to reduce beam induced motion and preferred particle orientation, respectively.

2.1.4.2 Approaches to investigating macromolecular complexes and their interactions

Using cryoEM and cryoET, it is also possible to image complex protein interactions, as well as their association with other non-proteinaceous material, such as lipid bilayers, nucleotides or polysaccharides. Several examples of this can be found in examples such as (Pfeffer et al. (2015); Zeev-Ben-Mordehai et al. (2014); Brown et al. (2015); Nguyen et al. (2015)). Samples purified recombinantly or isolated from cellular extract can be plunge frozen as described above. As the technique of cryo-plunging preserves the protein in solvent, the native molecular interactions are preserved, which allows

them to be imaged through single particle analysis or tomography. These aspects make cryoEM unique in the field of structural biology.

Further to directly applying samples to the grid for plunge freezing, experiments can also be performed directly on the electron microscopy grid. The grid is glow discharged prior to plunge freezing, adding charge to make the carbon more hydrophilic. As such, the grid itself can act to pull down molecules. This can then be used to probe further interactions with potential co-binding molecules. This is especially useful if one component can only be purified in a medium that is not conducive to cryoEM, such as glycerol, high salt or at low pH. In this case, the grid essentially acts as a filter or mini-dialysis surface.

2.1.4.3 Macromolecular interactions in their native cellular context

The study of the architecture and organization of cells using electron microscopy has traditionally focused on freeze-substituted, plastic embedded and sectioned samples using an ultramicrotome. Although useful, these samples require the fixation and staining of cells, and do not contain many of the fine ultra-structural details that many structural biologists may find interesting. Several alternatives have recently been developed, allowing the native structures of cells to be elucidated and probed. Here I will focus on the growing of adherent cells on gold-mesh, carbon-coated electron microscopy grids, and associated developments.

Cells that grow adherently in culture grow in a planar manner on the surface of the support. Although hydrophobic, the carbon that sits on top of electron microscopy grids can be coated in a surfactant that makes it more attractive for cell culture,

such as fibronectin or poly-L-lysine. Gold grids must be used, as regular copper grids are toxic to cells. Coated grids are placed into the regular cell culture dish and cells grown as normal. Some adherent cell types exhibit very thin peripheral regions that are approximately 100 nm around the region of the periphery of the cell. Thicknesses on this scale can be penetrated by the electron beam and are suitable for tomographic data collection. The interior of the cell is also accessible, though this requires the use of focused ion beam milling/scanning electron microscopy or FIB-SEM (Rigort et al. (2012)). Here, a beam of gallium ions is directed towards an area of interest, such as the nuclear region, that ablates above and below this region leaving a lamella of a specified thickness. This allows the collection of tomographic data that gives details of cellular architecture that was previous unavailable due to the thickness, and, downstream processing such as sub-volume averaging (Asano et al. (2015); Mahamid et al. (2016)).

2.1.5 Introduction to electron microscopy

The electron microscope was first developed by Ernst Ruska and Max Knoll in 1933. Continued development of the electron microscope lead to commercialization by a number of companies, including Siemens, Phillips and Zeiss, in the 1960s and included both transmission and scanning electron microscopes. Current transmission electron microscopes (TEMs) are far more advanced than their predecessors, with developments in magnetic lens quality, vacuum quality, precision engineering and electronics, the development of image filters, charge-coupled device (CCDs) and di-

rect detection cameras and field emission guns (FEG) as a source of emission being just a few improvements made to current electron microscopes. Equally as important has been the development of automated acquisition procedures and software to control the operation of microscopes. Electron microscopes used in structural biology typically have an information transfer limit of between 1.2 – 1.6Å (although this can be higher in microscopes used for materials science), and the main limitation in determining atomic structures in biology is the nature of the sample.

2.1.5.1 Electron sources and coherence

Electron sources for electron microscopes are typically either a tungsten filament, a lanthanide borate (LaB_6) filament, a Schottky-FEG or a cold-FEG. The coherence of the electron source is very important for high-resolution imaging, so most high-resolution microscopes in electron cryo-microscopy will use a Schottky-FEG tip. The distinction between a FEG and a LaB_6 or Tungsten tip is that a FEG is finely sharpened to a point, and then a voltage is applied along that tip that draws electrons toward its fine end. This causes the electrons to produce a small field around the tip and the opening of the Wehnelt chamber from which the extraction voltage is applied. The electrons produced by the tip are then accelerated to a desired voltage (300kV) through the gun lenses and gun coils. As the electrons are concentrated toward the tip of the gun, they are extracted with a lower energy spread, and hence the range of wavelengths of the electrons is relatively low. This vastly improves the coherence of the electron beam.

The difference between Cold-FEGs and Schottky-FEGs is the temperature at

which they are operated, with Schottky-FEGs being heated using an extraction voltage. Cold-FEGs typically have a greater coherence due to their smaller physical tip size, but have a lower lifetime due to their greater propensity for surface contamination at lower vacuum. Schottky-FEGs are the more popular choice for high resolution biological TEM, due to a trade-off between a relatively high spatial coherence and their practicality (lifetime).

2.1.5.2 Image formation

The electron beam is then collimated and focused through a two or three lens condenser system, dependent on microscope model. This serves to produce a parallel beam for imaging, and reduce on- and off-axis coma. The coherent and parallel beam will then hit the sample. A thin sample, such as those used in electron cryomicroscopy, will act as a weak-phase object, that can be assumed to behave as described by the weak-phase approximation (WPA) where the phase modulation is proportional to the intensity fluctuations in the image. This allows us to assume a linear contrast transfer function (CTF) to describe image formation. If we consider the way in which information is transferred to an image in the electron microscope, we can describe the phase contrast transfer function mathematically as (Nagayama (2011)):

$$sin\gamma(\mathbf{k}) = 2\pi(-\frac{1}{2}\Delta z\lambda\mathbf{k}^2 + \frac{1}{4}C_s\lambda^3\mathbf{k}^4) \tag{2.1}$$

where Δz is defocus (µm), λ is the wavelength, $C_s$is the spherical aberration and

k is the spatial frequency.

This equation contains terms for the components of the microscope that affect and the modulation of contrast in our image. Adjusting either the wavelength (Voltage) or the defocus will change the way in which the contrast is modulated. However, for a given microscope that is not spherical aberration corrected, the spherical aberration is constant and during an experiment the accelerating voltage will not be changed. The only practical way of modulating contrast in images is to change the defocus. In an EM image, the scattered and unscattered beam interfere producing an oscillating contrast transfer function that must be corrected for later (see also section 5.1.1). Applying an amount of defocus changes the relative path difference of the scattered and unscattered beams, and increases the amount of contrast visible in the image at low resolutions. Electrons interacting with the sample will be scattered elastically, and be re-focussed by the objective lens into the back focal plane (BFP). At the back focal plane, the image will roughly represent the frequency space representation of that image, which can be described using Fourier theory.

Once the electron beam has passed through the objective aperture, it can then be reformed into an image through passage of the intermediate and projection lenses. These determine the magnification of the final image. Alternatively, the electron beam can enter an image filter (the most common variant a Gatan Imaging Filter or GIF (Gatan, Inc)). A GIF separates electrons according to their energies by passing the electron beam through a complex array of electromagnetic lenses. Although we have assumed the WPA, not all electrons that interact with sample will have behave elastically. These inelastically scattered electrons become incoherent and contribute

to the noise in the reformed image. However, because they have lost energy, they can be separated from the incident electron beam. We centre the GIF's energy selecting "slit" to the zero-loss electron peak, which restricts the electrons passing through the GIF to only those electrons that have conserved energy, i.e. "zero-loss" electrons. After passing through the GIF, the electron beam can then be reformed to produce an image with less noise contribution from inelastically scattered electrons.

2.1.5.3 Methods for data collection in electron cryo-microscopy

Data acquisition strategies for electron cryo-microscopy are mostly dependent on whether one works with (i) homogeneously expressed "single particles" of protein or other macromolecular entities, or (ii) whether the sample will be more pleomorphic in nature, for example, single, non-regular macromolecular assemblies, or cells, that are often arranged in a more native context.

Single particle analysis is the collection of micrographs that contain a field of view of protein, or virus, that have been highly purified and isolated to a high homogeneity. In this strategy for structure determination, vitrified specimens (see 2.1.5) are exposed to a high-dose from the electron beam, and a projection image produced for that field of view. Many images are collected and processed, so that the different orientations of the particles contained within the micrographs can be determined, for example using classification methods such as principle component analysis or k-means clustering on the particles in 2-dimensions. Once a robust analysis has been performed on the possible 2-dimensional orientations of the sample as it is embedded in the projection images, the 2D classes can then be used to reconstruct the 3-dimensional

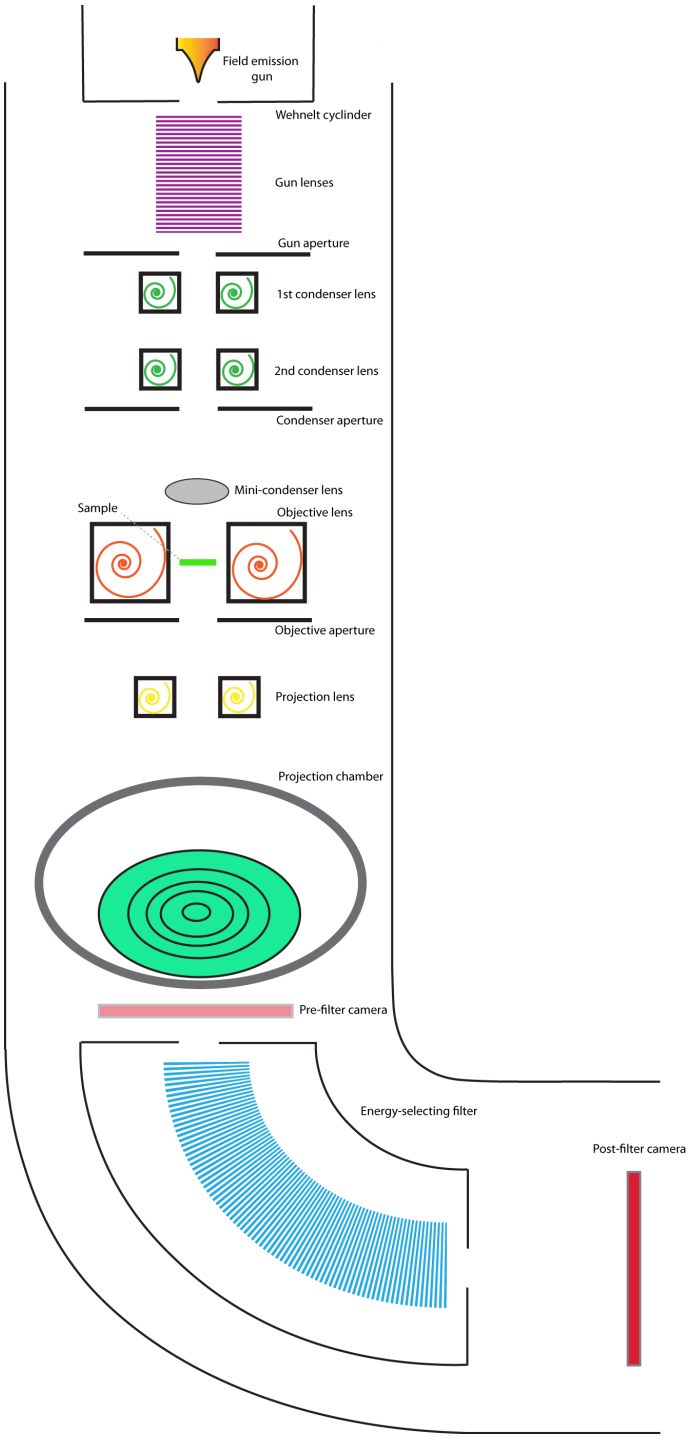

Figure 2.3 – Schematic of a typical 2-condenser lens, field emission gun electron-cryo-microscope, equipped with post-column energy selecting filter. This arrangement is typical for the Tecnai range of electron microscopes (FEI, Eindhoven), the type of microscope used for the majority of cryoEM in this thesis.

structure of that particle, as each orientation represents a slice in the 3-dimensional Fourier transform of the complex. If a previously determined (often low resolution) 3-dimensional reference is not available (or to avoid initial model bias), the 2D classes can be used to produce an initial 3D model by using techniques such as common lines or sinograms, tilt-pair analysis or random conical tilt (e.g. on negatively stained data sets). As each 2-dimensional projection is compared to the 3-dimensional reference, and the orientation determined, the 3-dimensional structure is iteratively refined, and the resolution of the structure increases up until a point at which the correlation between two half maps of the particle dataset no longer increases and the structure has "converged". This correlation represents the Fourier shell correlation for the 2 half maps, and currently determines the resolution at which we define the final structure to be. For a recent review on single particle methods, especially in the era of direct electron detection, see Elmlund and Elmlund (2015).

Electron cryo-tomography is the other main imaging modality used in electron cryo-microscopy, and is used to determine the 3-dimensional volume of a single pleomorphic object that would otherwise be unsuitable for single particle methods. Images are acquired sequentially through tilting the stage of the electron microscope to angles typically ranging from +/- 60° with images acquired, for example, every 3°. In this way, a 3-dimensional picture can be determined of the sample as each tilt angle at which an image of that object is acquired represents one orientation of it. However, as the sample approaches 90° it becomes too thick to image, and it is not possible to get a full 360° dataset of the object resulting in a "missing wedge" of information. Attempts to compensate for this missing wedge have been attempted,

for example using dual-axis tomography (Iancu et al. (2005)). However, despite best efforts, missing information still remains, and must be compensated for in any structural analysis. One of the drawbacks to electron cryo-tomography is the need to split the total dose applied to an object over multiple tilt images before radiation damage becomes predominant. This is in contrast to single particle where the entire dose, say $80e^-/A^2$, can be applied to produce one image that can be subsequently dose weighted to recover the high resolution information (Grant et al. (2015)). In electron cryo-tomography that same $80e^-/A^2$ would need to be split over the images across the range for that tomogram (for example, +/- 60 = 40 images), resulting in individual tilt images with much lower contrast. Furthermore, the thickness of the sample increases by the cosine of the tilt angle resulting in samples of much greater thickness at higher tilts, reducing the signal-to-noise ratio in images even further. Indeed, studies have suggested that much of the high resolution information is lost at high tilt, and potentially detracts from the resolution one can achieve (Bartesaghi et al. (2012)). Despite this, attempts have been made to weight images in tomographic series appropriately by their tilt angle and their dose (Galaz-Montoya et al. (2016); Bharat et al. (2015)) and combined with judicious choice of data acquisition schemes (Hagen et al. (2017)) recent studies have shown that tomographic data can produce structures via sub-volume averaging that are comparable to those of single particle methods (Schur et al. (2016)). Sub-volume averaging involves averaging recurrent molecules within tomograms that are then aligned to one another in an iterative fashion and averaged to produce a structure of that sub-volume with greater signal-to-noise and higher resolution.

The above two modalities illustrate how an electron cryo-microscope can (i) be used to produce data that can reveal atomic information on biological questions while at the same time (ii) serving as a cell biological tool to reveal native, *in situ* information on cellular structural context.

2.1.5.4 Electron detection and a push to increased resolution and signal-to-noise

Recent advancements in detectors for electron microscopy have allowed the digitization of the electron image that previously required the use of radiation-sensitive film and scanners. CCD (charge-coupled devices) cameras were the first major step toward routine electron cryo-tomography data collection (for review see Faruqi and Subramaniam (2000)). CCDs allowed data to be acquired while performing the tilt series without having to change film and also enabled its automation, making it much less time-consuming. However, the use of a scintillant in CCDs leads to a lack of fidelity in the localization of an electron to a pixel in the detector, especially at high voltages (Faruqi and Henderson (2007)).

To overcome this problem, direct electron detectors (DEDs) have been developed in the field of structural biology that have greatly increased the DQE to which an electron can be detected, as well as the frame-rate for image acquisition. DEDs have no scintillator, and utilize a CMOS (complementary metal–oxide–semiconductor) architecture that allows the direct detection of the electrons on the detector. The further development of back-thinned detectors reduces the medium through which the electron needs to pass in order to be registered in the electronics even further,

thereby increasing the DQE (Li et al. (2013); McMullan et al. (2014)). The concomitant ability to record data with a high frame rate has meant that it is possible to track beam induced movements within the sample that can be computationally corrected for (Li et al. (2013); Fernandez et al. (2013); Liao et al. (2013)). This has lead to a great increase in the attainable resolution for biological specimens and macromolecular structure determination (Bartesaghi et al. (2015)).

Here I use single particle cryoEM, cryoET, and fluorescence microscopy to directly image and characterize the transport of dynein-engaged adenovirus along microtubules. The current understanding of dynein motility is mostly limited to the structural basis for its procession along microtubules, association with its cellular processivity factor dynactin and the recruitment of a cargo adaptor protein to the dynein/dynactin complex, BicD1 (Kon et al. (2012); Schmidt et al. (2012, 2014); Urnavicius et al. (2015)). The association and arrangement of dynein with respect to a *bona fide* cargo, viral or cellular, is yet to be visualized. Similarly, the arrangement and structure of the dynein tail domain, and how the tail interacts with a potential cargo, if at all, remains elusive. In this chapter, I determine the dynamics and architecture of dynein bound to adenovirus in a reconstituted system, visualize how dynein and adenovirus may interact as a complex with microtubules, and elucidate the molecular determinants on the viral surface required to mediate this interaction.

2.2 Materials and Methods

2.2.1 Preparation of microtubules

To polymerize microtubules *in vitro*, 10µl purified tubulin (Cytoskeleton, Inc) (1µl hiLyte-488 tubulin was added for fluorescent microtubules) at 1 mg/ml was mixed in a 1:1 ratio with Polymerization buffer (20% Dimethylsulfoxide, 160 mM PIPES pH 6.9, 2 mM GTP, 2 mM $MgCl_2$, 4 mM EGTA) and incubated at 37°C for approximately 30 minutes. 2 µl of paclitaxel at 10 mM was then added to the mixture and incubated for a further 10 mins. For TIRFM assays, the microtubules were spun for 10 minutes at full speed using a tabletop centrifuge. For electron microscopy studies, polymerized microtubules were applied to a two-step glycerol cushion (40% glycerol, 80 mM PIPES pH 6.9, 2 mM EGTA, 1 mM GTP and 30 µm Paclitaxel) and centrifuged at 29000x rpm for 30 minutes. The microtubule pellet was then resuspended into 100 µl 80 mM PIPES pH 6.9, 2 mM EGTA, 1 mM $MgCl_2$, 1 mM GTP and 30 µm Paclitaxel.

2.2.2 Dynein-dependent recruitment of adenovirus to microtubules

The purified porcine dynactin and human recombinant dynein tagged with mGFP used in this study produced by the laboratory of Andrew Carter, Medical Research Council Laboratory of Molecular Biology, Cambridge, UK. Adenovirus at either pH 7 or pH 5 was mixed with recombinantly-expressed full length dynein at 0.07 mg/ml (Schlager et al. (2014)) and incubated for 5 - 10 mins in buffer (30 mM HEPES, pH

7.2, 2 mM MgAc, 1 mM EGTA, 1 µm DTT and 2 µm ATP). Prior to plunge freezing the appropriate microtubule concentration was determined visually by fluorescence microscopy. 4 µl of the microtubule preparation was added to a glow-discharged (plasma cleaned) C-flat 2 µm holey carbon electron microscopy grid (Electron Microscopy Sciences) and incubated for 20 seconds. The microtubules were then wicked via blotting from the side using filter paper (Whatman). 3 µl adenovirus-dynein mixture was then applied to the grid and incubated for 20s after which 1 µl 10 nm gold-BSA nanoparticles (Aurion) was added. The grid was then plunge frozen in liquid ethane (section 2.2.2).

2.2.2.1 pH-treatment of adenovirus for dynein interaction studies

A 5 µl aliquot of a purified adenovirus sample (Wodrich et al. (2010)) was diluted 1:1 with 0.1M sodium citrate buffer, pH 5, and incubated on ice for approximately 1 hour. The adenovirus was then applied to a mini-dialysis "Slide-A-Lyzer™", with a 20KDa MWCO (ThermoFisher) and floated on top of 10000 times sample volume of buffer (30 mM HEPES, pH 7.2, 2 mM MgAc, 1 mM EGTA, 1 µm DTT and 2 µm ATP). The dialysis reaction performed for 10-15 minutes until the virus was again at pH 7, after which the virus was used experimentally within 5 to 10 minutes. The pH of the low pH virus mixture was tested using pH tester strips (Thermo Fisher). Alternatively, the adenovirus was diluted 1:5 in buffer (30 mM HEPES, pH 7.2, 2 mM MgAc, 1 mM EGTA, 1 µm DTT and 2 µm ATP), resulting in a lower concentration of adenovirus on the grid.

2.2.2.2 Heat treatment of adenovirus for dynein interaction studies

In order to replicate conditions of the theoretical state of adenovirus after entry (i.e. without pentons/penton fibers), adenovirus were incubated at 48°C for 10 minutes in a heat block (Russell et al. (1967)). The heat-treated virus was then incubated at pH 5 in Sodium Citrate, pH 5 and then mixed with microtubules and dynein as described in section 2.2.3.

2.2.3 Investigation of dynein tail complex interaction with adenovirus

The purified recombinant dynein tail complex and the dynein heavy chain construct used in this study were produced by the Carter Lab, Medical Research Council Laboratory of Molecular Biology, Cambridge, UK. Adenovirus at either pH 7 or pH 5 was mixed with either recombinantly expressed dynein tail complex (containing the full length dynein intermediate chain (DIC), light intermediate chain (LIC), light chain (LC8), Tctex and RobI as well as residues 1-1074 of the N-terminus of the heavy chain) (Urnavicius et al. (2015)) or the N-terminus of the dynein heavy chain (residues 1-615), both at a final concentration of 0.07 mg/ml. The mixture was then incubated for 10 minutes, added to grids and plunge frozen as described in section 2.2.4, with the modification that some grids did not have gold nanoparticles added.

2.2.4 Plunge freezing

Once the sample was prepared on electron microscopy grids and was suitable for plunge-freezing, the grids were plunge frozen in an ethane/propane mix (this mixture has less propensity to become solid during freezing than ethane alone). A cooling bath of liquid nitrogen was prepared in a dewar and an ethane/propane mixture condensed into a separate cup cooled to liquid nitrogen temperatures (77K). The ethane/propane mixture was cooled to liquid nitrogen temperatures. The sample grid was held by tweezers, and the tweezers transferred to the manual plunging apparatus. The back-side of the grid was then blotted using Whatman #1 filter paper (GE Healthcare) and plunged rapidly into the ethane/propane.

2.2.5 Preparation of isolated herpesvirus capsids

2.2.5.1 Virus purification and capsid isolation

The HSV1 capsid purification largely follows previous work carried out in (Dohner et al. (2006)) and the full method can be found in Appendix 1.

2.2.6 Total Internal Reflectance Fluorescence (TIRFM) motility assays

TIRFM assays performed in this study were based on protocols and procedures outlined in (Schlager et al. (2014)) and will be described here.

Reagents:

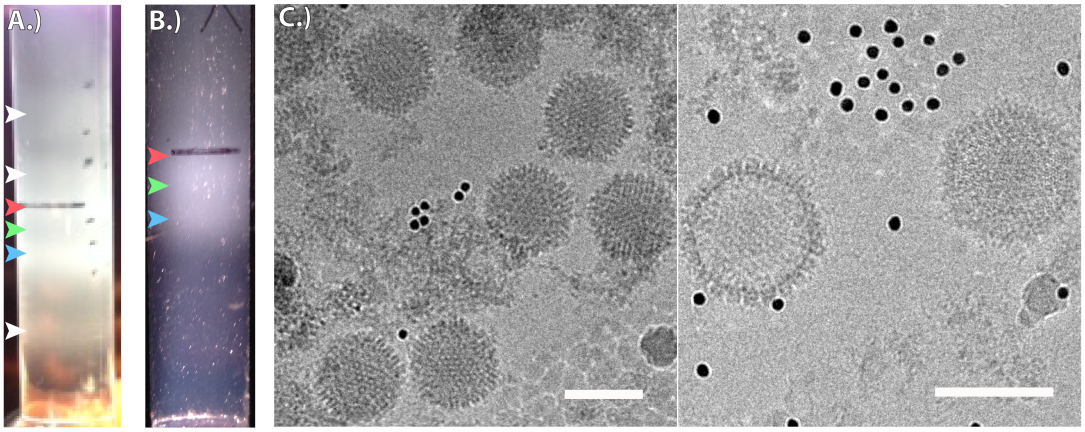

Figure 2.4 – Virus preparation and isolation of capsids from cellular supernatant. A.) Virus preparation isolated from cellular supernatant and B.) capsid isolates produced from virus preparation shown in A.). More light scattering bands can be seen by light scattering in A, indicating more contaminants (white arrows). The different types of capsid run to different positions in the nycodenz gradient, with A-capsids at the top (devoid of DNA) (red arrow), B-capsid in the middle (green arrow) and C-capsids at the bottom (blue arrow) (Radtke et al. (2010)). The horizontal lines are equivalent to the halfway mark of the tube. The bands seen in B.) correspond to the middle bands seen in A.), just below the halfway mark. C.) shows capsids prepared on electron microscopy grids from B.). Scale = 100 nm.

1. BRB80: 80 mM PIPES, 2 mM MgCl2 and 1 mM EGTA, pH 6.9

2. P-BRB80: 80 mM PIPES, 2 mM MgCl2, 1 mM EGTA, 30μM paclitaxel and 1.5 mM GTP, pH 6.9

3. G-BRB90: 40% glycerol, 80 mM PIPES, 2 mM MgCl2, 1 mM EGTA, 30μM paclitaxel and 1.5 mM GTP, pH 6.9

4. DLB: 30 mM Hepes, 2 mM MgAc, 1 mM EGTA, 10% glycerol, 1 mM DTT, 5μM paclitaxel, pH 7.2

5. DLB-BSA: As for DLB + 12.5μg/ml BSA

6. Gloxy: 2mg Catalase, 15mg Glucose Oxidase, 100μl 1xBRB80

7. Motility Mix: 1xDLB-BSA, 1 mM ATP, 1μl Gloxy, 0.45% glycerol, 1μl betamercaptoethanol

Microtubules containing biotin were produced to allow adherence to the glass slide. This required tubulin-biotin, porcine tubulin and hiLyte-647 tubulin (Cytoskeleton, Inc.) mixed in a 1:9 ratio and polymerized in a 1:2 ratio of BRB80:P-BRB80 at 37°C for 30 minutes.

Flow chambers containing immobilized microtubules were subsequently prepared. A glass microscopy slide (Agar Scientific) with two thin strips of doubly sided adhesive tape was prepared, and the space between the two strips incubated with poly-l-lysine-conjugated to polyethylene glycol (PLLPEG) (SuSoS AG), in order to produce a hydrophobic surface. After the PLLPEG was dry, the slide was washed with de-ionized water. Coverslips (22 x 22 mm No. 1.5H glass coverslips (Marienfield))(previously washed in 3M NaOH, Decon80 (Decon Laboratories Ltd) and 60% nitric acid) were then glow discharged for 10 minutes and placed onto the glass slide with the glow discharged surface facing towards the glass slide. PLLPEG conjugated to biotin was then flowed into the gap between glass slide and coverslip, and incubated for 10 minutes. The PLLPEG-biotin was then washed with motility mix. 2 mg/ml of streptavidin was then flowed into the chamber and incubated for 5 minutes. The chamber was then mixed with motility mix. The pre-made biotinylated, hiLyte 647-labelled microtubules were then diluted in BRB80 and incubated in the chamber for 8 minutes. After washing with motility mix, the glass slide was ready for experimentation.

The herpesvirus capsid *in vitro* motility experiments were performed at room

temperature with a total internal reflection fluorescence (TIRF) microscope (Nikon) using a 100× objective (Nikon, 1.49 NA Oil, APO TIRF). The imaging system was equipped with 488 nm, 561 nm and 641 nm lasers. Images were acquired with an EM-CCD camera with a pixel size of 105 x 105 nm (Andor, UK). Experiments were controlled through the use of µManager software (http://micro-manager.org/wiki/Micro-Manager).

The adenovirus *in vitro* motility assays were performed at room temperature using a Olympus IX83 TIRF microscope (Olympus) equipped with a 100x objective (Olympus, 1.49 NA Oil APO TIRF) and equipped with 405 nm, 488 nm, 561 nm and 640 nm lasers. Images were acquired using an Evolve EMCCD 512x512 camera with a 16 x 16 µm pixel size (Photometrics, USA). Experiments were controlled through the use of Olympus cellSens Dimension software (Olympus).

2.2.6.1 *In vitro* motility assays of herpesvirus capsids

A motor protein mix (dynactin/dynein, 2:1) was prepared with a final dynein concentration of 0.1 mg/ml. For the *in vitro* motility assays, 5µl of capsid was added to the motor protein mixture and incubated for an hour before use in the experiment. The mixture was then applied to the chamber and imaged in three light channels; dynein at 488 nm, herpes capsids at 594 nm and the microtubules at 647 nm.

Viruses were counted manually from a projection of the experimental time course.

2.2.6.2 *In vitro* motility assays of adenovirus

As with herpesvirus capsids, the dynactin/dynein ratio was 2:1 with a final dynein concentration of 0.1 mg/ml. *In vitro* motility assays were used to compare the relative dynamics of pH 7 and pH 5-treated adenovirus. pH 5-treated adenovirus was prepared in the same way as described in section 2.2.2.1. Prior to loading into the flow chamber, adenovirus was incubated with the motor protein mix. In the case of pH 5-treated adenovirus the incubation lasted a maximum of 10 minutes. Adenovirus, dynein and microtubules were then imaged in three light channels; dynein at 488 nm, adenovirus at 594 nm and microtubules at 647 nm.

Investigation of adenovirus movement was also attempted using HeLa-generated cytosol (provided by the lab of Harald Wodrich, University of Bordeaux, Bordeaux, France). In this assay, the DLB-BSA component of the Motility mix was replaced with isolated cytosol from the HeLa cells.

The total number of viruses determined to be present in a dataset over the experimental time course was assessed using a maximum projection of every image taken during acquisition. The projection was thresholded so that only the top 1% of brightest signal in the histogram of the 594 nm channel were visible. The viruses were then counted using any signal that occupied a greater than $10px^2$. The viruses that were observed co-localized to microtubules in the images were counted manually.

2.2.7 Data acquisition for electron cryo-tomography

Tomograms were acquired using a Tecnai TF30 "Polara" Microscope (FEI, Eindhoven) operating at 300kV or a Tecnai TF30 "F30" microscope operating at 200kV. The Polara microscope was equipped with a "Quantum" energy filter, and a post energy filter mounted K2 Summit Direct electron detector (Gatan, Inc.), whereas the F30 was equipped with a 4k x 4k Gatan UltraScan CCD camera. Data using the K2 Summit detector were acquired in counting mode, with aligned frames produced 'on the fly', using the combined filter for image alignment in Digital Micrograph (Gatan, Inc.). Data were acquired using SerialEM (Boulder, Colorado) (Mastronarde (2005)). Tomograms were collected bidirectionally using an angular range of -60 to +60, -40 to +60 or -45 to +45, with either 3° or 4° increments. Total doses for a single tilt series ranged from 60eÅ^{-2}to 80eÅ^{-2}.

2.2.8 Data processing of electron cryo-tomograms

Tomographic reconstructions of tilt series were carried out using IMOD (The Boulder Laboratory for 3D Electron Microscopy of Cells, Colorado) and the resulting tomograms visualized and segmented using the Amira visualization software (Visualization Sciences Group, FEI, 2012).

Datasets	MotionCorr?	No. Particles	Total Dose ($e^-/Å^2$)	Å/pixel	Resolution (0.143)(Å)
pH 7 Adenovirus	No	4056	~50	1.35	5.0
pH 5 Adenovirus	Yes	2007	~30	1.35	5.2
pH 5 to pH 7, with DynH5	Yes	2264	~30	1.35	4.2
pH 5 to pH 7, with whole Dynein Tail	Yes	1478	~50	1.39	5.8
pH 7 ΔpIX Adenovirus	Yes	4034	~50	1.35	4.8

Table 2.1 – Summary of datasets used for single particle analysis.

2.2.9 Data collection for single particle analysis and 3D structure determination

Data was collected using either a Titan Krios Microscope with sampling of 1.39 Å/pixel or a Tecnai TF30 "Polara" Microscope (FEI, Eindhoven) with sampling of 1.35/pixel operating at 300kV, equipped with a Gatan Imaging Filter "Quantum" energy filter, and a post energy filter mounted K2 Summit Direct electron detector (Gatan, Inc.). Movie frames per micrograph were collected with either a total dose of 30eÅ^{-2}or 50eÅ^{-2}, dependent on the dataset, with individual frames acquired either every 0.2s or 0.5s, respectively. Image alignment and motion correction of micrographs was carried out using the MotionCorr software (UCSF, Li et al. (2013)), and aligned movies also written out for further processing and per-particle movement correction downstream. Single particle refinement was performed using Relion 1.3 or 1.4 (Scheres (2012)). Resolutions were determined using the "Gold Standard" 0.143 Fourier shell correlation (FSC) cut-off. (Information of statistics for individual datasets, including resolutions, can be found in Table 2.1). All structure maps were visualized using Chimera (UCSF) (Pettersen et al. (2004)).

Difference mapping between pH 7, pH 5 and ΔpIX adenovirus structures: The SPA structures of pH 7, pH 5 and ΔpIX (Table 2.1) were rescaled to a mean density of zero (with a standard deviation of 1) and then bandpass filtered to resolutions between 6-100 Å. This was performed using Bsoft (Heymann (2001)). The pH 5 and ΔpIX structures were then subtracted from the pH 7 structure using Chimera (UCSF) (Pettersen et al. (2004)). The difference in standard deviations from the

mean density of voxel positions was displayed on the pH 7 structure for both the pH 5 and ΔpIX in order to indicate regions of the structure that show the most diffence (see Figures 2.7-2.9).

2.3 Results and Discussion

2.3.1 TIRFM reveals the dynamics of viral trafficking *in vitro*

2.3.1.1 Transport of herpesviruses reveals a minimalist cargo-recruitment machinery within the inner tegument layer

The ability of dynein to bind to herpesvirus capsids has been shown previously (Radtke et al. (2010)), but the necessary viral and cellular factors are still unknown. Therefore, in order to assess the ability of dynein to interact with and transport HSV1 capsids, I reconstituted the HSV1 cargo *in vitro* in a reductionist recombinant system with dynein. Dynactin binds to dynein and greatly increases its processivity along microtubules, but the dynein-dynactin interaction is mediated by cellular co-factors, such as Bicaudal D (BicD)(Schlager et al. (2014)). To test whether herpesvirus capsids could move along microtubules in the presence of dynein and dynactin, microtubules labelled with biotin were immobilised onto coverslips in flow chambers and incubated with GFP-tagged dynein, dynactin and mCherry-labelled HSV1 capsids for 10 minutes. The dynein-dynactin-capsid mixture was allowed to flow into the motility chamber and the reaction imaged using TIRFM. Over a 5 minute time-course,

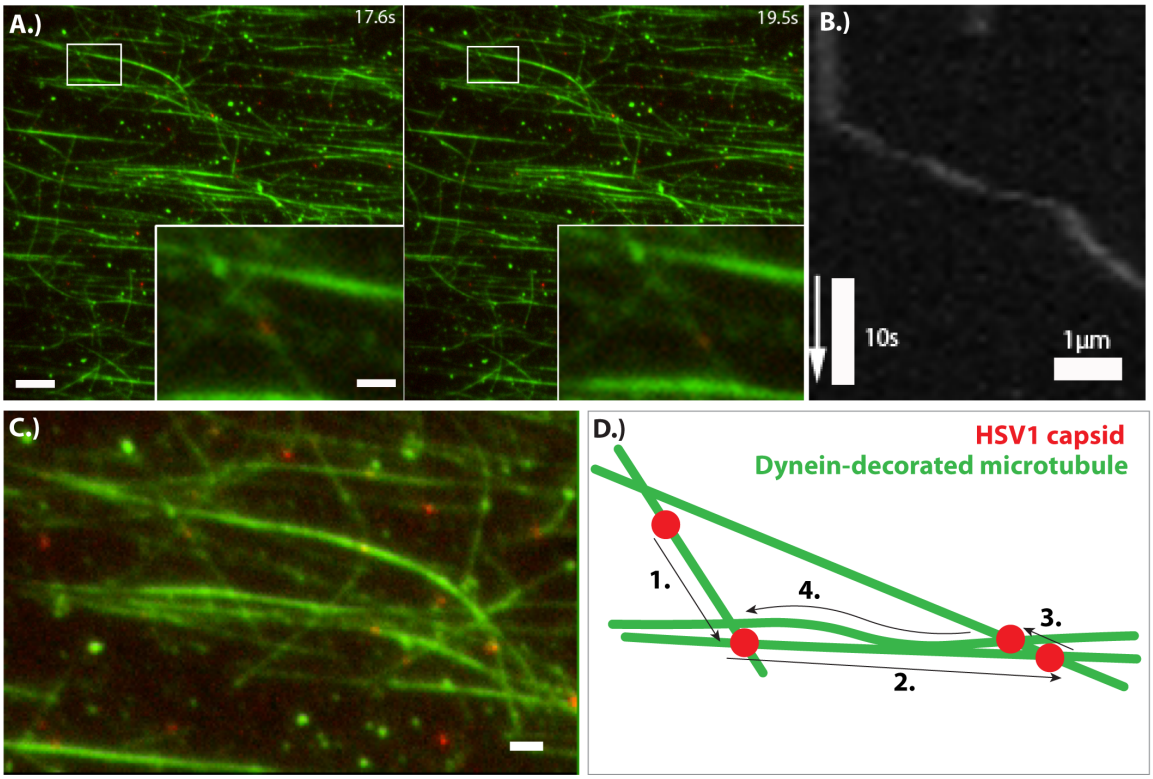

Figure 2.5 – Total Internal Reflectance Fluorescence Microscopy (TIRFM) images and kymograph of a single movement along a microtubule (enlarged, inset) of a HSV1 VP26-mCherry capsid. Shown are two time points (A., left and right respectively). B.) Kymograph representing the movement along the inset microtubule (from A.). C.) Larger field of view shown inset in A.) showing microtubules in the immediate area. D.) Schematic of C.) showing the behaviour during the data acquisition (from 1. to 4.) of the HSV1 capsid as it changes between microtubules. Scale: A.) = 5 µm (Inset = 1 µm). B.) = 1 µm

HSV1 capsids could be observed to interact with microtubules, and in some instances move along microtubules (Figure 2.5). However, only 15 capsids exhibited movement, out of a total of 527 (3%). Of these 15 capsids, the distance travelled ranged from approximately 1.8 µm to 10 µm. The speed of movement that was observed was 0.3 µm/s (Figure 2.5B). Although the number of HSV1 capsids observed to move along microtubules was low, the ability to detect these capsids moving suggests that dynein and dynactin are able to facilitate microtubule based transport of the HSV1 capsids, albeit inefficiently in this experiment. The number of capsids that co-localised to microtubules was greater, with approximately 220 capsids (42%) co-localising with a microtubule.

Although it is unlikely that capsids would have a propensity to bind to microtubules in the absence of dynein or dynactin, a control experiment leaving these motor components out would help to ascertain the signifance of the microtubule association of the capsids, and support these observations. The absence in this experiment of any cellular co-factors present to facilitate dynein/dynactin recruitment. This suggests that a component of the capsid may be able to mediate this interaction, and future studies are required to determine i.) which component of the capsid, e.g. in the tegument of HSV1, is binding to the dynein/dynactin complex and ii.) whether in the prescence of a cellular co-factor the movement or association with microtubule would be blocked (through competition for the dynein/dynactin complex). Due to this currently being just a single dataset, further experiments need to be done to optimise and validate these findings.

2.3.1.2 Recruitment of dynein to adenoviruses bound to microtubules is enhanced upon pH 5 treatment

TIRFM was used to assess the dynein-dependent association of adenovirus with microtubules to determine whether there was an effect on the recruitment and transport of the viruses by exposure to a pH 5 environment. Untreated, pH 7 adenoviruses exhibited a mostly diffuse behaviour (Figure 2.6), often engaging dynein-decorated microtubules briefly and then dispersing back into the buffer solution. Over the course of two separate experimental repeats, 20 time-lapse stacks were acquired, each lasting 115 seconds. For each datset, the projection of the time course was produced, highlighting viruses entering the evanescent field. The projection images revealed that in these 20 datasets, a total of 2106 viruses could be observed. Of these, 418 could be seen to co-localised with a microtubule (20%).

When adenoviruses were incubated with a low pH buffer (0.1M sodium citrate buffer, pH 5) prior to introduction to the dynein motor and the flow chamber, the viruses accumulated into foci on microtubules (Figure 2.6). For 2 experimental repeats, where adenovirus was pre-exposed to the pH 5 buffer prior to mixing with dynein/dynactin, 1495 viruses could be observed entering the evanescent field from 26 time-lapse datasets each lasting 115s. Of these, 908 viruses either associated briefly, or remained associated, with a microtubule at a point during the time course (60%) (Figure 2.6). This suggested that the recruitment of dynein was enhanced by exposure of the virus to low pH. Indeed, some viruses remained associated with the microtubules for the length of the experimental time course.

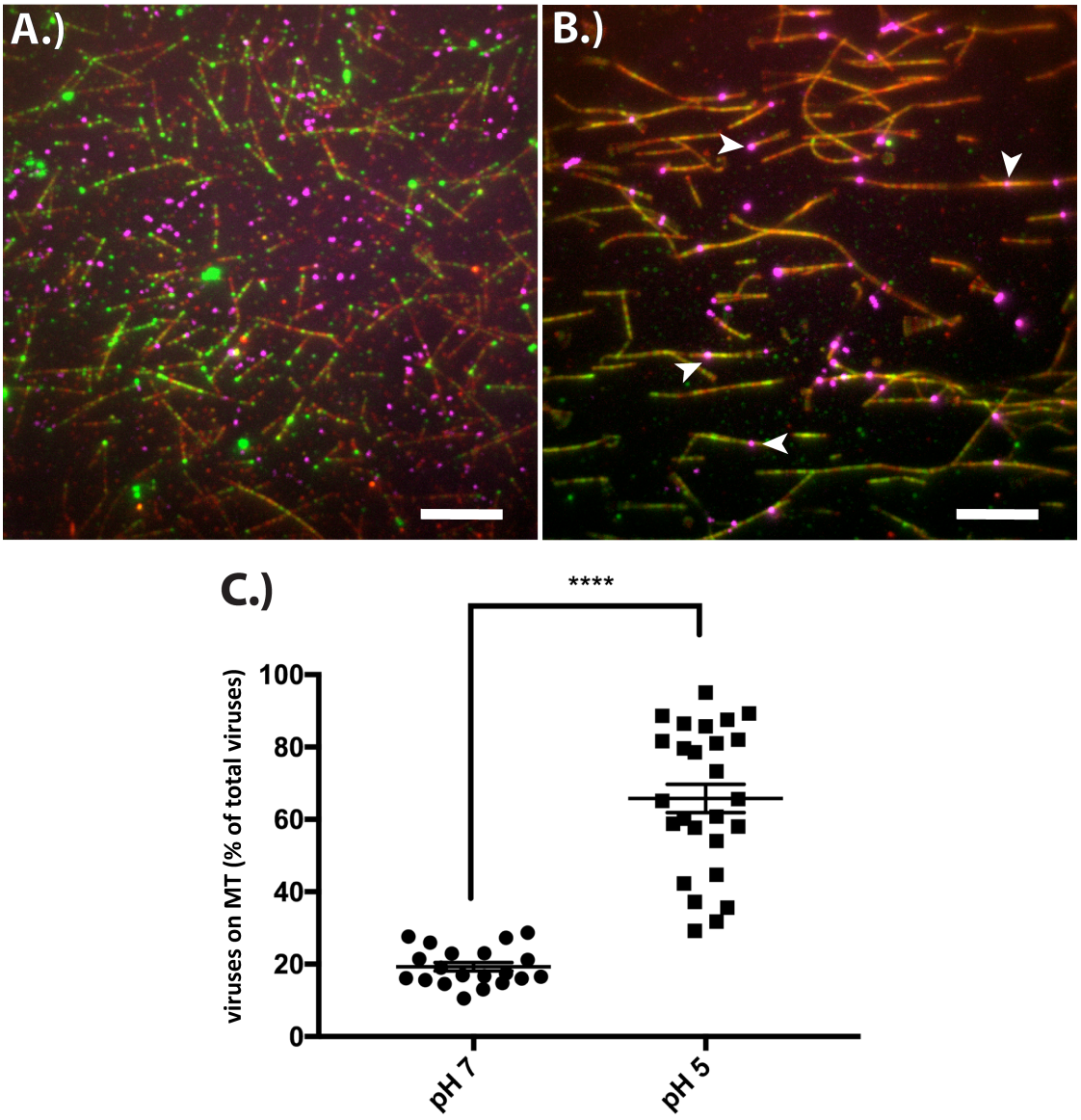

Figure 2.6 – **TIRFM of dynein-mediated adenovirus trafficking**. A.) untreated, pH 7 adenovirus. B.) pH 5-treated adenovirus (at half the cargo concentration compared to pH 7). White arrows indicate fluorescent spots in B.) where there is accumulation of 594 nm signal (magenta) on a microtubule (red/green). Red = microtubules (647 nm), green = dynein (488 nm) and magenta = adenovirus (594 nm). Scale = 5 µm. C.) Dot plot of the percentage of viruses that colocalise with microtubles at any point during the experimental time course in cases where the adenovirus is pre-exposed to i.) pH 7 or ii.) pH 5. Bars shown represent standard error of the mean. Four asterisks represent $P \leq 0.0001$, which was determined using a Mann-Whitney U test.

Although there was an increase in the ability for adenoviruses to localise to microtubules upon pre-exposure of the adenovirus to pH 5, no movement of the viruses along the microtubule was observed. The prescence of steric hinderances due to close proximity to many dynein or dynein/dynactin complexes may contirubute to the lack of movement observed. Studies by Schlager et al. (2014), McKenny et al. (2014) and Urnavicius et al. (2015) suggest that an intact triple complex of dynein, dynactin and a cofactor is required to observe processive movement of dynein along microtubules. The absence of a potential co-factor in these assays may be a cause of the observed lack of processive movement of adenovirus.

2.3.2 Structural determination of the adenoviral surface at pH 5

2.3.2.1 Structure determination of a ΔpIX-adenovirus variant

Pseudo-atomic models of adenovirus have been determined by two different studies (Reddy and Nemerow (2014); Liu et al. (2010)). However, the two models have significant differences in their assignment of proteins to regions of the capsid, resulting in the inability to interpret which components of the adenovirus may interact with dynein. The model of assignment in a paper from Liu et al. suggest that a four helix bundle on the surface of adenovirus was part of protein pIX, which was instead assigned as pIII by Reddy and Nemerov. Therefore, in order to validate the two structures, I determined the single particle structure of a ΔpIX-variant of adenovirus to 4.5 Å. This revealed that the surface protein was indeed pIX, supporting the model

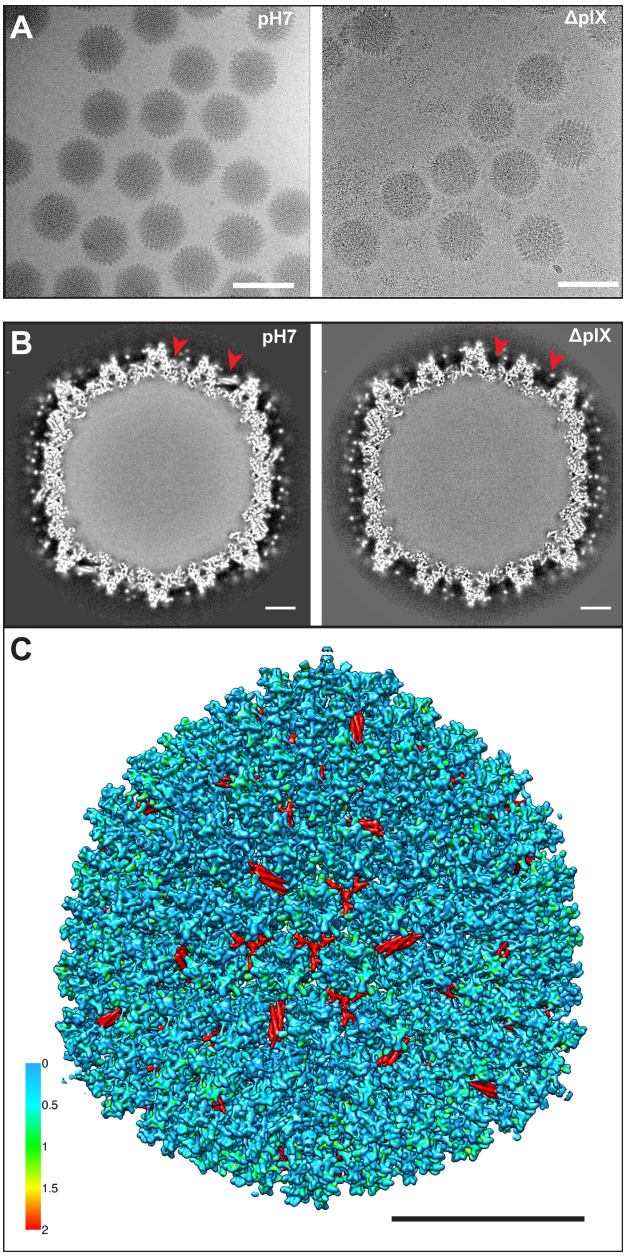

Figure 2.7 – Structural comparison of wildtype adenovirus and a ΔpIX variant. A.) Representative micrographs of wildtype adenovirus (at pH 7, left) and ΔpIX adenovirus (at pH 7, right). Scale = 100 nm. B.) Individual slices through the 3-dimensional reconstruction of wildtype adenovirus and ΔpIX adenovirus determined by single particle analysis filtered to 6 Å. Red arrows indicate the density positions (white) in each slice where pIX should reside. In the ΔpIX virus, the density is absent. Scale = 100 Å. C.) 3D structure of the wildtype, pH 7, adenovirus coloured to highlight difference in density between the wildtype adenovirus structure and the ΔpIX adenovirus structure. Both maps were normalised and scaled to a mean of 0, with a standard deviation of 1. The scale represents the difference in standard deviations from the mean density of those voxel positions, and indicates regions of the stucture that show the most diffence between the structures (blue = smallest, red = largest). Scale = 350 Å.

proposed by Liu et al. (Figure 2.7). The statitstics for the stucture determination are shown in Table 2.1.

The major difference of the ΔpIX adenovirus structure and the wildtype is the absence of a four helix bundle and four anchoring regions (triskelion) between the hexons. This is shown in a difference map, whereby the ΔpIX structure is normalised, filtered to 6 Å and subtracted from the wildtype structure (Figure 2.7, Figure 2.8). Furthermore, a cross-correlation of 0.82 determined on a 50 px^3 box centred on a single four helix bundle between the two structures further indicated that there was a major absence of density. A cross-correlation of 1 would indicate the structures are identical. At 4.5 Å, the ΔpIX structure shows very little difference other than this to the wild-type, pH 7, structure. The triskelion-shaped anchoring regions between the hexons have been suggested to act as a "cement" that holds together individual hexons (Liu et al. (2010)). The ability to refine the structure of the ΔpIX virus to 4.5 Å suggests that in fact the capsid is relatively stable in the absence of pIX. Furthermore, the presence of the four helix "coiled-coil" suggests that pIX may perform other functions in the adenovirus life cycle. The four anchoring regions between the hexons may provide a stable platform to form a rigid hold on the virus for a putative molecular motor.

2.3.2.2 The C-terminal coiled-coil of pIX is destabilized when exposed to low pH

To assess the structure of adenovirus under conditions more representative of an acidified endosome, I attempted to determine structural differences in the adenovirus capsid under low pH conditions. Adenovirus incubated at pH 5 for approximately

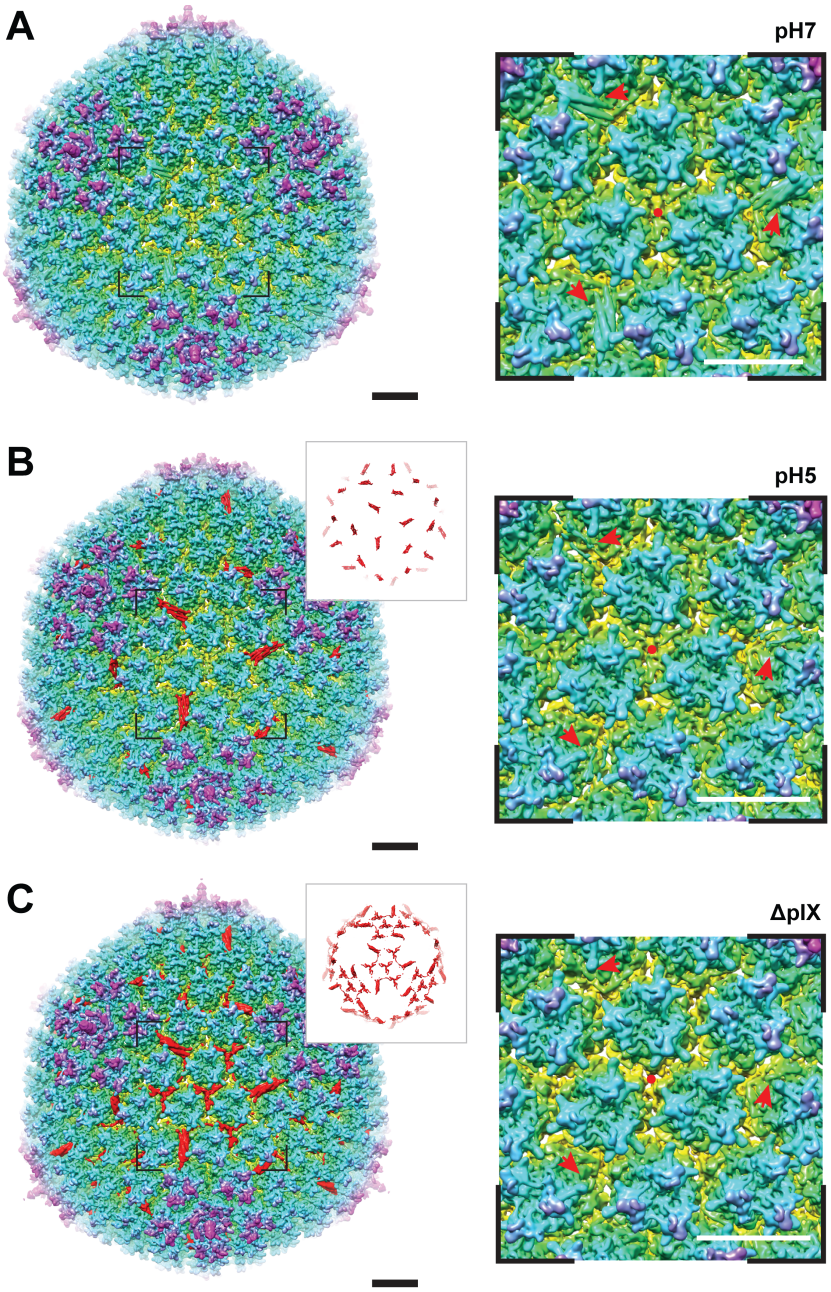

Figure 2.8 – Exposure to low pH results in the partial unfolding of surface protein pIX. A.) CryoEM structure of adenovirus at pH 7 filtered to 6 Å with N-terminal coiled-coil region of pIX highlighted by red arrows (right). B.) CryoEM structure of adenovirus at pH 5, filtered to 6 Å. The normalised difference map of this structure with that shown in A.) is shown in red (red therefore indicates missing densities). Inset shows remaining density present at the point where the N-terminus of pIX should be. Red dot represents the centre of the 3-fold axis. C.) CryoEM structure of the ΔpIX variant of adenovirus, with the normalised difference map between this structure and that shown in A.) shown in red (and inset without virus structure). The two difference maps highlight that pIX is only partially disrupted at low pH, with the N-terminal coiled-coil region mostly disordered (red arrows). Maps are coloured by radius, from yellow (inner) to magenta (outer). Scale = 100 Å.

1 hour was plunge frozen and imaged using electron cryo-microscopy (Figure 2.8). Single particle analysis of adenovirus at pH 5 to 5 Å revealed that the surface four-helix bundle of pIX was disordered with respect the the pH 7 structure (Figure 2.9). Density differences on the normalised and filtered maps (to 6 Å) revealed the main differences between the structures residing in the coiled-coil region of pIX, with differences ranging between one or two standard deviations of the mean density (Figure 2.8, Figure 2.9). Furthermore, a cross-correlation of 0.87 determined on a 50 px^3 box centred on the four helix bundle between the pH 7 and pH 5 structures further indicated that there was a major difference in the structure of the four helix-bundle. The cement regions of pIX in-between the hexon regions were present in the pH 5 structure with respect to the pH 7 structure (Figure 2.9). This suggests that the capsid remains mostly intact during acidification, and that if the capsid is destabilized within the endosome during entry, other factors are likely involved.

2.3.3 pH-dependency of dynein tail component binding to adenovirus

2.3.3.1 Localized classification of N-terminus of the dynein heavy chain

The ability of dynein to bind to adenovirus with a greater propensity at pH 5 has been discussed in section 2.3.1.2, and I attempted to explore this aspect structurally using electron cryo-microscopy. Adenovirus exposed to pH 5 were dialyzed with a pH 7 buffer and then incubated with an N-terminal fragment of the dynein heavy chain (NHC)(residues 1-615)(Urnavicius et al. (2015)), which is part of the tail portion

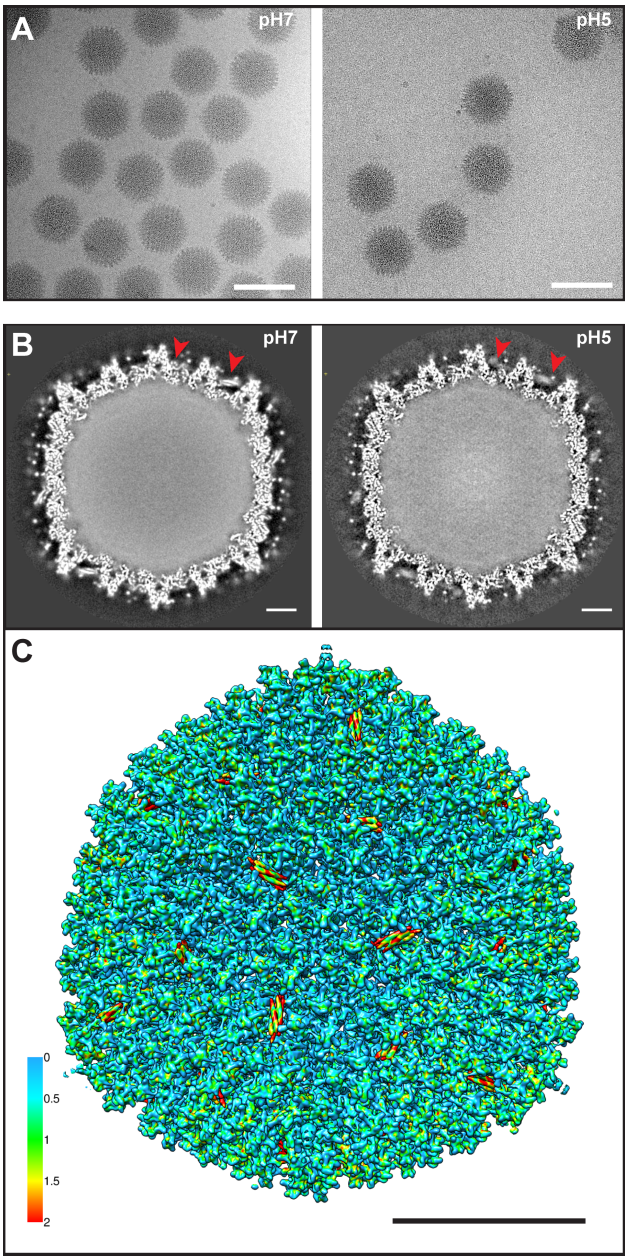

Figure 2.9 – Structural comparison of wildtype adenovirus at pH 5 and pH 7. A.) Representative micrographs of wildtype adenovirus (at pH 7, left) and adenovirus in 0.1M sodium citrate buffer at pH 5 (right). Scale = 100 nm. B.) Individual slices through the 3-dimensional reconstruction of pH 7 adenovirus (left) and pH 5 adenovirus (right) determined by single particle analysis, and filtered to 6 Å. Red arrows indicate the density positions (white) in each slice where pIX should reside. The density for pIX appears smeared (i.e. less defined, due to conformational heterogeneity). Scale = 100 Å. C.) 3D structure of the wildtype Adenovirus coloured to highlight difference in density between the wildtype adenovirus structure and the adenovirus structure at pH 5. Both maps were normalised and scaled to a mean of 0, with a standard deviation of 1. The scale represents the difference in standard deviations from the mean density of those voxel positions. (blue = smallest, red = largest). Scale = 350 Å.

onto which other dynein subunits bind (e.g. LC8, LIC, Txtex and RB1). Dynein has previously been shown to have a half life of binding to adenovirus of 9.2 minutes after exposure to pH 5 (Scherer and Vallee (2015)). The NHC and the pre-exposed adenovirus were incubated together within 10 minutes of the dialysis of the adenvoirus to pH 7. When the adenovirus is pre-exposed to pH 5, the NHC complex forms an electron dense "cloud" around the adenovirus, whereas without pre-exposure to pH 5, the NHC remains mostly diffuse in the background ice (Figure 2.10). A control using a protein without any known propensity to associate with adenovirus would further help to highlight the specificity of this interaction to the NHC construct, however, dynein has been previously shown to specifically interact with the adenovirus hexon in infected cell lysates (Bremner et al. (2009)).

Projection images of the viruses that associated with the NHC were subjected to single particle analysis, and the structure of the adenovirus determined to 4.2 Å (Figure 2.11, Table 2.1). Although no densities were apparent for the NHC construct on the surface of the adenovirus, it is likely that any potential association of the NHC with hexon would be difficult to see due to an symmetry mismatch between the icosahedral reconstruction of the virus, and the asymmetric association of the NHC. To visualize the NHC on the surface of the virus, I attempted to locally reconstruct individual hexons of the adenovirus in order to do an asymmetric comparison (Ilca et al. (2015)). This was performed on 803 of the 2264 particles in the dataset. The 3D structure produced from the virus particles within the micrographs contributing to the final structure was subtracted from the particle images, producing particles containing only densities that did not contribute to the final 3D structure. This

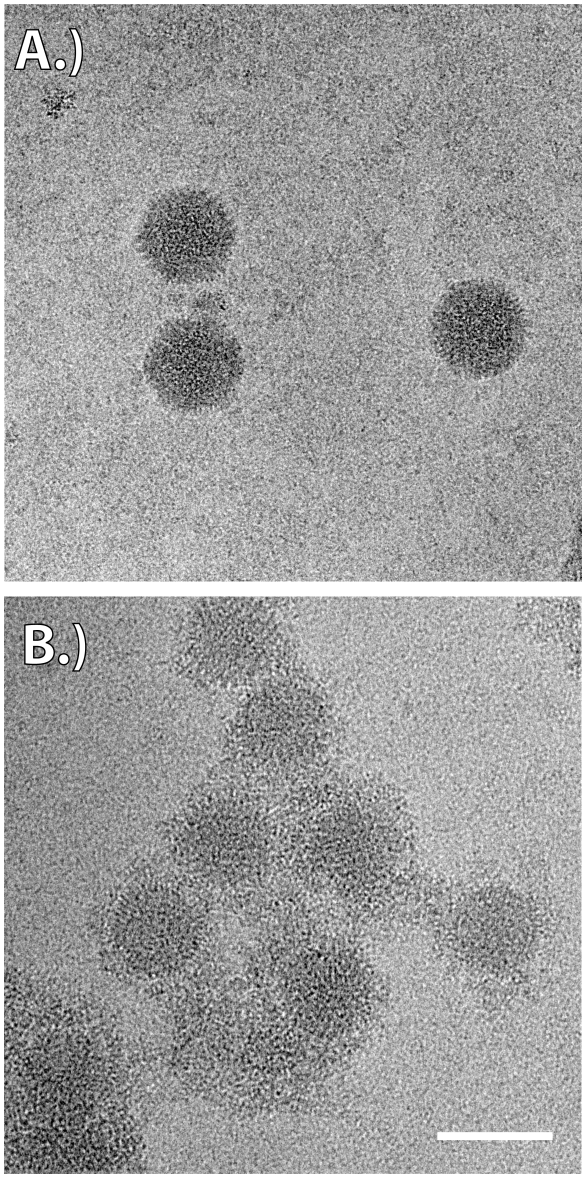

Figure 2.10 – **Comparison of N-terminus of the dynein heavy chain (NHC) association with adenovirus under pH 7- and pH 5-treated conditions**. Representative micrographs of NHC in the presence of A.) adenovirus without pre-exposure to pH 5 buffer and B.) after pre-exposure of the adenovirus to 0.1 M sodium citrate, pH 5 and subsequent dialysis of the adenovirus into pH 7 buffer. The NHC "cloud" in the pH 5 treated case suggests that NHC associates preferentially with pH 5-treated adenovirus, and the absence of protein in the background (c.f. A.) and B.)) suggests that at pH 7 the NHC has less propensity to associate with the adenovirus. Scale = 100nm.

subtraction of the virus used the Euler angles and orientations determined for each virus during the 3D refinement (Figure 2.11A). The position of a specific vector on the virus (determined using the 3D structure) relating to the position of hexon was then used to extract a sub-particle for each symmetry-related vector, centered on the hexon. The projected hexon positions in each particle image were then used as centres for the extraction of sub-particles (Figure 2.11B). The sub-particles were then subjected to 3-D classification without refinement, assessing the contributions in the image that did not belong to the virus capsid. The determined classes were then related back to a separate sub-particle image stack containing the virus contributions, and sub-particle reconstructions of the hexons containing subtracted and non-subtracted averages of the hexons compared (Figure 2.11C).

Using this approach, I was able to classify hexons that did or did not contain densities above the hexon (Figure 2.11C). The densities that I observed were amorphous in nature, and did not show any clear structure. Previous work has suggested that the adenovirus hexon protein was the main binding partner for dynein (Scherer and Vallee (2015); Scherer et al. (2014)). I observed no specific densities, however, I could classify clear bound and unbound hexons suggesting an incomplete coverage of the protein around the adenovirus capsids, and that the ability for hexons to bind to the NHC varied across the viral surface, most likely in a random and probabilistic fashion.

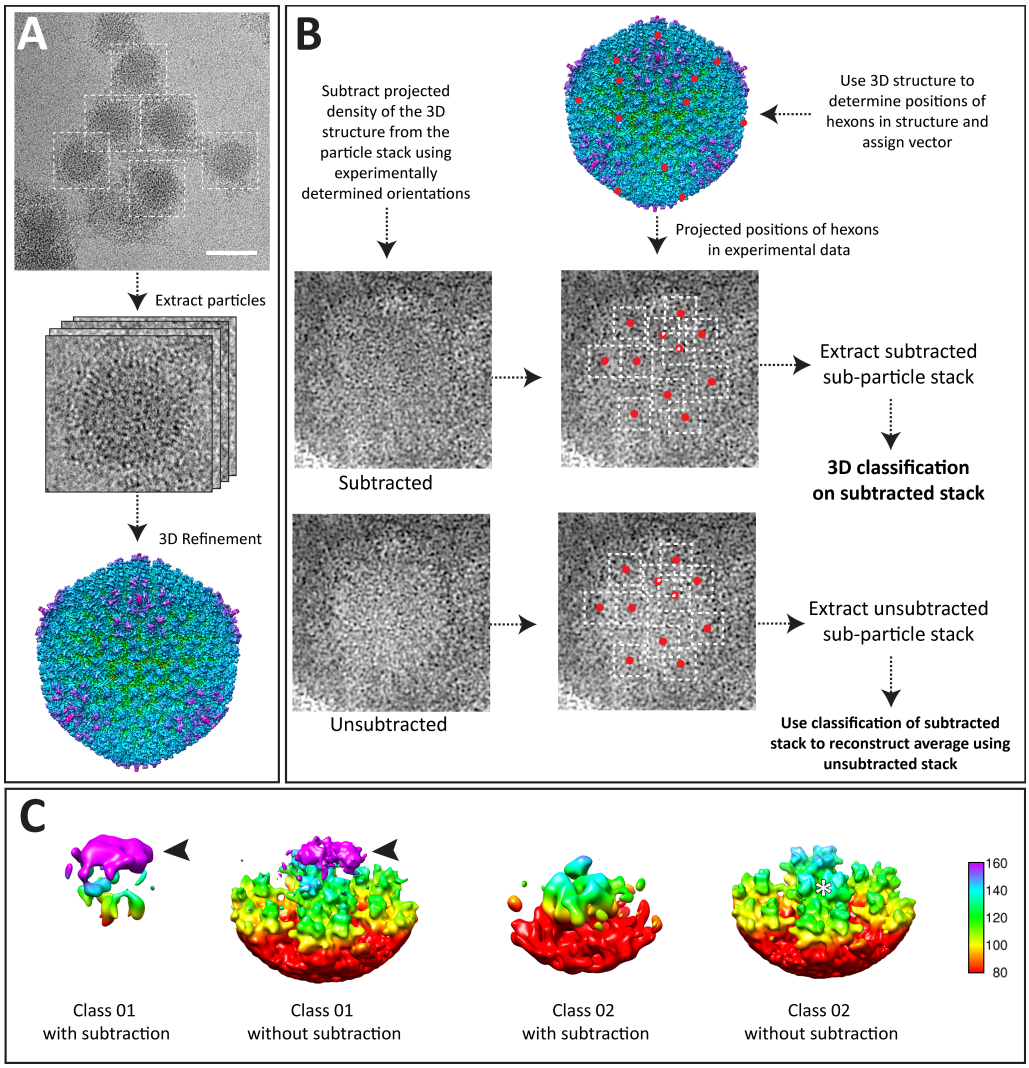

Figure 2.11 – Determination of viral hexons containing additional densities for the NHC construct. A.) The NHC-associated adenovirus was first reconstructed using SPA to determine the 3D structure of the virus. Scale = 100 nm. B.) The 3D structure was then used to determine the positions of hexons on the viral surface and the associated vector then used to determined the position of all hexons in each particle projection. A sub-particle stack was made containing sub-particle projections at the position for each hexon in the particle. A separate sub-particle stack was made, but which had the density contribution of the adenovirus subtracted. 3D classification on the subtracted stack was performed to produce classes based solely on the NHC material outside of the virus density. C.) Classes determined using the subtracted sub-particle stack were used to produce reconstructions centred on the hexon (white asterisk), and which either did or did not contain contributions for the virus density. In Class 1, extra density was observed with and without subtraction above the hexon at around 160 Å (Black arrow). This density is missing from Class 2. Scale shown represents height of the structure from the base of the subparticle box (270 $Å^2$) in Å.

2.3.3.2 Recruitment of the dynein tail is enhanced by pH treatment

A full length dynein tail complex was next used to assess how dynein may interact with adenovirus. The dynein tail is around 30 nm in length, and consists of a number of individual proteins that associate around the N-terminus of the dynein heavy chain, for example, dynein intermediate chain (DIC), light intermediate chain (LIC), light chain (LC8), Tctex and Roadblock 1 (RobI). Previous studies have suggested, through immunohistochemistry, that the interaction between dynein and adenovirus is most likely mediated by the dynein LIC (Bremner et al. (2009)) and the LIC has recently been shown to also be important for the binding of the dynein tail to other cellular cargoes (Schroeder et al. (2014)). It is therefore important to investigate whether the interaction of dynein changes in the presence of LIC.

Incubation of the dynein tail complex with pH-treated adenovirus resulted in the extensive decoration of the adenovirus (Figure 2.12). The dynein tail complex is highly variant and flexible, and this is evident when viewing the full dynein complex (Figure 2.12C). The complex lies against the sides of the adenovirus (Figure 2.12A, D), and also causes the clustering of adenoviruses. From a total of 1478 pH 5-treated viruses in 418 micrographs, 468 (32%) exhibited some form of association with the dynein tail complex. This is in contrast to the association between the dynein tail complex and adenovirus that has not been exposed to pH 5, where 13 from a total of 98 viruses (13%) showed an association or proximity with the tail complex. However, in the latter case the decoration of adenovirus faces by the tail (observed in Figure 2.12A) was not observed. It may be the case that active and inactive conformations

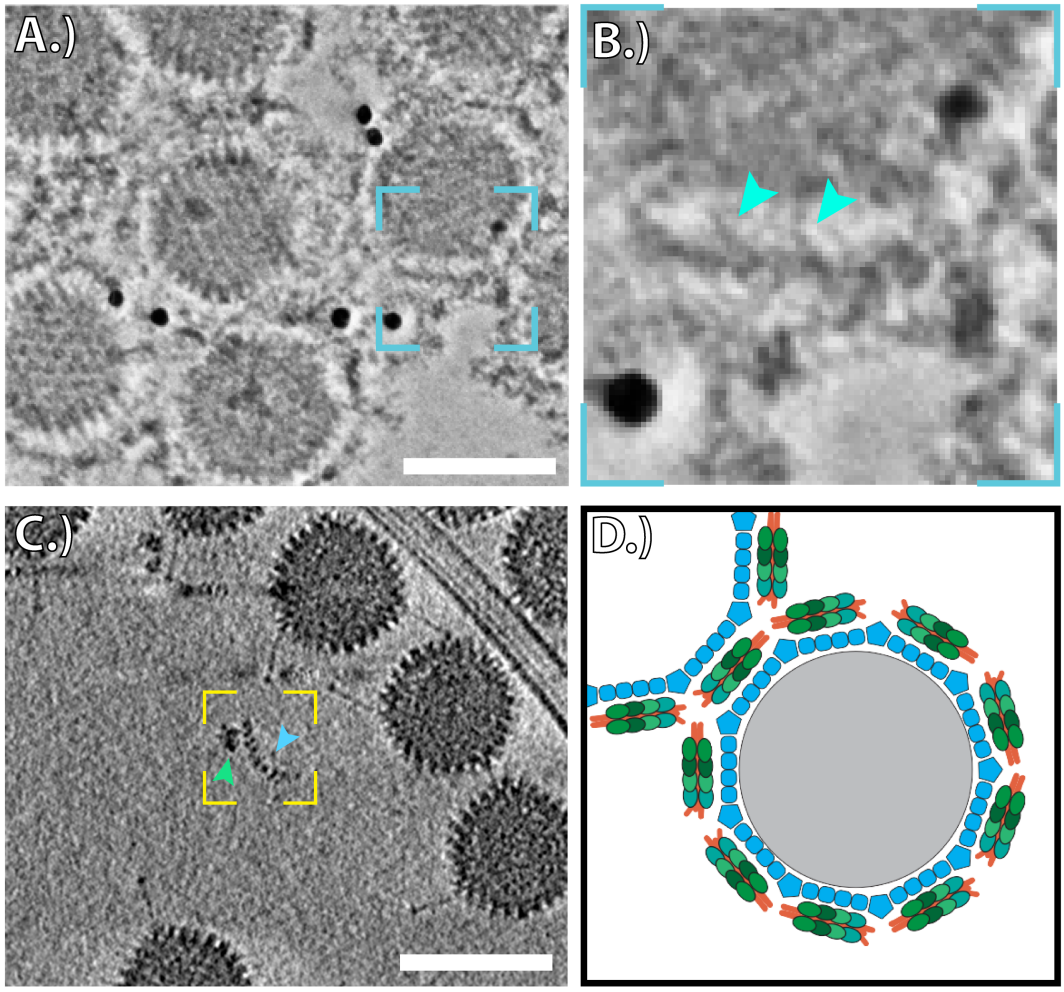

Figure 2.12 – Association of the dynein tail complex with adenovirus in a pH-dependent manner. A.) Dynein tail incubated with pH 5-treated adenovirus and 10 nm gold nanoparticles. B.) enlarged images of area indicated in blue in A.). Arrows indicate density extending to/from the dynein and the adenovirus. C.) Electron cryotomography slice of full length dynein in the presence of microtubules and adenovirus. The tail region is clearly visible next to the motor domain (blue and green arrows, respectively) and is approximately 30 nm in length (c.f. tail length in A and B). This is consistent with the size of the tails in A.). D.) Schematic model of the dynein tail arrangement visible in A.). Scale = 100 nm.

exist that may affect the cargo binding propensity of the dynein tail, and a number of differing structural isoforms for the dynein tail arrangement have been viewed previously (Amos (1989)). Localized reconstruction of the dynein tail complex resulted in only a small amorphous density, that was more difficult to classify in bound and unbound classes as explained in section 2.3.3.1 (data not shown). This indicates that the interaction surface with the tail is extensive and the data shown in Figure 2.12 would suggest that the tail does not localize to a specific part of the virus. Observation of densities between the tail and adenovirus in Figure 2.12B would indicate that a direct interaction does occur, possibly mediated by protein pIX.

Electron cryo-tomography of the tail-adenovirus complex using a Volta phase plate (VPP) revealed how the tail associates in 3D with the adenovirus (Figure 2.13). As was illustrated in Figure 2.12, the tail often aligned length ways against the face of the adenovirus. However, the tail was often highly variant in its association, with only part of the tail making contact with the viral surface. It could also be observed that the dynein tail lay orthogonally to the electron beam. Sub-volume averaging of tail-adenovirus contact site revealed the two layers, relating to the adenovirus surface and the tail complex but no discernible structure of the tail could be produced, presumably due to highly flexible association (data not shown). The high contrast visible in the tomograms meant that putative components of the tail could be visualized, such as the WD40 domain of the dynein intermediate chain (IC) (Figure 2.13B). The size of the tail region of dynein, ~30 nm, is consistent with previous observations (Chowdhury et al. (2015)).

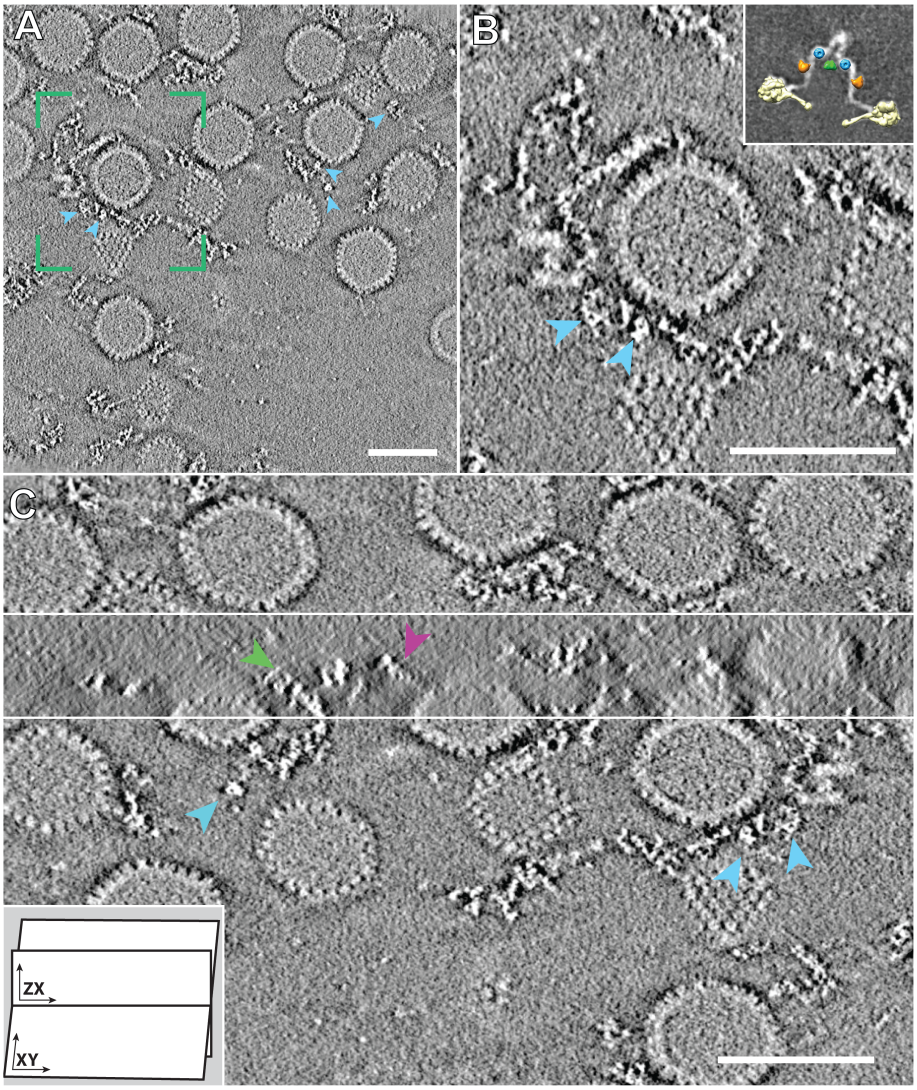

Figure 2.13 – Electron cryo-tomogram of adenovirus interacting with the dynein tail complex after exposure of the adenovirus to a pH 5 environment (contrast inverted). A.) XY projection of 5 tomographic slices. Blue arrows indicate dynein tails in which the WD40 domain of the intermediate chain (IC) is visible. B.) Enlarged image of green region indicated in A.), where the WD40 domain of IC is also indicated (blue arrow). An inset is shown taken from Chowdhury et al. (2015), in which a proposed model for the dynein is shown (blue = WD40 of IC, orange = light intermediate chain (LIC) and green = light chain 7 (LC7)). C.) Oblique view of XY and XZ views for the projection slice shown in A.), reflected vertically about Y. The blue arrow indicates IC WD40 domain of the tail complexes (Chowdhury et al. 2015). The dynein tail is visible in XZ (Green arrow). Magenta arrow shows a penton fibre of the adenovirus. Scale = 100 nm.

2.3.4 Electron cryo-tomography of dynein-mediated adenovirus trafficking on microtubules

2.3.4.1 Heat-treatment of adenovirus results in collapse of the capsid and release of DNA

Heat denaturation is a common practice used in the field of adenovirus virology (Russell et al. (1967) Strunze et al. (2011)), used to release or expose components of the virus that would otherwise be contained within the capsid shell. I attempted to use a similar procedure to release putative dynein binding components of the adenovirus. Adenovirus disruption has been suggested to occur upon internalization into endosomes, with penton, hexon, and pIX release occurring at this stage (Martin-Fernandez et al. (2004)). I attempted to disrupt adenoviruses using mild heat-treatment at 48°C for 10 minutes. The viruses were also incubated at pH 5 after exposure to heat. The resultant capsids were then mixed with dynein and microtubules to attempt to reconstitute the binding of adenovirus to the microtubules. Imaging by electron cryo-microscopy/tomography revealed that heat-treated capsids were disrupted, and penton bases had been released. This was the case for 91 (80%) of the 114 adenoviruses observed in 11 tomograms. In many cases the capsid shell was incomplete and the genome lost (Figure 2.14B). From these data, I observed 3 events of dynein bound to capsids that were fully intact, and that still had pentons attached. One of these dyneins could be in the process of mediating an interaction of the adenovirus with a microtubule (Figure 2.14C). The disruption of the capsids suggest that heat-disruption of adenoviruses for the study of cytoskeletal trafficking

was an inappropriate method.

Previous studies of adenovirus entry have suggested this disruption is essential, as the vDNA needs to be released for it to be able to pass through the nuclear pore (Martin-Fernandez et al. (2004)). Although true that the size exclusion limit of the nuclear pore would preclude capsid entry (Pante and Kann (2002)), disruption at such an early stage is illogical. The cold temperatures used to synchronize adenovirus infection in the study also introduces errors, as this disrupts microtubule networks, as well as capsids, which have been shown to be sensitive to cold temperatures (and is even a method for penton disruption)(Martinez et al. (2015)).

2.3.4.2 pH 5-treated adenovirus can support the recruitment of multiple dynein bound to the microtubule

To further analyze the propensity for dynein to recruit adenovirus to microtubules *in vitro* I attempted to mimic conditions that may be encountered in the endosome, through the use of pH 5 treatment only (as has been discussed in section 2.3.1.2 using *in vitro* TIRFM motility assays). Adenovirus capsids were treated as explained in section 2.3.3, except in this case polymerized microtubules were added to the plunge frozen mixture. Previous studies on the effect of pH on adenovirus capsids are conflicting, with some studies suggesting a pH 5 environment destabilizes capsids (Pérez-Berná et al. (2012)) while other studies suggest a stabilization of capsids (Rexroad et al. (2006)). Analysis of capsids produced in this study by electron cryo-microscopy showed that the virus capsids were mostly intact and had retained encapsidated vDNA.

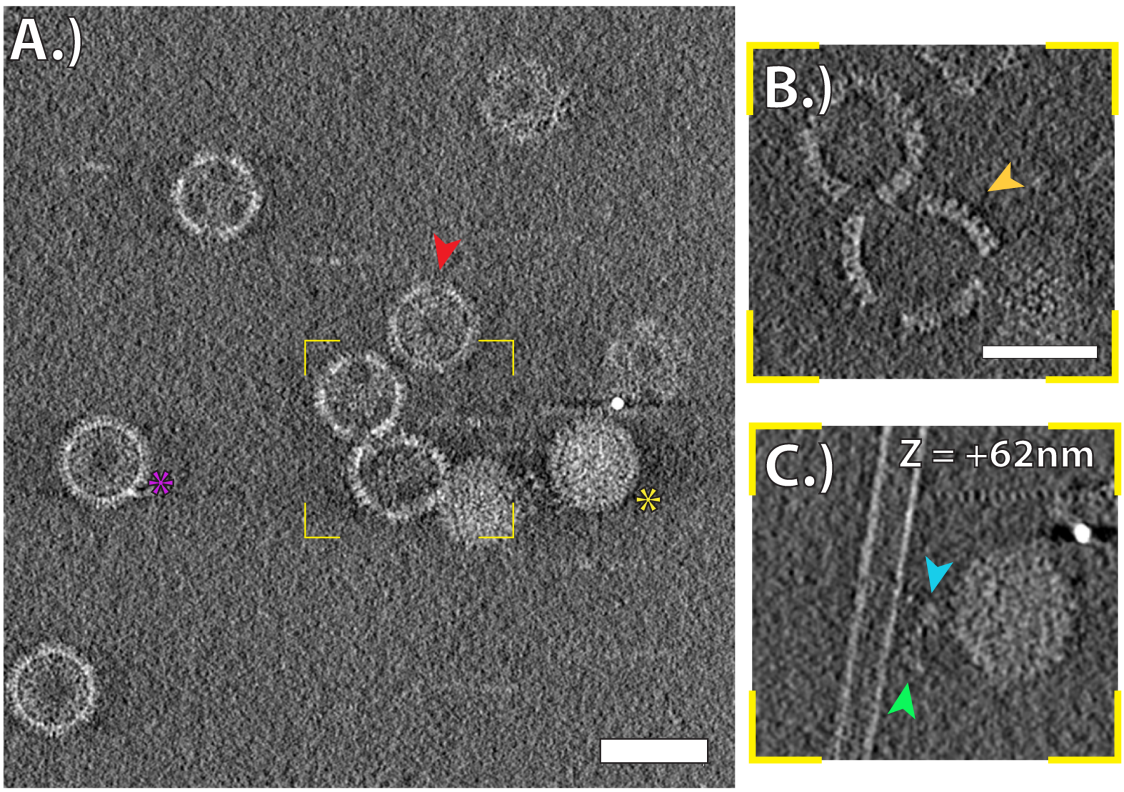

Figure 2.14 – Electron cryo-tomography of heat-treated adenoviruses. A.) Field of view of heat-treated adenovirus capsids. Purple asterisk = capsids with dissociated viral DNA (vDNA), Yellow asterisk = intact capsid with vDNA. Red arrow = capsid shell with dissociated pentons. Scale = 100 nm. B.) Middle 10-slice projection of the disrupted adenovirus capsid indicated by the orange arrow. Scale = 70 nm. C.) Projection slices of an intact adenovirus capsid bound to a dynein dimer engaged on a microtubule 62 nm above the field of view shown in A.). Blue arrow indicates tail region of the dynein, and green arrow indicates the motor region. Scale is same as B.). Contrast has been inverted.

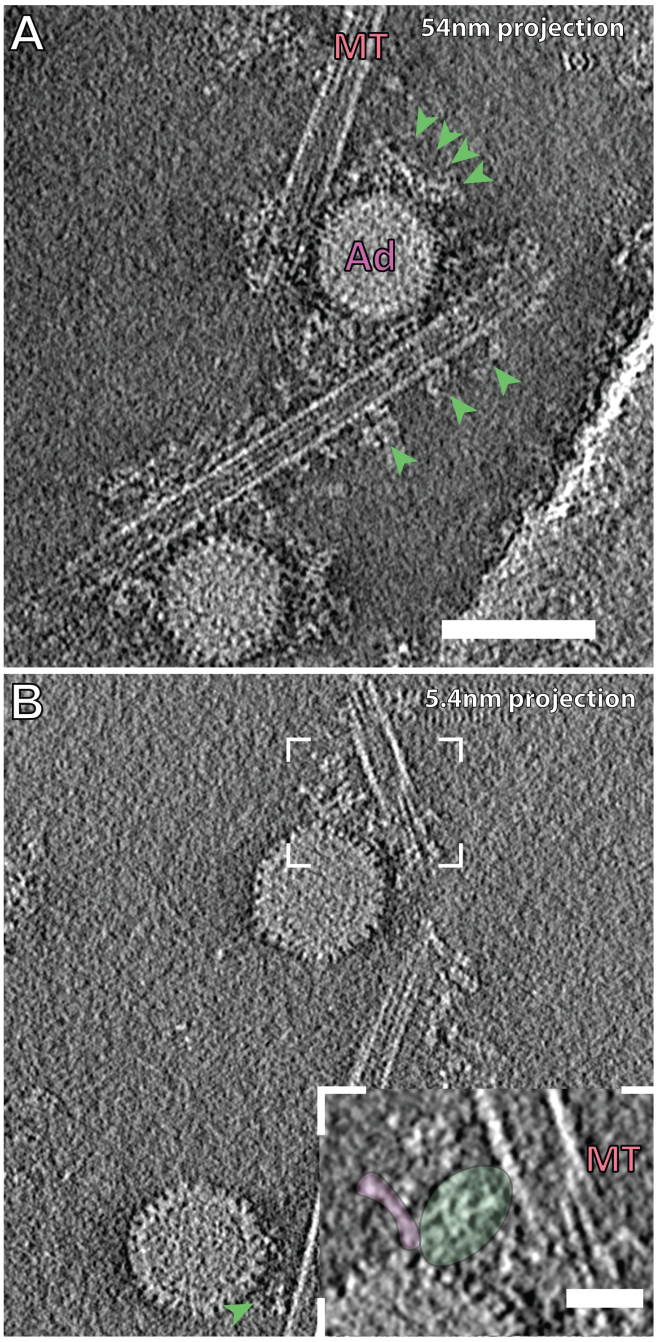

Figure 2.15 – Electron cryo-tomography of multiple dynein can engage a single adenovirus at once, while bound to microtubules. A.) Projection of tomographic slices showing microtubule-associated adenovirus, pre-exposed to pH5. The adenovirus has been bound by multiple dynein molecules. Green arrows highlight densities for dynein. B.) Projection of tomographic slices prepared the same as in A.) where dynein have localized on one side of an adenovirus capsid. The penton of the adenovirus is visible projecting away from the capsid (magenta, inset), whereas the dynein can be seen to make contact with both microtubule and adenovirus (green, inset). Scale = 100 nm (inset = 25 nm). Contrast inverted.

Adenovirus could be recruited to microtubules by dynein, and densities that clearly linked the dynein tail domain with the microtubule were visible (Figure 2.15). Initial experiments using simple dilution of the adenovirus in pH 5 buffer with pH 7 buffer resulted in samples with a low concentration of adenovirus. In order to increase the concentration of adenovirus present on the EM grids, dialysis was used to raise the pH of the adenovirus from pH 5 to pH 7. In 30 tomograms acquired from 7 experimental sessions (3 using dialysis and 4 using dilution), I observed dynein densities extending between the adenovirus and microtubule on 42 occasions, from a total of 101 viruses that were within ~50 nm proximity to a microtubule (42%). The majority of viruses came from the dialysis experiments (83 from 101). In these 3 experiments, 32% of virus association with microtubule was dynein-mediated. These values compare to the *in vitro* motility experiments, where 61% capsids bound to microtubules. One reason for the lower binding in the cryoEM experiments could be due to the air/water interface, which would disrupt the microtubule-dynein-adenovirus association. In some tomograms, multiple dynein were bound, making total dynein association hard to quantify (see section 2.3.1.2).

The density of protein in cases where individual dynein could be seen in between the adenovirus and microtubule resembles that of the dynein dimer as previously seen by electron microscopy (Burgess et al. (2003); Roberts et al. (2009); Imai et al. (2015)). The data show that the recruitment of multiple dynein molecules on one adenovirus is possible (Figure 2.15, Figure 2.16), which is consistent with previous observation with the dynein tail (in section 2.3.3.2). Furthermore, snapshots within tomograms showed that the tail of the full length dynein dimer can lie flat against the

face of the adenovirus (Figure 2.16). The arrangement of the dynein while engaged with the adenovirus mostly showed a large conformational flexibility, where one head of the dynein motor domain remained bound and the rest of the complex was free and flexible. The large size of dynein, coupled to its significant conformational heterogeneity precluded the possibility of averaging via sub-volume averaging. The tail of dynein, though observed to be laying flat in some instances (Figure 2.16C), exhibited variability in its interaction with the adenovirus. The difficulty of observing features oriented along the z-axis with high accuracy reduces the ability to see the tail when it is not oriented in XY, but the variability may suggest that the tail has different registries.

2.3.4.3 Dynein-adenovirus-microtubule global architecture

The large amount of conformational flexibility made sub-volume averaging of the dynein-adenovirus-microtubule complex difficult. Therefore, in order to determine an overall architecture of the complex, I attempted to segment and isolate individual components of the system, to see the arrangement of the tail and motor with respect to virus and microtubule. This was further helped by determination of the virus orientation within the tomogram using an adenovirus structure already published in the electron microscopy databank (EMDB)(EMD-1579; Pérez-Berná et al. (2009)). The structure was filtered to low resolution (60 Å) and then scaled to the appropriate voxel size (binned 4, 5.4 Å/pix). It was then refined against the position for the adenovirus inside the tomographic volume, and the orientation with the greatest cross correlation after refinement determined as the approximate position of the adenovirus.

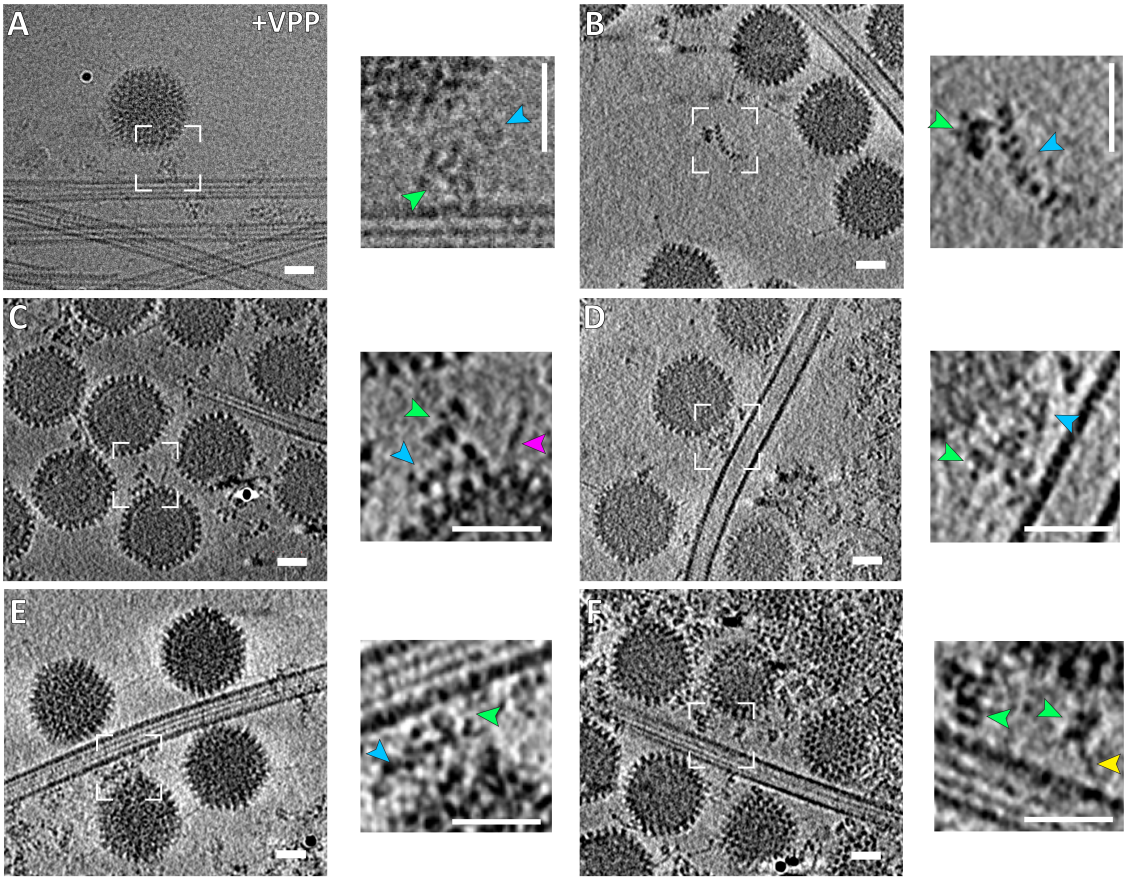

Figure 2.16 – Assessment of the interaction between dynein, adenovirus and microtubules by electron cryo tomography. A.) High dose projection image of a dynein engaged adenovirus bound to microtubule. Inset: green arrow = motor domain of dynein, blue arrow = tail region. B.) Slice from an electron cryo-tomogram of a dynein dimer free in buffer. Inset: green arrow = dimer dynein motor domain, blue arrow = structured, extended tail region of approx. 30 nm. C.) Slice from a electron cryo-tomogram of a dynein bound to an adenovirus, where the flexible tail is shown lying flat against the adenovirus, consistent with previous data shown (section 2.3.3.2). Inset: green arrow = motor domain, blue arrow = tail region, magenta arrow = penton fibre of adenovirus. D.) Slice from an electron cryo-tomogram of a dynein dimer engaged with microtubule and adenovirus. Inset: green arrow = dynein motor domain dimer, where the circular AAA+ ring is visible. Blue arrow = tail region extending toward the adenovirus. E.) Slice from an electron cryo tomogram showing multiple dynein bound between the adenovirus and microtubule. F.) Slice from an electron cryo-tomogram of two dynein dimers bound to adenovirus. Inset: green arrows = motor domains of the two dynein. Yellow arrow = the ~12 nm stalk domain shown as it interacts with microtubule. Scale = 25 nm for all images.

Segmentation was performed semi-manually using a Gaussian blur tool in the Amira suite of software (FEI, Eindhoven). In this approach, the Gaussian tool blurred the density to a user-defined Gaussian width, and then highlighted densities with a similar intensity. By using this approach I was able to select densities that were of a similar threshold in a given area, and track the densities through the 3-dimensional volumes. This is shown in Figure 2.17.

The segmented volume of dynein bound to the adenovirus is roughly the shape that we would expect for a a dynein dimer (Figure 2.18). The motor domain shows a clear connection to the stalk, which is around 12 nm in length and consistent with other studies (Mizuno et al. (2007)). The crystal structure of the dynein motor domain fits well into the density adjacent to the microtubule (Figure 2.18B), further indicating correct assignment of density (PDB ID: 3VKG; Kon et al. (2012)). The densities adjacent to the adenovirus are more difficult to determine, as there is no previously determined high-resolution structure through which to interpret what is seen in the segmentation. When comparing tails from different datasets, the dynein tail appears very long and flexible, and extends for approximately 30 nm in solution (Figure 2.16), which is consistent with other data shown in previous sections and in the literature (Chowdhury et al. (2015)).

The penton fibre of the virus can be observed in the raw tomogram, and the localization of the penton fibre is better determined when taking into account the approximate alignment of the EMD-1579 adenovirus structure into the tomogram. The tail density of the dynein makes contact with the adenovirus in a peripentonal region. I also segmented the microtubule-dynein-adenovirus complex in 3 other to-

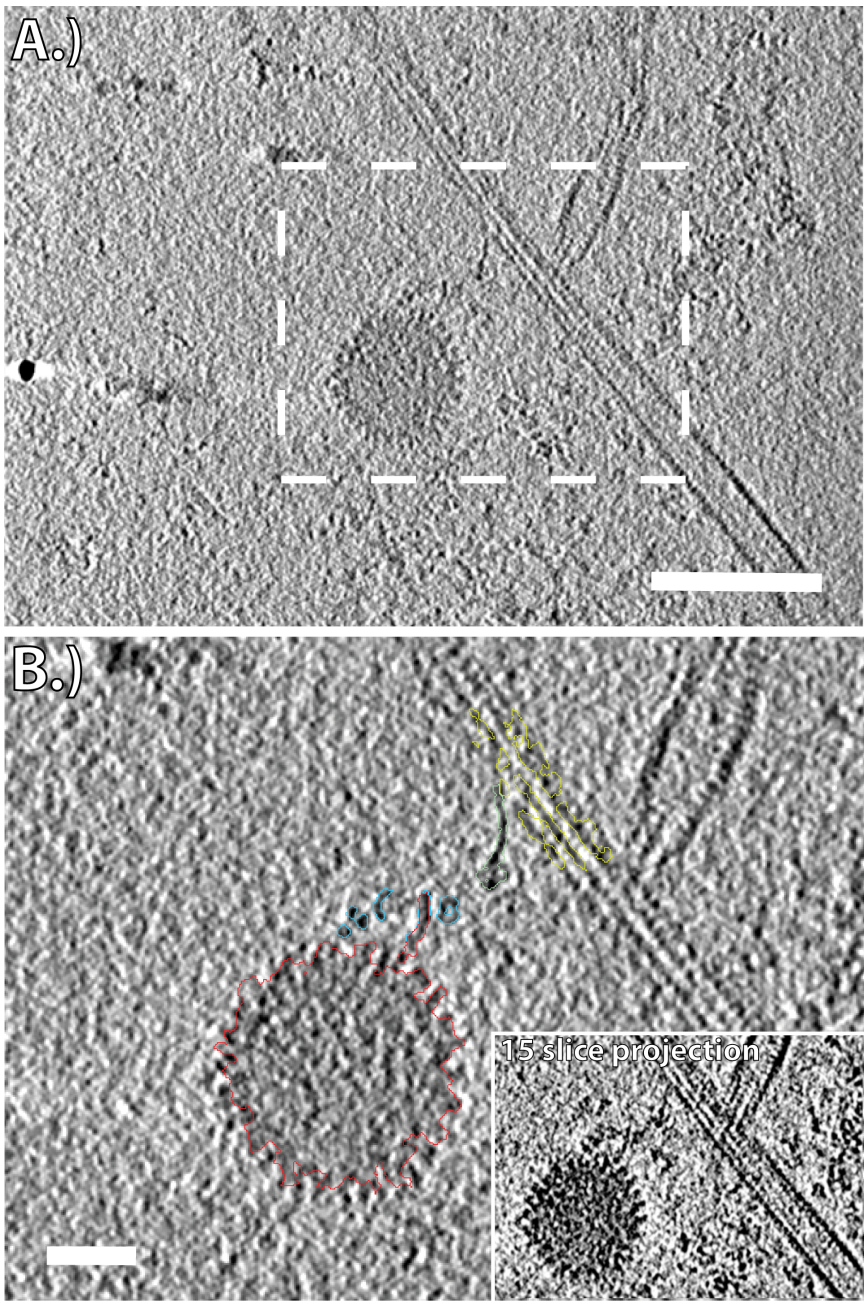

Figure 2.17 – Segmentation of tomograms to isolate dynein transport events. A.) Single tomographic slice showing dynein interacting with adenovirus. Scale = 100 nm. B.) Enlarged images in marked box in A.) showing the different highlighted densities for the components of the system; microtubule in yellow, dynein motor domain in green, the dynein tail region in blue and the virus in red. Scale = 25 nm. Inset = 8.1 nm (15 slice) Z-projection image through the tomogram showing the whole density for the dynein. Full segmentation can be seen in Figure 2.18.

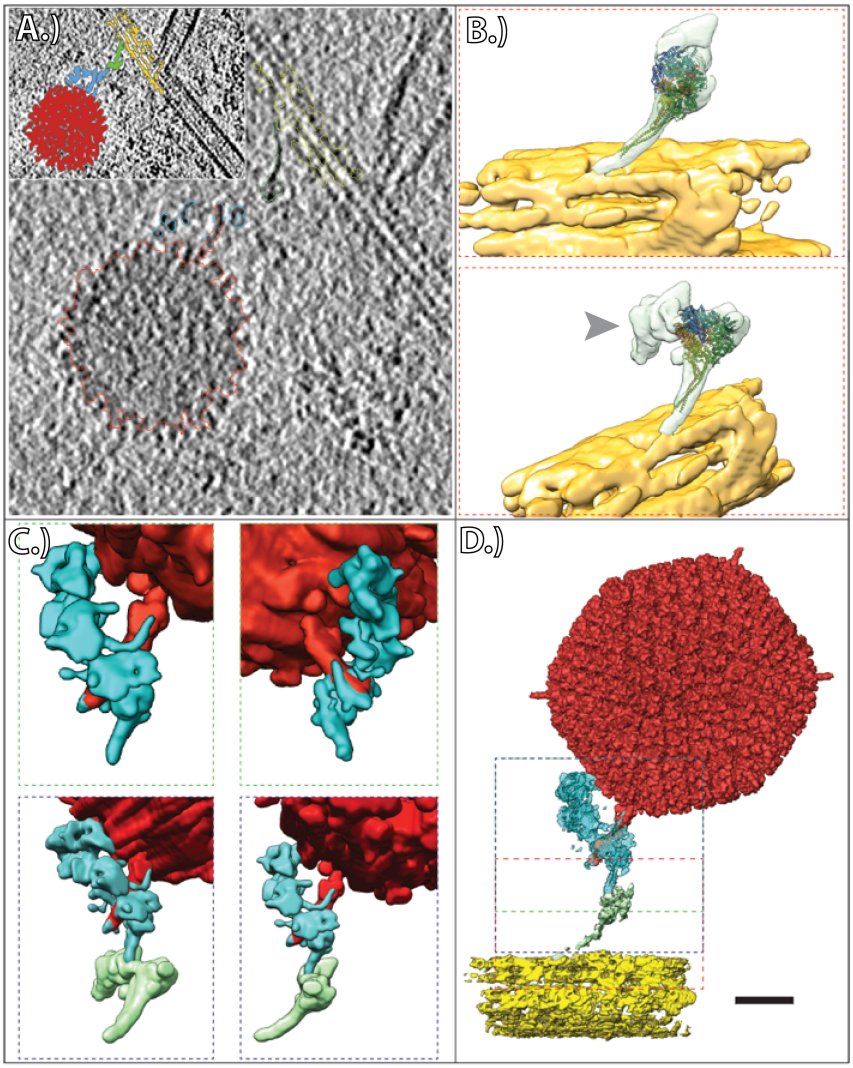

Figure 2.18 – Full segmentation of an individual dynein-recruitment event (see also Figure 2.17). A.) Tomographic slice of the event (inset, 8.1 nm Z-projection image) with the colours for components shown (yellow = microtubule, green = dynein motor domain, blue = Dynein tail domain, and red = adenovirus). B.) Filtered rendering of the segmented volume showing the regions adjacent to the microtubule. The crystal structure of the dynein motor domain has been placed into the segmented density (PDB = 3VKG; Kon et al. (2012)). The segmented density of the second head of the motor domain without the stalk is shown (gray arrow). C.) Filtered rendering of the segmented volume showing the regions adjacent to the adenovirus. The penton fibre of the adenovirus is shown in red. Densities representing the tail domain are shown in blue, and run above the penton fibre. D.) Whole segmentation of the event, with the adenovirus density replaced with the sub-volume-determined alignment of the EMD-1579 structure filtered to 60 Å. The alignment matches the approximate positions of the penton fibers, suggesting the dynein tail interacts with the virus in the peripentonal region. Scale = 20 nm.

mograms where there is i.) enough detail to see where the tail binds, ii.) there are no other dyneins in this region that may make assignment of motor and tail regions difficult and iii.) I was able to determine the orientation of the virus in the tomogram. The segmentation and alignment of these events also show that the tail tends to bind in a peripentonal region. This is the region in which protein pIX resides, making a pIX-dynein tail interaction a possibility. The precise localization of the tail still needs to be determined, but a specific interaction is unlikely. A combination of transient electrostatic interactions with the flexible loop regions of the hexon (Scherer and Vallee (2015)) and a putative interaction with pIX could serve as a strong enough interaction to allow the active transport of adenovirus by dynein.

2.3.5 Viruses expose surface proteins that promote the recruitment of dynein during trafficking to the nucleus

The results hitherto reported present a model for dynein recruitment that argues for a co-evolved mechanism for dynein association and transport by viruses. Herpesviruses are able to traffic processively *in vitro* in the absence of any cellular processivity co-factors. This argues in favour of a component of the herpesvirus, mostly likely either UL36 or UL37, mediating this interaction (Pitts et al. (2014); Zaichick et al. (2013)). Similarly, in the case of adenovirus, I have determined that i.) dynein association with adenovirus is increased after exposure of adenovirus to pH 5 and ii.) the only observable structural change that occurs on the surface of adenoviruses during acidification in the endosome is the disruption of a coiled-coil region of pIX.

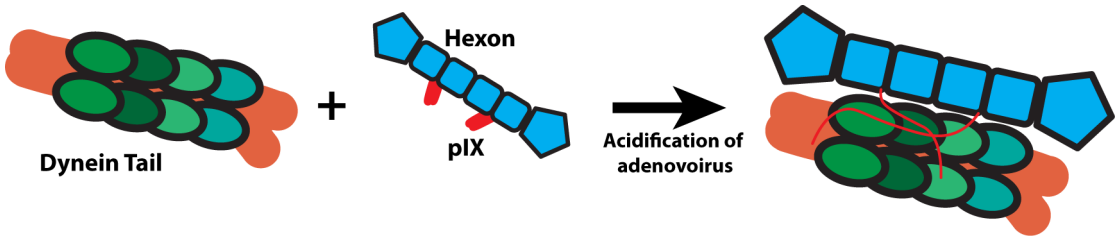

Figure 2.19 – A model for the pH dependent recruitment of the dynein tail to the adenovirus capsid, mediated by the pIX protein of adenovirus. The acidification of the capsid disrupts the coiled-coil of pIX, causing it to unfold. As the virus capsid re-renters the cytosol, pIX interacts and refolds with the dynein tail complex, and potentially dynactin, resulting in a transport competent motor complex bound to adenovirus.

Such coiled-coil regions are a common motif that is seen in cargo-adaptor proteins such as BicD, Hook3 and NudE, which are cellular processivity factors for dynein transport (Kardon and Vale (2009)). A model of how this may occur is shown in Figure 2.19. The disruption of the coiled-coil region in pIX may represent a co-factor for which the tail of dynein can bind as it refolds upon re-exposure to a pH 7 environment and could occur in a similar way to the BicD N-terminus, as shown structurally by Urnavicius et al. (2015).

The model for the organization, taking into account the multiple data presented, is shown in Figure 2.20. The model incorporates the evidence presented, to show a dynein tail that lies flat against the virus, in a pH dependent manner. The structural flexibility inherent to the dynein complex is taken into account, with the motor domain free to move with respect to cargo, which is most likely needed to allow the free-ratcheting of the linker regions to facilitate movement. pIX incorporation into the tail is a potential novel cargo-adaptor for dynein-mediated transport.

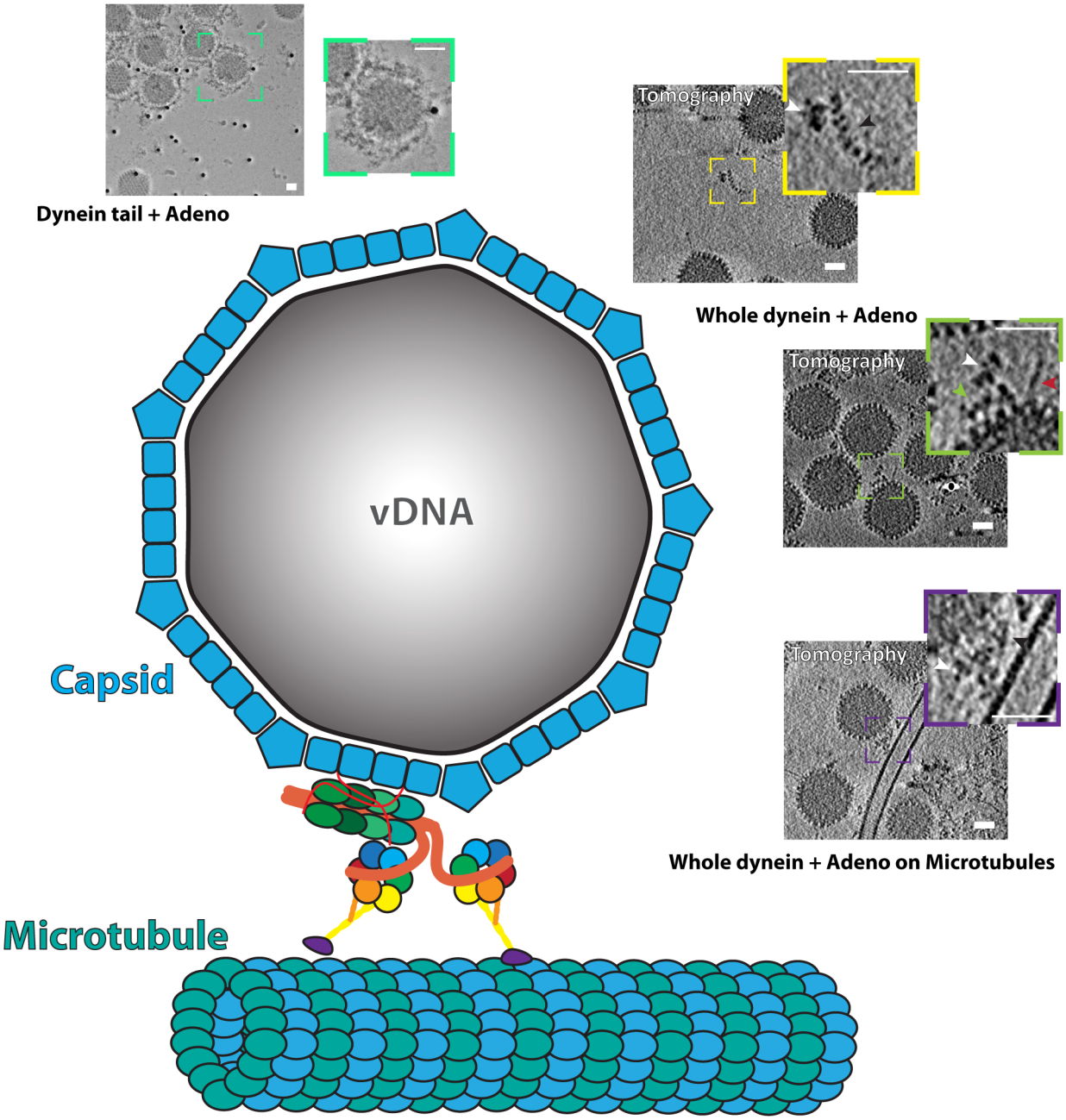

Figure 2.20 – Schematic model of the putative dynein-adenovirus complex bound to a microtubule. This describes how a putative dynein-adenovirus complex bound to a microtubule may be arranged. Scale bars = 25 nm.

2.4 Concluding Remarks

The propensity of viruses to evolve mechanisms able to subvert cellular machinery that are essential for a cell's viability is most likely one of the reasons why viruses remain and will continue to be a successful vector for life. The findings presented here represent another example of this. Structural homology of pIX to cellular cargo-adaptor proteins allows the virus to be recruited by the dynein retrograde transport machinery, hijacking an efficient means by which to traffick to the nucleus, and thereby replicate quickly and efficiently. The expression of a cargo-adaptor protein on the viral surface allows the virus to be independent of an external adaptor that may be down-regulated by the cell. A number of viruses have been suggested to hijack the cellular machinery (Dodding and Way (2011)), and this study represents a first step to structurally determine the characteristics of viral transport by the dynein motor, as well the first to show the architecture of the dynein tail and how it may interact with a putative cargo. Future work will focus on stabilizing the tail and cargo, to allow a higher resolution determination of the structure and interaction. Similarly, this approach may also be important in characterizing the interaction for other cargos, and determining the similarity of this process *in situ.* Cellular studies would allow the direct visualization of whether (i) the dynein complex exists *in situ* conjugated to the plus-end directed kinesin motor and (ii) whether multiple dynein complexes associate with the virus at the site of microtubule binding and transport.

Cellular electron cryo-tomography is still a developing technique, and the ability of the technique to elucidate transient structural biology within cells still remains to be

explored. In Chapter 3, I will attempt to explain and characterize what is visible using electron cryo-tomography *in situ* and, using sub-volume averaging, discuss factors that may limit resolution for structure determination.

3

Towards visualization of virus transport *in situ*

3.1 Introduction

3.1.1 Cellular electron cryo-tomography as a cell biological tool

Electron cryo-tomography (cryoET) is a technique used to reconstruct 3 dimensional structures of biological samples in their native, frozen hydrated state. By freezing cells (or other relevant specimens) in vitrified ice and taking a series of images on an electron microscope at different viewing angles, it becomes possible to visualize unique pleomorphic events and large macromolecular organizations (e.g. lattices) that would be otherwise very difficult to reconstitute *in vitro* (Brandt et al. (2010); Hagen et al. (2015); Schur et al. (2015); Zeev-Ben-Mordehai et al. (2016); Sirohi et al. (2016);

Bartesaghi et al. (2015)). Furthermore, frequently occurring molecular structures can be averaged together to create higher resolution maps, a technique generally referred to as sub-tomogram averaging.

Recent technical developments in cryo electron microscopy (cryoEM) have resulted in the ability to image vitrified specimens with unprecedented signal-to-noise ratios, allowing the analysis of biological structures and features at a much higher level of detail than previously. These developments include zero-loss energy filters and direct electron detectors, both of which have vastly improved the quality of tomographic data acquisition (Li et al. (2013); McMullan et al. (2014); Koster et al. (1997)), and led to the determination of novel macromolecular complexes and viruses, as well as the structure determination of pleomorphic complexes and the *in situ* architecture of cells (Asano et al. (2015); Mahamid et al. (2016); Fukuda et al. (2015); Matthies et al. (2016); Schur et al. (2015); Zeev-Ben-Mordehai et al. (2016); Sirohi et al. (2016); Bartesaghi et al. (2015)).

Cellular cryo-tomography has been used in the past to highlight many different aspects of biology, such as the structural analysis of nuclear pore complexes in membranes (Rigort et al. (2012); Mahamid et al. (2016)), the visualization of cell-cell contacts at cadherin junctions (Al-Amoudi et al. (2007)), novel microtubule associated lumenal bodies *in situ* (Garvalov et al. (2006)), as well as the molecular sociology of proteasomes in cells (Asano et al. (2015)), the trafficking of viruses (Ibiricu et al. (2013, 2011)), the molecular arrangement of proteasomes (Brandt et al. (2010)) and the ability to probe the molecular architecture of multi-cellular organisms (Harapin et al. (2015)), to name a few.

The development of vitreous samples for cryoEM/T (section 2.1.4) was further extended to the preservation of cells and tissues in their native state, for example through high-pressure freezing (Al-Amoudi et al. (2004)) and production of vitreous sections (CEMOVIS) of tissues and large cells for downstream analysis using electron cryo-microscopy. Similarly, methods were developed concomitantly that allowed individual cells to be imaged on electron microscopy grids, albeit in areas thin enough for passage of an electron beam (Plitzko et al. (2002)).

Previously, cells could only be imaged with high detail through the application of plastic embedding, which required the fixation and staining of material to enhance contrast and features in the biological material when analyzed via electron microscopy (McEwen and Marko (2001)). This attempted to combat the low signal to noise found in images of cryo-samples. However, chemical fixation and the random, sometimes ambiguous staining prevents elucidation of molecular details. This precludes the opportunity of sub-volume averaging, as the entities observed in the images/tomograms produced via this techniques are stained and destroyed during the process.

This then, is one of the true powers of electron cryo-tomography; the ability to interpret, process and reconstruct biological macromolecules that are intact, in their native environment and to infer cell biological insight from structure determination and structural cellular context.

3.1.2 Emergent technologies that drive the field forward

3.1.2.1 Sample thinning and targeting rare events

The main limitation of using an electron microscope for analysis of cells is the limited penetration depth for electrons, the maximum for which, in a frozen-hydrated specimen, is typically around 1 µm (Baumeister (2002)). This has led to the emergence of technologies that allow imaging of inner regions of cells, as well as that of tissues.

CEMOVIS (cryo-electron microscopy of vitreous sections) is a technique that allows the preparation of thin sections from high-pressure frozen biological material (Al-Amoudi et al. (2004)). The frozen-hydrated specimen is typically preserved at liquid nitrogen temperatures and maintained under a nitrogen atmosphere. It is then sectioned using a diamond knife that can cut very thin sections typically on the order of 25-100 nm. The resultant sections can reveal structures in regions that are hard to access (Al-Amoudi et al. (2004)), and attempts have also been made to average structures produced via CEMOVIS (Al-Amoudi et al. (2007)). The implementation and method of CEMOVIS does however result in artifacts, and the use of a knife to section material can produce compression artifacts resulting in irregular distortions to the sample and that are difficult to correct for (Hagen et al. (2015); Al-Amoudi et al. (2005)).

In order to mitigate cutting artifacts, an alternative means of thinning vitrified cells has been developed. CryoFIBSEM (cryo-focused ion beam milling and scanning electron microscopy) is a technique that utilizes the established methods of FIBSEM commonly used in materials science and semi-conductors (some applications of which

are discussed in Reyntjens and Puers (2001)). CryoFIBSEM involves the milling of a region of an adherently grown cell (although this can also be performed on high-pressure frozen samples) to ablate away regions above and below a specified plane to leave a lamellae of frozen-hydrated material that can be subsequently image using electron cryo-tomography (Marko et al. (2007); Rigort et al. (2012)). FIBSEM has also been applied to plastic embedded sections (Narayan and Subramaniam (2015)).

One advantage of cryoFIBSEM over CEMOVIS is the former technique's ability to produce sectioned samples that are free from compression artifacts. Although susceptible to surface contaminants sublimated from the protective platinum layer, sample transfer, or from the nearby carbon support as the gallium ion beam ablates away surfaces above and below (Rigort et al. (2012)), the lamellae and biological structure are fully preserved. This means that sub-volume averaging of data from multiple lamella of the same sample can be used to produce, potentially, high resolution structures of macromolecules *in situ* (Hagen et al. (2015); Mahamid et al. (2016); Asano et al. (2015)).

3.1.2.2 Increasing contrast

This move to analyze native cellular structures has come concomitantly with a push towards the development of technologies such as Zernike phase plates, and more recently Volta phase plates (VPP) (Danev et al. (2014); Murata et al. (2010)). Applying the principles of phase contrast microscopy invented by Fritz Zernike (Zernike (1942)) has been a long term goal in the electron microscopy field as a technique that greatly increases contrast of weak-phase objects in electron cryo-microscopy, features that are

typically of low inherent contrast. Phase plates introduce an ~90° phase shift into the scattered beam with respect to the unscattered beam. This change in phase in the scattered beam results in an image in which the phase difference is represented as a change in apparent contrast, as would be typical for interactions in the sample that do not act as weak-phase objects. This is discussed in greater detail in Chapter 5.

Cellular electron tomography suffers from inherent low contrast, that limits the interprebility of tomograms generated from electron microscopy data, and also limits out ability to do sub-tomogram averaging. Phases plates offer a means to increase the contrast we can observe *in situ*. Zernike phase plates and Volta phase plates have been used recently to analyze cellular processes, with significant improvements in the amount of detail that can be observed and averaged. Zernike phase plates (ZPP), which utilize a carbon film with a small "pinhole" through which the unscattered beam passes without any retardation of the phase, whereas the scattered beam passes through the carbon film with a 90° or 270° phase shift. This has allowed detailed studies to be carried out of assembly intermediates of cyanophages as they infect cyanobacteria and the effect that infection of these viruses has on overall cellular morphology (Dai et al. (2013)).

The Volta phase plate (VPP, also referred to as hole-free phase plate) is an alternative to the ZPP and has an electrostatic basis for induction of phase shift in the unscattered beam, term a beam-induced phase shift (BIPS) (Danev et al. (2014)). The VPP has been used to observe various cellular phenomena, and has been utilized in conjunction with other emergent techniques described above (Mahamid et al. (2016); Asano et al. (2015); Fukuda et al. (2015)).

3.1.3 Perspectives in cryoET of cells

Structural biology currently presents an averaged perspective on biology, that precludes the possibility of determining rare biological structures. It relies on techniques based on the production of protein (or macromolecules) at high concentrations, often homogeneously, that are presented outside of their native context and not undergoing their biological function, for example in protein over-expression. This approach is then combined with further approaches that utilize this homogeneity to produce either crystals of proteins, images of similar conformational isolates in different orientations (single particle analysis), or similarly, 3-dimensional volumes of the same protein (sub-volume averaging). Approaches have been attempted to extract and solve separate conformational intermediates (Bai et al. (2015)) but the need for large numbers of particles for high resolution determination limits the technique to isolated proteins/complexes. However, biological processes are often mediated through a range of interactions and intermediates in the context of the cell. Cellular electron cryo-tomography is the only technique that provides the means to view structures and their functional interactions inside cells.

The observation of protein complexes in cells is severely limited due to the need for the feature of interest to reside in an area less than ~1 µm thick. This greatly limits the range of biological processes that can be observed using this approach. In addition to technical improvements to produce better samples or increase data quality, the localization of biological features of interest and making them easier to find and interpret is also another key frontier that is emerging to increase the scope

of the technique.

One such approach is the use of correlative methods to allow the targeting of biological phenomena with a greater spatial accuracy for cryoFIBSEM, such as CLEM (Schellenberger et al. (2014); Schorb and Briggs (2014)). The combination of CLEM techniques with those such as light sheet fluorescence microscopy (LSFM), 3-dimensional structured illumination microscopy (3D-SIM) and localization microscopy, offer the potential for coupling the many complementary techniques for cryoET, such as CLEM and cryoFIB/SEM (Hoyer et al. (2016); Chen et al. (2014); Kaufmann et al. (2014); Schermelleh et al. (2008)). The ability in the future to localize events in Z, which limits the current CLEM techniques, would be particularly important to link CLEM to cryoFIBSEM, and not just limit accurate CLEM to thin regions of the cell. Applying these super-resolution fluorescence techniques to 3-dimensional microscopy reproducibly with the transfer of uncontaminated samples between microscopes under cryo conditions is the next challenge, though some studies have demonstrated the feasibility of such an approach (Kaufmann et al. (2014); Wolff et al. (2016)). CryoCLEM allows imaging of native cells in a frozen-hydrated state, as well as providing information about overall cellular context. Data presented in this chapter suggest that the collection of only a few small datasets (~500 particles), ideally with correlative fluorescence information, is enough to produce a structure on the order of 20-25 Å.

In this chapter I discuss an approach for the determination of structural information in the context of cell biology. The extensive use of classical electron microscopy in cell biology already means that there are numerous biological systems that could be adjusted to be amenable to electron cryo-tomography and take advantage of its

more native environment. Judicious fluorescent labelling and application to appropriate biological systems could help electron cryo-tomography to link between high resolution imaging of cellular structure and low resolution cell biological context.

3.1.4 *In situ* structure determination of macromolecules in their biological context

It is possible to avoid the thickness limit by focusing attention on the cell periphery. These areas of the cell are generally thin enough to be successfully imaged, and are accessible via a much more widely and routinely used route of specimen preparation for many structural and cellular biologists. Understanding the cell periphery is also crucial to understanding many biological mechanisms. These include, but are not limited to, cell signaling, translation, exocytosis, endocytosis, viral entry and egress and cytoskeletal organization and trafficking (Dodonova et al. (2015); Cyrklaff et al. (2007); Brandt et al. (2010); Ibiricu et al. (2011, 2013)).

This approach has also been implemented with a great deal of success, for example when studying polysomes (Brandt et al. (2010)), herpesvirus infection, assembly and egress of L-particles, and transport in axons (Maurer et al. (2008); Ibiricu et al. (2013, 2011)), microtubule lumenal bodies (Cyrklaff et al. (2007)), as well as RNP vaults (Woodward et al. (2015)). In this chapter, I attempt to assess the information that can be gained from sub-volume averaging within single tomograms in intact non-thinned cells. I place this in the context of localization of rare events and discuss the potential for cellular electron cryo-tomography in an era of enhanced signal-to-noise afforded

by the use of imaging filters and direct detectors. My data show that information is contained within the tomogram to allow structure determination to around ~18 Å, and that these structures can be put back into their original context to increase interprebility. I also show that the low resolution structural determination of viruses *in situ* is possible, which offers the potential for the isolation of conformationally disctinct infection intermediates.

3.2 Materials and Methods

3.2.1 Cell culture and plunge freezing

U87MG cells and U2OS cells were seeded and grown on poly-l-lysine- coated gold mesh carbon coated holey carbon grids (Electron microscopy sciences) in Dulbecco's modified eagle medium (DMEM) (Gibco) supplemented with 10% fetal bovine serum. The cells were grown to approximately 60-80% confluency, or until 1-2 cells per grid square. The grids were supported in 2x9-well µ-slide co-culture dishes (Ibidi). Adenovirus particles were cultured and isolated as has been described previously (Wodrich et al. (2010)). For infection of U2OS cells with adenovirus, 4 µl of adenovirus was mixed in 200 µl of DMEM. 50 µl was applied to each grid and incubated with the cells for 10-20mins before plunge freezing. Grids were plunge frozen in an ethane/propane mix, cooled to liquid nitrogen temperature using a manual blotting apparatus, blotted from the backside of the grid for between 2 and 4 seconds.

3.2.2 Electron microscopy

Tomograms were acquired using a Tecnai TF30 "Polara" Microscope (FEI, Eindhoven) operating at 300kV. The microscope was equipped with a Gatan Imaging Filter "Quantum" energy filter, and a post energy filter mounted K2 Summit Direct electron detector (Gatan, Inc.). Data were acquired in counting mode, with aligned frames produced 'on the fly', using the combined filter for image alignment in Digital Micrograph (Gatan, Inc.). Dose, pixel size, magnification and tilt angle information can be obtained in Table A.2 within the Appendix. Data were acquired using SerialEM (Boulder, Colorado) (Mastronarde (2005)).

3.2.3 Tomogram reconstruction, segmentation and sub-volume averaging

Tilt series outputted from the microscope were aligned and reconstructed using the IMOD software package (Kremer et al. (1996)). CTF correction, where applicable, was also performed using IMOD. A global defocus was determined for the whole tomogram, which was then used to correct individual tilts in the tilt series, taking into account the change in eucentricity across the projection images at high tilts. Phase flipping was then performed on each tilt image and the tomogram reconstructed using this phase flipped image stack. Sub-volume averaging of microtubules was performed using PEET (also part of IMOD) (Nicastro et al. (2006)). Particles were picked from tomograms binned 4 times, using scripts based on TEMPy (Farabella et al. (2015)) that evenly sampled at 4 nm intervals (based on the size of one tubulin monomer)

through a straight line defined by the user, with each particle oriented parallel to the line. These particles were then used for iterative sub-volume refinement, with further refinement applied on 2 times binned and unbinned tomograms. Custom scripts were used to relate reconstructions between the binning levels of the tomograms to utilize the respective Euler angles and translational information. Sub-volume averages were acquired at binning levels of 4,2 and 1 for the U87MG tomogram (final pixel size = 4.22 Å at binning 1), and binning levels of 4 and 2 for the U2OS tomogram (final pixel size = 4.6 Å at binning 2). Symmetrization of the microtubules was performed using custom scripts, and utilized the prior knowledge from the unsymmetrized structure that the microtubules contained 13 protofilaments, with 4 nm tubulin monomer spacing.

The particle dataset was split in half at random prior to sub-volume averaging and each half dataset independently averaged during refinement, including symmetrization. Each run of sub-volume averaging at every bin level for the reconstruction was performed three times: one on the first random half dataset, the second on the second half and a third on the combined data. In the case of the U2OS tomogram, at the end of refinement particles with a cross correlation of less than 0.2 were excluded. In the case of both tomograms, if any particles had centers within 4 nm of each other, the particle with the lower cross correlation was excluded. Resolution determination was assessed through FSC at 0.143 between the two half set reconstructions ('gold standard'). Structures shown in the paper are from the combined dataset, filtered to the resolution cut-off determined by FSC0.143. Curves were determined using a number of different masks, specifically: no mask, the final microtubule structure bi-

narised at a noiseless threshold and extended with a soft edge (thresholded mask), a hard edge cylinder or soft edge cylinder of approximate microtubule size (Figure 3.5F). FSC curves and masks for "gold-standard" FSC determination were generated using EMAN2 (Tang et al. (2007)).

Refinement of the adenovirus structure was performed using PEET, utilizing an option to not produce a new map after each iteration of refinement. The virus reference structure (EMDB-1574) was filtered to 60 Å prior to alignment. The determined position and orientation of the picked particle was then used to symmetrize it and produce a reconstruction. We also produced a "back-plotted' tomogram, where the virus particles in the tomographic volume were substituted with the reconstruction using a custom script that utilized the translation offsets and Euler angles for each given particle position.

Segmentation and representation of tomograms (including back-plotted tomograms) was performed and viewed using the visualization software Amira (FEI, Eindhoven). Sub-volume averaging structures and back-plotted coordinate models were viewed using Chimera (UCSF) (Pettersen et al. (2004)).

3.3 Results and Discussion

3.3.1 CryoET of the cellular periphery

Using a 300 keV FEG electron microscope with post-energy filter mounted direct electron detector (Gatan K2 Summit), we first aimed to assess visually what infor-

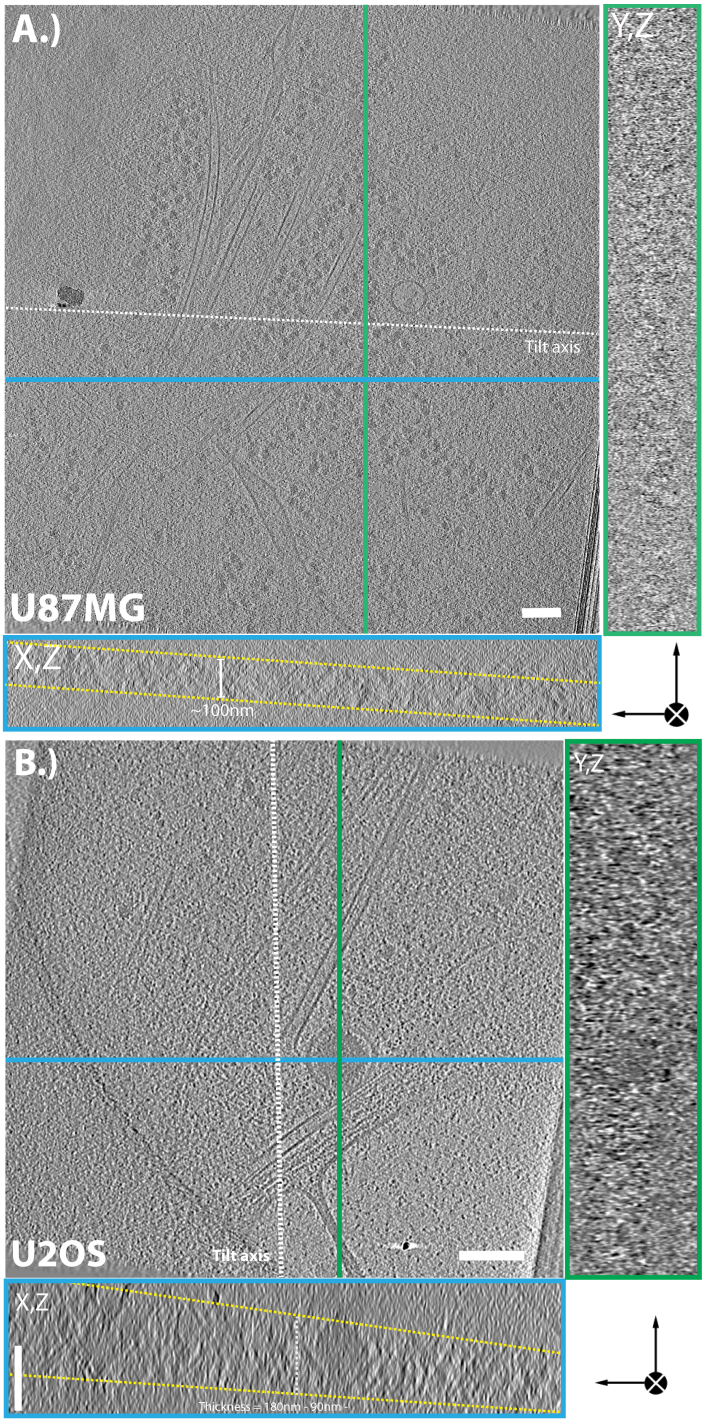

Figure 3.1 – Comparison of cellular electron cryo-tomograms from U87MG and U2OS cell lines. A.) Tomographic slices in 3-dimensions (XY, XZ and YZ) of U87MG tomogram used for analyses in Figure 3.2 and 3.4. The position of XZ (blue line) and YZ (green line) is shown in relation to the XY slice. Scale = 100 nm. B.) Tomographic slices in 3-dimensions (XY, XZ and YZ) of U2OS tomogram used for analysis in Figure 3.5. The position of XZ (blue line) and YZ (green line) is shown in relation to the XY slice. Yellow lines indicate the thickness of the ice. Scale = 100 nm.

mation could be gained by following relatively regular and populous features within single tomograms of adherent human cells. This was carried out for two tomograms from two different cells lines: 1) U87MG cells and 2) U2OS cells. Figure 3.1 shows the relative thickness of the ice layer between the two tomograms, with the U2OS tomogram being twice as thich in some areas as the U87MG tomogram.

I discriminated the different components of the cytoskeleton, such as intermediate filaments, F-actin and microtubules (Figure 3.2C, E and F) due to their characteristic structural signatures. The overall level of detail in these tomograms was very high, allowing us to clearly discern, e.g. for the cytoskeletal structures, considerable sub-structural detail. For F-actin, we could observe the zig-zag nature of F-actin (Figure 3.2F, green line), a 2.8 nm repeat feature, as well as the globular features of individual actin monomers within the filament (Fujii et al. (2010)). Similarly, the intermediate filaments showed a rather smooth parallel tubular architecture slightly wider in diameter (10 nm) than actin filaments (7 nm), consistent with their tightly packed, cylindrical structure (Herrmann et al. (2007)).

However, the greatest level of detail visible in the tomogram was found when considering the microtubules. Protofilaments were visible in the top and bottom views of the microtubules. Furthermore, the tubulin lattice in the microtubule wall was evident with the 4 nm spacing of tubulin monomers being distinguishable through top, bottom and middle slices of the microtubules (Figure 3.2E), suggesting a high level of detail in the tomogram. I was also able to visualize more transient states in these filaments, such as a microtubule plus end in the process of disassembly (Figure 3.2C) (Koning et al. (2008)).

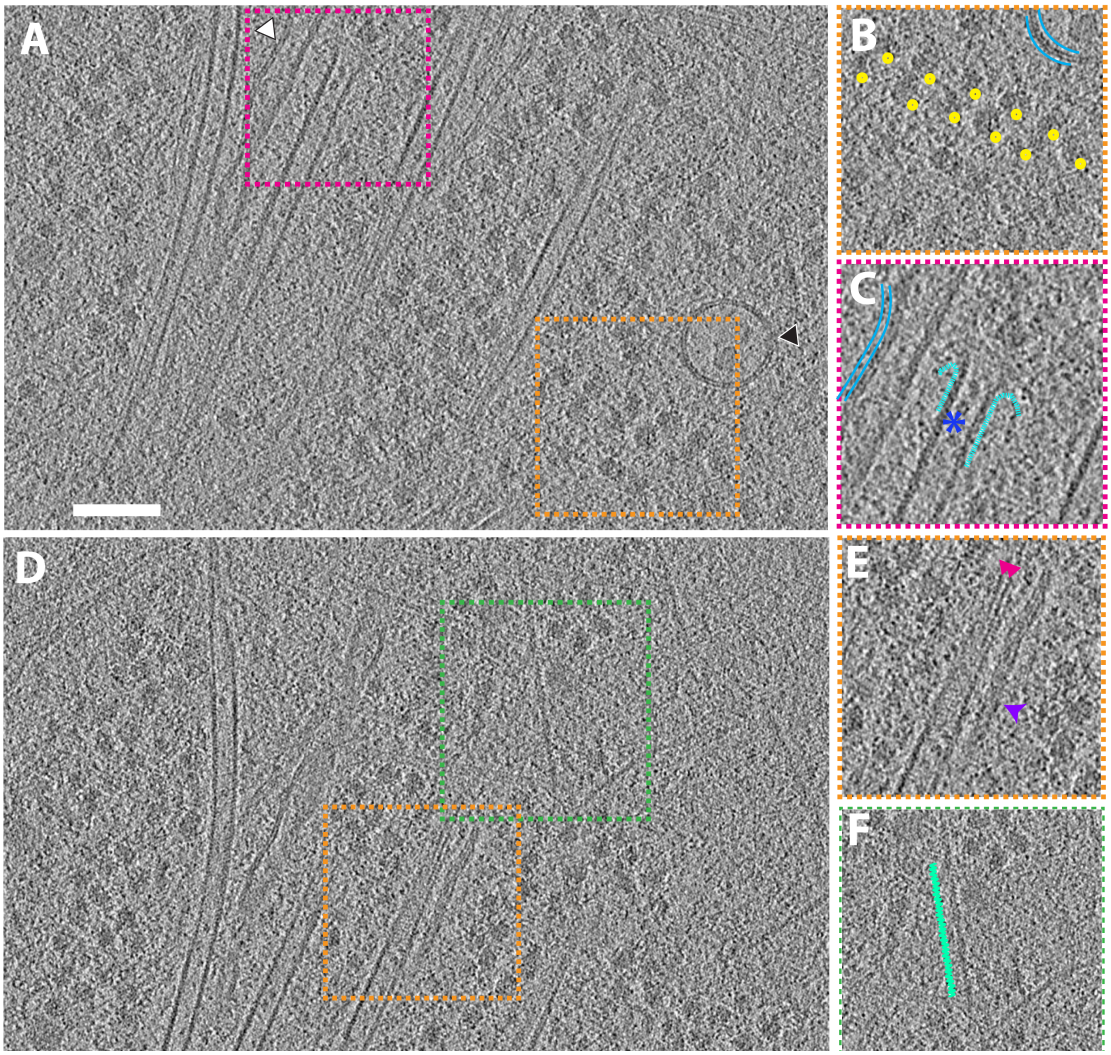

Figure 3.2 – CryoET of a peripheral region of an adherent U87MG neuronal cell line imaged using direct electron detection. (A) Slice through tomogram at the periphery of U87MG cell, containing a number of cellular features such as (B) polysomes and (C) de-polymerizing microtubule in proximity to the endoplasmic reticulum with microtubule luminal bodies (blue asterisk). White and black arrows in (A) represent the endoplasmic reticulum and a lysosome, respectively. (D) Another slice through the same tomogram, showing the diversity of cytoskeletal elements visible in a snapshot of the cell periphery; (E) microtubule protofilaments (pink arrows)(top-view), intermediate filaments (purple arrow) and (F) actin (green). Squares outlined by colored dashed lines in (A) and (D) indicates positions of areas in (B and C) and (E and F), respectively. Scale bar; 100 nm. All tomographic slices are individual slices with a voxel size of 4.22 Å.

As well as elements of the cytoskeleton, the tomogram also showed less regular, more globular features. Ribosomes were often arranged into polysomes (Figure 3.2B), as has been characterized previously (Brandt et al. (2010)). A single Ribonucleoprotein "Vault" (Woodward et al. (2015)) could be observed, in close proximity to a microtubule and potentially engaged with a dynein motor (Figure 3.3). The putative AAA+ domain of a dynein motor complex as well as the respective stalk regions projecting onto a nearby microtubule are visible (Figure 3.3)(Roberts et al. (2009)). Vaults are ribonucleoprotein organelles that are thought to recruit and store mRNAs. This function has led to the suggestion that they act as a transport vector between the nucleus and cytosol (Chugani et al. (1993)). This observation adds credit to the idea that Vaults are important in the transportation of mRNAs and other cargoes inside cells. Further to macromolecules, organelles could also be identified, such as the lysosome and the endoplasmic reticulum (Figure 3.2B, white and black arrows), with the 6-8 nm thick membrane bilayer visible.

3.3.2 *In situ* sub-volume averaging from a single tomogram

In order to assess the potential resolution achievable from this tomogram of a peripheral area of an U87MG cell, I performed sub-volume averaging of microtubule segments (Figure 3.4). Due to the fact that the microtubules were oriented roughly perpendicular to the tilt-axis for the tomographic series, I expected that I would be able to compensate to some extent the information lost due to the CTF, as different apparent defoci of extracted volumes caused by tilting of the sample would compen-

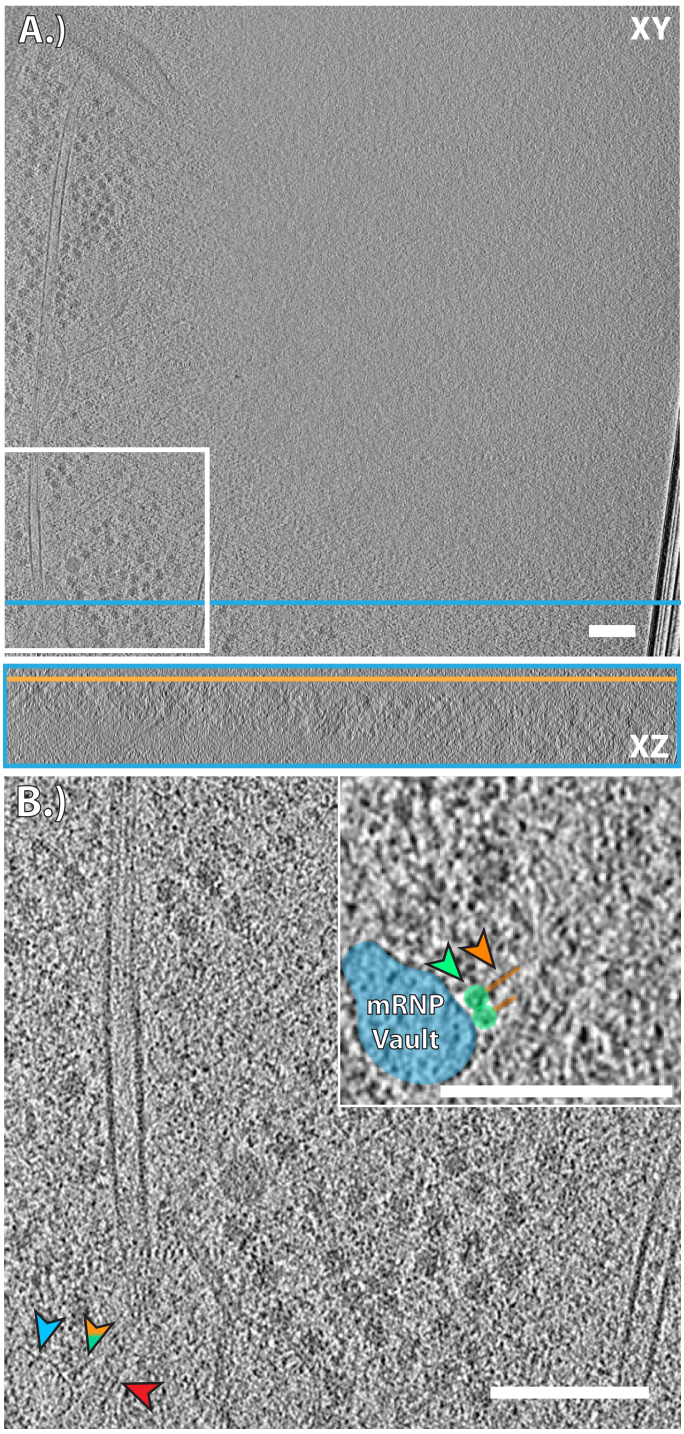

Figure 3.3 – Structural context of Vault protein in U87MG tomogram. (A) Box outlined by a dashed line in the XY slice (along the orange line in XZ; XZ sliced along the blue line XY) indicates the position of vault within the tomogram. (B) zoom into area inside the white box in (A). The blue arrow and area (inset) highlights the position of the ribonucleoprotein Vault, the green/orange arrows highlights the dynein dimer (green = AAA+ domain and orange = stalk domain) and the red arrow highlights the top of the microtubule in contact with the dynein dimer. Scale bars = 100 nm.

sate for some of the lost information. The resultant microtubule structure has 13 protofilaments, with tubulin monomer spacing of ~4 nm, consistent with the current understanding of the microtubule structure in vivo. As the sampling of the tomogram precluded the possibility of discerning the microtubule seam in these structures, I applied a 13 fold helical symmetry to the final model to produce the final structure. The gold standard Fourier Shell Correlation curve of the resultant microtubule structure (Figure 3.4B) indicated a resolution of 18.5 Å (Figure 3.4D). A prominent local peak occurred at a spatial frequency equivalent to ~22 Å resolution (Figure 3.4D and Figure 3.5). Analysis of the Fourier spectrum of the microtubule structure indicated a strong layer line at this resolution, as has been seen for other microtubule structures (Alushin et al. (2014)). The calculated defocus and the nominally acquired microscope defocus differed by up to 1 µm. Combined with a range of defoci across the tomogram (due to eucentric height), it is difficult to determine an overall single defocus. I therefore proceeded with the IMOD determined defocus (Xiong et al. (2009)) as basis for comparisons.

The resulting microtubule structure is of correct size and shape to fit a crystal structure of the tubulin αβ-dimer (PDB: 1TUB) (Figure 2B, inset). Due to the nature of tomographic data acquisition, where a range of defoci likely exist within the same dataset, the zeroes of the CTF will not be clearly visible in a sub-tomogram average if a structure that prevails throughout the field of view in a single tomogram is used for sub-volume averaging. Our analysis suggests that the sub-volume averaging performed from this single tomogram is however very likely limited in resolution by the number of particles contained within the tomogram; here 4056 sub-volumes of 25

nm x 25 nm contributed to the final average.

In the case of single particle reconstruction methods, resolution has been shown to be very sensitive to the applied electron dose (Bartesaghi et al. (2014)). An element where the dose may be important in sub-tomographic averaging is when incorporating high tilts into the final sub-volume average. Studies have shown that lower tilt images are the main contribution to good resolution sub-volume averages (Bartesaghi et al. (2012)) and recent strategies have been developed to down weight the contribution of higher tilts (Bharat et al. (2015)). However, high tilts can be very important in the reduction of back-projection artifacts from gold fiducials in tomograms, which may otherwise interfere with the interpretation of rare individual events in cellular tomograms.

Sub-volume averaging of microtubules in the U2OS cellular tomogram (Figure 3.5) resulted in a microtubule structure of 25 Å. This resolution was determined without a mask as use of a mask appeared to produce noise in regions of the FSC curve where the 0.143 cut-off would have been taken, as shown in Figure 3.6. Due to the higher magnification, and resultant smaller field of view, only a quarter of the number of particles could be picked with respect to the U87MG tomogram (Table A.1). Only particles with a cross-correlation coefficient (CCC) score above 0.2 after alignment were included in the final average. Removal of particles below this threshold removed the majority of the microtubule particles that were in the thicker regions of the tomogram (Figure 3.6). A thickness gradient from ~90 to ~180 nm existed across this tomogram (Figure 3.1B). It therefore seems likely that the main contribution to the low CCC in this model is due to the increased thickness. However, it has been shown

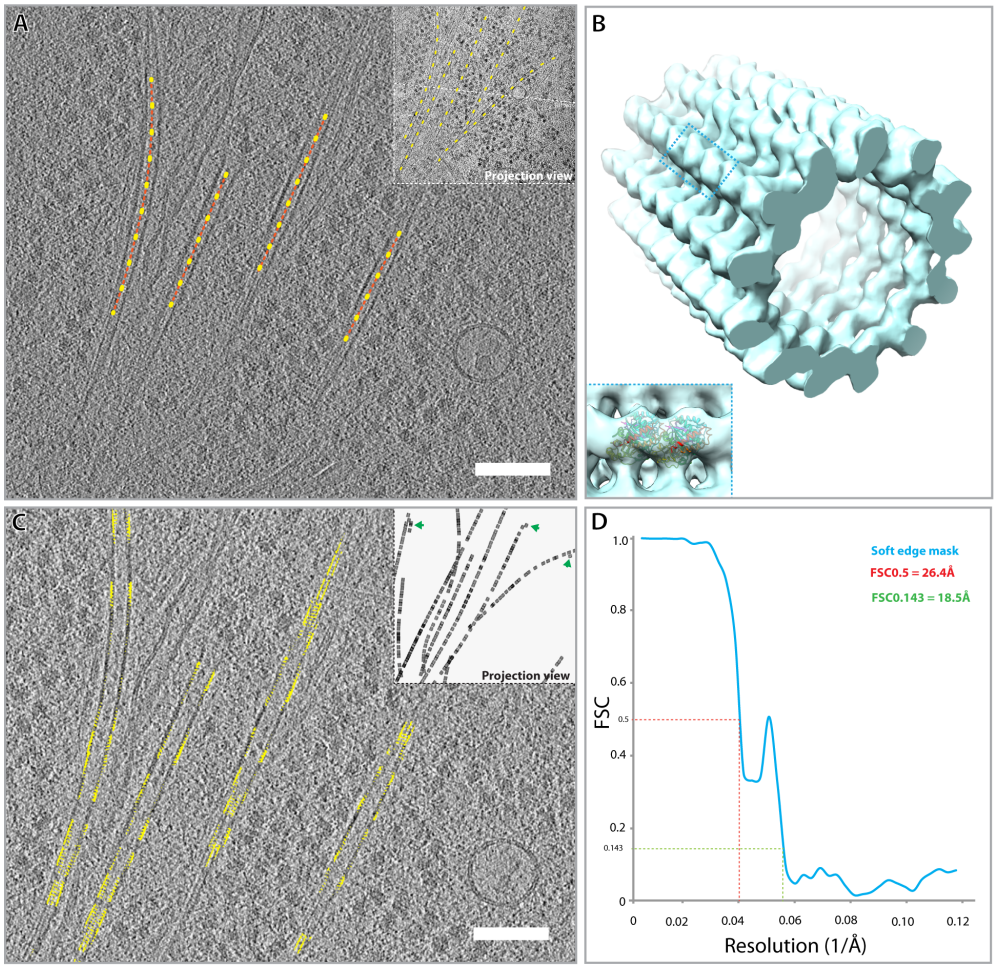

Figure 3.4 – Sub-volume averaging of microtubules. (A) Schematic model of how microtubules were picked for sub-volume averaging shown in the context of a single tomographic slice and as a projection of the whole tomogram (inset). (B) Resulting sub-volume average of the microtubule from the tomogram shown in (A) filtered to 18.5 Å according to the calculated gold standard FSC, at threshold 0.143. (C) Tomographic slice overlaid with the equivalent slice in the back-plotted tomogram and projection (inset) of the microtubule average shown in (B). Green arrows represent outlier particles. These outliers represent particles in regions of the tomogram that may be less well aligned (i.e. edge of tomogram) and are included in the final average. (D) Gold standard FSC curve for the microtubule structure determined from the tomogram. The FSC was produced using a soft-edge cylindrical mask. Scale bar for (A) and (C) is 100 nm.

before that filamentous objects with the tilt axis perpendicular to the direction along which they propagate suffer from distortions that may affect their potential to align accurately (Mastronarde (1997)). Interestingly, these microtubules aligned parallel to the tilt axis, suggesting the alignment may be dependent on the tilt axis.

In the case of this second microtubule sub-volume average structure, the fall-off in cross correlation between the two independent halves of the dataset did not reach zero (Figure 3.5), suggesting that there is an alignment of noise during the refinement of the structure, possibly introduced by particles from the thicker regions of the sample. This is confirmed through comparison with the non-CTF corrected FSC curve, which was generated by replacing the CTF-corrected tomogram with its non-CTF corrected equivalent, without further alignment of the particles. Since this changes the noise floor, the noise correlation disappears, as evidenced by the near zero values of the non-CTF corrected FSC curve at higher resolutions (Figure 3.9).

3.3.3 Back-plotting of sub-volume average structure into the tomogram results in a 3-dimensional context for structural interaction

The ability to gain biological insights from cryoET data depends on our ability to detect the *in situ* context of our biological feature of interest. We used the refined positions and orientations of the individual particles contributing to the average to place the microtubule structure back into the tomogram. The microtubule average was back plotted into the raw tomogram, which is of low signal-to-noise and thus it

is difficult to directly visualize molecular interactions. In this instance, I applied two methods: a) direct back plotting of the sub-tomogram average structure using the positions and orientations determined during alignment, and b) refining the orientation of a known structural feature into the respective position in the tomogram, in this case performed for an adenovirus virus capsid.

Sub-volume averaging of the microtubule was performed as described above. For the adenovirus re-orientation, I used PEET to fit a previously determined viral structure (EMDB ID 1574, (Fabry et al. (2009))) into our tomographic viral feature. The orientation of this structure was then refined and placed into the tomogram according to the determined orientation.

To validate the accuracy of the alignment of the EMDB structure to the adenovirus contained within the tomogram, I performed icosahedral averaging of the single adenovirus within the tomogram, according to the Euler angles determined during the alignment of the EMDB map. The resultant symmetrically averaged structure yielded a resolution of 77 Å, when compared to a low-pass filtered map of EMDB-map at 20 Å (Figure 3.5F). The icosahedral average of the single virus before and after orientation refinement is presented in Figure 3.7. The symmetrized adenovirus structure allowed for direct visualization of the trimeric hexon proteins on the virus surface, as well as of the 12 penton bases. Icosahedral symmetrization of the virus in the absence of any refinement yielded no discernible structure (Figure 3.7) indicative of a lack of symmetry axis orientation and possible position inaccuracy. This analysis shows that the information contained in our tomogram was able to produce signal to 77 Å (Figure 3.5E, 3.5F) from only 60 copies of an asymmetric unit, with the noisy

FSC curve being indicative of particle number-based limitation. The demonstrated potential for the differential structural determination of sub-populations of virus and protein structures *in situ* provides promising and exciting possibilities for dissecting dynamic processes and subtle structural changes *in situ*.

The resultant "segmented" tomogram (Figure 3.5C, 3.5D), allowed for directly viewing the 3-dimensional spatial organization of the microtubule network of an adenovirus undergoing viral entry. The ability to determine the orientation of the virus with respect to the cell membrane allowed the visualization of the position of the adenovirus penton fibre as it interacts with the plasma membrane during entry (Figure 3.5C, 3.5D). The bilayer of the plasma membrane could clearly be followed around the virus in x,y and z, the curvature being indicative of the process of entry being fairly advanced.

3.3.4 Evaluation of CTF correction of tomograms for *in situ* sub-volume averaging

Sub-volume averaging of structures from single tomograms is routine until the resolution approaches the first zero of the CTF function for the defocus at which the tomogram was acquired. In order to derive accurate information past the first zero, it is important that one corrects the CTF. Phase flipping in IMOD was sufficient in a single tomogram to recover the information contained in particles across the field of view. The CTF corrected structure of the microtubule from the U87MG tomogram has an FSC0.143 of 18.5 Å, and interpretable information persists in the FSC

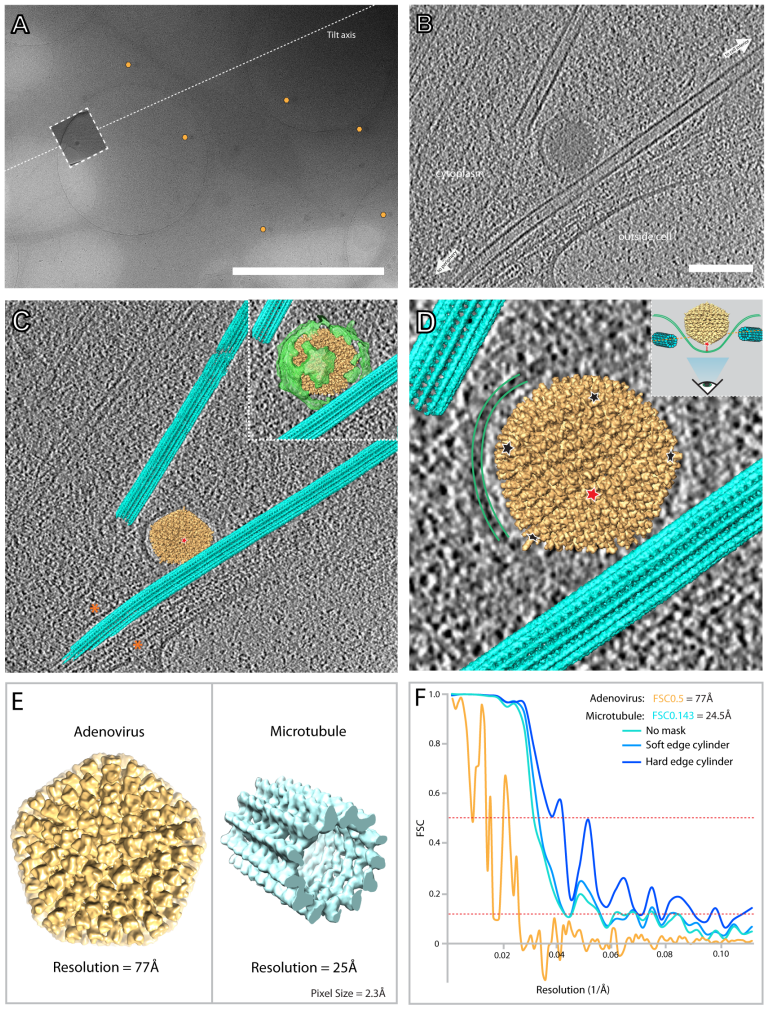

Figure 3.5 – Endosomal entry of Adenoviruses as a case for structure determination *in situ*. (A) Low magnification image (9500x, nominal) of the field of view of an U2OS cell infected with adenoviruses (marked by yellow hexagons). The tilt axis is shown as a white dotted line. (B) High magnification (95000x, nominal) slice of a tomogram taken at the position shown by the dotted box in (A) at approx. 5.2 µm defocus. (C) Tomographic slice titled by ~45° angle relative to the slice shown in (B), with the microtubule (cyan) structure and an adenovirus (yellow) structure (filtered to 20 Å – EMDB-1574) back-plotted into the tomogram. Green (inset) shows a view of manually segmented surrounding endosomal membrane. Orange asterisks denote the peripheral F-actin. (D) View from below the adenovirus, showing the localization of the penton bases of the adenovirus (red and black asterisks). (E) Left: Adenovirus structure (yellow) produced from the icosahedral average of the *in situ* adenovirus determined using the calculated Euler-angles of the back plotted virus and subsequent sub-tomographic averaging. Right: microtubule structure (cyan) produced from this tomogram. Adenovirus is approx. 960 Å in diameter. Microtubule is approx. 25 nm in width. (F) FSC curves of the single adenovirus (yellow) and the microtubule average (cyan – green). The colour of the curve indicates the type of mask used in the final gold standard FSC determination of the microtubule. Resolution stated is unmasked. Scale bars are 2 µm and 100 nm for (A) and (B), respectively.

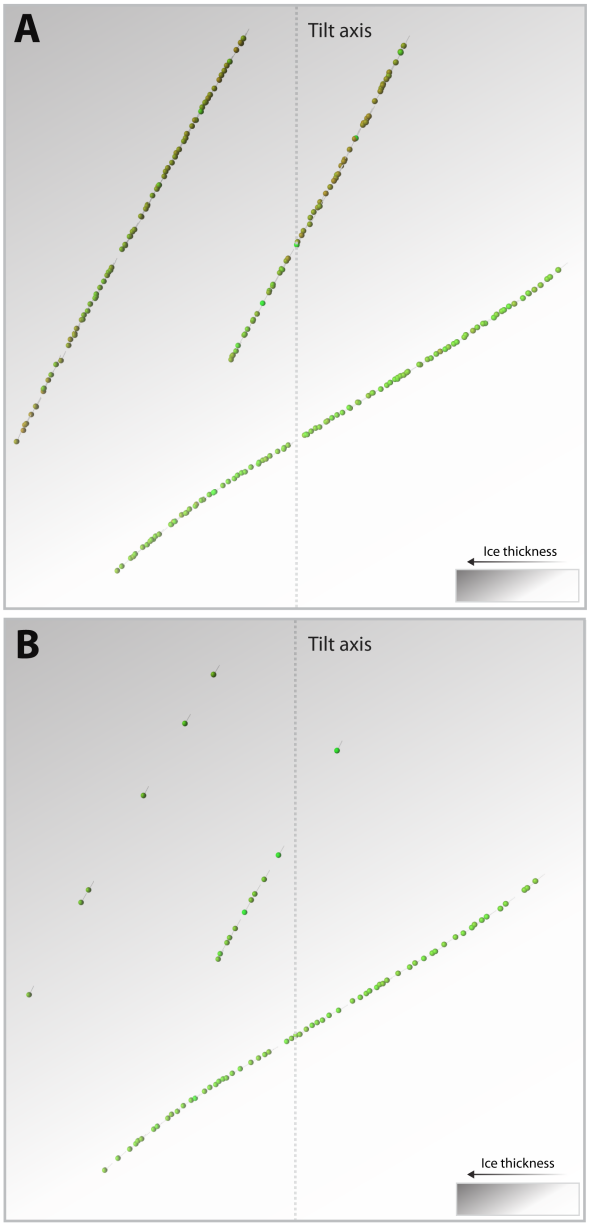

Figure 3.6 – Model of the linear model used to determine the microtubule structure in Figure 3.5. A) Orange/green spheres determine the position relative to the tilt axis of sub-volumes with high (green) and low (orange) cross correlation to the average. B) Model of sub-volumes after removal with a cross correlation of 0.2. Black and white gradient in both A and B approximated the thickness gradient across the tomogram.

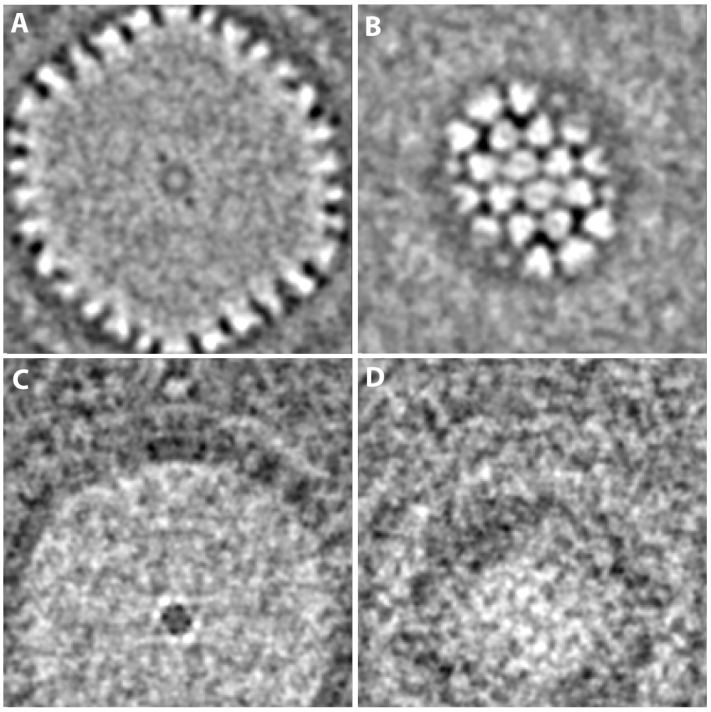

Figure 3.7 – Symmetrized structure of the Adenovirus in the U2OS tomogram. A) and B) shows the middle and top slice, respectively, of the adenovirus structure shown in Figure 3.5 after symmetrization of the virus using the refined Euler angles resulting from an orientation search for EMDB-1574 filtered to 20 Å. C) and D) shows the middle and top slice, respectively, prior to any refinement, rotationally or translationally, against EMDB-1574.

to around 17 Å. Without CTF correction, the amount of information in the structure falls off at around 25 Å (Figure 3.8A). In the case of the U2OS tomogram, the non-CTF corrected structure is interpretable to 32 Å due to the CTF induced phase change, but is increased to a resolution of 24.5 Å after CTF correction (Figure 3.8B).

Interestingly, the calculation of the defocus in IMOD of each tomogram was different to the nominal defocus of the microscope by as much as 0.5 µm (see Table A.2 in Appendix). Even accounting for inaccuracies in defocus determination of the microscope (Danev and Baumeister (2016)), this is still a large discrepancy. The CTF curves for the calculated defoci are shown in Figure 3.8C for each tomogram. To better determine the accuracy of the CTF correction, an 'ideal' microtubule structure was built by fitting atomic models of symmetrized tubulin monomers from a microtubule structure (PDB ID: 3J2U, Asenjo et al. (2013)) into the sub-tomogram averages determined here. These atomic models were then Gaussian blurred in Chimera to Nyqvist frequency and matched in sampling and box size to the respective sub-tomogram average. The FSCs between this 'ideal' structure and the CTF and non-CTF corrected averages are shown in Figure 3.10. For both structures, CTF correction resulted in a more accurate structure, with the u87mg microtubule (Figure 3.10A) displaying a particularly obvious phase flip correction. However, a small dip below zero at around 25 Å in the U2OS CTF-corrected FSC (Figure 3.10B, purple line) may well indicate an inaccuracy in defocus determination.

Approaches that have been implemented recently (Galaz-Montoya et al. (2016); Bharat et al. (2015)) whereby individual sub-volumes are tilt-dependently CTF corrected should prove to be much more accurate in determining a per-particle CTF

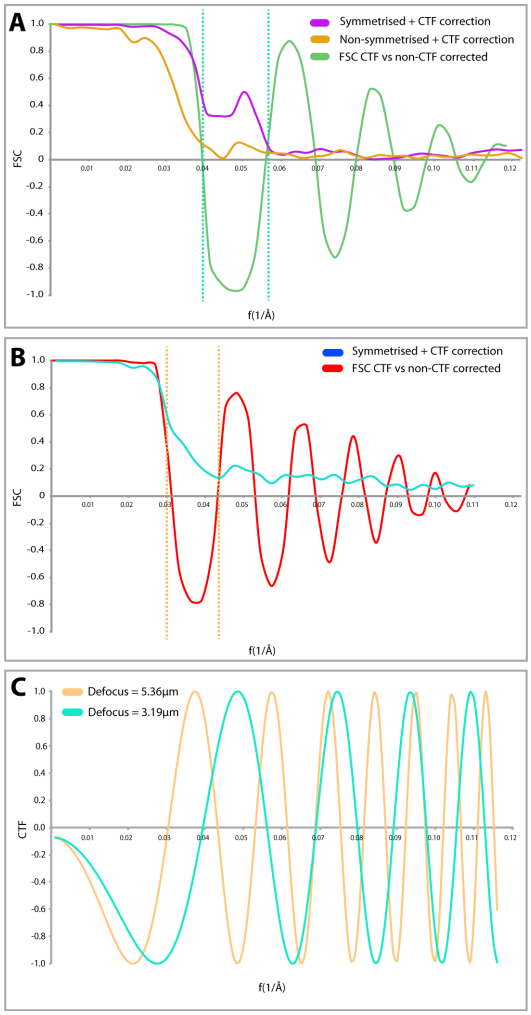

Figure 3.8 – Sub-volume averaging *in situ* in a single tomogram is enough to correct for the CTF, and results in a corrected sub-volume averaged structure. (A) CTF curves of sub-volume averages produced from CTF corrected sub-volume average microtubule from the tomogram of the U87MG cell before (orange) and after (magenta) symmetrization. The green curve represents the FSC of the non-CTF corrected average when compared to the CTF-corrected structures in both cases. This produces the expected negative correlation due to the effect of the CTF (green dotted line). (B) FSC curve of the CTF-corrected U2OS cell microtubule reconstruction (blue). FSC of the equivalent non-CTF corrected when compared to the CTF-corrected structure (red). Lack of fall-off to zero of the CTF corrected structure is due to alignment of noise during symmetrization of the microtubule average after alignment. (C) CTF calculation for the determined defoci for the tomograms in (A) (cyan) and (B) (brown). Phase flipping, and the range of defoci of particles within the tomograms has compensated for the inverted contrast and node of zeroes caused due to the oscillations in the CTF. This indicates that the range of defoci within a tilt series is enough to compensate for a single nominal acquisition defocus. Mask used to produce the FSC are a soft cylindrical mask in A) and no mask in B).

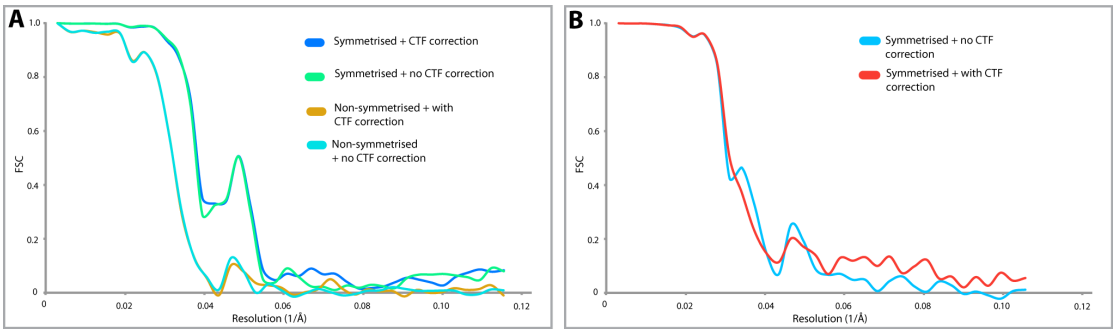

Figure 3.9 – Comparison of "gold standard" FSC curves for CTF and non-CTF determined structures. A) U87MG tomogram and B) U2OS tomogram.

correction. These approaches may yield a much more accurate determination of particle eucentricity across the tilt series, as a custom per-particle defocus and Z-position within the tomogram can be determined. This should result in sub-volume averages that yield better results, particularly for single tomograms, or datasets with only a low number of particles.

3.3.5 Determination of virus structure *in situ* improves understanding of virus-host interaction

The current structural understanding of virus-host interactions stem mainly from studies using co-crystalized complexes, small angle scattering and sub-volume averaging of *in vitro* constituted systems, such as virus-like particles. Analysis of cells as they enter cell using the approach outlined in this chapter may pose a new means to investigate structural intermediates during viral entry. The increased signal-to-noise ratio in the images gained from the use of direct detection allowed molecular process in high detail in the cell, as well as average structures to an intermediate resolution capable of bridging the gap between structural context and molecular resolution (Fig-

ures 3.4 and 3.5). The structural context of virus-cell processes in a model cell line is the closest one may currently come to reconstituting a disease-like state. The ability to localize structures in their cellular context (Figure 3.5, 3.7), and sub-volume average different conformers of the virus as it progresses through its various stages of its life cycle (Figure 3.5C, 3.7), will allow me to determine which viral proteins are lost, which cellular proteins it interacts with, what other biological macromolecules and pathways the virus recruits or hijacks in this dynamic process. Being often easily recognizable due to their unique structural signatures viruses also constitute ideal tools to probe cellular processes. Furthermore, the structural determination of cellular factors co-localizing with the virus during infection allows novel forms of therapy to be investigated.

3.4 Concluding Remarks

In this chapter, I have discussed methods and data that allow for assessing the wealth of detail that can be mined from a single tomogram. Resolutions of 77 Å from a single symmetrized icosahedral virus and 18.5 – 24.5 Å from relatively few numbers of microtubule segments gives me a good indication that in many cases, the amount of information present even in a single tomograms is substantial, and something that, given the right biological problem and system, may lead to novel insight complementing structural models many laboratories are building using canonical techniques. Improvements in microscopic hardware, software workflows, sample preparation and transfer, and computational processing will require future investment if cryoET is to

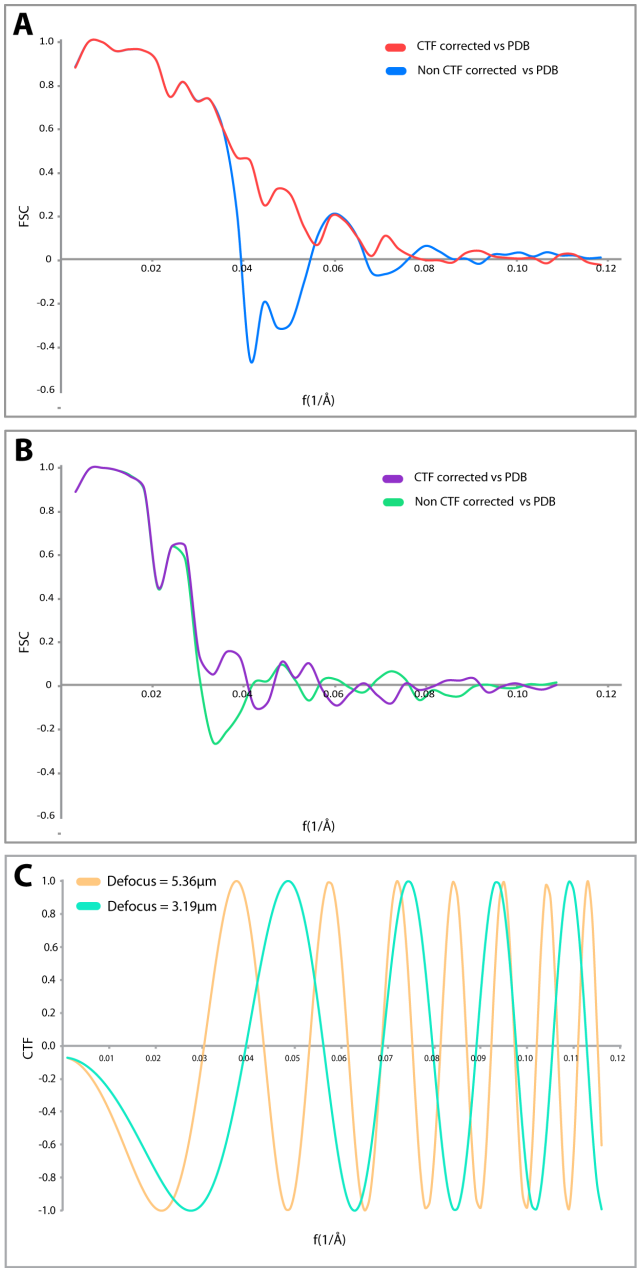

Figure 3.10 – Comparison of sub-volume averaged microtubule structures with a PDB-generated "ideal" 13 protofilament model highlights aberrant points in the structure. The effect of the CTF on elements of the sub-tomogram averaged microtubules structures are shown for A) U87MG and B) U2OS tomograms. A) shows a pronounced dip below zero between 0.040 – 0.055 corresponding to the theoretical first negative oscillation of the CTF of the microscope, shown in C). An equivalent dip is also visible in B) (c.f. figure 3.8).

realize its full potential.

In the following chapter, I discuss work towards a fully integrated solution to a biological question, combining information from a number of techniques spanning the entire resolution spectrum. The improvement of what can be discerned from cryo-tomography data of cells must come from other techniques, as discussed in the introduction to this chapter. These techniques allow us to build up a specific and contextual model that can be probed further and at higher resolution by electron cryo–tomography. Sub-volume averaging and structure determination of elements *in situ* allow us to further improve our mechanistic understanding on a structural level through combination with techniques such as X-ray crystallography, single particle analysis and small-angle X-ray scattering.

4

Determination of the transport and membrane dynamics of herpesvirus capsids during nuclear egress

4.1 Introduction

4.1.1 Herpesvirus life cycle

Herpesviruses enter the cell through the fusion of the host and herpesviral membranes, a process mediated by glycoprotein B (Heldwein et al. (2006)) and requiring the participation of several other virally encoded glycoproteins, D, H and L (Cooper and Heldwein (2015)). Once inside the cytoplasm of the cell, HSV is transported to the nucleus by cytoplasmic dynein via microtubule-based transport (Dodding and Way (2011)) (see Chapter 2). At the outer nuclear membrane, the capsid associates with

importin β, most likely through interaction with either pUL25, pUL36 or both. This holocomplex then associates with Nup214 and/or Nup358 of the nuclear pore complex (NPC) and results in the injection of the viral genome into the nucleus through the NPC (Le Sage and Mouland (2013)). Inside the nucleus, the viral DNA is replicated and the viral genes are transcribed and translated. Nascent capsids assembled in the nucleus require a mechanism of escape from the nucleus. The size exclusion limit of the nuclear pore complex is limited to 39 nm (Pante and Kann (2002)), therefore the ~120 nm diameter capsids must utilize another means of escape from the nucleus. Herpesviral nuclear egress has been extensively studied (Mettenleiter (2004); Mettenleiter et al. (2006)). A primary envelopment at the inner nuclear membrane (INM) into the lumen and subsequent de-envelopment at the outer nuclear membrane (ONM) has been viewed using classical electron microscopy. The process was traditionally viewed as being specific to herpesviruses. However, it was recently shown that eukaryotic cells are also able to transport large cargoes from the nucleus, such as large aggregated RNP complexes (Speese et al. (2012)), suggesting this may be a form of divergent evolution where a cellular pathway has been subverted and modified to serve the virus' needs. Ongoing investigation into the role of Torsin AAA+ ATPase (Jokhi et al. (2013)) and other players may one day reveal a cellular structural homology to herpes nuclear egress.

4.1.2 Nuclear egress of herpesvirus capsids

Two viral proteins play a key role in the envelopment of nascent herpesvirus capsids at the INM, as recently reviewed by Hellberg et al. (2016). These proteins are designated in alphaherpesviruses as pUL34 and pUL31. pUL34 is a type 2 integral membrane protein that is expressed in early infection. It localizes to the INM and forms a diffusive layer when expressed alone in cells. pUL31, in contrast to pUL34, is a soluble protein that is diffuse within the nucleus when expressed in cells. When co-expressed in the cell, pUL34 and pUL31 form peri-nuclear vesicles and, subsequently, discrete puncta along the INM (Klupp et al. (2007)). Investigations of the membrane modulation activity of pUL34/pUL31 (nuclear egress complex (NEC)) using giant unilamellar vesicles (GUVs) *in vitro* showed that in isolation, this complex is able to mediate the formation of vesicles (Lorenz et al. (2015); Bigalke et al. (2014)). It was further shown that when expressed in isolation and tethered to nickel GUVs via a 6-Histidine-tag (His-tag), pUL31 alone could produce membrane deformation characteristics and an amorphous protein layer at the INM *in vivo* (Lorenz et al. (2015)). This behavior suggested that these two proteins might mediate the envelopment of nascent herpesvirus capsid into primary enveloped particles (in the lumen between the INM and ONM). In this model, pUL34 forms the membrane tether that recruits pUL31 to the INM (Figure 2.1). pUL31 interacts with herpesvirus capsids and causes a deformation of the INM that leads to primary vesicles able to transcend the luminal barrier between the INM and outer nuclear membrane (ONM). Once at the ONM, through an unknown mechanism that is, in Pseudorabies virus (PrV) at least, not gB,

gD or gH/gL dependent, the vesicles fuse with the ONM and become de-enveloped resulting in nascent capsid in the cytoplasm (Mettenleiter et al. (2006); Hellberg et al. (2016)).

Besides pUL31 and pUL34, other herpesviral proteins have been implicated in playing a crucial but more accessory role in nuclear egress (Cibulka et al. (2012)). The nuclear lamina is an important structural feature of the nucleus, that is involved in the regulation of gene expression, DNA replication and chromatin stability and dynamics (Burke and Stewart (2013)). HSV1 requires a means to clear the nuclear lamina, to allow space for capsid association with the nuclear egress complex (NEC) and subsequent transport across the INM into the lumen. pUL31 is a phosphoprotein and during escape from the nucleus, capsids accumulate at the INM without being trafficked in cases where a viral kinase, pUS3, is knocked-down. pUS3 has further been shown to phosphorylate both pUL31, pUL34, A- and B- type lamins and Emerin, the latter of which are important proteins in the nuclear lamina. pUS13 is another herpeviral protein that has been implicated in this phosphorylation cascade. pUS3 and pUS13 result in the activation of phosphokinase C producing a cascade of phosphorylation that causes the dissolution of nuclear lamin, which is essential for the nuclear egress of herpesvirus capsids (Cibulka et al. (2012))(Figure 2.1).

The mechanistic basis and precise geometrical relation through which the NEC recruits and envelops the nascent capsid still remains elusive. Previous *in vitro* studies suggested that the molecular arrangement of the NEC complex may be hexagonal in nature. However this could be only shown in 2-dimensions, and in a non-native lipid environment (Bigalke et al. (2014)). Recent structural information on the nuclear

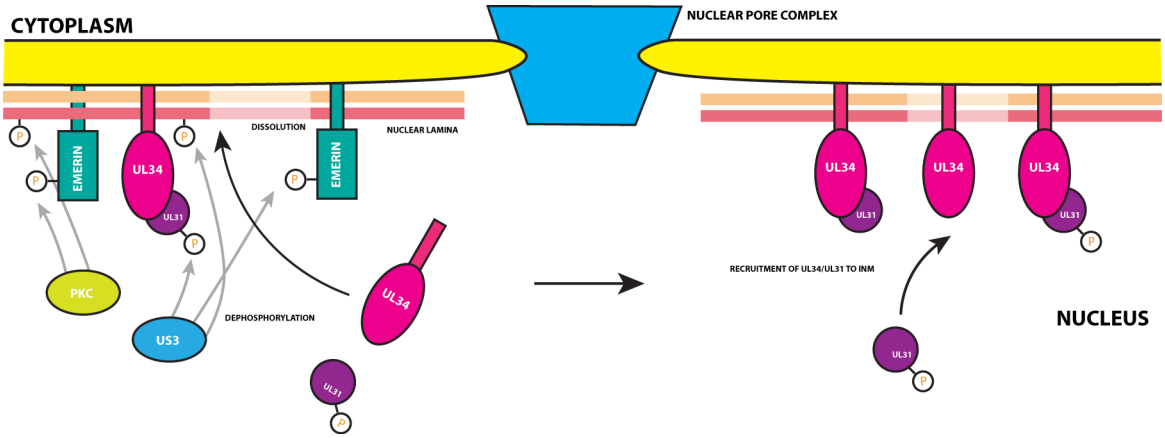

Figure 4.1 – Summary of the interaction network at the nuclear lamin of the inner nuclear membrane (INM). Dephosphorylation of the lamin network by pUS3 and Phosphokinase C results in the dissolution of the lamina, and recruitment of pUL34 and subsequently pUL31 to the INM.

egress complex (Bigalke and Heldwein (2015); Leigh et al. (2015); Zeev-Ben-Mordehai et al. (2015); Walzer et al. (2015); Lye et al. (2015)) has revealed the atomic basis for the heterodimeric interaction between pUL31/pUL34 in PrV, HSV1 and Human cytomegalovirus (HCMV).

The dynamics of how herpesvirus capsids move through the INM during egress from the nucleus has not yet been determined. Similarly, there is a poor understanding of how the nuclear egress complex forms at the INM, induces curvature and leads to the formation of perinuclear vesicles. Here I investigate this process using 3-dimensional structured illumination microscopy (3D-SIM), as well as fast, live cell fluorescence imaging. I will discuss these results alongside concomitant efforts using cryoEM and cryoFIB/SEM to determine the integrated model for how herpesviruses control the nuclear egress of nascent capsids.

4.1.3 General introduction to fluorescence microscopy

Fluorescence is a phenomenon that has been documented since the 19th century, beginning with George G. Stokes' description in 1852 of the ability of light emitted from fluorspar to change wavelength when irradiated with ultraviolet (UV) light (Stokes (1852)). The development of a fluorescence microscope that could utilize this physical characteristic of emission was first produced in 1914 by Oscar Heimstädt. However, most modern fluorescence microscopes are much more complex than this one, and would not be possible if not for the development of emission filters in 1929 by August Hirt and dichroic mirrors in 1967 by Johan Sebastiaan Ploem, which paved the way for fluorescent material to be imaged with a high spectral separation as required. However, until an easier and more specific way of labeling the sample could be produced, the technique relied heavily on finding the right fluorophore and was limited to certain biological phenomena.

Fluorescence relies on the excitation of an appropriate chromophore usually containing a conjugate double bond system and the delocalization of p-electron orbitals over adjacent bonds. When an electron is excited, it is elevated to a higher energy state. As the electron falls back through the vibrational states, non-radiative energy is lost vibrationally. Therefore, when it drops to its original electronic state and releases energy in the form of light, this light is shifted to a longer wavelength due to the vibrational energy lost.

The discovery of Green Fluorescent Protein (GFP) and the subsequent optimization of its spectral properties (Tsien (1998)) allowed a whole new range of samples

to be probed in both live and fixed cells. Its subsequent directed evolution resulted in the production of GFP variants with improved spectral properties, such as less overlap in emission and excitation spectra, reduction in photo-bleaching, and an improved quantum yield. Similarly, variants have also been produced that fluoresce at a range of different emission wavelengths (other than 505 nm of GFP), such as mCherry (594 nm), blue fluorescent protein (BFP) (445 nm), yellow fluorescent protein (YFP) (527 nm), mOrange, cyan fluorescent protein (CFP) (476 nm), etc, means that simultaneous multicolour imaging of a range of different biological entities is now possible.

In order to follow a biological process using a fluorescence-based system, such as a microscope, it is important to define the resolution to which that system can separate two spatially distinct fluorescent foci. For a diffraction-limited system, the Abbe diffraction limit describes the maximal diameter (d) to which two points can be separated:

$$d = \frac{\lambda}{2nsin\Theta}$$

where λ is the wavelength used to image the object, ϑ is the incident light angle, and n is the refractive index of the light path. 2nsinϑ is another term for numerical aperture (NA). In practical terms, the Abbe diffraction limit roughly equates to the amount of diffracted light that can be refocused into an image by the objective lens of the microscope, which is also dependent on focal length. If the optical system is no longer able to resolve two point sources with a given spatial distance, the resolution is diffraction-limited. The Rayleigh criterion describes the separation of the point-

spread function (PSF) from two fluorescent objects (Figure 4.2A).

4.1.4 3-Dimensional structured illumination microscopy (3D-SIM)

Developments in fluorescence microscopy has resulted in the implementation of microscope able to image with sub-diffraction (of light) resolutions, a field known as super-resolution microscopy. Techniques such as stimulated emission depletion (STED) microscopy, photo-activated light microscopy/stochastic optical reconstruction microscopy (PALM/STORM) and 3D-SIM (for reviews see Schermelleh et al. (2010); Wolff et al. (2016)) have allowed the dissection of synaptic vesicle movement (Westphal et al. (2008)), the sub-diffractive organization of previously unseen cytoskeletal components of axonal processes (Xu et al. (2013)) and the 3-dimensional organization of chromatin and the nuclear pore complexes in the nuclear periphery (Schermelleh et al. (2008)), respectively.

3D-SIM is the only super-resolution technique that robustly provides the appropriate sample and optical conditions needed for routine live-cell imaging (Schermelleh et al. (2010)), as it can utilize common "native" fluorophores (green fluorescent protein (GFP), mCherry etc), and does not require the pre-fixation and immuno-staining of material. Although there is a move to now utilizing these fluorophores for super-resolution microscopy (Kaufmann et al. (2014)), STED and PALM/STORM often require a high fluorescent yield from fluorophores in order to produce the requisite statistics or optical deformation (bleaching) needed to allow sub-diffractive imaging.

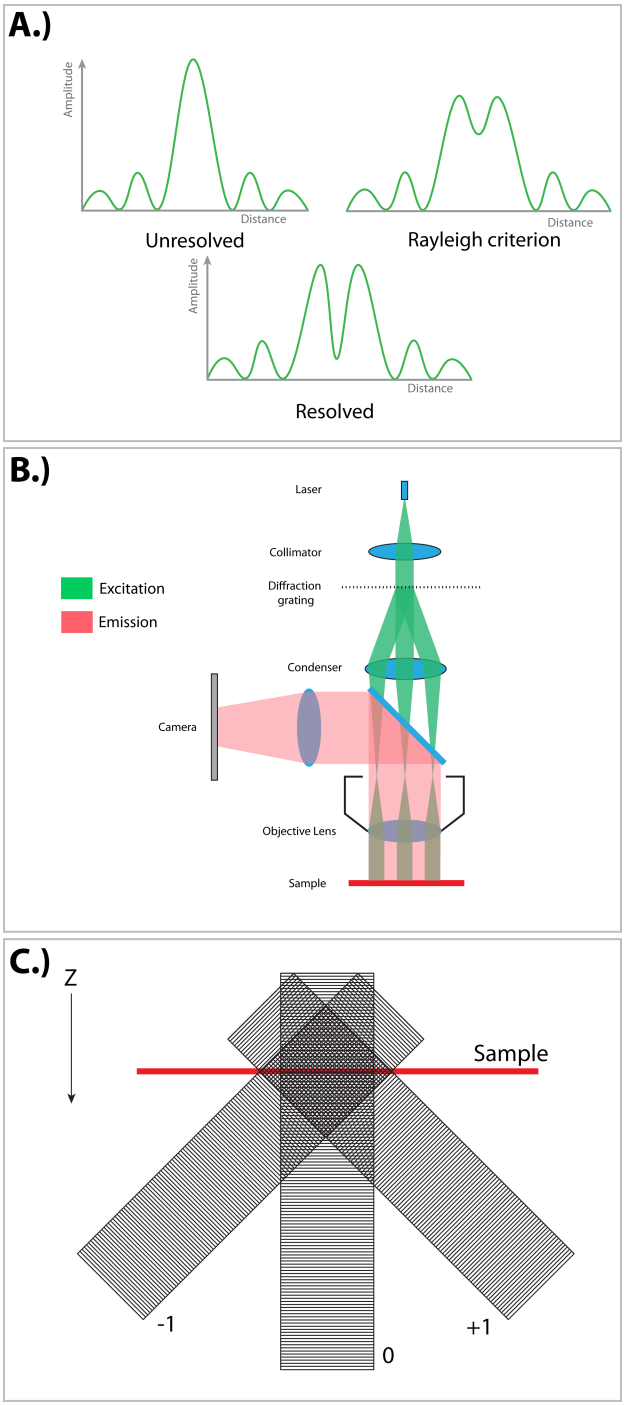

Figure 4.2 – Summary of the optical setup, and beam conditions in 3D-SIM. A.) The Rayleigh criterion for determination of the minimum resolution in an optical system. B.) Schematic of the microscope organization for 3D-SIM, adapted from (Gustafsson et al. (2008)). C.) Diagram of the three-beam illumination pattern at the focal plane during image acquisition in 3D-SIM and how the 0 order, +1 order and the -1 order beams contribute towards it. Note the striped illumination pattern in all 3 dimensions. X is going into the page, Y from left-right and Z up-down.

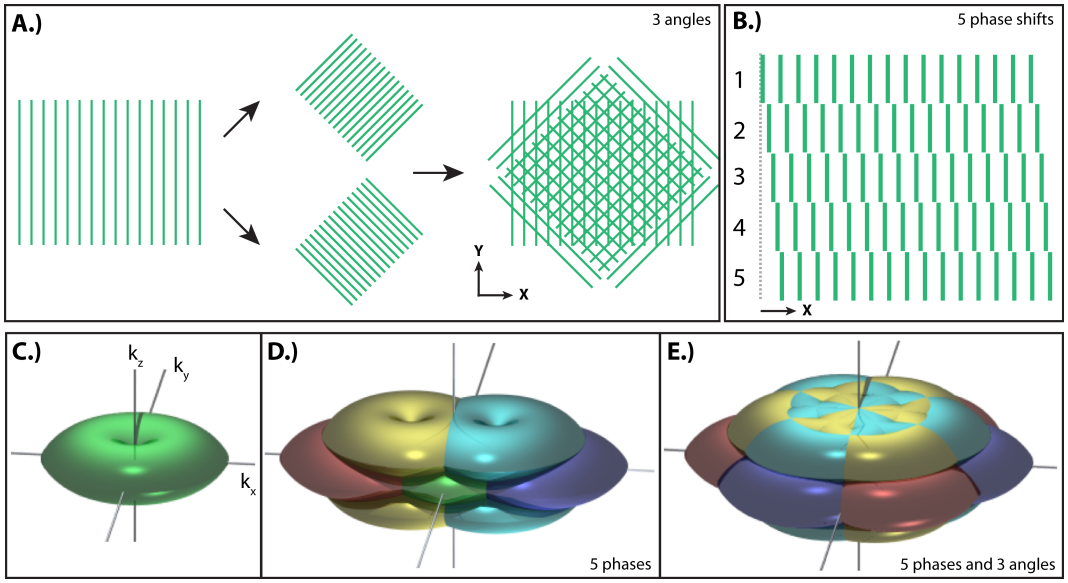

Figure 4.3 – Illustration of phase shift and angle change during acquisition of data for 3D-SIM. A.) Schematic view of the structured illumination in the XY plane, illustrating the 3 angles used to acquire at each Z plane. B.) Representation of the phase shift of the structured illumination at each Z-plane. 5 images are collected at differing phases. Altogether, 15 images (3x tilted images and 5x phase shifted images) form one stack image for a given Z plane. C.) Optical transfer function (OTF) of an image using widefield illumination, with the frequency domain information in X,Y and Z represented as k_x, k_y and k_z, respectively. D.) OTF of an image acquired using structured illumination with 5 different phase shifts at different Z-positons through the sample. Subsequent computational reconstruction allows the 5 phase images to be separated to extend the information towards higher frequencies E.) OTF of a 3DSIM stack acquired with 5 phase shifts and 3 angles at different Z-positions through the sample. Tilting the illumination pattern allows the information to be covered in all all directions, and results in the volumetric resolution increase. C.), D.) and E.)are adapted from Schermelleh et al. (2008) (credit to Lothar Schermelleh).

One further flaw to these two techniques is their elongated point spread function in the Z-direction of imaging (Schermelleh et al. (2010)) resulting in the inability to determine the Z-position of the fluorescent signal of interest. Various flavours of these techniques have produced results that circumvent these issues to an extent (Nagerl et al. (2008); Xu et al. (2013)), but still represent a work in progress.

3D-SIM allows the volumetric imaging of cells and other material with resolutions in the range of ~120 nm in the X and Y directions and ~300 nm in the Z direction. The laser light path (usually 3 wavelengths) is passed through a physical grating, where the light diffracts to produce a pattern of constructive interference. A further modulation of the wavelength in the Z direction is also produced through the interference between beams of 3 different diffraction orders, +1, 0 and -1 (Figure 4.2). This 3 dimensional, modulated illumination is adjusted to illuminate the object at 3 different angles and 5 different phase positions (Figure 4.2). Thus, each image plane must be imaged 15 times per Z-position. The spacing between the stripes in the illumination at the image plane is close to the ~200 nm (wavelength dependent) resolution limit of a conventional light microscope. The structured illumination interferes with the fluorescent signal in the sample, and causes higher-order information, which would normally escape detection through the objective lens, to be shifted to a lower-order position in frequency space and therefore become detectable. The acquired data are then reconstructed computationally and higher-order information is reassigned in frequency space to its origin, and through reverse Fourier transform a high-resolution reconstructed 3-dimensional volume is rendered (Schermelleh et al. (2008); Gustafsson (2000); Gustafsson et al. (2008)).

I here use 3D-SIM and widefield deconvolution microscopy to gain insights into the dynamics of nuclear egress of herpesviral capsids. Current X-ray tomography data (see Appendix 2, supplemental information for Hagen et al. 2015) suggest that during viral infection, the number of type-1 (infoldings of the INM) and type-2 (infoldings of both the INM and ONM) nucleoplasmic reticula (NR) infoldings into inner regions of the nucleus increase (Malhas et al. (2011)). An increase in the surface area of the INM from which viral capsids can escape could potentially suggest a viral role in the remodeling of nuclear membranes during infection. In the case of type-2 NR infoldings, this would also provide the capsids with close access to the cytoplasmic compartment and, possibly, microtubule and motor protein-based, directed transport. In the case of type-1 NR, this provides a potentially more efficient route into the lumenal space between the INM and ONM. I aim to view the type-1 and type-2 NR directly during viral infection, determine the transport dynamics of viral egress and directly image the movement of viral capsids across the INM and NR in live cells.

4.2 Materials and Methods

4.2.1 3D-SIM imaging conditions

Cells were grown on high-precision 22 x 22 mm No. 1.5H glass coverslips (Marienfeld Superior) or in µ-Dish, high glass bottom 35-mm dishes (Ibidi GmbH, Martinsried, Germany) to a confluency of 70%–80% in 10% (w/v) fetal bovine serum in Dulbecco's modified Eagle medium (DMEM; GIBCO-Invitrogen). Before imaging,

the medium was replaced with pre-warmed Opti-MEM (GIBCO-Invitrogen). Three-dimensional structured illumination microscopy (3D-SIM) (Gustafsson et al., 2008) on live-cell samples was performed using an OMX V3 Blaze system (Applied Precision, GE Healthcare) (Strauss et al. (2012)) equipped with a 60x/1.42 NA PlanApo oil-immersion objective (Olympus), a 488 nm diode laser with standard filter sets, and Edge sCMOS cameras (PCO).

To allow live-cell imaging under physiological conditions, the OMX microscope was modified with an incubation apparatus and objective heater for medium-term imaging under standard live cell conditions (37 °C and 5 % CO2). The OMX V3 Blaze system parameters were adjusted for temperature-dependent changes in immersion oil refractive index with single layers of TetraSpeck fluorescent microspheres (Life Technologies), and optical transfer functions (OTFs) were generated from individual 110 nm diameter 505/515 nm fluorescent microspheres (Life Technologies). Phase parameters were adjusted for optimal imaging at 488 nm, and data was acquired using an appropriately matched immersion oil. 3D-SIM data were acquired with a Z-distance of 125 nm and with 15 images per plane (five phases, three angles). The raw data was computationally reconstructed using a Wiener (high-frequency) filter and channel- and temperature-specific OTFs employing the softWoRx 6.0 software package (GE Healthcare) to obtain a super-resolution 3D image stack of 32-bit depth, with a pixel size of 40x40 nm. Typically nuclei imaged were in between 6µm and 12µm in height. The reconstructed data was thresholded for each channel to the stack modal grey value (representing the centre of the background intensity level) and converted to 16-bit tiff-stacks.

4.2.2 Live-cell conditions: phase, oil and pitch calibrations

Due to the change in refractive indices at higher temperatures and the shift towards a dedicated 37°C objective, there became a need to recalibrate the 3D-SIM system to optimize for the new live cell conditions. In 3D-SIM, phase determines the position, in 3-dimensions, of the stripes produced by the diffraction grating that are used to illuminate your object of interest. The structured 3-dimensional illumination changes relative position at the focal plane depending on the phase shift that is put into the 3-beams that produce the illumination. The refractive index of the oil changes the focal plane of this structured illumination and therefore a.) the point of optimal focus in the beam path on the sample plane and b.) the number of phase orders able to enter the back focal plane. This latter consideration can be also adjusted according to the pitch of the mirror. Therefore, we calibrated the microscope to 2 wavelengths: 488 nm and 594 nm. The structured illumination profile is shown in Figure 4.2C. In order to ensure that the object at the focal plane is illuminated with 1st and 2nd order stripe frequencies (essential in producing a good reconstruction) (Figure 4.2C) the modulation of the illumination in the z-direction must be optimal at the focal plane for all 3 angles. By adjusting the phase settings, this Z-modulation was adjusted to be optimal at the focal plane. New symmetric optical transfer functions (OTF) were determined for beads at the coverslip focal plane. For green, the refractive index of the immersion oil whereby the point spread function (PSF) was symmetrical was 1.518. For red, this was 1.520. These PSFs were used to create OTF used for data reconstruction.

Optimal phase values were determined for immersion oils of 1.518, 1.520, 1.522 and 1.524 at their respective focal planes. The reason for this was that the oil determines the focal plane of the light path at the sample, and therefore the depth of focus for optimal reconstruction of the 3D-SIM data.

4.2.3 Cell culture

4.2.3.1 UL34-GFP/UL31-EFN cells (RIE3134-GFP)

This cell line was kindly provided by Thomas Mettenleiter (Federal Institute for Animal Health, Riems, Germany)(Klupp et al. (2007)). The cells were cultured in 10% fetal bovine serum, Dulbecco minimal essential medium (10%-DMEM) (Gibco) supplemented with 0.1mg/ml penicillin/streptomycin (Gibco).

Live-cell imaging: During imaging, the cells were grown to 80% confluency on µ-Dish 35mm-high glass bottom dishes (Ibidi) which contains a glass bottom of thickness 170 µm ± 10 µm. The cells were grown in 10%-DMEM until the point of imaging, at which point the medium was replaced with Opti-MEM reduced serum medium lacking Phenol Red (Invitrogen). The cells were placed into a pre-warmed customized dish-holder that was of the size of a standard glass microscopy slide. The cells were kept at 37°C and kept under 5% CO2 atmosphere.

Live-cell room temperature imaging: The cells were grown on 22mm x 22mm coverslips of specified thickness 1.5H(170 µm ± 5 µm) (Marienfeld). At 80% confluency, cells were transferred to an aluminium 2-plate sandwich holder, where the coverslip was sealed between two aluminium plates with halocarbon oil. Opti-MEM reduced

serum medium without Phenol Red was then placed to the top of the 'well' in the top plate and sealed with another coverslip, also sealed with halocarbon oil. This created an airtight chamber between the cell layer and the top coverslip, separated by medium.

4.2.3.2 NIH-3T3-LBR-GFP and wild-type cells

These cell lines and MCMV were provided by Jens-Bernhard Bosse (Enquist Lab, Princeton University, USA)(Bosse et al. (2012)). The cells provided were of 3 different types: NIH-3T3 wild-type, NIH-3T3-LBR-GFP-sort 2 and NIH-3T3-LBR-GFP-sort 3 (LBR = lamin B receptor). Here, the difference between the sort 2 and sort 3 cell lines is that the sort 3 cells round has been subjected to an extra round of fluorescence activated cell sorting (FACS), to achieve a greater level of expression of the LBR-GFP construct being stably expressed. A key observation between the sort 2 and sort 3 cell line is that the greater expression of LBR-GFP results in a greater frequency of nuclear artifacts related to the nuclear membrane. Hence, sort 2 was the preferred cell line for investigation.

Live-Cell imaging: as described in 4.2.3.1.

Viral Infection with Murine Cytomegalovirus (MCMV): Cells were firstly grown to 80% confluency on µ-Dish35mm-high glass bottom dishes (Ibidi). 30 µl of MCMV-VP26-mCherry stock (1.65×10^8 particles), resulting in a multiplicity of infection (MOI) of 3 was added to 2ml of growth medium and left for 28 hours post-infection. At this point cells were imaged directly on the microscope.

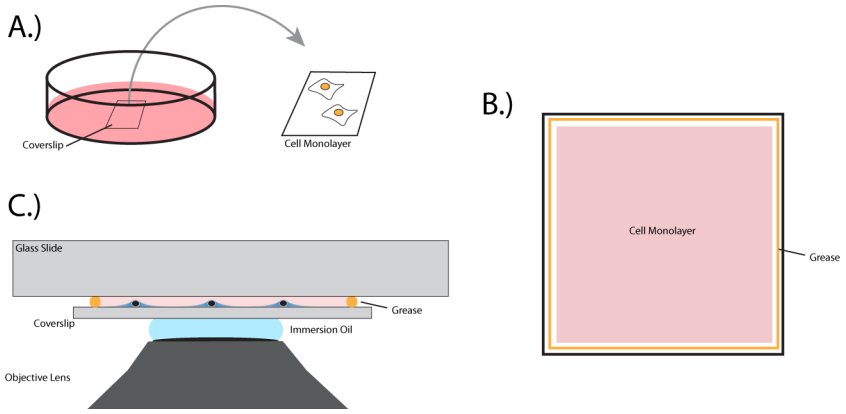

Figure 4.4 – Diagram of the arrangement of coverslip and slide for live-cell imaging. A.) represents a top view representation of the arrangement on the coverslip. B.) shows a top-view of a mounted coverslip. Shown in yellow is the layer of silicon which seals the confluent cell layer from the outside environment. In darker blue is shown the confluent cell layer.

4.2.3.3 Rabbit kidney epithelial cells (RKLBR-GFP-GFP)

This cell line was kindly provided by Thomas Mettenleiter (Federal Institute for Animal Health, Riems, Germany). The cells stably express a GFP-labelled lamin-B receptor along the inner nuclear membrane and were cultured in 10% fetal bovine serum, Dulbecco minimal essential medium (10%-DMEM) (Gibco) supplemented with 1mg/ml penicillin/streptomycin (Gibco).

Live-Cell imaging: as described in 4.2.3.1.

Viral Infection with Pseudorabies Virus (PrV): Cells were firstly grown to approx. 80% confluency on µ-Dish35mm-high glass bottom dishes (Ibidi). 10 µl of PrV-RFP stock (1x10^9 particles), resulting in an MOI of approx. 10, was added to 2ml of growth medium and left for 7 hours post-infection. At this point cells were imaged directly on the microscope. PrV virus was provided Jens-Bernhard Bosse.

4.2.3.4 Physiological imaging conditions

In order to image cells under physiological conditions, at 37°C and 5% CO2, cells were initially imaged using MaT-Tek dishes (MatTek Corp.), which have a 150mm +/- 10mm glass coverslip fixed to the underside. This approach proved to be much more practical than the former, and utilized a purpose built aluminium dish-holder that conformed to the size specifications of a glass slide. The reconstruction quality of the 3D-SIM data acquired with this arrangement was very good, albeit only in the green channel. In order to keep auto-fluorescence down, and reduce background signal, a Phenol red-free, pH-stable medium was used for imaging.

Data acquired in the Mat-Tek dishes largely resembled that of previous data. However, data produced by the MatTek dishes resulted in reconstructions that contained more aberrations and looks visually poorer after reconstruction using the calibrated OTFs. The alignments of the microscope are calibrated such that the amount of phase shift generated as light passes through the glass coverslip is dependent on the thickness of the glass. As the accuracy of the glass slide used for the Mat-Tek dishes was lower than that of standard coverslips, another glass-bottomed dish produced by Ibidi with similar dimensions was used, as measurements of the glass bottom proved to be consistently much closer to the 170 µm +/- 5 µm for which the OMX V3 is optimized.

4.2.4 Electron cryo-microscopy, focused ion beam milling and sub-volume averaging

The materials and methods for the electron cryo-microscopy, the focused ion beam milling and sub-volume averaging for the work described in this chapter can be found in (Hagen et al. (2015)), a copy of which can also be found attached to the appendix of this thesis. This work was performed by Christoph Hagen, Alistair Siebert and Kyle Dent.

4.3 Results and Discussion

4.3.1 Optimization of Live Cell 3D-SIM

4.3.1.1 Initial testing of live-cell conditions: room temperature

In order to determine the optimal conditions for the imaging of live cells using 3D-SIM, the appropriate conditions for cell growth were determined. Initial tests at room temperature utilized cells grown on coverslips with a layer of silicone gel around its edge, placed onto a glass slide and mounted in pre-warmed phosphate buffered saline or medium (shown in Figure 4.4).

To examine whether it was possible to use 3D-SIM to probe herpesvirus nuclear egress, I imaged RIE3134-GFP cells constitutively co-expressing the herpesvirus proteins pUL31 and pUL34, which together form the nuclear egress complex (NEC)(Figure 4.5). The intensity of fluorescence in the RIE3134-GFP cells at 488 nm excitation was very high. The previously described 'speckles' and nuclear lamin staining typical

of this cell line were observable (Figure 4.5)(Klupp et al. (2007); Hagen et al. (2012)) . The formation of these 'speckles' ran along type 1 and type 2 nucleoplasmic reticula (Malhas et al. (2011))(also see Z, Y and Z, X projections, Figure 4.7) in a bead-on-a-string fashion. It was also possible to acquire time-lapse data of the RIE3134-GFP cells at 6 x 30 second time intervals (Figure 4.5). The level of bleaching remained relatively low, and was easily compensated for using histogram matching (Schindelin et al. (2012)). The pUL31/34 perinuclear vesicles moved in a Brownian manner, with no directed movement observable (Figure 4.5C), perhaps due to lack of viral protein present to target the NEC perinuclear vesicles through the lumen of the inner and outer nuclear membranes (Klupp et al. (2007)). Unexpectedly, pUL34-GFP can be seen in small speckles in areas outside of the nucleus. However, as the outer nuclear membrane is continuous with the endoplasmic reticulum and, further, pUL31 is able to remodel membranes, and it is not unreasonable to assume that pUL31/34 complexes may be found there.

4.3.1.2 Testing of live-cell conditions: 37°C

At the coverslip, adherent photosphere beads fluorescing in the green (525 nm) channel produce a symmetric point spread function (PSF) using oil of refractive index 1.518 and beads fluorescing in red (615 nm) produce a symmetric PSF using an oil at a refractive index of 1.520. These oils created imaging conditions at 37°C that were equivalent for oils of refractive indices of 1.512 (green) and 1.514 (red) at room temperature. As these oils are therefore optimized during calibration with beads for the focal plane to be at the coverslip, it was important to test with various oils a con-

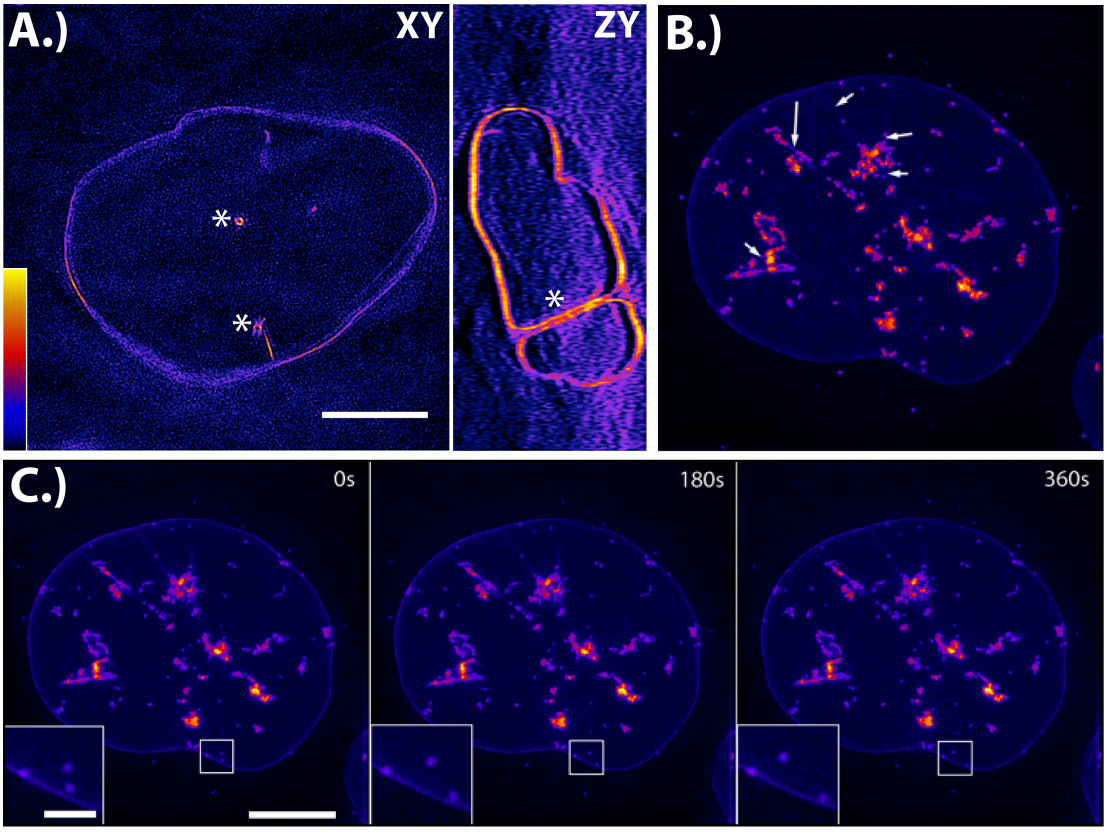

Figure 4.5 – Live cell 3D-SIM of RIE3134-GFP cells imaged at room temperature. A.) pUL34-GFP-decorated INM of a RIE3134-GFP cell, which highlights the presence of type-2 nucleoplasmic reticula (NR)(white asterisk). B.) Example of RIE3134-GFP cell line displaying the perinuclear vesicle morphology described previously (Klupp et al. (2007)). Arrows highlight perinuclear vesicles that are associated with type-1 NR. C.) Time-lapse 3D-SIM of cell shown in B.), with 3 time points highlighted at 0, 180 and 360s. Inset shows diffusive movement of free perinuclear vesicles. Scale = 5 µm. Inset scale = 1 µm. Coloured scale in A.) indicates the relative intensity of the observed fluorescence of GFP from low (black) to high (yellow).

dition whereby cells could be imaged at an optimal depth of focus at approximately the centre of the nucleus.

Figure 4.6 shows XY projection images of a nucleus of a RIE3134-GFP cell imaged at 37°C and 5% CO2. This is presented in widefield deconvolved and 3D-SIM and is produced from the same raw data SIM stack. 3D-SIM performed on live cells under physiological conditions showed an increase in the amount of detail we can observe. The resolution achieved was ~120 nm in the lateral direction and ~300 nm in the axial direction, similar to data acquired at room temperature. In the top right of the images, a network of vesicles can be resolved where individual vesicles can be resolved from the background. Similarly, fine details of the aggregated vesicle structures can be separated from the blur, and distinct structures can be discerned. In the Z-plane (not shown) these vesicles can also be resolved, though at lower resolution. The speckles associated with structures that appear to be type 1 nucleoplasmic reticula, and the vesicular aggregates line these structures and are not diffuse throughout the nucleus. This type of alignment along the type-1 nucleoplasmic reticulum can be observed in Figure 4.7.

4.3.2 3D-SIM of RIE3134-GFP cells

As has been previously discussed, model systems for studying complex viral systems are invaluable in elucidating functional relations between proteins, both viral and cellular. The EFN porcine-epithelial pUL34-GFP/pUL31 (RIE3134-GFP) cell line expresses the viral proteins pUL34 and pUL31, which are components of the nuclear

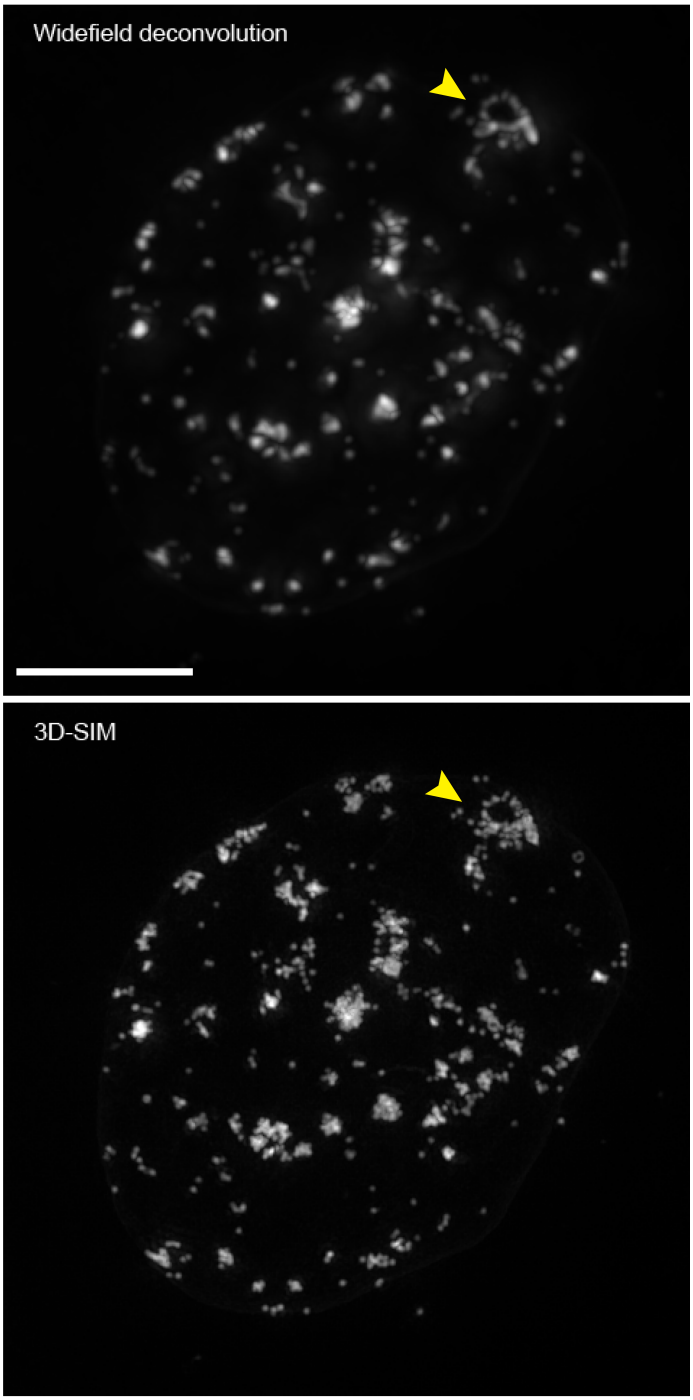

Figure 4.6 – Comparison of projection images of RIE3134-GFP nuclei taken from the same SIM stack and processed using widefield deconvolution and 3D-SIM reconstruction. The cells were imaged under physiological live cell conditions (37° and 5% CO_2) and subjected to widefield deconvolution (top) and 3D-SIM reconstruction (middle). The increase in resolution of fine features within the pUL34-GFP vesicular speckles in the 3D-SIM image is observable (yellow arrows). Distinct puncta are visible in the 3D-SIM case, that are not visible in the deconvolved image. Scale = 5 µm.

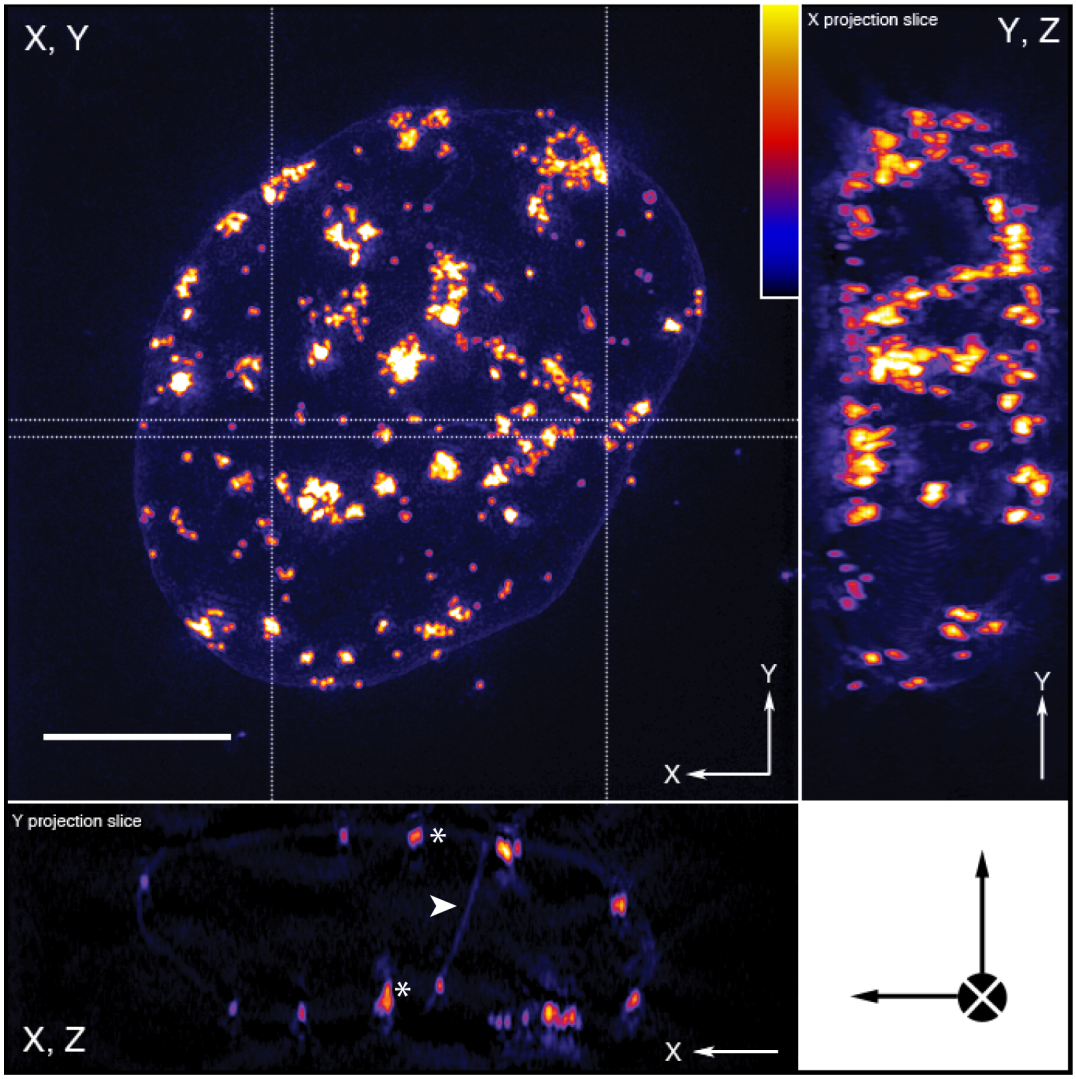

Figure 4.7 – Slices through a 3D volume of a porcine epithelial-like embryonic kidney cell determined by live-cell 3D-SIM at 37°C (~120 nm lateral resolution). Thickness of XZ and YZ projections is indicated by dashed lines in the XY projection. RIE3134-GFP cells were imaged at room temperature and in Opti-MEM® without Phenol Red. The arrow marks the fluorescent signal along nuclear membrane and represents nucleoplasmic reticula type 1 structures. pUL31/34-GFP 'speckles' could be observed to align with these Type 1 structures in 'beads-on-a-string' string fashion (asterisk). Similarly striking is the fluorescent signal that pUL34-GFP causes in the membrane, giving a clear outline of the nucleus. Scale = 5µm. Coloured scale indicates the relative intensity of the observed fluorescence of GFP from low (black) to high (yellow).

egress complex in Pseudorabies virus. The pUL31/34 complex arranges into perinuclear vesicles in these cells (Figure 4.5 and 4.7) (Klupp et al. (2007)). In this cell line I observed two fluorescent features; the UL31/34 "speckles" morphology described above and a nuclear rim staining, presumably caused by pUL34-GFP at the INM in the absence of pUL31 (Figure 4.5). From a total of 38 3D-SIM stacks acquired of the RIE3134-GFP cells (21 at room temperature, and 17 at 37°C), 70% of cells showed the "speckled" peri-nuclear vesicle morphology (from a total of 68 cells imaged)(although selection of cells to be imaged was subjective). The formation of perinuclear vesicles can only occur when pUL31 and pUL34 are co-expressed. Expression of pUL34 results in a phenotype where the fluorescent signal is distributed along the INM. This is consistent with transient transfection experiments (Klupp et al. (2007)). Loss of expression of pUL31 in this cell line would theoretically produce the INM-stained phenotype, whereas, because pUL31 is not fluorescently labelled, cells lacking pUL34 expression would not produce any fluorescence.

The observed peri-nuclear morphology is consistent with the theory that these individual ~120 nm diameter vesicles cluster together, and align along invaginations that resemble type 1 nucleoplasmic reticula (Figure 4.7). In MCMV, INM invaginations, here termed 'pits', can be observed to align along the replication compartment (Figure 4.8). These pits would presumably function to increase the amount of surface from which capsids can bud into the lumen between INM and OMN. Given the lack of capsids visible in the membranes of cells, it is difficult to confirm at the current time whether the above is an artifactual situation or whether this does serve to benefit the virus during nuclear egress.

4.3.3 Widefield Imaging of MCMV and PrV infection

An mCherry-tagged variant, MCMV-mCherry, was used to probe capsid formation and egress in the nucleus (Bosse et al. (2012)). NIH-3T3 LBR-GFP sort 2 (hence referred to as 3T3-LBRGFP-2) cells were grown and infected with MCMV-mCherry and imaged using 3D-SIM. The Lamin-B receptor-GFP construct stably expressed in this cell line formed very similar features to cells that express only pUL34-GFP (Klupp et al. (2007)). In the centre of all infected nuclei from 56 deconvolved stacks, an mCherry-dense structure formed that typically showed a 'horseshoe'-like structure, taking up roughly 50-70% of the nuclear volume (Figure 4.8). This is most likely the site for capsid assembly inside the nucleus. However, it was not possible to image nuclei using 3D-SIM due to significant bleaching in the red channel as well as a deterioration in the lamin-B receptor signal (which was used to stain the nuclear membrane) during prolonged infection.

As an alternative to MCMV, I also attempted to visualize the infection of PrV in rabbit kidney cells stably expressing LBR-GFP (RKLBR-GFP). Due to a lack of photostability in the PrV viruses it was also not possible to obtain 3D-SIM data on whole virus infection of RKLBR-GFP cells. However, the fluorescence of LBR-GFP in the RKLBR-GFP cell line appeared to be brighter than in the 3T3-LBRGFP-2 cells. Similarly, the PrV-mRFP virus appeared brighter than the MCMV-mCherry. PrV-mRFP infection progressed differently to that of MCMV, with the large "horse-shoe" replication centre visible for MCMV-mCherry not being present but, rather, a highly motile mass of individual capsid molecules being visible (Figure 4.8). In

contrast to MCMV, PrV-mRFP-infected nuclei mostly contain smaller foci of capsid signal representing replication compartments, with the majority of fluorescence forming smaller, highly mobile foci that would be consistent with individual capsids of PrV-mRFP. The diffusive capsids could not be observed to interact or move across the membrane (egress) in the 9 datsets acquired.

However, widefield microscopy provided a few insights into the mechanism of capsid nuclear egress. MCMV-SCP-mCherry replicates to a much slower extent than PrV-mRFP, taking approximately 24 hours for nuclear clearance to commence (Bosse et al. (2012)) compared to a 6 hour period for PrV-mRFP of RKLBR-GFP cells. This results in a different fluorescent profile in the nuclei of the infected cells (Figure 4.8). In the case of MCMV-mCherry it was possible to discern some global co-localization of LBR and virus. In this case, the LBR outlining the INM showed visible nuclear 'pits' that invaded the centre of the nucleus. These 'pits' could be observed to align along the boundaries of the replication compartment (Figure 4.8). In 32 of the 56 deconvolved widefield stacks collected (from 3 experiments), 'pits' running adjacent to the MCMV replication centres could be observed. The presence of a greater capsid signal along the boundaries of the replication compartments could suggest that these structures may facilitate capsid association with the INM. Work is still needed to determine whether these invaginations align along the replication centre due to a virally-induced mechanism or whether the replication compartment forms around artificial nuclear structures produced by over-expression of LBR-GFP in the NIH-3T3 cells.

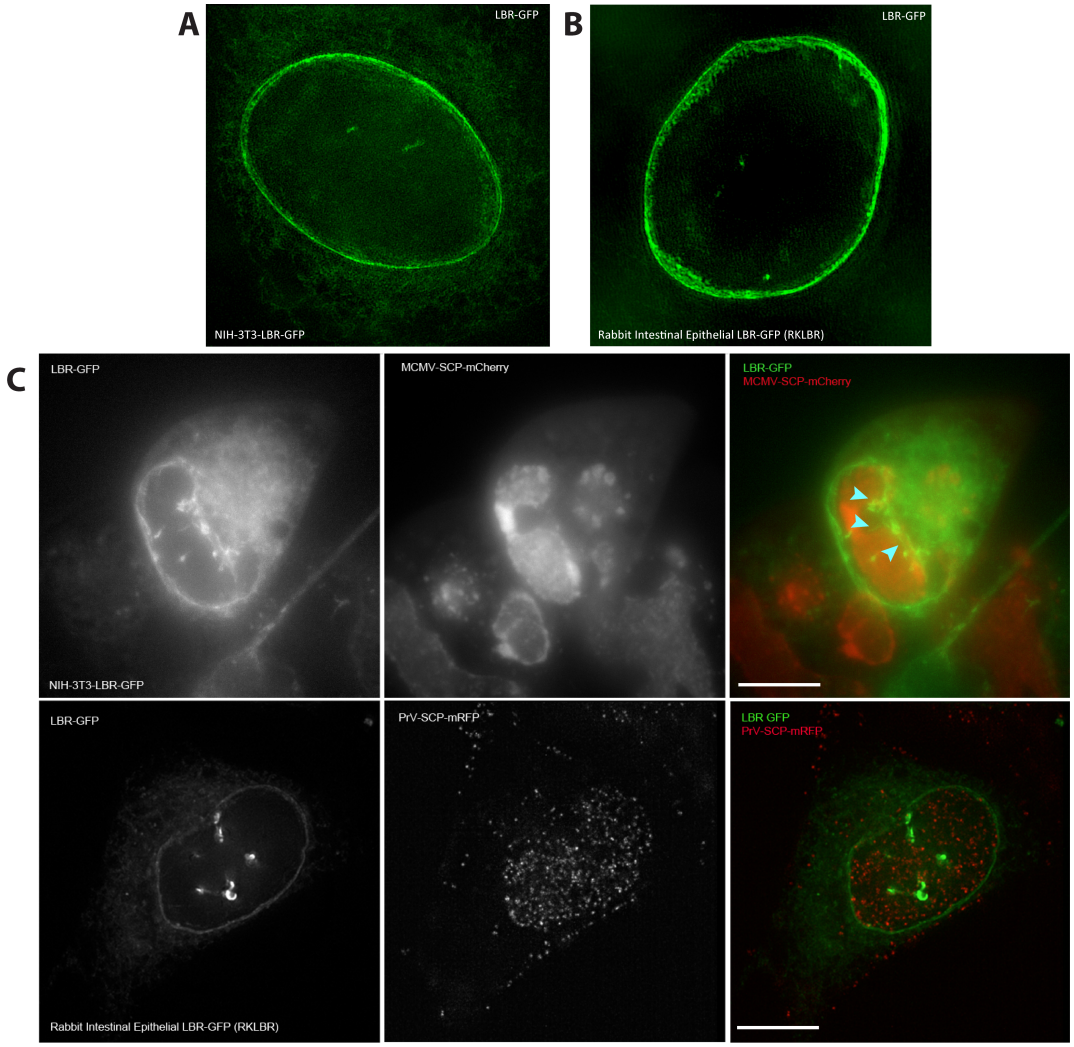

Figure 4.8 – Projection images of widefield substacks taken from MCMV-infected NIH-3T3-LBRGFP cells PrV-infected and RKLBR-GFP cells. A.) Projection image taken from the central 10 slices of a reconstructed 3DSIM volume of a NIH-3T3-LBR-GFP cell. B.) Projection image taken from the central 10 slices of a reconstructed 3DSIM volume of a Rabbit Intestinal Epithelial LBR-GFP cell. C.) Projection images of substacks taken from MCMV-infected NIH-3T3-LBRGFP cells (top) and PrV-infected RKLBR-GFP cells (bottom) 28 hours and 7 hours post-infection, respectively. Large replication centers visible in the case of the MCMV-infected cell, while in the case of the PrV-infected cell, diffuse speckles can be observed, presumably representing free, diffuse capsid. Cyan arrows show representative 'pits' that run adjacent to the replication centre. Scale = 5 µm.

4.3.4 Electron cryo-tomography and focused ion beam milling of pUL31/34 peri-nuclear vesicles

To gain a greater insight into the nature of the pUL31/34 perinuclear vesicles, cryo-focussed ion beam milling/scanning electron microscopy (FIB/SEM) was performed on the RIE3134-GFP cells (FIB/SEM: Rigort et al. (2012)). This technique is a method of thinning the cells in such a way that their native architecture is preserved in a frozen hydrated state and with relatively few artifacts (in comparison to CEMOVIS, Al-Amoudi et al. (2004)) while at the same time allowing the production of sectioned samples thin enough to image using electron microscopy. Plunge frozen RIE3134 cells were sectioned using FIB/SEM, where the cells were targeted to leave lamella in regions of the cells predicted to be the nucleus. The lamellae containing the pUL31/34 perinuclear vesicles were imaged using electron cryo-tomography (cryoET).

The resultant tomograms contained perinuclear vesicles (Figure 4.9), which exhibited a regular array of density on the inside that was presumably the pUL31/34 layer. The high density of protein on the inside of the vesicles provides an explanation to the high degree of fluorescence exhibited by this cell line using 3D-SIM (see sections 4.3.1 and 4.3.2). Tangential slices through the tomograms show that the pUL31/34 vesicles are mostly spherical and vary in size only slightly, with a median diameter of 100 nm. The regular densities observed in the tomograms form a mostly complete lattice, that covers the entire vesicle. This is in contrast to other similar lattices, for example the HIV1 immature Gag coat (Schur et al. (2015)) that often contained gaps in the lattice at 5-fold vertices. A pure hexagonal lattice would be unable to form a

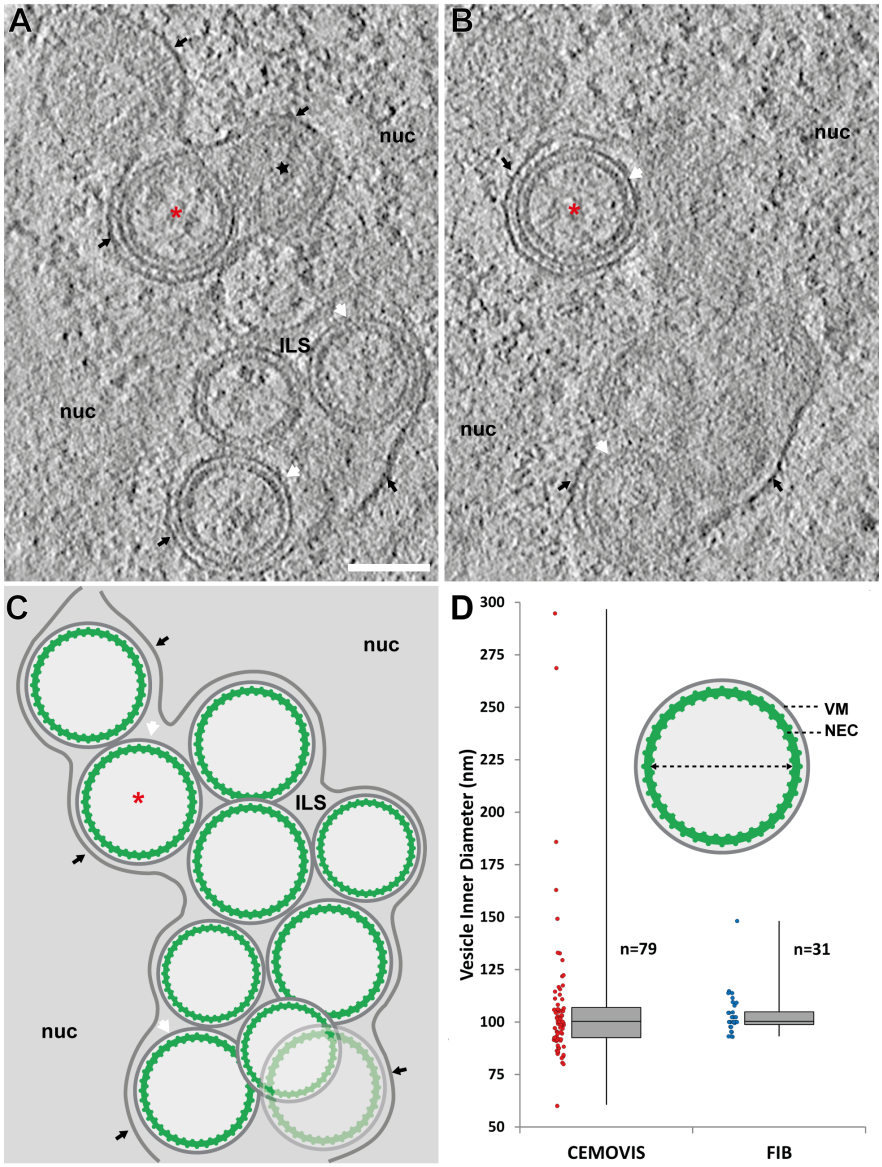

Figure 4.9 – Slices and schematic of peri-nuclear vesicles within an electron cryo-tomogram of a cryoFIB lamella. (A–B) Slices through an electron cryo-tomogram of a lamella prepared by cryoFIB, interpreted schematically in (C). Vesicles not shown in the experimental map slices are depicted semi-transparently. ILVs are tightly surrounded by the INM (black arrows) and are closely related in size, exhibiting diffuse contents. The NEC coat (green) appears to nearly cover the entire inner surface of the vesicle membrane (white arrows). A fuzzy layer of density attributed to the C-terminal GFP of pUL34-GFP surrounds each vesicle in the intraluminal/perinuclear space (ILS). Red asterisks highlight a near spherical vesicle from which measurements of NEC coat parameters were taken (in Figure 4.12). Scale bar, 100 nm. nuc, nucleus. (D) Box-plot of the distribution of vesicle sizes (vesicle inner diameter: dashed line in inset vesicle) measured in 3D from BK cells prepared for tomographic electron imaging by CEMOVIS (red) and cryoFIB (blue). The distributions share a median of 100 nm. VM, vesicle membrane. (Hagen et al. (2015)). Data were acquired by Christoph Hagen and Alistair Siebert.

spherical structure, hence defects, where the lattice rule breaks down, or pentons, are needed. The inside of the pUL31/34 vesicles contain only diffuse material. The INM can be clearly observed around the entire bunch of vesicles, and exhibits a type-1 nucleoplasmic reticulum behaviour. These features can also be observed in the 3D-SIM data, and also in X-ray tomograms of the same cell line (Hagen et al. (2012)). These X-ray tomograms also show the nucleoplasmic reticula, supporting the observation that nuclear egress and enhanced invagination of the INM may be coupled (Hagen et al. (2015), appendix). On the inside of the INM, and proximal to the vesicles, a density could be observed that could represent the C-terminal GFP tag of the pUL34 transmembrane protein that forms the NEC. This would mean that the C-terminal tag is contained within the reducing environment of the INM/ONM lumen, which is continuous with the ER and may explain to some degree the low level of bleaching observed in this cell line.

4.3.5 Sub-volume averaging of pUL31/34 peri-nuclear vesicles

To enhance the interpretation and information that could be gleaned from the pUL34/31 perinuclear vesicles, sub-volume averaging was attempted, in order to visualize features to a higher resolution. The high degree of decoration, combined with the periodicities visible in the vesicles (see Figure 4.9A and 4.9B) suggested a regular arrangement. In order to attempt to assign components of the NEC layer, the vesicles from 3 tomograms were analyzed for their ability to converge to a given sub-volume

average. 31 vesicles were modelled as spheres, and diameters approximated from the average. By determining the mean radius, the membranes for each vesicle could be aligned to one another approximately, resulting an initial average of well aligned averages along 2 axes. The third axis, Y, which can be defined as perpendicular to the vesicle membrane, then needed further alignment in order to determine the rotational orientation of the NEC about that axis.

A curved mask that spanned the spherical volume was produced that masked the regions that did not relate to the NEC layer. Using a reference free-approach sub-volumes, centered around the periphery of the vesicles, of about 40 nm, were extracted from the tomograms and aligned to reference particles from the vesicle. Refinement around the Y axis resulted in a sub-volume average that displayed a P6 symmetry. To enhance the structure even further, and taking into account the symmetry, the NEC was oversampled in an attempt to contribute as many asymmetric particles to the average as possible. Oversampled particles that converged onto one another (i.e. duplicates) were removed. The final average was then extended to a larger box using the determined Euler angles for each particle in each vesicle. In total, 9 vesicles were averaged, but averages from each vesicle were not combined due to the variation in respective curvature that could be found in the vesicles.

The sub-tomogram average of the NEC coat layer on the inside of pUL31/34 perinuclear vesicles showed that it consists of two distinct protein layers, the membrane distal (MD) and membrane proximal (MP) layers (Figure 4.10). Although both layers exhibit P6 symmetry with a lattice spacing of 11 nm, the MP shows a separate density arrangement, that shows a 6 nm lattice spacing, offset from the MD by around 30°.

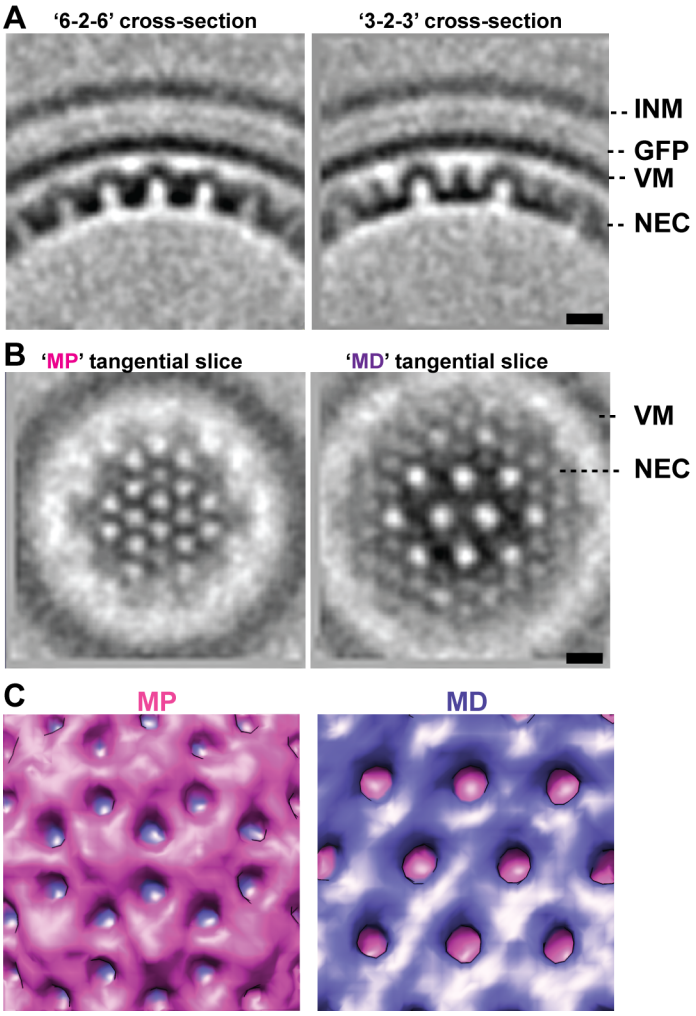

Figure 4.10 – Sub-tomogram average of a pUL31/34 perinuclear vesicle at 35 Å resolution. (A) Sub-tomogram average of a pUL31/34 perinuclear vesicle at 35 Å resolution, in which we observe the volume at a slice that passes through a 2-fold axis and intercepts adjacent 6-fold (6-2-6) or 3-fold axes (3-2-3), respectively. Scale bar, 10 nm. (B) Tangential slices through membrane proximal (MP) and membrane-distal (MD) layers of the sub-volume averaged structure. Each layer exhibits a P6 symmetry with lattice spacing of 11 nm. The MP layer exhibits a p6 lattice with a spacing of 6 nm that is offset from the MD lattice by 30 nm. Scale bar, 10 nm. (C) Surface views rendered from the vesicle exterior and the vesicle interior show characteristic features of the MP (shown in pink) and MD (shown in magenta) layers. (Hagen et al. (2015)). Sub-volume averging of the perinuclear vesicles was performed by Kyle Dent.

The pUL31/34 heterodimers form an archway, running from the MD layer, up into the MP layer and back down again (Figure 4.10A). When centered on the "3-2-3" axis, the adjacent interaction of pUL31/34 can be observed as a density rising straight up (Figure 4.11).

4.3.6 CryoET and FIBSEM reveal the NEC defines a precise vesicle geometry to accommodate capsids

The NEC coat forms two, closely linked hexameric lattices, the relationship between which tightly controls the size and shape of the vesicle for which it is formed (Figure 4.12). This tight regulation of size helps to maximize the surface area for recruitment of capsid, while retaining the optimal size that can maximize the interactions between the NEC and capsid. This presumably means that as few as possible UL34/31 dimers are wasted during egress and allows efficient transport. *In situ*, the lattice would need to accomodate defects either in the form of pentameric vertices or open gaps in order to accomodate a spherical arrangement as the utilisation only of hexons as a building block for the formation of spherical vesicles is not possible. The vesicles observable in figure 4.9A are not perfectly spherical.

The electron cryo-microscopy studies described in this chapter have revealed the model of peri-nuclear vesicle formation at the INM, and by extension, how capsids may be recruited for transport across it. pUL34 and pUL31 form NEC heterodimers at the INM, and associate to form a planar arrangement, most likely initiated by interaction with the herpesvirus capsid. The planar lattice exhibits the 11 nm spacing previously

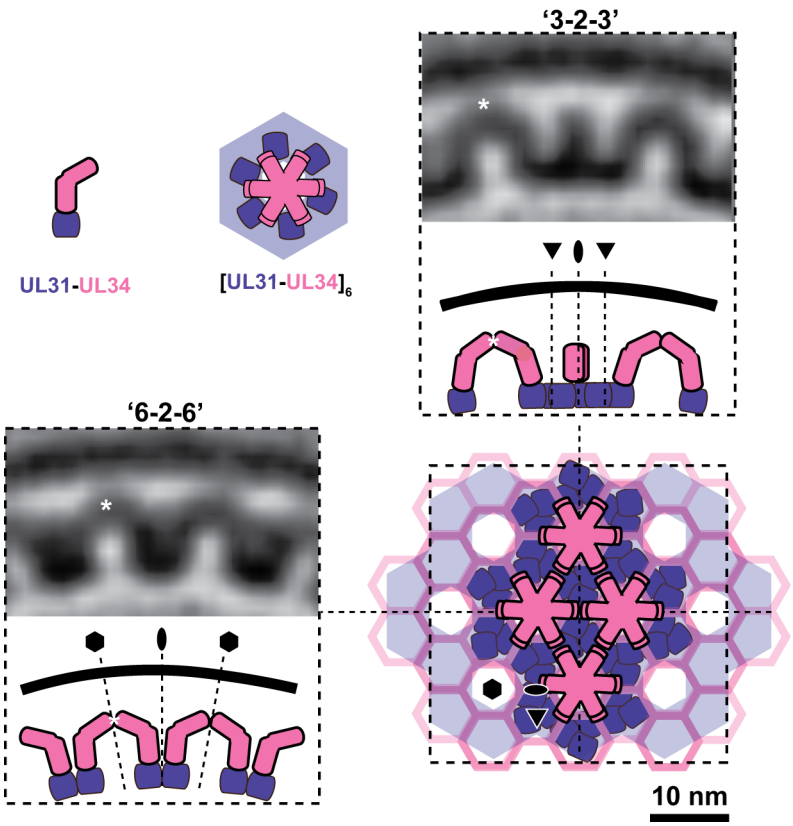

Figure 4.11 – The model for the arrangement of the NEC coat (bottom right). The interactions of pUL31/34 heterodimers is shown alongside cross-sectional views of the NEC coat average (c.f. Figure 4.10A). The archway motif is marked by a white asterisk. pUL34 (magenta), i.e the membrane bound protein, and pUL31 (purple), form the MP and MD layers, respectively. The evidence for this arrangement is also supported by Klupp et al. (2007). (Hagen et al. (2015)). This work was carried out by Kyle Dent.

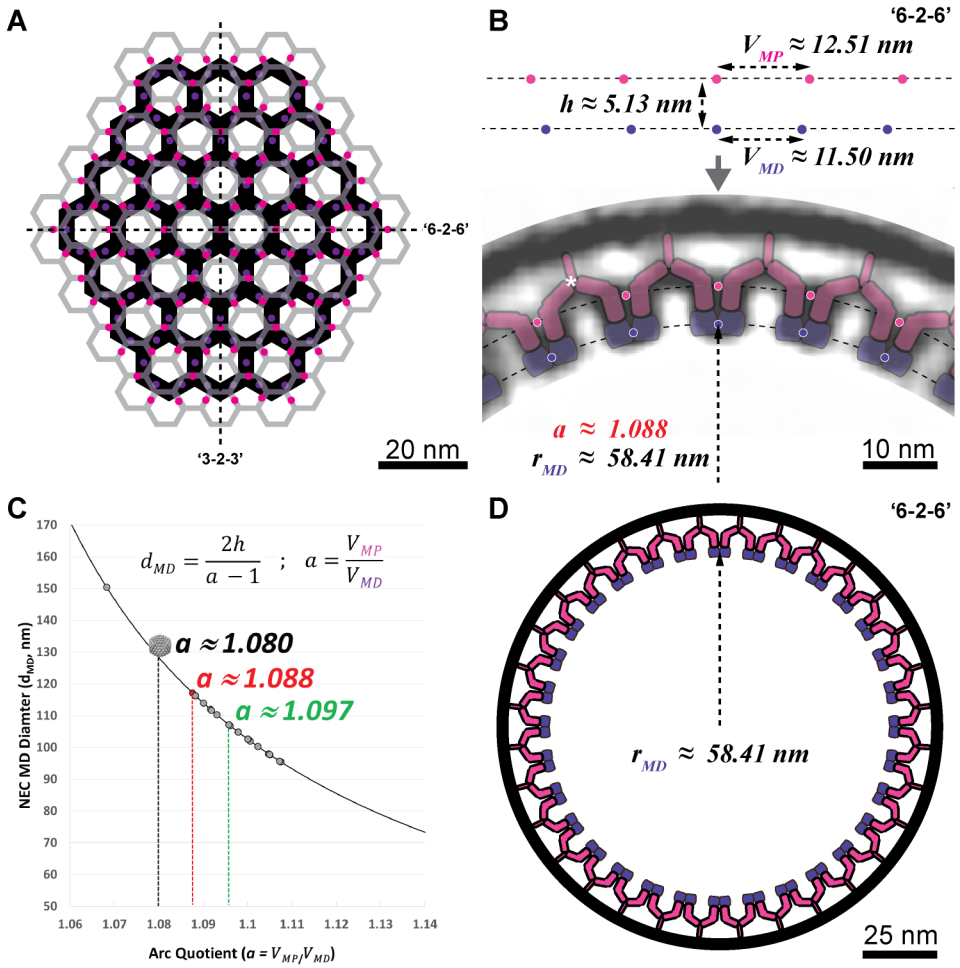

Figure 4.12 – Schematic model of the NEC in peri-nuclear vesicles. (A) A schematic model of the NEC where characteristic layers are represented as they appear in tangential slices (Figure 4.9). Alignment of pink and purple points will result in formation of curvature defined by the radial separation of each layer (parameter "h"). (B) Cross-sectional view of the NEC coat average is modeled according to parameters (h, VMD, and VMP) measured from the experimental average (red asterisk, figure 4.9C). Magenta (MP) and purple (MD) circles highlight that hexagonal layers of characteristic repeat distances (VMD and VMP) interact via the pUL31/34 heterodimer interface to induce a defined curvature. An arch keystone is marked with a white asterisk. (C) The NEC coat diameter between opposite MD layers (dMD) is plotted as a function of a (the arc quotient), and experimentally determined vesicle sizes from cryoFIB-prepared samples are shown as colored circles. The vesicle modeled in (B) is represented in red, while the mean vesicle size is indicated in green and a coated capsid by the respective symbol in gray, each with their respective a values. These values are plotted assuming that VMD is constant, while VMP is hypothesized to vary, owing to flexibility within coat. (D) The resulting model in the context of an entire vesicle cross-section produced by extrapolation. pUL34 (magenta) and pUL31 (purple) make up the MP and MD layers, respectively. (Hagen et al. (2015)). Analysis was performed by Kyle Dent and Christoph Hagen.

shown by (Bigalke et al. (2014)). Rearrangement of the pUL34 region during the formation of the MP drives the budding of the INM into the lumen. Recruitment of further NEC dimers at the periphery of the nascent lattice occurs, until the steric interference of the MD and MP layers results in the vesicle being unable to curve any further.

Structural determination of the UL31/34 complex by X-ray crystallography has recently revealed the atomic basis for their interaction, and could be used to suggest cellular proteins with structural homology to the NEC (Bigalke and Heldwein (2015); Leigh et al. (2015); Lye et al. (2015); Walzer et al. (2015)). The most interesting observation is that pUL31 contains a conserved zinc-finger motif which has been shown to be essential for proper function of the pUL31/34 complex (Zeev-Ben-Mordehai et al. (2015)). Fitting of the crystal structures to the sub-volume average described in this chapter, supplemented by (small angle X-ray scattering) SAXS data (Zeev-Ben-Mordehai et al. (2015); Hagen et al. (2015)), allows the approximate regions that interact within the structure used as a basis for the structural determination of putative cellular counterparts.

4.3.7 Integrative structural biology of nuclear egress

Super-resolution fluorescence microscopy (3D-SIM) allowed me to observe that pUL31/34 perinuclear vesicles form GFP-dense "bunches" on the nuclear periphery. The ability to visualize the INM using residual pUL34-GFP distributed along it provided the observation that perinuclear vesicles often associate with type-1 and type-2 nucle-

oplasmic reticula, the latter of which often formed tubes that traverse the nucleus connecting the cytoplasm of both sides (Figure 4.7). Using the insights gained from this pUL31/34 cell line, and moving towards virus-infected cells, we were able to extend this model to show that these structures may also occur in virus-infected cells (Figure 4.8). Such structures could potentially provide a large surface area at which herpes egress could take place.

These features have been seen in static, classical plastic embedded studies of MCMV-infected cells, in parallel studies (Villinger et al. (2015)), and although no clear role has been determined for their appearance in infected systems, they may still have some role in nuclear egress. Infection of cells with PrV resulted in a different behaviour of nascent viral capsids in the nucleus when compared with MCMV-infected cells (Figure 4.8). Replication centers of the PrV capsids in the nuclei were much more diffuse. Recent data has shown that diffusive transport seems to be the primary means of escape through the nuclear interior towards the periphery, and that nuclear remodeling of cells during infection increases efficiency of this diffusive process (Bosse et al. (2015, 2014)). The nucleoplasmic reticula could represent one effect of nuclear membrane remodeling by viruses.

4.4 Concluding Remarks

Here, I have presented super-resolution data of GFP-tagged constructs expressed and imaged in live cells to a resolution on a par with comparable fixed work in 3D-SIM. The approach outlined and data produced are reproducible for multiple wavelengths,

given correct optical system calibrations. I demonstrate that it is possible to perform 3D-SIM in live cells using conventional fluorescent proteins. The different results for different biological systems (e.g. NEC vs Capsids) highlight that the local environment in which a fluorophore resides is a major determinant of whether that fluorophore will be more or less photostable.

The work described and analyzed in this chapter form an attractive model to describe how and why the NEC is able to form perinuclear vesicles, how this relates to the biological function of the NEC in relation to capsid recruitment, and how these factors relate to the overarching biology of herpesvirus egress. Nuclear egress is roughly analogous to processes observed for viruses at the plasma membrane, for example in the case of HIV budding (Sundquist and Kräusslich (2012)), in which the immature Gag protein forms an initial hexagonal coat, that maintains the spherical shape of budding HIV1 virions. A cellular equivalent for herpesvirus nuclear egress has yet to be determined, but several leading protein candidates have been suggested that may play a similar role for the transport of large cellular cargoes out of the nucleus (Jokhi et al. (2013); Speese et al. (2012); Hatch and Hetzer (2014)).

In the following chapter, I discuss an emergent method for contrast enhancement in electron cryo-microscopy; the Volta phase plate (VPP). The use of the VPP has great potential to increase the observable detail for sub-volume averaging studies. The potential to automate its use and its relative stability over earlier phase plate models should also make it a practical solution needed for high-risk complicated experiments typical for FIB/SEM and cellular tomography (Danev et al. (2014); Mahamid et al. (2016)). I will discuss its practicality and application in molecular cryo-tomography,

and assess its implementation in modern day cryo-electron microscopes. I will go on to suggest improvements for the acquisition of data and, furthermore, its potential for automated data acquisition. Use of VPPs to acquire cellular data have, and will, improve the contrast, and hence the range and detail of biology observable in cryoET.

5

Application of phase plates in molecular electron cryo-tomography

5.1 Introduction

5.1.1 Principle of phase contrast microscopy

Phase contrast microscopy is a technique for contrast enhancement of material in transmission microscopy invented by Fritz Zernike (Zernike (1942)). The relative ease of implementation in light microscopy has made it a routine technique used in almost every biology lab as a way to view cellular material and cell dynamics. Phase contrast light microscopy allows the observation of unaltered, live specimens without the need for staining. Bright field light microscopy methods lack the necessary

contrast to observe the higher resolution features in the sample, as the low scattering propensity of the material being imaged often results in little to no contrast observable in the image. This is a fundamental limit intrinsic to the weak phase approximation, and the way in which elastic scattering (when energy from the interaction with the photon/electron is conserved) occurs.

The development of phase contrast methodologies for electron microscopy has been more difficult, despite ideas for how a phase plate may be implemented in an electron microscope existing since almost immediately after Fritz Zernike's invention, for example by Hans Boersch (Boersch (1947)). The need for a high vacuum within an electron microscope has made the design of a phase plate complicated, as any contamination on the surface will change the optics and the quality of the resultant image. Similarly, precise alignment of the phase plate on the order of microns, requires complicated mechanics to control and hold the plates in the correct optical location at the back focal plane.

Although the implementation of phase contrast differs between the two techniques (Figure 5.1), the physical basis by which light and electrons are modulated and affect the image remains broadly the same. If we consider the ways in which a wave can interact with an object as it passes through it, we can have two types of interaction: a scattering event that alters the amplitude of the wave as it comes out of the sample and as such produces amplitude contrast; or a scattering event that alters the phase of the wave as it comes out of the sample and produces phase contrast.

In a conventional microscope, amplitude contrast predominates as this scattered light is in plane with the unscattered beam and as they diffract produce constructive

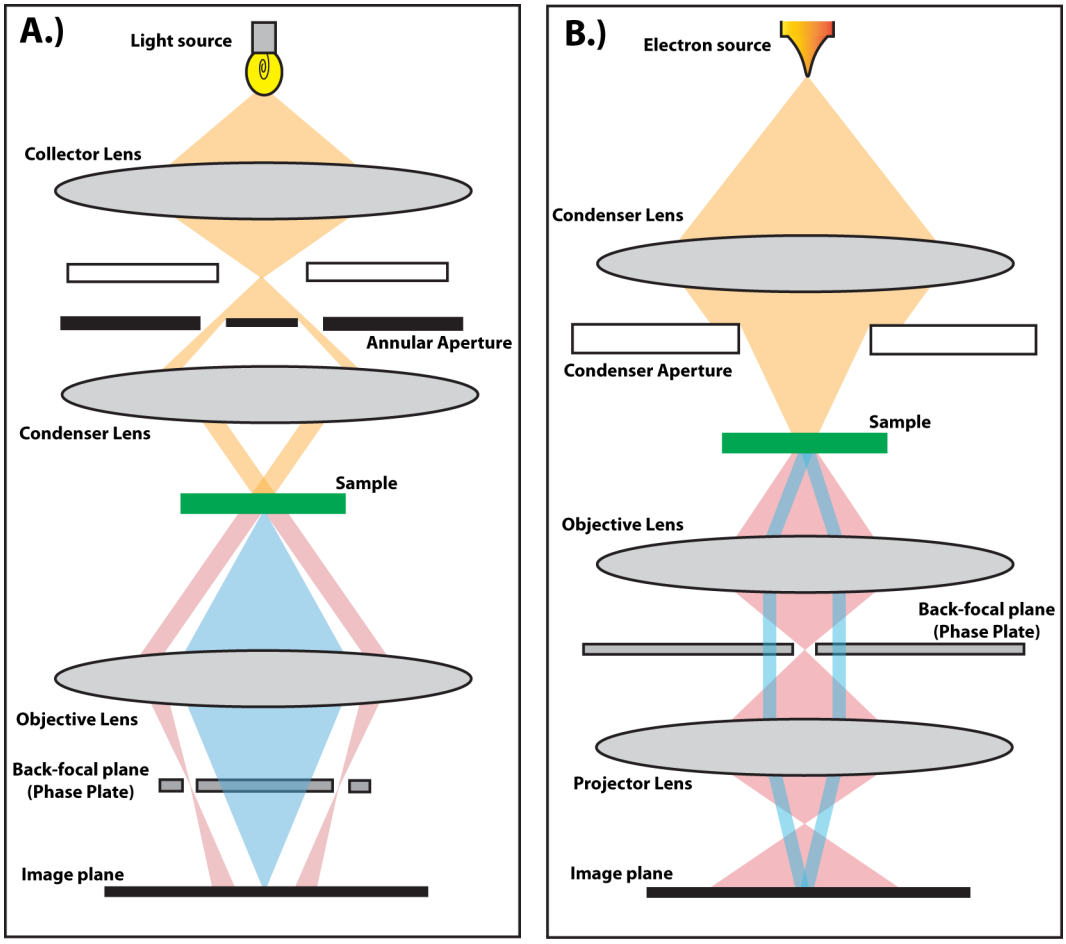

Figure 5.1 – Simplified schematic comparison of phase contrast methods employed in A.) a phase contrast light microscope and B.) a single condenser electron microscope with a Zernike phase plate. The illumination beam is shown in yellow, with the scattered and unscattered wave fronts indicated in blue and red, respectively. Both schemes share the common element of the introduction of a 90° phase shift for the scattered wavefront at the back focal plane. The resultant phase shift produces interference between the scattered and unscattered waves that result in the appearance of amplitude contrast in the image produced.

and destructive interference, which appears as modulations of contrast in the image. The phase contrast is shifted either 90° or 270° out of phase of the unscattered beam and is therefore out of plane. The key to phase contrast microscopy is to introduce a 90° phase shift into the scattered, phase shifted beam, so that this is then re-shifted back into plane of the unscattered beam to cause their interference (Figure 5.2).

If we consider the electron microscope, an image in which there is no variation in contrast can be represented as is shown in Equation 5.1. The ability to introduce a phase shift into the scattered beam requires the physical manipulation of the optical path, for example in the back focal plane of the objective lens, which can subsequently alter the intensity in the image (Equation 5.2). This can be described mathematically (Nagayama (2011)) :

$$|e^{i\vartheta(\mathrm{r})}|^2 = 1 \tag{5.1}$$

$$|\{FT^{-1}[H(\mathbf{k})]\} * e^{i\vartheta(\mathrm{r})}|^2 \neq 1 \tag{5.2}$$

where H represents a spatial filter residing in the back focal plane, defined in frequency space, $\mathbf{k}$, and the term $e^{i\varphi}$ represents the object. This describes how the convolution of the scattered beam ($e^{i\varphi}$) with a modulation in the back focal plane of the microscope ([H($\mathbf{k}$)]) may result in a change in intensity of the resultant beam.

There are a several different approaches one can use to introduce a phase shift into the scattered beam, but here I will describe three: defocus phase contrast (DPC), where an image is acquired using an illumination beam out of focus at the specimen

plane; Zernike phase contrast (ZPC), where a carbon film with a small pinhole is inserted into the back focal plane; and Volta phase contrast (VPC), which utilizes an electrostatic charge that builds up on the surface of a carbon film.

Imaging the sample using either an under-focused or over-focused beam alters the path difference between the scattered beam and unscattered beam, producing a change in modulation of contrast in the resulting image compared to when at focus (Unwin (1971)). The image has a variable amount of phase shift and information that varies at different spatial frequencies for different defoci such that i.) negative oscillations appear and ii.) points of zero information occur as the transfer function oscillates between positive and negative (c.f. Figure 3.8C). For example, phases can be shifted by 90° (positive contrast), some by 180° (no contrast) or others by 270° (negative contrast). In an electron microscope, a defocus can be used to compensate for the spherical aberration of the objective lens. The defocus at which the spherical aberration maximally compensates for oscillations in the CTF out to the highest resolution frequency approaching zero capable for that microscope is known as the Scherzer defocus (Scherzer (1949)).

The phase contrast transfer function used to describe how non-phase shifted contrast is passed into an image can be defined (Nagayama (2011)):

$$sin\gamma(\mathbf{k}) = 2\pi(\frac{1}{2}\Delta z\lambda\mathbf{k}^2 + \frac{1}{4}C_s\lambda^3\mathbf{k}^4) \tag{5.3}$$

where Δz is the defocus (µm), λ is the wavelength, C_s is the spherical aberration, and k is the spatial frequency.

To take into account the phase shift induced by a phase plate, a term needs to be added that accounts for the extra phase shift. This has been implemented in CTF correction algorithms, such as ctffind4 (Rohou and Grigorieff (2015)). If we represent the overall phase shift in the image as χ, the image phase shift can be written thus (Rohou and Grigorieff (2015)):

$$\chi(\lambda, |\mathbf{k}|, \Delta z, C_s, \nabla) = \pi\lambda|\mathbf{k}|^2(\Delta z - \frac{1}{2}\lambda^2|\mathbf{k}|^2 C_s) + \Delta\phi$$

where the phase shift, χ, is a function of the wavelength (λ), defocus (Δz), spherical aberration (C_s), the additional phase shift induced by the phase plate ($\Delta\varphi$) and k is the spatial frequency.

Conventionally, when considering DPC, the modulation of phase contrast is determined using a sine function. However, when we consider a Zernike phase plate (or Volta phase plate) inserted into the back focal plane of the microscope, the CTF equation for a phase plate device becomes a cosine function, due to the 90° shift. Furthermore, the modulation of the scattered beam is uniform across the wave front, such that a consistent phase shift exists over the range of frequencies on which it acts (cut-on frequency), the determinants for which will be described in section 5.1.2.

5.1.2 Types of phase plates in electron microscopy

The development of phase plates for electron microscopy has relied mainly on two methods as to generate the desired phase shift of the unscattered beam (Figure 2.3). Either a physical object in the path of the scattered beam can be used to shift the

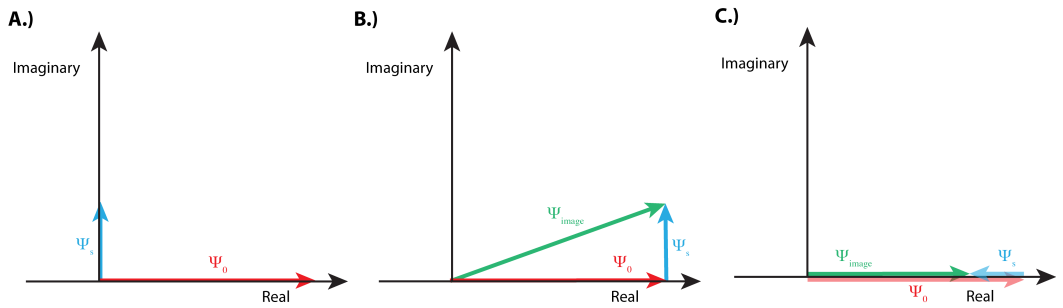

Figure 5.2 – Representation of the relationship between phase shift of the scattered and unscattered beams when considering weak phase objects. Argand diagram of the relationship between the phase of the scattered and unscattered beams when considering weak phase objects. In an Argand diagram the length of the vector represents the amplitude of the wave. In EM, one detects intensities that are the square of the amplitudes. The phase of the wave is described by the angle the vector makes with the real axis. A.) The scattered beam is shifted by 90° with respect to the unscattered beam. B.) The sum (green) of the scattered (blue) and unscattered (red) waves gives the imaging wave. The amplitude of the imaging wave is very similar to the amplitude of the unscattered wave, resulting in poor contrast. C.) A phase plate introduces a phase shift into the the scattered wave, such that there is a larger difference in the amplitude between the imaging wave and the scattered wave, resulting in a greater contrast in the image. Figure adapted from Lindsay Baker/John Rubenstein.

phase while leaving the unscattered beam unaltered (Zernike phase plate)(Danev and Nagayama (2001); Kanaya et al. (1958)), or that a differential electrostatic lens created at the back focal plane can similarly retard the phase of the scattered beam with respect to the unscattered (Shiue et al. (2009); Unwin (1970)). In this section, I will attempt to describe the principles of how this phase shift is generated by these two alternative methods.

5.1.2.1 Zernike phase plate

The Zernike phase plate (ZPP) is the canonical type of phase plate that has traditionally been used in light microscopy, and consists of an aperture assembly with a continuous carbon film. The carbon film contains a very small hole in its centre, through which the unscattered beam passes. As the scattered beam originates from

the sample upon interaction with the electron beam, it interacts with the carbon film and is phase shifted by 90° (Figure 5.3b). Early ZPPs utilized holes that were on the order of 10-20 µm (Kanaya et al. (1958); Badde and Beimer (1970)) which resulted in modest contrast enhancement. One limitation of early ZPP designs was their propensity to accumulate contamination on the surface of the carbon film, the charging of which by the electron beam can cause spurious phase and amplitude modulations that result in aberrant images (Danev and Nagayama (2001)). One solution to this has been to add a further layer of carbon onto the phase plate, which produces a conductive layer onto the surface contamination of the original assembly (Danev et al. (2009)). This dissipates charge as it builds up on the surface of the phase plate. Further developments have also taken into account the advantage of heating the phase plate during use, which can help to bake-out and evaporate contaminants on the surface (Murata et al. (2010)).

5.1.2.2 Volta phase plate

Hans Boersch hypothesized the ability for electrostatic lenses to induce phase shifts in the electron beam in the electron microscope in 1947 (Boersch (1947)). Attempts to create these electrostatic lenses in the back focal plane have been tried in various studies since (Shiue et al. (2009); Unwin (1970)). However, the Volta phase plate (VPP, or hole-free phase plate), which utilizes an electrostatic potential, but works in a very different way, is currently at the forefront of electron microscopy as the most robust and automated method for routine phase plate data acquisition. In the previous section, I described how ZPPs were prone to contaminant-based charging

effects close to the pinhole of the carbon film, and that these caused artifacts in images using these phase plates. VPPs, in contrast to ZPPs, do not contain a pinhole, but rather a continuous carbon film that resides at the back focal plane of the objective lens. The surface contamination that occurs on the ZPP also occurs on the VPP (Nagayama (2011); Danev et al. (2014)), however, in the case of the VPP, this is used to generate the phase shift of the scattered electron beam (Figure 5.3c). The incident, unscattered electron beam is focused to a point in the back focal plane, at which the VPP resides. The incident electron beam causes surface changes on the VPP which results in charging of contamination. This creates an electrostatic potential local to the incident beam, which produces a "Beam-induced phase shift (BIPS)" (Danev et al. (2014)) that causes an ~90° phase shift in the scattered electron beam. Interestingly, the VPP is unstable for up to a week when installed into an electron microscope, suggesting surface contamination must first reach a steady state in the column of the electron microscope (Danev et al. (2014)).

5.1.3 Biological applications of phase plates in electron microscopy

The main justification for the development of phase contrast electron microscopy using phase plates is to increase the contrast visible in electron cryo-microscopy images without applying a high defocus, and the related aberrations that results from such an approach. Conventional, non-phase plate electron cryo-microscopy relies on a low-dose acquisition scheme, that is of an inherently low signal to noise ratio. Further-

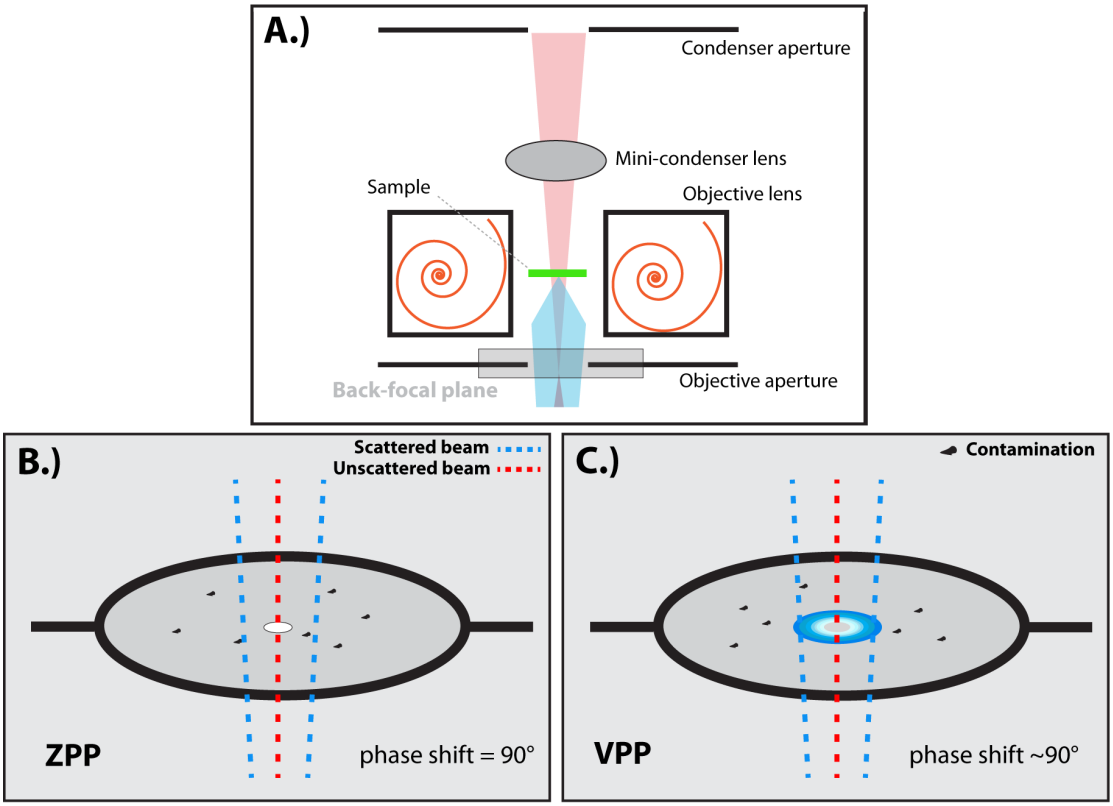

Figure 5.3 – Schematic of two types of phase plate, the Zernike phase plate (ZPP) and the Volta phase plate (VPP). A.) Schematic of the arrangement of the back-focal plane with respect to sample (green), objective lens (red) and the condenser aperture. B.) Diagram of how a Zernike phase plate would look in the back focal plane. A small pinhole in a continuous carbon film allows the unscattered beam to pass with no phase shift and defines the cut-on frequency for spatial frequencies at which a 90° phase shift is introduced. C.) Diagram of a Volta phase plate with schematic potential gradient highlight in varying shades of blue. Vaporization of contamination existing on the surface of the carbon film creates a local electrostatic potential that introduces a phase shift into the scattered beam. Any contamination in the path of the unscattered beam is quickly dispersed, creating the electrostatic gradient. The phase shift introduced is ~90°, dependent on the strength of the Volta potential generated.

more, the defocus and aberration based approach described in section 5.1.1 (DPC) produces negative frequencies at different resolutions that result in image artefacts. The use of a phase plate allows the in-focus acquisition of data, while at the same time increasing the contrast in images. These properties are advantageous to many techniques within electron cryo-microscopy, such as single particle analysis (SPA), electron cryo-tomography and sub-volume averaging, as the alignment of particle images with higher contrast is potentially easier and may afford an increase in the resolution of biological structures from fewer particles (Murata et al. (2010)).

Recent developments in the use of both Zernike and Volta phase plates have led to a number of significant biological insights. In a pioneering example, ZPPs were recently used to determine, *in situ,* the assembly intermediates of cyanophages as they infect and replicate inside cyanobacteria (Dai et al. (2013). Significantly, the low number of events visible in cells, and the low throughput of data acquisition still allowed the sub-volume averaging of a number of different intermediates that were significant in determining insights into the mechanism of how DNA associates with viruses and is packaged.

A previous study had shown that ZPPs could also be used to reconstruct structures of macromolecules to a sub-nanometer resolution using single particle methods, for the first time using a phase plate to show secondary structural elements (Murata et al. (2010)). This was also performed using less than 5000 particles, which represents a significant advance in the potential for the technique. Furthermore, a separate study has shown the potential for the use of ZPPs in the study of frozen-hydrated mammalian cells (Fukuda and Nagayama (2012)). In this study, Fukuda et al. were

able to demonstrate that, *in situ*, membrane protein complexes could be observed in cells, on their native membrane in their native context, as well as demonstrating the vastly improved contrast of biological features in the cytosol. This represents a significant potential that will be a main application for phase plates; the determination of rare events in their native context.

Recent studies using the VPP to visualize cells have, like ZPPs, allowed the determination of structures *in situ*. The greater practicality of the VPP makes it a much more robust technique for studies with precious samples, such as FIB/SEM experiments. These two techniques were recently combined to great effect in several studies, such as the determination of conformational variants of the 26S proteasome and the structural determination of the nuclear pore *in situ* in the interior of cells (Asano et al. (2015); Mahamid et al. (2016); Fukuda et al. (2015)).

Single particle electron cryo-microscopy (SPA) using the VPP in-focus has led to the structural determination of protein complexes of less than 200kDa to resolutions approaching the atomic (Danev and Baumeister (2016); Khoshouei et al. (2016)). This represents a significant increase in resolution over the ZPP, however, it must be noted that the implementation of the VPP is more robust and more amenable to automated and medium/long term data collection than the ZPP (Danev et al. (2014)), which mostly requires laborious, manual data collection (Murata et al. (2010)). Although exciting, the application of VPPs to SPA methods is only useful when considering protein complexes less than 200kDa, as the technology becomes an over-complication for SPA experiments, where conventional DPC methods would be more likely to result in a higher resolution (Bartesaghi et al. (2015)), although it may prove that 3-

dimensional classification analyses may benefit from the improved contrast, i.e. along the lines of Bai et al. (2015).

Phase plates are an emergent technology that may be used to improve the contrast in electron cryo-microscopy images, providing a means for the visualization of rare molecular events normally inaccessible to conventional cryoEM methods. Studies using VPPs are beginning to be released from laboratories around the world as the technology becomes more widely available (Chlanda et al. (2016)). In this chapter, I describe some of the problems associated with the use of VPPs, and discuss the scope for the VPP to enable the more routine higher resolution structural determination of molecular processes *in vitro*. As the technique becomes more widespread and the potential for sub-volume averaging to higher resolutions increases (Khoshouei et al. (2017)), the potential pitfalls and improvements in how the VPP can be used should be explored. I will present my findings in the context of the visualization of the dynein tail interaction with adenovirus, and the example of the HSV1 surface glycoprotein B expressed on lipid vesicles (Zeev-Ben-Mordehai et al. (2016); Maurer et al. (2013)).

5.2 Materials and Methods

5.2.1 Sample preparation

5.2.1.1 Dynein/Adenovirus

The sample was prepared as described in Chapter 2, Section 2.2.3.

5.2.1.2 Glycoprotein B

Glycoprotein B samples were prepared by Benjamin Vollmer using the method described in Zeev-Ben-Mordehai et al. (2016), but with the change that Human Embryonic Kidney 293 (HEK293) cells were used to produce the vesicles, rather than Baby Hamster Kidney (BHK) cells.

5.2.2 Electron microscopy

The data were collected on an FEI Krios electron microscope (microscope m02, electron Bio-Imaging Centre [eBIC], Diamond Light Source Ltd., UK) with Dan Clare and C. Alistair Siebert using FEI Tomo software, equipped with an XFEG, and operated at 300 kV. Tilt series were acquired on a post-energy filter mounted Gatan K2 Summit direct electron detector with a 1.781 Å pixel size and a defocus range of between 300-600 nm. The Titan Krios was equipped with a ceramic-heated Volta phase plate (Danev et al. (2014)). The electron microscope was aligned by Dan Clare and C. Alistair Siebert for the use of the Volta phase plate as has been described elsewhere (Fukuda et al. (2015)). Alignments were carried out before each automated tomography session was set-up on the microscope. Before acquisition of a new tilt series, the position of the Volta phase plate was changed to a fresh region of the carbon film not used for data collection. Subsequent charging of the phase plate was performed on the previous region for data acquisition. The aperture assembly for the Volta phase plate was left to stabilize for 5 minutes before activation. Once the sample was centered on carbon, in a region of no interest, the beam was exposed

to the sample and Volta phase plate and dose accumulated until the contrast at the desired defocus (~500 nm) become more pronounced. Once a noticeable phase shift was observed, a tomogram was collected. In some cases tracking before was not used, whereas in others the tomogram was tracked before and after acquisition of a new tilt image.

Tilt series were acquired using a tilt range of either +/- 60° or +/- 45°, bidirectionally from 0° to -45/-60° and then 3° to 45/60° and contained a total dose ranging between 60-100 $e^-/Å^2$ with an angular sampling of 3°. Tilt images were acquired with dose fractionated, counted frames recorded every 0.2s per tilt. Frames were corrected using motionCorr (Li et al. (2013)) and micrographs for each tilt combined into tomography tilt series and reconstructed into tomograms using IMOD (Kremer et al. (1996)).

5.3 Results and Discussion

5.3.1 Assessment of quality of data acquired with a Volta phase plate

5.3.1.1 Herpesvirus glycoprotein B

Herpesvirus glycoprotein B (gB) is a surface membrane protein expressed on the HSV1 virion and serves as the main fusogen for the entry of HSV1 into cells. In order to model the mechanism by which glycoprotein B can mediate the fusion of two lipid bilayers, it is important to understand both the pre-fusion and post-fusion

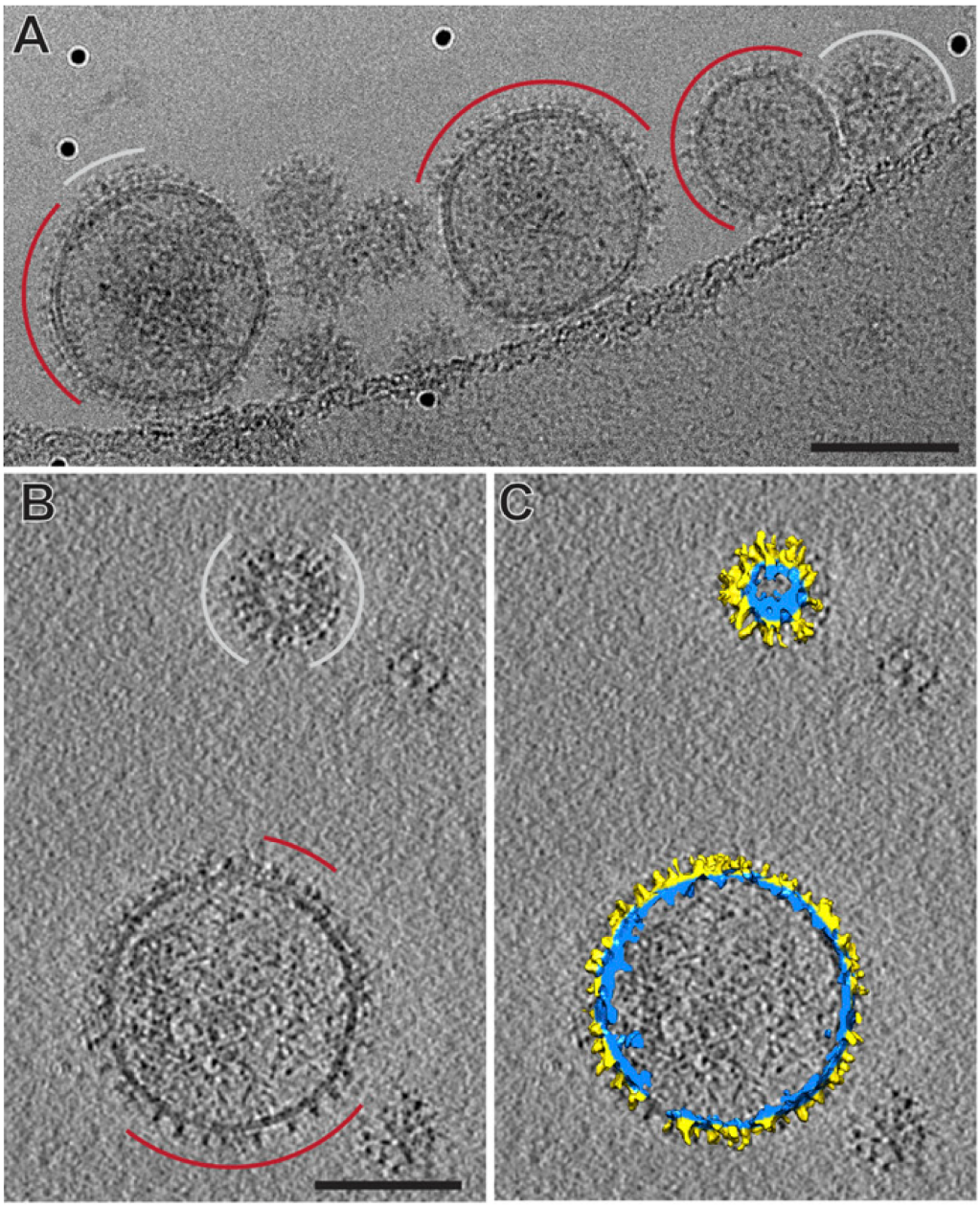

Figure 5.4 – Electron cryo-tomography of gB-enriched vesicles without a VPP. Modified from Zeev-Ben-Mordehai et al. (2016). A.). Electron cryo-microscopy images and B.) tomography slices of extracellular vesicles containing membrane-bound gB taken from Zeev-Ben-Mordehai et al. (2016). C.) shows a segmented form of the vesicles shown in B.). Red arcs represents the pre-fusion conformation of gB, while white arcs represent the post-fusion form. The pre-fusion form is more prevalent on larger vesicles with lower curvature (Zeev-Ben-Mordehai et al. (2016)). Scale = 100 nm.

conformations of gB and to attempt to isolate dynamic conformations in between. The post-fusion conformation of gB has been determined before using X-ray crystallography (Heldwein et al. (2006)), but attempts to determine the high resolution structure of the pre-fusion conformation are so far unsuccessful. A recent study published a low resolution conformation of gB, thought to be pre-fusion, using a natively anchored, lipid vesicle-bound form of gB using electron cryo-tomography and sub-volume averaging (Zeev-Ben-Mordehai et al. (2016)). This study was largely limited by the inherent low contrast obtained in cryo-tomograms, and data was collected using a VPP to see if the contrast of features observable in the tomograms could be improved.

Tomograms of gB anchored to lipid vesicles have been published (Zeev-Ben-Mordehai et al. (2016)). Figure 1 from Zeev-Ben-Mordehai et al., 2016 is shown in a modified form in Figure 5.4. gB visible on the surface of lipid vesicles exists in multiple conformations, with vesicles exhibiting both the pre-fusion form (red) and the post-fusion form (white). Using the VPP, data were acquired of lipid vesicle-anchored gB, and the results are shown in Figure 5.5. The resultant tomograms show gB-decorated vesicles with greater contrast, where the post-fusion and pre-fusion forms of gB are visible, similar to that shown in Figure 5.4. The lipid bilayer of the vesicles is also visible. One striking feature is the ability to trace and follow individual gB molecules in 3-dimensions. This reveals that gB often tend to associate on the surface of vesicles in pentameric or hexameric arrays (Figure 5.5B), and these are visible especially in top views of vesicles. The increased contrast should enable the greater determination of structural and conformational intermediates of gB through sub-volume averaging

of the data, as was done in Zeev-Ben-Mordehai et al. (2016). Similar studies, carried out on the Influenza fusogen haemaglutinin (HA), also used the increased contrast provided by the VPP to be able to observe fusogenic intermediates, and determine the arrangement of HA as it causes hemi-fusion of membranes. The tomograms acquired here are, visually, of comparable quality (Chlanda et al. (2016)).

5.3.1.2 Dynein/Adenovirus

The tail region of dynein is a complex, flexible multi-component protein that is difficult to see using conventional electron cryo-tomography (see Figures 2.15 and 2.16). In order to better characterize the interaction of the tail complex of dynein with adenovirus, I used the improved contrast afforded by the use of the VPP. Projection images of the tail bound to adenovirus shows that it associates extensively along the face of the adenovirus (Figure 5.6A). Tomograms using the VPP of these same preparations increase our ability for this to be observed in three dimensions, and be viewed in high detail (Figure 5.6). The improved contrast in Z allows the observation that the dynein tail complex also lays flat along the adenovirus in this direction. This is in direct contrast to data acquired with no VPP, where the dynein tail complex is much more difficult to observe directly, and can only be inferred through XY slices. It is now possible to discern that multiple tails also associate around the viruses, which may play role in determining the directionality of movement *in situ* where the number of motors may play a role in this "tug-of-war" between minus-end directed dynein and the plus-end directed kinesin (Rai et al. (2016)).

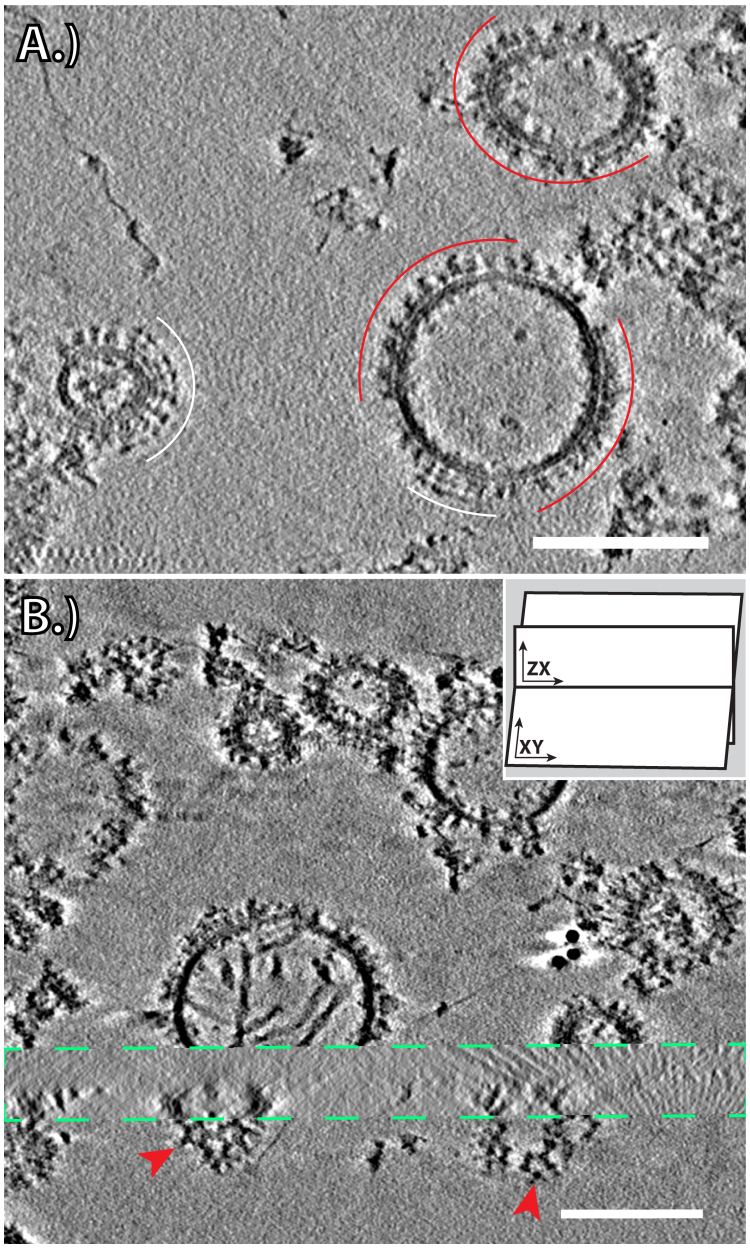

Figure 5.5 – Electron cryo-tomography of gB-enriched vesicles with a VPP. A.) Tomographic slice of gB-decorated extracellular vesicles acquired using the Volta phase plate. Regions of vesicles with majority of the gB in the post-fusion conformation is shown by the white line, and those where the majority is the pre-fusion is shown by the red line. Compared with Figure 5.4, the contrast is greatly enhanced. B.) Orthographic views in XY and XZ of another tomogram, where the top views of some vesicles are highlighted with red arrows. The red arrows show that the gB are arranged in many cases in a pentagonal or hexagonal arrangement, suggesting that the association of gB is ordered. The increased contrast in Z enabled the observation of membrane bilayers, and of gB in 3-dimensions with greater detail (green box). Scale = 100 nm. Samples were prepared by Ben Vollmer.

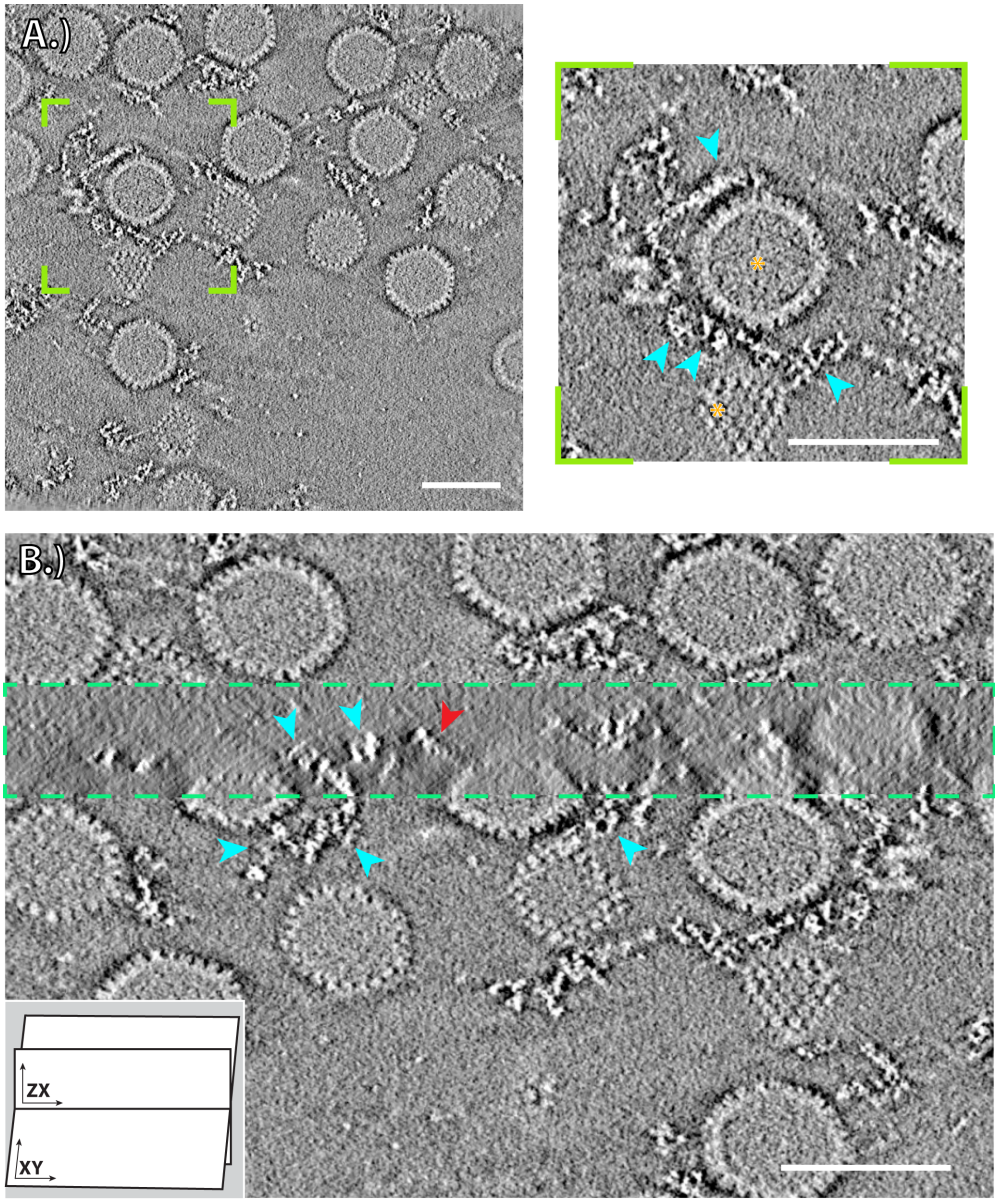

Figure 5.6 – Electron cryo-tomogram of adenovirus interacting with the dynein tail complex after treatment of the adenovirus to a pH 5 environment (contrast inverted). A.) XY projection slice of 5 tomographic slices. Green box represents inset, which shows dynein tails associating and interacting with adenovirus (blue arrow). Adenoviruses are marked with orange asterisks. B.) Oblique view of XY and XZ (green dotted line) views for the projection slice shown in A.). The blue arrows indicate tail complexes. Interestingly, the detail visible for the tail in the XZ direction is very strong, and we can see high detail despite the large conformational variation in the dynein tail complex. Red arrow shows a penton fibre of the adenovirus in the XZ direction.

5.3.2 Factors affecting data quality

During acquisition of data a number of issues arose that required judicious trial and error to correct for. The use of the Volta phase plate in SPA and cryoET has been proposed to be an automated means of acquisition of high contrast data (Danev et al. (2014)), that may help in the structure determination of rare conformational intermediates and of smaller proteins. I present some findings in this chapter which describe issues that have hampered this goal, and suggest solutions that may make it more feasible in the future.

In order to effectively use a VPP, the pivot point calibrations for image shift and beam shift must be highly accurate. This is so that the imaging conditions can be "on-plane", where the beam is focussed to a single point on the carbon film of the VPP as it is residing in the back-focal plane of the objective lens. The way this can be done is described in (Fukuda et al. (2015)). However, I will consider some of the important aspects that may affect data quality here. The "on-plane" condition is required so that the incident beam remains unscattered by the Volta potential, while at the same time applying a phase shift of ~90° to be applied to the scattered beam. Any slight deviation from the on-plane condition will result in the loss of contrast in the image (Figure 5.7), as this phase shift would be applied also to the unscattered beam and the 90° difference in phase between the scattered and unscattered beams lost. Therefore, the loss of the "on-plane" condition is one of the main factors for a loss in contrast during data acquisition.

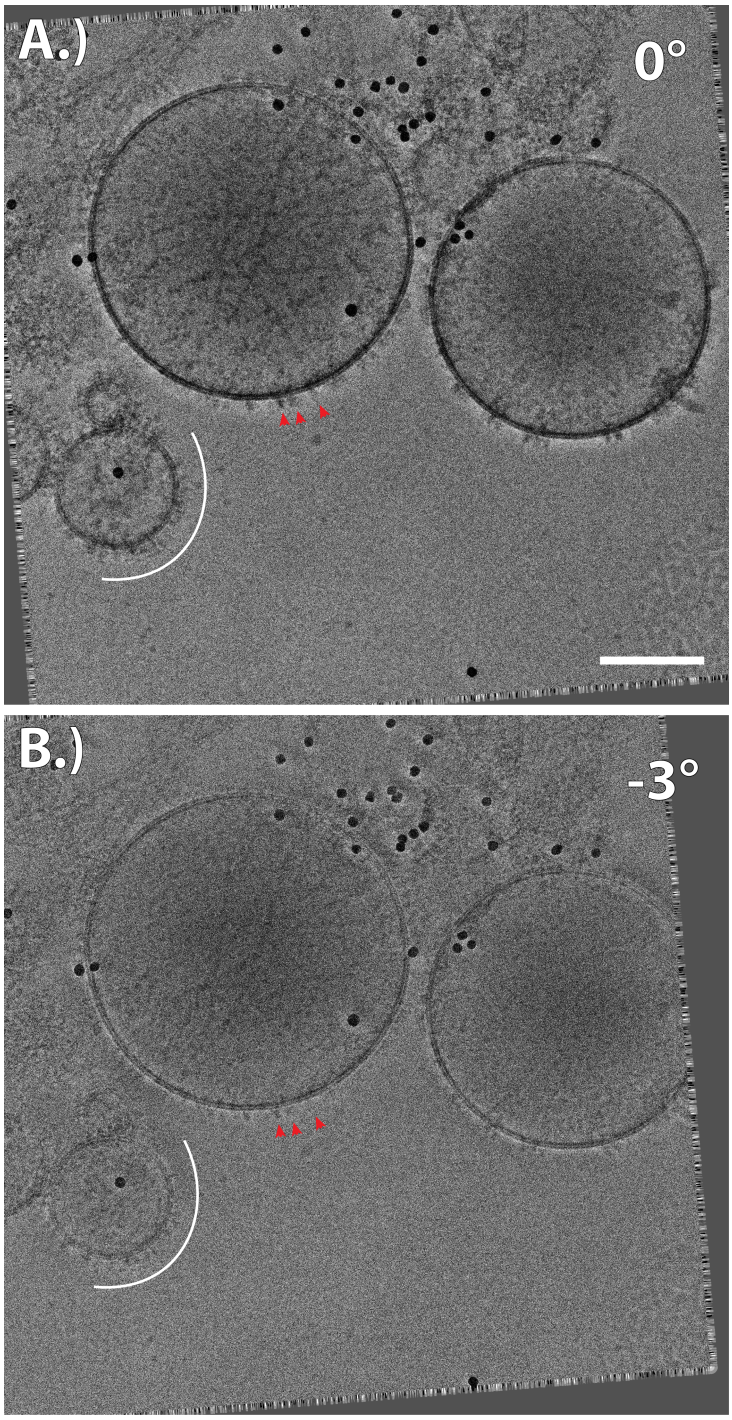

Figure 5.7 – Two images from an aligned tilt series acquired using the Volta phase plate. A.) 0° image taken at the beginning of the tilt series. White line indicates the post-fusion conformation of gB, and the red arrows indicate three pre-fusion gB proteins. B.) next image in the tilt series, taken at -3°. The contrast visible in the image has been lost, and the three pre-fusion gB proteins are barely visible when compared to A.). Similarly, the post-fusion conformation is also much less visible (white). Scale = 100 nm.

5.3.2.1 Lens normalization and beam shift pivot points

The focal abilty of electromagnetic lenses used in transmission electron microscopy (TEM) is controlled by adjusting the current that passes through their electromagnetic coils. Adjusting the focal strength of the lenses to a specific need then necessitates different lens currents in order to produce a certain focal length for a given magnification or focal point. For example, in order to produce an illumination beam of a given size or convergence/divergence, the condenser lenses must be adjusted to the appropriate lens setting that is required to produce a beam with those characteristics. Similarly, the objective lens current determines the strength of the objective lens, and therefore its resolving power. However, the need to switch between optical modes in a TEM during operation results in a hysteresis of the electromagnetic lenses as the current changes between optical modes. For example, as the objective lens is used for a certain magnification, e.g. low magnification, and then subsequently changed to a lens current more suitable for another use, e.g. higher magnification, the change in lens current will not be to the level that the user of the microscope set, as the current will not quite reach the desired value. This results in a change in apparent objective focus (in the objective lens), magnification (in the projector lenses) or in apparent beam focus (in the condenser lenses).

In an FEI electron microscope, the condenser and objective lens current values are determined by the user of the electron microscope, once they have decided upon a set of beam conditions that result in a beam suitable for their desired application and magnification. Typically it is also useful to have several functional modes; an interme-

diate magnification for finding sample and for tracking the imaging area during a tilt series, a high magnification for data acquisition (record area) and another high magnification setting that has an additional beam shift to an area used for focusing and for high magnification tracking (typically, other than the additional beam shift, the imaging parameters are the same). In order to compensate for the effect of hysteresis during data acquisition, it is a recommended procedure to cycle through these modes a number of times, such that the lenses of the microscopes become accustomed to these settings and further normalize the record parameter to the parameters used in the intermediate magnification. Changing between this magnification and the record magnification cyclically incurs a reproducibility to this action and allows the beam position to be stabilized.

When using the Volta phase plate, this normalization of the beam becomes critically important. In order to accurately position the cross-over of the beam at the back-focal plane onto the phase plate, the lens power of the C1, C2 and C3 lenses need to be kept constant over the course of the use of VPP. Any hysteresis in the condenser lenses or objective lens when switching modes during data acquisition could potentially result in a change in the "on-plane" conditions of the VPP and may lead to a change, or total loss of, contrast modulation in the resulting image (Figure 5.8). The normalization of the lenses is normally considered to be a routine procedure in electron cryo-tomography data acquisition, as the settling of the beam prior to data acquisition to makes the beam more stable and reproducible. In theory, this should also hold true in the acquisition for VPP data. However, the routine for charging and producing the Volta potential may preclude this possibility.

The record parameters are first set, with the the alignment of the VPP set to be "on-plane" just before charging of a new Volta potential at a point on the phase plate. The position is then exposed to the electron beam for a time period that results in the build up of contrast in the image (or, for Fukuda et al. (2015), a specified amount of charge, in the nanoCoulomb (nC) range, has built). This can take between 5 and 10 minutes. The amount of charge that needs to be put onto the VPP to cause the BIPS is an element hard to quantify, and the precise phase shift introduced difficult to determine (and may require determination of CTF during downstream processing). Once an adequate BIPS has built up, the tomogram is commenced. In both SerialEM (Mastronarde (2005)) and FEI Tomography (Tomo) software (FEI company, Eindhoven), both commonly used for automated data acquisition, the first step in the acquisition procedure is to take an intermediate magnification image to correct for tilt backlash of the stage, and to normalize the lenses. One effect this may have is that when the microscope adjusts back to the record/focus/track beam condition, any hysteresis may change the apparent "on-focus" conditions, changing the amount of phase shift in the scattered/unscattered electron beam (Figure 5.8). One solution to this may be to run a "phase plate hysteresis" cycle, whereby an iterative cycle of phase plate calibrations in the record parameter, followed by setting of view parameters and then re-alignment of the phase plate, may help to produce a more accurate current setting between view and record on the correct "on-plane" point on the phase plate.

Another consideration for VPP data acquisition is whether to define a region on the tilt axis where an image is taken at each tilt to keep track of the acquisition area

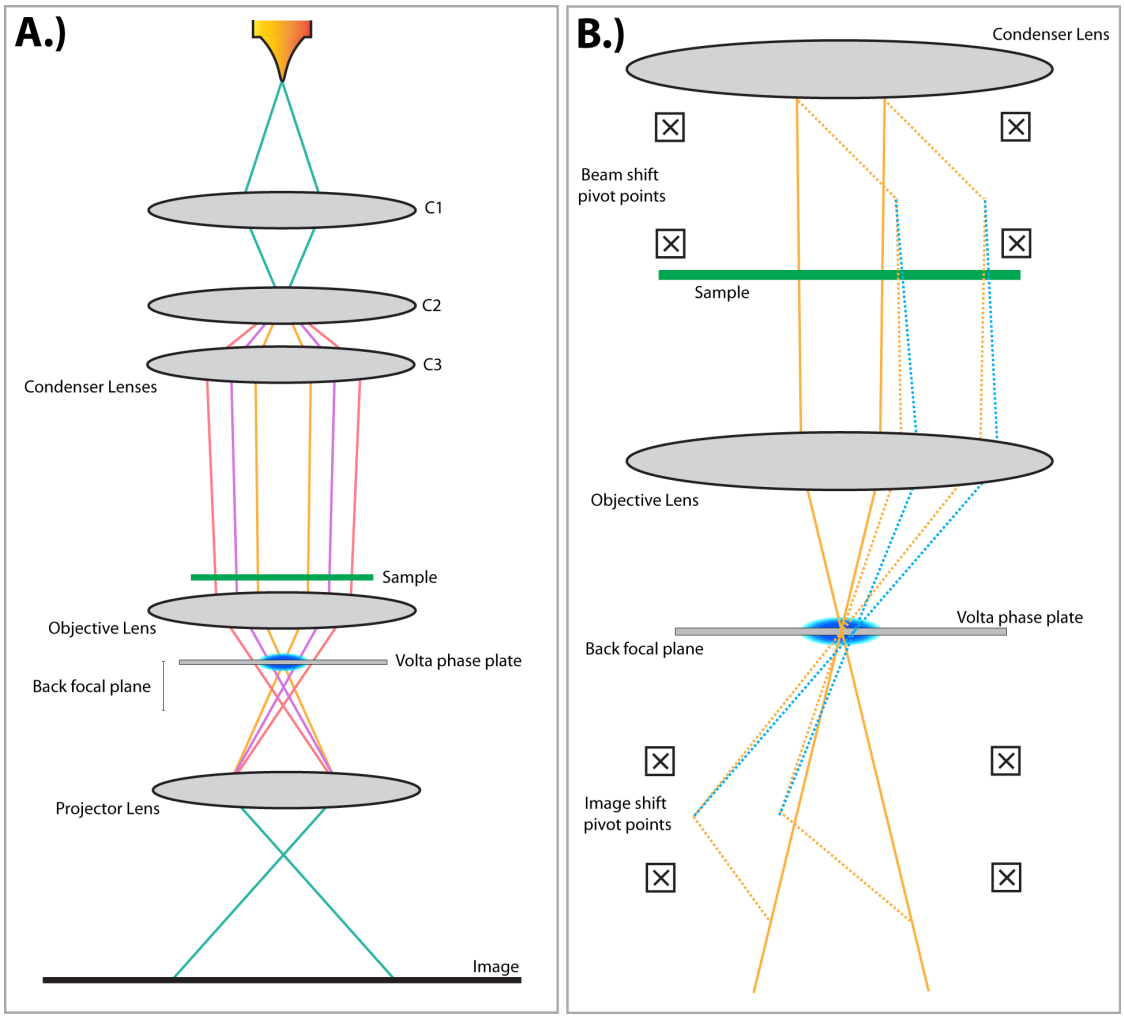

Figure 5.8 – Comparison of beam conditions in an electron microscope whereby "off-plane" imaging conditions may become evident using a VPP. A.) Partial ray diagram illustrating how changes in lens strength in the condenser system may affect the ability of the beam to be "on-plane" with the VPP at the back-focal plane. In orange is drawn an "on-plane' beam, in red a completely "off-plane" beam and in magenta is drawn an "off-plane" beam that still intersects with part of the Volta potential on the VPP. This latter beam may result in partial, or aberrant, modulation of contrast in the image. B.) Schematic illustration of how beam and image shifts are used in EM to image regions away from the sample of interest. Note how the image still passes, when pivot points are accurately calibrated, through the same point in the back focal plane as the unshifted image. A mis-aligned beam shift pivot point will result in a beam which focuses away from the Volta potential in the back focal plane.

as the tilt series progesses. This involves acquiring tracking images at each tilt on a position away from the desired area that can be used to determine a compensatory image/beam shift in record. This tracking area utilizes a image/beam shift in order to image away from the area of interest. In order to leave the Volta potential undisturbed during data acquisition, the beam tilt alignments need to be calibrated precisely, so as to position the tilted image shifted beam to be co-incident with the Volta potential (Figure 5.8). Similarly, any applied beam/image shift applied to the record beam to compensate for movement away from the desired point during tilt series acquisition may result in a similar behaviour as to those observed for lens normalization, as the record beam may not reproducibly hit the point in the back focal plane where the phase plate potential and the beam are "on-plane" (Figure 5.8).

Data were acquired with a tracking area and without, where in both cases tracking was performed on the record image, post acquisition. From 66 tomograms collected (from both the gB and dynein tail datasets), variable contrast (Figure 5.7) was observed in 27 tilt series (41%). The first 16 of the 66 tomograms were collected using tracking before, in which 14 (88%) showed contrast variations. Not using tracking before for tilt series aqcuisiton after the first 16 tomograms came at the expense of robust tracking, and tilt series were of varied quality in terms of consistent field of view, and loss of record area during acquisition of a tilt series. The lack of tracking was mitigated by the use of higher dose in the record images. The potential reason for the more consistent contrast without tracking is most likely because of poor phase plate calibrations, beam shift pivot point alignments, lens hysteresis and mechanical instability (which will be discussed further in the next section). These factors result

in the formation of satellite Volta potentials close to the original, as well as the incident beam not being central onto the Volta potential producing lower contrast and a smaller phase shift of the scattered beam.

5.3.2.2 Mechanical instability of the phase plate assembly

As has already been discussed in the previous section, conservation of "on-plane" conditions during data acquisition is essential to produce consistent phase contrast in images through the acquisition of a tilt series. The Volta phase plate used in this chapter for data acquisition consists of an aperture on which a continuous carbon film is attached. The carbon film, and surrounding aperture assembly is heated to 200°C during operation (Danev et al. (2014)) in order to prevent the build up of contamination that would otherwise make the VPP unusable. The overall stability of this assembly may be an aspect that affects the performance and consistency of the VPP during data acquisition.

In an ideal situation, the beam conditions would be optimized to be "on-plane" at the desired magnification and dose. The VPP would be perfectly aligned to reside at the cross-over of the beam in the back-focal plane and a beam induced phase shift could occur allowing data acquisition with high contrast at focus. If the VPP were to physically move from this position during data acquisition, then the VPP would no long be "on-plane" with the electron beam, and would result in a loss of the BIPS, similar to described in Figure 5.8 (i.e. movement of VPP in Z, rather than a change in beam cross-over).

Beam induced movement of the VPP during data acquisition was recently at-

tributed to the loss of phase shift during tilt data acquisition in a recent study by Sharp et al. (2017), suggesting that the VPP may suffer from mechanical instability. The observations made of the VPP data acquired during automated data acquisition show no clear trend in the loss of the BIPS, with the loss sometimes happening in the whole of the second half of a bidirectional tilt series, after returning to zero (which involves an intermediate image acquisition for back-lash correction, suggesting lens normalization causing this) or in other cases occurring in random images through a tilt series (Figure 5.7). This latter case would suggest phase plate instability, as this would be a more random, stochastic process and vibrational movement in the carbon film would be of a more random nature. Interestingly, a tilt series in which this random appearance of loss of BIPS occurs may be subsequently followed by the acquisition of a tilt series which has very consistent phase shift. As the VPP would be at a new area, it is likely that using a region of the carbon film that is central may be more likely to vibrate when exposed to a beam, and cause random loss of the BIPS.

It may be necessary to investigate the stability of the phase plates, observe if they are vibrating and, if so, correlate this to certain positions on the phase plate and ascertain whether movement of the VPP in Z could be causing loss of BIPS.

5.4 Concluding Remarks

The ability for VPPs to greatly improve the contrast, and detail in electron cryo-tomograms is well documented (Danev et al. (2014); Danev and Baumeister (2016);

Khoshouei et al. (2017, 2016); Mahamid et al. (2016); Fukuda et al. (2015)), and has huge potential in allowing the routine, relatively robust acquisition of data at focus. However, as with all emergent technologies, there are a number of hurdles, discussed in this chapter, that need to be addressed before the use of VPPs can become a fully automated part of cryoET data acquisition. The current implementation of VPPs requires frequent manual intervention to rectify problems, in order to ensure the collection of the best possible data. Future work in addressing lens hysteresis and phase plate stability would be two engineering solutions that may increase data quality and reproducibility for cryoET. However, issues due to lens normalization and beam shift pivot points are aspects that can be currently addressed, through thorough and regular alignment checks of both the phase plate and the microscope, and through judicious choice of acquisition software, necessitating bespoke acquisition routines that take into account the potential for lens hysteresis during data acquisition.

Many applications that may benefit form the extra contrast generated through the use of the VPP, such as the acquisition of FIB/SEM lamellae or of the cell periphery (Mahamid et al. (2016); Grange et al. (2017)), will still be limited by the low numbers of biologically relevant areas for data acquisition in the sample and automation with be unsuitable. However, cases such as those presented in this chapter, in which the sample is relatively diffuse across the surface of the grid would greatly benefit from the routine acquisition of VPP tomographic datasets for downstream sub-tomographic studies. The automation of the VPP offers a potential route for the high resolution determination of molecular structures, where a high number of sub-particles can be acquired from tomograms, with sufficient contrast in X,Y and Z, to produce novel

biological insight that other techniques, such as single particle analysis, cannot.

6

Thesis Summary and Common Themes

The data in this thesis represent an emerging theme in structural and cellular biology, where structural data in isolation, and *in situ*, can be linked to observations made in whole cells and directly related to one another through judicious choice of complementary techniques. Dynamic processes, such as transport of viruses, often do not lend themselves to structural determination using the now more conventional single particle cryoEM type structural techniques due to their transient, large and flexible nature.

Chapter 2 describes a recombinant approach, where a complex system was characterized using a combination of structural and fluorescent techniques producing a model of cytoskeletal transport by the large, 1.4MDa motor, dynein. In chapter 3, I describe an approach to further build on the information from chapter 2, with the aim to visualize dynein transport and viral entry directly in the native environment

of the cell. I describe how the information contained in tomograms obtained *in situ* contain enough information to bridge the "resolution gap" between super-resolution microscopy and electron microscopy. However, the difficulty in localization and imaging specific, relevant biological events currently still limit this approach. Chapter 4 adds another level of complexity to describe a biological process from cellular to atomic level detail, using the aforementioned approaches through the combination of super-resolution microscopy and cryoET. Finally, in Chapter 5, I focus on one of the most promising means for improving the level of detail that can be obtained on a structural level for all of the above approaches. Indeed, the Volta phase plate (VPP) is used with significant increase in contrast to visualise the interaction of the dynein tail complex with adenovirus (Chapter 2).

The use of cryoET to directly view association of the full length dynein motor with adenovirus, combined with SPA of the adenovirus during pH treatment to reveal structural intermediates, allowed me to reveal a putative explanation for how dynein can directly interact with the adenovirus (Chapter 2). The flexibility observed when dynein is bound to the microtubule explains how it remains free to recruit cellular co-factors, such as dynactin or BicD1, as it leaves a large and flexible surface area for binding. Similarly, the observation of multiple dynein motors bound to a single virus enabled us to observe how the large scale recruitment of dynein to viral and endosome cargoes, during transport, may be arranged. The use of TIRF microscopy to image adenovirus recruitment to microtubules further helped to verify the effect of pH on dynein recruitment to adenoviruses, with pH 5 treatment being responsible for a significant switch in low to high propensity for dynein association with aden-

ovirus. Subsequent first attempts towards viewing the dynein motor in complex with cargoes *in situ* (Chapter 3) revealed that although steps need to be taken to increase abundance or specifically target transport events, the high level of detail that can be viewed inside the cell means that in future the characterization of the interaction during transport should be fruitful, provided the correct combination of techniques are used.

An *in situ* approach is described in the case of capsid transport out of the nucleus in the process of herpesvirus nuclear egress (Chapter 4). The complementary information gained through live-cell 3D-SIM, cryoFIB/SEM and cryoET revealed the mechanism and extent of the association of the pUL31/34 nuclear egress complex with the inner nuclear membrane, and its membrane modulating capability. The above methods are costly to implement, and require expertise across a range of highly complex and difficult to implement techniques. Improvements in electron and fluorescence microscopes and their combination into bespoke systems, molecular biology (such as techniques like CRISPR; (Sander and Joung (2014))) and improvement in contrast enhancement technologies, such as better and larger direct detectors or VPPs (Chapter 5), may in the future lead to the correlative EM/FM-based dissection of specifically labelled biological systems, in almost all sub-cellular organelles and in a frozen-hydrated, native state. Combining this with information gained in recombinant systems that reduce the system to minimal components, allows for a comprehensive structural and mechanistic characterization by complementing the structural resolution and dynamics that can be obtained *in situ*.

References

Al-Amoudi A, Chang JJ, Leforestier A, McDowall A, Salamin LM, Norlén LPO, Richter K, Blanc NS, Studer D, Dubochet J (2004) Cryo-electron microscopy of vitreous sections. *The EMBO Journal* 23:3583–3588.

Al-Amoudi A, Díez DC, Betts MJ, Frangakis AS (2007) The molecular architecture of cadherins in native epidermal desmosomes. *Nature* 450:832–837.

Al-Amoudi A, Norlén LPO, Dubochet J (2004) Cryo-electron microscopy of vitreous sections of native biological cells and tissues. *Journal of Structural Biology* 148:131–135.

Al-Amoudi A, Studer D, Dubochet J (2005) Cutting artefacts and cutting process in vitreous sections for cryo-electron microscopy. *Journal of Structural Biology* 150:109–121.

Alushin GM, Lander GC, Kellogg EH, Zhang R, Baker D, Nogales E (2014) High-resolution microtubule structures reveal the structural transitions in $\alpha\beta$-tubulin upon GTP hydrolysis. *Cell* 157:1117–1129.

Amos LA (1989) Brain dynein crossbridges microtubules into bundles. *Journal of cell science* 93 (Pt 1):19–28.

Asano S, Fukuda Y, Beck F, Aufderheide A, Förster F, Danev R, Baumeister W (2015) A molecular census of 26S proteasomes in intact neurons. *Science* 347:439–442.

Asenjo AB, Chatterjee C, Tan DY, DePaoli V, Rice WJ, Diaz-Avalos R, Silvestry M, Sosa H (2013) Structural Model for Tubulin Recognition and Deformation by Kinesin-13 Microtubule Depolymerases. *CellReports* 3:759–768.

Azubel M, Koivisto J, Malola S, Bushnell D, Hura GL, Koh AL, Tsunoyama H, Tsukuda T, Pettersson M, Häkkinen H, Kornberg RD (2014) Nanoparticle imaging. Electron microscopy of gold nanoparticles at atomic resolution. *Science* 345:909–912.

Badde HG, Beimer L (1970) Der Einfluß einer streuenden Phasenplatte auf das elektronenmikroskopische Bild. *Zeitschrift für Naturforschung A* 25:760–765.

Bai XC, Rajendra E, Yang G, Shi Y, Scheres SH (2015) Sampling the conformational space of the catalytic subunit of human γ-secretase. *eLife* 4:1485.

Bartesaghi A, Lecumberry F, Sapiro G, Subramaniam S (2012) Protein secondary structure determination by constrained single-particle cryo-electron tomography. *Structure* 20:2003–2013.

Bartesaghi A, Matthies D, Banerjee S, Merk A, Subramaniam S (2014) Structure of β-galactosidase at 3.2-Å resolution obtained by cryo-electron microscopy.

Proceedings of the National Academy of Sciences of the United States of America 111:11709–11714.

Bartesaghi A, Merk A, Banerjee S, Matthies D, Wu X, Milne JLS, Subramaniam S (2015) 2.2 Å resolution cryo-EM structure of β-galactosidase in complex with a cell-permeant inhibitor. *Science* 348:1147–1151.

Baumeister W (2002) Electron tomography: towards visualizing the molecular organization of the cytoplasm. *Current Opinion in Structural Biology* 12:679–684.

Bewley MC, Springer K, Zhang YB, Freimuth P, Flanagan JM (1999) Structural Analysis of the Mechanism of Adenovirus Binding to Its Human Cellular Receptor, CAR. *Science* 286:1579–1583.

Bharat TAM, Russo CJ, Löwe J, Passmore LA, Scheres SHW (2015) Advances in Single-Particle Electron Cryomicroscopy Structure Determination applied to Subtomogram Averaging. *Structure* 23:1743–1753.

Bigalke JM, Heldwein EE (2015) Structural basis of membrane budding by the nuclear egress complex of herpesviruses. *The EMBO Journal* 34:2921–2936.

Bigalke JM, Heuser T, Nicastro D, Heldwein EE (2014) Membrane deformation and scission by the HSV-1 nuclear egress complex. *Nature Communications* 5:4131.

Boersch H (1947) Über die Kontraste von Atomen im Elektronenmikroskop. *Zeitschrift für Naturforschung A* 2:615.

Bosse JB, Bauerfeind R, Popilka L, Marcinowski L, Taeglich M, Jung C, Striebinger

H, von Einem J, Gaul U, Walther P, Koszinowski UH, Ruzsics Z (2012) A beta-herpesvirus with fluorescent capsids to study transport in living cells. *PLoS ONE* 7:e40585.

Bosse JB, Hogue IB, Feric M, Thiberge SY, Sodeik B, Brangwynne CP, Enquist LW (2015) Remodeling nuclear architecture allows efficient transport of herpesvirus capsids by diffusion. *Proceedings of the National Academy of Sciences of the United States of America* 112:E5725–33.

Bosse JB, Virding S, Thiberge SY, Scherer J, Wodrich H, Ruzsics Z, Koszinowski UH, Enquist LW (2014) Nuclear herpesvirus capsid motility is not dependent on F-actin. *mBio* 5:e01909–14.

Bowman BR, Baker ML, Rixon FJ, Chiu W, Quiocho FA (2003) Structure of the herpesvirus major capsid protein. *The EMBO Journal* 22:757–765.

Brandt F, Carlson LA, Hartl FU, Baumeister W, Grünewald K (2010) The Three-Dimensional Organization of Polyribosomes in Intact Human Cells. *Molecular Cell* 39:560–569.

Bremner KH, Scherer J, Yi J, Vershinin M, Gross SP, Vallee RB (2009) Adenovirus transport via direct interaction of cytoplasmic dynein with the viral capsid hexon subunit. *Cell Host & Microbe* 6:523–535.

Bröcker C, Engelbrecht-Vandré S, Ungermann C (2010) Multisubunit tethering complexes and their role in membrane fusion. *Current Biology* 20:R943–52.

Brown A, Shao S, Murray J, Hegde RS, Ramakrishnan V (2015) Structural basis for stop codon recognition in eukaryotes. *Nature* 524:493–496.

Burgess SA, Walker ML, Sakakibara H, Knight PJ, Oiwa K (2003) Dynein structure and power stroke. *Nature* 421:715–718.

Burke B, Stewart CL (2013) The nuclear lamins: flexibility in function. *Nature reviews. Molecular cell biology* 14:13–24.

Carter AP, Garbarino JE, Wilson-Kubalek EM, Shipley WE, Cho C, Milligan RA, Vale RD, Gibbons IR (2008) Structure and Functional Role of Dynein's Microtubule-Binding Domain. *Science* 322:1691–1695.

Chang YW, Chen S, Tocheva EI, Treuner-Lange A, Löbach S, Søgaard-Andersen L, Jensen GJ (2014) Correlated cryogenic photoactivated localization microscopy and cryo-electron tomography. *Nature Methods* 11:737–739.

Chen BC, Legant WR, Wang K, Shao L, Milkie DE, Davidson MW, Janetopoulos C, Wu XS, Hammer JA, Liu Z, English BP, Mimori-Kiyosue Y, Romero DP, Ritter AT, Lippincott-Schwartz J, Fritz-Laylin L, Mullins RD, Mitchell DM, Bembenek JN, Reymann AC, Böhme R, Grill SW, Wang JT, Seydoux G, Tulu US, Kiehart DP, Betzig E (2014) Lattice light-sheet microscopy: imaging molecules to embryos at high spatiotemporal resolution. *Science* 346:1257998–1257998.

Cheng N, Trus BL, Belnap DM, Newcomb WW, Brown JC, Steven AC (2002) Handedness of the Herpes Simplex Virus Capsid and Procapsid. *Journal of Virology* 76:7855–7859.

Chlanda P, Mekhedov E, Waters H, Schwartz CL, Fischer ER, Ryham RJ, Cohen FS, Blank PS, Zimmerberg J (2016) The hemifusion structure induced by influenza virus haemagglutinin is determined by physical properties of the target membranes. *Nature microbiology* 1:16050.

Chowdhury S, Ketcham SA, Schroer TA, Lander GC (2015) Structural organization of the dynein-dynactin complex bound to microtubules. *Nature Structural and Molecular Biology* 22:345–347.

Chugani DC, Rome LH, Kedersha NL (1993) Evidence that vault ribonucleoprotein particles localize to the nuclear pore complex. *Journal of cell science* 106 (Pt 1):23–29.

Cibulka J, Fraiberk M, Forstova J (2012) Nuclear actin and lamins in viral infections. *Nature* 494:331–335.

Cooper RS, Heldwein EE (2015) Herpesvirus gB: A Finely Tuned Fusion Machine. *Viruses* 7:6552–6569.

Cyrklaff M, Kudryashev M, Leis A, Leonard K, Baumeister W, Menard R, Meissner M, Frischknecht F (2007) Cryoelectron tomography reveals periodic material at the inner side of subpellicular microtubules in apicomplexan parasites. *Journal of Experimental Medicine* 204:1281–1287.

Dai W, Fu C, Raytcheva D, Flanagan J, Khant HA, Liu X, Rochat RH, Haase-Pettingell C, Piret J, Ludtke SJ, Nagayama K, Schmid MF, King JA, Chiu W

(2013) Visualizing virus assembly intermediates inside marine cyanobacteria. *Nature* 502:707–710.

Danev R, Nagayama K (2001) Transmission electron microscopy with Zernike phase plate. *Ultramicroscopy* 88:243–252.

Danev R, Baumeister W (2016) Cryo-EM single particle analysis with the Volta phase plate. *eLife* 5:439.

Danev R, Buijsse B, Khoshouei M, Plitzko JM, Baumeister W (2014) Volta potential phase plate for in-focus phase contrast transmission electron microscopy. *Proceedings of the National Academy of Sciences of the United States of America* 111:15635–15640.

Danev R, Glaeser RM, Nagayama K (2009) Practical factors affecting the performance of a thin-film phase plate for transmission electron microscopy. *Ultramicroscopy* 109:312–325.

Dodding MP, Way M (2011) Coupling viruses to dynein and kinesin-1. *The EMBO Journal* 30:3527–3539.

Dodonova SO, Diestelkoetter-Bachert P, von Appen A, Hagen WJH, Beck R, Beck M, Wieland F, Briggs JAG (2015) A structure of the COPI coat and the role of coat proteins in membrane vesicle assembly. *Science* 349:195–198.

Dohner K, Radtke K, Schmidt S, Sodeik B (2006) Eclipse phase of herpes simplex virus type 1 infection: Efficient dynein-mediated capsid transport without the small capsid protein VP26. *Journal of Virology* 80:8211–8224.

Dubochet J, McDowall AW (1981) Vitrification of pure water for electron microscopy. *Journal of Microscopy* 124:3–4.

Elmlund D, Elmlund H (2015) Cryogenic electron microscopy and single-particle analysis. *Annual Review of Biochemistry* 84:499–517.

Fabry CMS, Rosa-Calatrava M, Moriscot C, Ruigrok RWH, Boulanger P, Schoehn G (2009) The C-Terminal Domains of Adenovirus Serotype 5 Protein IX Assemble into an Antiparallel Structure on the Facets of the Capsid. *Journal of Virology* 83:1135–1139.

Farabella I, Vasishtan D, Joseph AP, Pandurangan AP, Sahota H, Topf M (2015) TEMPy: a Python library for assessment of three-dimensional electron microscopy density fits. *Journal Of Applied Crystallography* 48:1314–1323.

Faruqi AR, Henderson R (2007) Electronic detectors for electron microscopy. *Current Opinion in Structural Biology* 17:549–555.

Faruqi AR, Subramaniam S (2000) CCD detectors in high-resolution biological electron microscopy. *Quarterly Reviews of Biophysics* 33:1–27.

Fernandez IS, Bai Xc, Hussain T, Kelley AC, Lorsch JR, Ramakrishnan V, Scheres SHW (2013) Molecular Architecture of a Eukaryotic Translational Initiation Complex. *Science* 342:1240585–1240585.

Flötenmeyer M, Weiss H, Tribet C, Popot JL, Leonard K (2007) The use of amphipathic polymers for cryo electron microscopy of NADH:ubiquinone oxidoreductase (complex I). *Journal of Microscopy* 227:229–235.

Fujii T, Iwane AH, Yanagida T, Namba K (2010) Direct visualization of secondary structures of F-actin by electron cryomicroscopy. *Nature* .

Fukuda Y, Laugks U, Lučić V, Baumeister W, Danev R (2015) Electron cryotomography of vitrified cells with a Volta phase plate. *Journal of Structural Biology* 190:143–154.

Fukuda Y, Nagayama K (2012) Zernike phase contrast cryo-electron tomography of whole mounted frozen cells. *Journal of Structural Biology* 177:484–489.

Galaz-Montoya JG, Hecksel CW, Baldwin PR, Wang E, Weaver SC, Schmid MF, Ludtke SJ, Chiu W (2016) Alignment algorithms and per-particle CTF correction for single particle cryo-electron tomography. *Journal of Structural Biology* 194:383–394.

Galbraith CG, Galbraith JA (2011) Super-resolution microscopy at a glance. *Journal of cell science* 124:1607–1611.

Garvalov BK, Zuber B, Bouchet-Marquis C, Kudryashev M, Gruska M, Beck M, Leis A, Frischknecht F, Bradke F, Baumeister W, Dubochet J, Cyrklaff M (2006) Luminal particles within cellular microtubules. *The Journal of Cell Biology* 174:759–765.

Grange M, Vasishtan D, Grünewald K (2017) Cellular electron cryo tomography and in situ sub-volume averaging reveal the context of microtubule-based processes. *Journal of Structural Biology* 197:181–190.

Grant T, Grigorieff N, Sundquist WI (2015) Measuring the optimal exposure for single particle cryo-EM using a 2.6 Å reconstruction of rotavirus VP6. *eLife* 4:e06980.

Grünewald K, Desai P, Winkler DC, Heymann JB, Belnap DM, Baumeister W, Steven AC (2003) Three-dimensional structure of herpes simplex virus from cryo-electron tomography. *Science* 302:1396–1398.

Gustafsson MGL (2000) Surpassing the lateral resolution limit by a factor of two using structured illumination microscopy. *Journal of Microscopy* 198:82–87.

Gustafsson MGL, Shao L, Carlton PM, Wang CJR, Golubovskaya IN, Cande WZ, Agard DA, Sedat JW (2008) Three-dimensional resolution doubling in wide-field fluorescence microscopy by structured illumination. *Biophysical Journal* 94:4957–4970.

Hackney DD (1996) The kinetic cycles of myosin, kinesin, and dynein. *Annual review of physiology* 58:731–750.

Hagen C, Dent KC, Zeev-Ben-Mordehai T, Grange M, Bosse JB, Whittle C, Klupp BG, Siebert CA, Vasishtan D, Bäuerlein FJB, Cheleski J, Werner S, Guttmann P, Rehbein S, Henzler K, Demmerle J, Adler B, Koszinowski U, Schermelleh L, Schneider G, Enquist LW, Plitzko JM, Mettenleiter TC, Grünewald K (2015) Structural Basis of Vesicle Formation at the Inner Nuclear Membrane. *Cell* 163:1692–1701.

Hagen C, Guttmann P, Klupp B, Werner S, Rehbein S, Mettenleiter TC, Schneider G, Grünewald K (2012) Correlative VIS-fluorescence and soft X-ray cryo-microscopy/tomography of adherent cells. *Journal of Structural Biology* 177:193–201.

Hagen WJH, Wan W, Briggs JAG (2017) Implementation of a cryo-electron tomog-

raphy tilt-scheme optimized for high resolution subtomogram averaging. *Journal of Structural Biology* 197:191–198.

Harapin J, Börmel M, Sapra KT, Brunner D, Kaech A, Medalia O (2015) Structural analysis of multicellular organisms with cryo-electron tomography. *Nature Methods* 12:634–636.

Hatch E, Hetzer M (2014) Breaching the nuclear envelope in development and disease. *Journal Of Cell Biology* 205:133–141.

Heldwein EE, Lou H, Bender FC, Cohen GH, Eisenberg RJ, Harrison SC (2006) Crystal structure of glycoprotein B from herpes simplex virus 1. *Science* 313:217–220.

Hellberg T, Paßvogel L, Schulz KS, Klupp BG, Mettenleiter TC (2016) Nuclear Egress of Herpesviruses: The Prototypic Vesicular Nucleocytoplasmic Transport. *Advances in virus research* 94:81–140.

Herrmann H, Bär H, Kreplak L, Strelkov SV, Aebi U (2007) Intermediate filaments: from cell architecture to nanomechanics. *Nature reviews. Molecular cell biology* 8:562–573.

Heymann JB (2001) Bsoft: image and molecular processing in electron microscopy. *Journal of Structural Biology* 133:156–169.

Hoyer P, de Medeiros G, Balázs B, Norlin N, Besir C, Hanne J, Kräusslich HG, Engelhardt J, Sahl SJ, Hell SW, Hufnagel L (2016) Breaking the diffraction limit of light-sheet fluorescence microscopy by RESOLFT. *Proceedings of the National Academy of Sciences of the United States of America* 113:3442–3446.

Iancu CV, Wright ER, Benjamin J, Tivol WF, Dias DP, Murphy GE, Morrison RC, Heymann JB, Jensen GJ (2005) A "flip–flop" rotation stage for routine dual-axis electron cryotomography. *Journal of Structural Biology* 151:288–297.

Ibiricu I, Huiskonen JT, Dohner K, Bradke F, Sodeik B, Grünewald K (2011) Cryo Electron Tomography of Herpes Simplex Virus during Axonal Transport and Secondary Envelopment in Primary Neurons. *PLoS Pathogens* 7:e1002406.

Ibiricu I, Maurer UE, Grünewald K (2013) Characterization of herpes simplex virus type 1 L-particle assembly and egress in hippocampal neurones by electron cryotomography. *Cellular Microbiology* 15:285–291.

Ilca SL, Kotecha A, Sun X, Poranen MM, Stuart DI, Huiskonen JT (2015) Localized reconstruction of subunits from electron cryomicroscopy images of macromolecular complexes. *Nature Communications* 6:8843.

Imai H, Narita A, Maéda Y, Schroer TA (2014) Dynactin 3D structure: implications for assembly and dynein binding. *Journal of molecular biology* 426:3262–3271.

Imai H, Shima T, Sutoh K, Walker ML, Knight PJ, Kon T, Burgess SA (2015) Direct observation shows superposition and large scale flexibility within cytoplasmic dynein motors moving along microtubules. *Nature Communications* 6:8179.

Jokhi V, Ashley J, Nunnari J, Noma A, Ito N, Wakabayashi-Ito N, Moore MJ, Budnik V (2013) Torsin Mediates Primary Envelopment of Large Ribonucleoprotein Granules at the Nuclear Envelope. *CellReports* 3:988–995.

Kanaya K, Kawakatsu H, Itō K, Yotsumoto H (1958) Experiment on the Electron Phase Microscope. *Journal of Applied Physics* 29:1046.

Kardon JR, Vale RD (2009) Regulators of the cytoplasmic dynein motor. *Nature reviews. Molecular cell biology* 10:854–865.

Kaufmann R, Schellenberger P, Seiradake E, Dobbie IM, Jones EY, Davis I, Hagen C, Grünewald K (2014) Super-resolution microscopy using standard fluorescent proteins in intact cells under cryo-conditions. *Nano Letters* 14:4171–4175.

Khoshouei M, Pfeffer S, Baumeister W, Förster F, Danev R (2017) Subtomogram analysis using the Volta phase plate. *Journal of Structural Biology* 197:94–101.

Khoshouei M, Radjainia M, Phillips AJ, Gerrard JA, Mitra AK, Plitzko JM, Baumeister W, Danev R (2016) Volta phase plate cryo-EM of the small protein complex Prx3. *Nature Communications* 7:10534.

Klupp BG, Granzow H, Fuchs W, Keil GM, Finke S, Mettenleiter TC (2007) Vesicle formation from the nuclear membrane is induced by coexpression of two conserved herpesvirus proteins. *Proceedings of the National Academy of Sciences* 104:7241–7246.

Kollman JM, Greenberg CH, Li S, Moritz M, Zelter A, Fong KK, Fernandez JJ, Sali A, Kilmartin J, Davis TN, Agard DA (2015) Ring closure activates yeast γTuRC for species-specific microtubule nucleation. *Nature Structural and Molecular Biology* 22:132–137.

Kollman JM, Polka JK, Zelter A, Davis TN, Agard DA (2010) Microtubule nucleating gamma-TuSC assembles structures with 13-fold microtubule-like symmetry. *Nature* 466:879–882.

Kon T, Oyama T, Shimo-Kon R, Imamula K, Shima T, Sutoh K, Kurisu G (2012) The 2.8Å crystal structure of the dynein motor domain. *Nature* 484:345–350.

Koning RI, Zovko S, Bárcena M, Oostergetel GT, Koerten HK, Galjart N, Koster AJ, Mieke Mommaas A (2008) Cryo electron tomography of vitrified fibroblasts: microtubule plus ends in situ. *Journal of Structural Biology* 161:459–468.

Koster AJ, Grimm R, Typke D, Hegerl R (1997) Perspectives of molecular and cellular electron tomography. *Journal of Structural Biology* 120:276–308.

Kremer JR, Mastronarde DN, McIntosh JR (1996) Computer visualization of three-dimensional image data using IMOD. *Journal of Structural Biology* 116:71–76.

Le Sage V, Mouland A (2013) Viral Subversion of the Nuclear Pore Complex. *Viruses* 5:2019–2042.

Lehmann M, Milev MP, Abrahamyan L, Yao XJ, Pante N, Mouland AJ (2009) Intracellular transport of human immunodeficiency virus type 1 genomic RNA and viral production are dependent on dynein motor function and late endosome positioning. *The Journal of biological chemistry* 284:14572–14585.

Leigh KE, Sharma M, Mansueto MS, Boeszoermenyi A, Filman DJ, Hogle JM, Wagner G, Coen DM, Arthanari H (2015) Structure of a herpesvirus nuclear egress

complex subunit reveals an interaction groove that is essential for viral replication. *Proceedings of the National Academy of Sciences of the United States of America* 112:9010–9015.

Li D, Betzig E (2016) Response to Comment on "Extended-resolution structured illumination imaging of endocytic and cytoskeletal dynamics". *Science* 352:527–527.

Li X, Mooney P, Zheng S, Booth CR, Braunfeld MB, Gubbens S, Agard DA, Cheng Y (2013) Electron counting and beam-induced motion correction enable near-atomic-resolution single-particle cryo-EM. *Nature Methods* 10:584–590.

Liao M, Cao E, Julius D, Cheng Y (2013) Structure of the TRPV1 ion channel determined by electron cryo-microscopy. *Nature* 504:107–112.

Liu B, Xue Y, Zhao W, Chen Y, Fan C, Gu L, Zhang Y, Zhang X, Sun L, Huang X, Ding W, Sun F, Ji W, Xu T (2015) Three-dimensional super-resolution protein localization correlated with vitrified cellular context. *Scientific Reports* 5:13017.

Liu HR, Jin L, Koh SBS, Atanasov I, Schein S, Wu L, Zhou ZH (2010) Atomic Structure of Human Adenovirus by Cryo-EM Reveals Interactions Among Protein Networks. *Science* 329:1038–1043.

Lorenz M, Vollmer B, Unsay JD, Klupp BG, García-Sáez AJ, Mettenleiter TC, Antonin W (2015) A single herpesvirus protein can mediate vesicle formation in the nuclear envelope. *Journal of Biological Chemistry* 290:6962–6974.

Lye MF, Sharma M, El Omari K, Filman DJ, Schuermann JP, Hogle JM, Coen

DM (2015) Unexpected features and mechanism of heterodimer formation of a herpesvirus nuclear egress complex. *The EMBO Journal* 34:2937–2952.

Mahamid J, Pfeffer S, Schaffer M, Villa E, Danev R, Cuellar LK, Förster F, Hyman Aa, Plitzko JM, Baumeister W (2016) Visualizing the molecular sociology at the HeLa cell nuclear periphery. *Science* 351:969–972.

Malhas A, Goulbourne C, Vaux DJ (2011) The nucleoplasmic reticulum: form and function. *Trends in Cell Biology* 21:362–373.

Mallik R, Gross SP (2004) Molecular motors: strategies to get along. *Current biology : CB* 14:R971–82.

Mallik R, Rai AK, Barak P, Rai A, Kunwar A (2013) Teamwork in microtubule motors. *Trends in Cell Biology* 23:575–582.

Marko M, Hsieh C, Schalek R, Frank J, Mannella C (2007) Focused-ion-beam thinning of frozen-hydrated biological specimens for cryo-electron microscopy. *Nature Methods* 4:215–217.

Martin-Fernandez M, Longshaw SV, Kirby I, Santis G, Tobin MJ, Clarke DT, Jones GR (2004) Adenovirus type-5 entry and disassembly followed in living cells by FRET, fluorescence anisotropy, and FLIM. *Biophysical Journal* 87:1316–1327.

Martinez R, Schellenberger P, Vasishtan D, Aknin C, Austin S, Dacheux D, Rayne F, Siebert A, Ruzsics Z, Gruenewald K, Wodrich H (2015) The amphipathic helix of adenovirus capsid protein VI contributes to penton release and postentry sorting. *Journal of Virology* 89:2121–2135.

Mastronarde DN (1997) Dual-Axis Tomography: An Approach with Alignment Methods That Preserve Resolution. *Journal of Structural Biology* 120:1–10.

Mastronarde DN (2005) Automated electron microscope tomography using robust prediction of specimen movements. *Journal of Structural Biology* 152:36–51.

Matthies D, Dalmas O, Borgnia MJ, Dominik PK, Merk A, Rao P, Reddy BG, Islam S, Bartesaghi A, Perozo E, Subramaniam S (2016) Cryo-EM Structures of the Magnesium Channel CorA Reveal Symmetry Break upon Gating. *Cell* 164:747–756.

Maurer UE, Zeev-Ben-Mordehai T, Pandurangan AP, Cairns TM, Hannah BP, Whitbeck JC, Eisenberg RJ, Cohen GH, Topf M, Huiskonen JT, Grunewald K (2013) The Structure of Herpesvirus Fusion Glycoprotein B-Bilayer Complex Reveals the Protein-Membrane and Lateral Protein-Protein Interaction. *Structure/Folding and Design* 21:1396–1405.

Maurer UE, Sodeik B, Grünewald K (2008) Native 3D intermediates of membrane fusion in herpes simplex virus 1 entry. *Proceedings of the National Academy of Sciences of the United States of America* 105:10559–10564.

McEwen BF, Marko M (2001) The emergence of electron tomography as an important tool for investigating cellular ultrastructure. *Journal of Histochemistry and Cytochemistry* 49:553–564.

McKenney RJ, Huynh W, Tanenbaum ME, Bhabha G, Vale RD (2014) Activation of cytoplasmic dynein motility by dynactin-cargo adapter complexes. *Science* 345:337–341.

McMullan G, Faruqi AR, Clare D, Henderson R (2014) Comparison of optimal performance at 300keV of three direct electron detectors for use in low dose electron microscopy. *Ultramicroscopy* 147:156–163.

Mettenleiter TC, Klupp BG, Granzow H (2009) Herpesvirus assembly: an update. *Virus research* 143:222–234.

Mettenleiter TC (2004) Budding events in herpesvirus morphogenesis. *Virus research* 106:167–180.

Mettenleiter TC, Klupp BG, Granzow H (2006) Herpesvirus assembly: a tale of two membranes. *Current opinion in microbiology* 9:1–7.

Mizuno N, Narita A, Kon T, Sutoh K, Kikkawa M (2007) Three-dimensional structure of cytoplasmic dynein bound to microtubules. *Proceedings of the National Academy of Sciences of the United States of America* 104:20832–20837.

Murata K, Liu XA, Danev R, Jakana J, Schmid MF, King J, Nagayama K, Chiu W (2010) Zernike Phase Contrast Cryo-Electron Microscopy and Tomography for Structure Determination at Nanometer and Subnanometer Resolutions. *Structure/Folding and Design* 18:903–912.

Nagayama K (2011) Another 60 years in electron microscopy: development of phase-plate electron microscopy and biological applications. *Journal of electron microscopy* 60 Suppl 1:S43–62.

Nagerl UV, Willig KI, Hein B, Hell SW, Bonhoeffer T (2008) Live-cell imaging of

dendritic spines by STED microscopy. *Proceedings of the National Academy of Sciences* 105:18982–18987.

Narayan K, Subramaniam S (2015) Focused ion beams in biology. *Nature Methods* 12:1021–1031.

Nguyen THD, Galej WP, Bai Xc, Savva CG, Newman AJ, Scheres SHW, Nagai K (2015) The architecture of the spliceosomal U4/U6.U5 tri-snRNP. *Nature* 523:47—-.

Nicastro D, Schwartz C, Pierson J, Gaudette R, Porter ME, McIntosh JR (2006) The molecular architecture of axonemes revealed by cryoelectron tomography. *Science* 313:944–948.

Nogales E (2015) The development of cryo-EM into a mainstream structural biology technique. *Nature Methods* 13:24–27.

Pante N, Kann M (2002) Nuclear pore complex is able to transport macromolecules with diameters of about 39 nm. *Molecular Biology of the Cell* 13:425–434.

Pasdeloup D, Blondel D, Isidro AL, Rixon FJ (2009) Herpesvirus Capsid Association with the Nuclear Pore Complex and Viral DNA Release Involve the Nucleoporin CAN/Nup214 and the Capsid Protein pUL25. *Journal of Virology* 83:6610–6623.

Pasdeloup D, McElwee M, Beilstein F, Labetoulle M, Rixon FJ (2013) Herpesvirus Tegument Protein pUL37 Interacts with Dystonin/BPAG1 To Promote Capsid Transport on Microtubules during Egress. *Journal of Virology* 87:2857–2867.

Pérez-Berná AJ, Marabini R, Scheres SHW, Menéndez-Conejero R, Dmitriev IP,

Curiel DT, Mangel WF, Flint SJ, San Martín C (2009) Structure and uncoating of immature adenovirus. *Journal of molecular biology* 392:547–557.

Pérez-Berná AJ, Ortega-Esteban A, Menéndez-Conejero R, Winkler DC, Menéndez M, Steven AC, Flint SJ, de Pablo PJ, San Martín C (2012) The role of capsid maturation on adenovirus priming for sequential uncoating. *Journal of Biological Chemistry* 287:31582–31595.

Pettersen EF, Goddard TD, Huang CC, Couch GS, Greenblatt DM, Meng EC, Ferrin TE (2004) UCSF Chimera–a visualization system for exploratory research and analysis. *Journal Of Computational Chemistry* 25:1605–1612.

Pfeffer S, Woellhaf MW, Herrmann JM, Forster F (2015) Organization of the mitochondrial translation machinery studied in situ by cryoelectron tomography. *Nature Communications* 6:8.

Pitts JD, Klabis J, Richards AL, Smith GA, Heldwein EE (2014) Crystal structure of the herpesvirus inner tegument protein UL37 supports its essential role in control of viral trafficking. *Journal of Virology* 88:5462–5473.

Plitzko JM, Frangakis AS, Nickell S, Förster F, Gross A, Baumeister W (2002) In vivo veritas: electron cryotomography of cells. *Trends in biotechnology* 20:S40–S44.

Radermacher M, Wagenknecht T, Verschoor A, Frank J (1986) A new 3-D reconstruction scheme applied to the 50S ribosomal subunit of E. coli. *Journal of Microscopy* 141:RP1–2.

Radermacher M, Wagenknecht T, Verschoor A, Frank J (1987) Three-dimensional structure of the large ribosomal subunit from Escherichia coli. *The EMBO Journal* 6:1107–1114.

Radtke K, Kieneke D, Wolfstein A, Michael K, Steffen W, Scholz T, Karger A, Sodeik B (2010) Plus- and minus-end directed microtubule motors bind simultaneously to herpes simplex virus capsids using different inner tegument structures. *PLoS Pathogens* 6:e1000991.

Rai A, Pathak D, Thakur S, Singh S, Dubey AK, Mallik R (2016) Dynein Clusters into Lipid Microdomains on Phagosomes to Drive Rapid Transport toward Lysosomes. *Cell* 164:722–734.

Reddy VS, Nemerow GR (2014) Structures and organization of adenovirus cement proteins provide insights into the role of capsid maturation in virus entry and infection. *Proceedings of the National Academy of Sciences of the United States of America* 111:11715–11720.

Rexroad J, Martin TT, McNeilly D, Godwin S, Middaugh CR (2006) Thermal stability of adenovirus type 2 as a function of pH. *Journal Of Pharmaceutical Sciences* 95:1469–1479.

Reyntjens S, Puers R (2001) A review of focused ion beam applications in microsystem technology. *Journal of Micromechanics and Microengineering* 11:287–300.

Rigort A, Bäuerlein FJB, Villa E, Eibauer M, Laugks T, Baumeister W, Plitzko JM (2012) Focused ion beam micromachining of eukaryotic cells for cryoelectron

tomography. *Proceedings of the National Academy of Sciences of the United States of America* 109:4449–4454.

Roberts AJ, Numata N, Walker ML, Kato YS, Malkova B, Kon T, Ohkura R, Arisaka F, Knight PJ, Sutoh K, Burgess SA (2009) AAA+ Ring and linker swing mechanism in the dynein motor. *Cell* 136:485–495.

Rohou A, Grigorieff N (2015) CTFFIND4: Fast and accurate defocus estimation from electron micrographs. *Journal of Structural Biology* 192:216–221.

Russell WC, Valentine RC, Pereira HG (1967) The effect of heat on the anatomy of the adenovirus. *Journal of General Virology* 1:509–522.

Russo CJ, Passmore LA (2014) Ultrastable gold substrates for electron cryomicroscopy. *Science* 346:1377–1380.

Sahl SJ, Balzarotti F, Keller-Findeisen J, Leutenegger M, Westphal V, Egner A, Lavoie-Cardinal F, Chmyrov A, Grotjohann T, Jakobs S (2016) Comment on "Extended-resolution structured illumination imaging of endocytic and cytoskeletal dynamics". *Science* 352:527–527.

Sander JD, Joung JK (2014) CRISPR-Cas systems for editing, regulating and targeting genomes. *Nature biotechnology* 32:347–355.

Schellenberger P, Kaufmann R, Siebert CA, Hagen C, Wodrich H, Grünewald K (2014) High-precision correlative fluorescence and electron cryo microscopy using two independent alignment markers. *Ultramicroscopy* 143:41–51.

Scherer J, Vallee RB (2015) Conformational changes in the adenovirus hexon subunit responsible for regulating cytoplasmic dynein recruitment. *Journal of Virology* 89:1013–1023.

Scherer J, Yi J, Vallee RB (2014) PKA-dependent dynein switching from lysosomes to adenovirus: A novel form of host-virus competition. *The Journal of Cell Biology* 205:163–177.

Scheres SHW (2012) RELION: Implementation of a Bayesian approach to cryo-EM structure determination. *Journal of Structural Biology* 180:519–530.

Schermelleh L, Carlton PM, Haase S, Shao L, Winoto L, Kner P, Burke B, Cardoso MC, Agard DA, Gustafsson MGL, Leonhardt H, Sedat JW (2008) Subdiffraction multicolor imaging of the nuclear periphery with 3D structured illumination microscopy. *Science* 320:1332–1336.

Schermelleh L, Heintzmann R, Leonhardt H (2010) A guide to super-resolution fluorescence microscopy. *Journal Of Cell Biology* 190:165–175.

Scherzer O (1949) The Theoretical Resolution Limit of the Electron Microscope. *Journal of Applied Physics* 20:20–29.

Schindelin J, Arganda-Carreras I, Frise E, Kaynig V, Longair M, Pietzsch T, Preibisch S, Rueden C, Saalfeld S, Schmid B, Tinevez JY, White DJ, Hartenstein V, Eliceiri K, Tomancak P, Cardona A (2012) Fiji: an open-source platform for biological-image analysis. *Nature Methods* 9:676–682.

Schlager MA, Hoang HT, Urnavicius L, Bullock SL, Carter AP (2014) In vitro reconstitution of a highly processive recombinant human dynein complex. *The EMBO Journal* 33:1855–1868.

Schmidt H, Gleave ES, Carter AP (2012) Insights into dynein motor domain function from a 3.3-Å crystal structure. *Nature Structural and Molecular Biology* 19:492–7– S1.

Schmidt H, Zalyte R, Urnavicius L, Carter AP (2014) Structure of human cytoplasmic dynein-2 primed for its power stroke. *Nature* 518:435–438.

Schorb M, Briggs JAG (2014) Correlated cryo-fluorescence and cryo-electron microscopy with high spatial precision and improved sensitivity. *Ultramicroscopy* 143:24–32.

Schroeder CM, Ostrem JML, Hertz NT, Vale RD (2014) A Ras-like domain in the light intermediate chain bridges the dynein motor to a cargo-binding region. *eLife* 3:e03351.

Schroeder CM, Vale RD (2016) Assembly and activation of dynein-dynactin by the cargo adaptor protein Hook3. *Journal Of Cell Biology* 214:309–318.

Schroer TA (2004) Dynactin. *Annual review of cell and developmental biology* 20:759–779.

Schur FKM, Hagen WJH, Rumlová M, Ruml T, Müller B, Kräusslich HG, Briggs JAG (2015) Structure of the immature HIV-1 capsid in intact virus particles at 8.8 A resolution. *Nature* 517:505–508.

Schur FKM, Obr M, Hagen WJH, Wan W, Jakobi AJ, Kirkpatrick JM, Sachse C, Kräusslich HG, Briggs JAG (2016) An atomic model of HIV-1 capsid-SP1 reveals structures regulating assembly and maturation. *Science* 353:506–508.

Shang Z, Zhou K, Xu C, Csencsits R, Cochran JC, Sindelar CV, Hyman Aa (2014) High-resolution structures of kinesin on microtubules provide a basis for nucleotide-gated force-generation. *eLife* 3:e04686.

Sharp TH, Faas FGA, Koster AJ, Gros P (2017) Imaging complement by phase-plate cryo-electron tomography from initiation to pore formation. *Journal of Structural Biology* 197:155–162.

Shiue J, Chang CS, Huang SH, Hsu CH, Tsai JS, Chang WH, Wu YM, Lin YC, Kuo PC, Huang YS, Hwu Y, Kai JJ, Tseng FG, Chen FR (2009) Phase TEM for biological imaging utilizing a Boersch electrostatic phase plate: theory and practice. *Journal of electron microscopy* 58:137–145.

Sirohi D, Chen Z, Sun L, Klose T, Pierson TC, Rossmann MG, Kuhn RJ (2016) The 3.8 Å resolution cryo-EM structure of Zika virus. *Science* 352:467–470.

Speese SD, Ashley J, Jokhi V, Nunnari J, Barria R, Li Y, Ataman B, Koon A, Chang YT, Li Q, Moore MJ, Budnik V (2012) Nuclear envelope budding enables large ribonucleoprotein particle export during synaptic Wnt signaling. *Cell* 149:832–846.

Stokes GG (1852) On the Change of Refrangibility of Light. *Philosophical Transactions of the Royal Society of London* 142:463–562.

Strauss MP, Liew ATF, Turnbull L, Whitchurch CB, Monahan LG, Harry EJ (2012) 3D-SIM Super Resolution Microscopy Reveals a Bead-Like Arrangement for FtsZ and the Division Machinery: Implications for Triggering Cytokinesis. *PLoS Biology* 10:e1001389.

Strunze S, Engelke MF, Wang IH, Puntener D, Boucke K, Schleich S, Way M, Schoenenberger P, Burckhardt CJ, Greber UF (2011) Kinesin-1-mediated capsid disassembly and disruption of the nuclear pore complex promote virus infection. *Cell Host & Microbe* 10:210–223.

Sundquist WI, Kräusslich HG (2012) HIV-1 Assembly, Budding, and Maturation. *Cold Spring Harbor Perspectives in Medicine* 2:a006924–a006924.

Tang G, Peng L, Baldwin PR, Mann DS, Jiang W, Rees I, Ludtke SJ (2007) EMAN2: an extensible image processing suite for electron microscopy. *Journal of Structural Biology* 157:38–46.

Taylor KA, Glaeser RM (1974) Electron Diffraction of Frozen, Hydrated Protein Crystals. *Science* 186:1036–1037.

Tsien RY (1998) The green fluorescent protein. *Annual Review of Biochemistry* 67:509–544.

Unwin PN (1971) Phase contrast and interference microscopy with the electron microscope. *Philosophical Transactions of the Royal Society B: Biological Sciences* 261:95–104.

Unwin PNT (1970) An Electrostatic Phase Plate for the Electron Microscope. *Berichte der Bunsengesellschaft für physikalische Chemie* 74:1137–1141.

Urnavicius L, Zhang K, Diamant AG, Motz C, Schlager MA, Yu M, Patel NA, Robinson CV, Carter AP (2015) The structure of the dynactin complex and its interaction with dynein. *Science* 347:1441–1446.

Villinger C, Neusser G, Kranz C, Walther P, Mertens T (2015) 3D Analysis of HCMV Induced-Nuclear Membrane Structures by FIB/SEM Tomography: Insight into an Unprecedented Membrane Morphology. *Viruses* 7:5686–5704.

Walzer SA, Egerer-Sieber C, Sticht H, Sevvana M, Hohl K, Milbradt J, Muller YA, Marschall M (2015) Crystal Structure of the Human Cytomegalovirus pUL50-pUL53 Core Nuclear Egress Complex Provides Insight into a Unique Assembly Scaffold for Virus-Host Protein Interactions. *Journal of Biological Chemistry* 290:27452–27458.

Westphal V, Rizzoli SO, Lauterbach MA, Kamin D, Jahn R, Hell SW (2008) Video-rate far-field optical nanoscopy dissects synaptic vesicle movement. *Science* 320:246–249.

Whyte JRC, Munro S (2002) Vesicle tethering complexes in membrane traffic. *Journal of cell science* 115:2627–2637.

Wickham TJ, Mathias P, Cheresh DA, Nemerow GR (1993) Integrins αvβ3 and αvβ5 promote adenovirus internalization but not virus attachment. *Cell* 73:309–319.

Wodrich H, Henaff D, Jammart B, Segura-Morales C, Seelmeir S, Coux O, Ruzsics Z, Wiethoff CM, Kremer EJ (2010) A capsid-encoded PPxY-motif facilitates adenovirus entry. *PLoS Pathogens* 6:e1000808.

Woehlke G, Ruby AK, Hart CL, Ly B, Hom-Booher N, Vale RD (1997) Microtubule interaction site of the kinesin motor. *Cell* 90:207–216.

Wolff G, Hagen C, Grünewald K, Kaufmann R (2016) Towards correlative superresolution fluorescence and electron cryo-microscopy. *Biology of the Cell* .

Woodward CL, Mendonça LM, Jensen GJ (2015) Direct visualization of vaults within intact cells by electron cryo-tomography. *Cellular and molecular life sciences : CMLS* 72:3401–3409.

Xiong Q, Morphew MK, Schwartz CL, Hoenger AH, Mastronarde DN (2009) CTF determination and correction for low dose tomographic tilt series. *Journal of Structural Biology* 168:378–387.

Xu K, Zhong G, Zhuang X (2013) Actin, spectrin, and associated proteins form a periodic cytoskeletal structure in axons. *Science* 339:452–456.

Zaichick SV, Bohannon KP, Hughes A, Sollars PJ, Pickard GE, Smith GA (2013) The herpesvirus VP1/2 protein is an effector of dynein-mediated capsid transport and neuroinvasion. *Cell Host & Microbe* 13:193–203.

Zeev-Ben-Mordehai T, Hagen C, Grünewald K (2014) A cool hybrid approach to the herpesvirus 'life' cycle. *Current Opinion in Virology* 5:42–49.

Zeev-Ben-Mordehai T, Vasishtan D, Hernández Durán A, Vollmer B, White P, Prasad Pandurangan A, Siebert CA, Topf M, Grünewald K (2016) Two distinct trimeric conformations of natively membrane-anchored full-length herpes simplex virus 1 glycoprotein B. *Proceedings of the National Academy of Sciences of the United States of America* 113:4176–4181.

Zeev-Ben-Mordehai T, Vasishtan D, Siebert CA, Grünewald K (2014) The full-length cell–cell fusogen EFF-1 is monomeric and upright on the membrane. *Nature Communications* 5.

Zeev-Ben-Mordehai T, Weberruß M, Lorenz M, Cheleski J, Hellberg T, Whittle C, El Omari K, Vasishtan D, Dent KC, Harlos K, Franzke K, Hagen C, Klupp BG, Antonin W, Mettenleiter TC, Grünewald K (2015) Crystal Structure of the Herpesvirus Nuclear Egress Complex Provides Insights into Inner Nuclear Membrane Remodeling. *CellReports* 13:2645–2652.

Zernike F (1942) Phase contrast, a new method for the microscopic observation of transparent objects. *Physica* 9:686–698.

Appendix A

Extended Methods

A.1 HSV1 purification and capsid isolation protocol

Baby Hamster Kidney (BHK) cells were seeded from a single confluent 175 cm^2 flask and cultured to 80-90% confluency in 11x175 cm2 tissue culture flasks. Once at this desired confluency, one flask was used to determine the mean cell count using a Neubauer chamber. Cells were washed with 17 ml 1xPBS, which was aspirated and 5 ml 0.1% Trypsin added to detach cells from the flask. The cells were resuspended in 25 ml 10% FBS-MEM. 10µl was placed into each side of the Neubauer chamber and the cells counted on each side. The average value of cells was taken.

The cell number was calculated thus:

$$Cells/Flask = cells \times 10^4 \times volume$$

The number of cells was then used to calculate the plaque forming units (PFU) of HSV1 needed to produce a multiplicity of infection (MOI) of 0.01 PFU/cell:

$$PFU_{total} = cellcount \times MOI$$

where volume per ml (V[ml]) = $\mathrm{PFU_{total}}$/titer.

The calculated volume of virus required to produce an infection with a MOI of 0.01 was added to 50 ml CO2-independent medium + 0.1% BSA (5 ml per flask). Each remaining flask was then washed with 17.5 ml 1xPBS and inoculated with 5 ml of inoculum for 1hr at room temperature on a rocking platform to prevent an uneven infection across the flasks. After 1hr, 20 ml 5%FCS-MEM was added to each flask and cells incubated at 37°C/5% CO2.

Cellular morphology was monitored during the infection. At a point at which the BHK cells had begun to round up from the flask, but before the majority of cells had detached, the cells were harvested. The desired morphology of the cells arose at around 29 hours post-infection. The supernatant from each flask was collected and centrifuged at 4000rpm for 20mins at 4°C in a JLA 10.500 rotor. The supernatant from this was then further centrifuged for 120mins at 4°C at 10000rpm in a JLA10.5000 rotor (18000g). The pellets produced at this stage were treated delicately, so as to prevent lysis of virions. The virions were not allowed to dry and were resuspended very slowly in 1.5-2 ml 20 mM MES, 200 mM KCl, 20 mM Tris; pH 7.2 (MKT Buffer) and allowed to swell overnight. The pellets were then resuspended via pipette and loaded onto a 20-40% nycodenz gradient. This was centrifuged at

20000rpm and the bands observed via light-scattering collected, aliquoted and snap frozen in liquid nitrogen. The samples were then stored at -80°C

Capsid Isolation:

Material:

1. MKT-buffer: 20 mM MES, 100 mM KCl, 30 mM Tris pH 7,4 in filtered water
2. 2x lysis-buffer (2% TX-100 in 2x MKT, pH 7,4) with 200, 1000, 2000 mM KCl
3. 20% sucrose (w/v) in MKT with 100, 500, 1000 mM KCl
4. 1 M DTT stock
5. 10 mg/ml DNase II in PBS
6. 10 mg/ml RNase in PBS
7. 10 mg/ml BSA in MKT (for blocking centrifuge tube-surface)
8. BRB80: 80 mM PIPES, 1 mM EGTA, 2 mM MgCl2; pH 6,8 with KOH (S2 fridge)
9. CBB or Acetate-buffer: 100 mM potassium acetate, 3 mM magnesium acetate, 5 mM EGTA, 10 mM HEPES +/- 5% (w/v) Sucrose; pH 7,4 with KOH
10. 1 M MgCl2 stock
11. Protease inhibitors (PIs): 500x AEL, 500x ABP, 250x PMSF (in methanol)

HSV1 virion aliquots produced as described above (ca. 5 *109 pfu/ml) were resuspended in an equal volume 2x lysis buffer with either 200, 1000 or 2000 mM KCl,

protease inhibitors (PI) and 10 mM DTT and then incubated at 30 min for 4°C. Prior blocking of centrifuge tubes was also done using 10 mg/ml BSA by incubating 10 min at RT. After 30mins, the capsids were sonicated in a water bath for 3-4 short pulses).

The sonicated capsids were then centrifuged through a 5 ml 20% sucrose cushion with respective KCl-concentration and 10 mM DTT in a SW 50.1 rotor for 30 min, at 30.000 rpm and 4°C. The pellets were resuspended in 200 µl BRB80 with 10 mM DTT, 10 mM MgCl2 and PIs. The capsids were then incubated on ice at 4°C to soften pellet and 100 µg/ml RNase & DNase added. In order to allow the RNase and DNase to work efficiently, the capsids were incubated at 37°C for 30 minutes and then sedimented in an ultracentrifuge, Rotor A-100-30, 77.500 rpm, 8 min, 4°C (or SW 50.1 with adapters, 30.000 rpm, 8 min, 4°C). Capsids were then resuspended in 70 µl CBB with PIs by incubating for 2 h at 4°C (to soften pellet) and sonicating (4 short pulses).

A.2 FSC curves for SPA experiments performed in Chapter 2

See Figure A.1 for comparison of the pH 7, pH 5, ΔpIX and NHC-bound adenovirus discussed in Chapter 2, and their respective FSC curves.

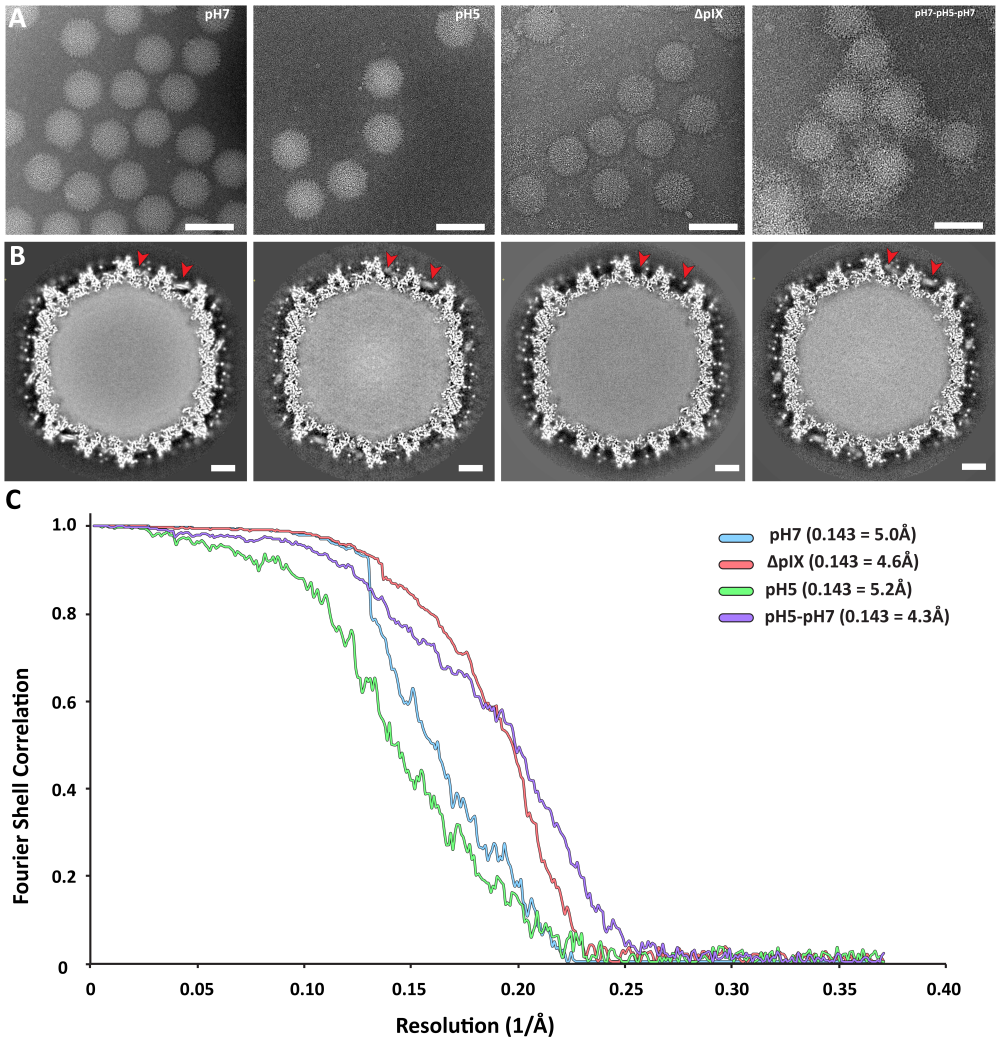

Figure A.1 – Fourier shell correlation curves for adenovirus structures determined using SPA in this thesis. A.) Representative single particle projection images for pH7, ΔpIX, pH5 and the DHC-N-associated, dialysed adenoviruses (from left to right) (contrast inverted). Scale = 100 nm. B.) Equivalent slices through the unmasked, unsharpened, single particle density maps of the reconstructed adenoviruses (from left to right). Note the presence and absence of the N-terminal region of pIX (red arrow). C.) Fourier Shell Correlation (FSC) of each SPA structure, after masking and sharpening in Relion 1.4.

A.3 Table of parameters for tomograms used for analysis in Chapter 3

See Table A.1 for comparison of the U87MG and U2OS tomograms used for the analysis in Chapter 3.

Tomogram:	U87MG cell	U2OS cell
Nominal microscope defocus (µm)	-5.0	-4.0
Reported defocus range in acquisition (µm)	-5.13 to -4.57	-4.16 to -3.49
Calculated defocus (µm)	-3.19	-5.39
Total dose (eÅ^{-2})	72.4	75.2
No. particles before symmetrisation	312	148
No. particles after symmetrisation	4056	1924
Tilt range (degrees)	-57 to +60	-45 to +45
Tilt sampling (degrees)	3	3
Calibrated magnification	10869x	21739x
Calibrated pixel size of average (Å)	4.22	4.6 (2.3 unbinnned)
Approximate ice thickness (nm)	80-100	150-180

Table A.1 – Table of parameters used for acquisition and sub-volume averaging of the microtubules from the U87MG and U2OS cell lines.

Appendix B

Published Works

Journal of Structural Biology xxx (2016) xxx–xxx

Contents lists available at ScienceDirect

Journal of Structural Biology

journal homepage: www.elsevier.com/locate/yjsbi

Cellular electron cryo tomography and *in situ* sub-volume averaging reveal the context of microtubule-based processes

Michael Grange, Daven Vasishtan, Kay Grünewald *

Oxford Particle Imaging Centre, Division of Structural Biology, Wellcome Trust Centre for Human Genetics, University of Oxford, Oxford, OX3 7BN, United Kingdom

ARTICLE INFO

Article history:
Received 7 April 2016
Received in revised form 27 June 2016
Accepted 28 June 2016
Available online xxxx

Keywords:
Electron cryo-tomography
Cellular architecture
Sub-volume averaging
Microtubules
Cytoskeleton
Dynein
Adenovirus
Electron cryo-microscopy
Virus trafficking
Viral entry
Retrograde transport
Endocytosis
in situ structure determination

ABSTRACT

Electron cryo-tomography (cryoET) is currently the only technique that allows the direct observation of proteins in their native cellular environment. Sub-volume averaging of electron tomograms offers a route to increase the signal-to-noise of repetitive biological structures, such improving the information content and interpretability of tomograms. We discuss the potential for sub-volume averaging in highlighting and investigating specific processes *in situ*, focusing on microtubule structure and viral infection. We show that (i) *in situ* sub-volume averaging from single tomograms can guide and complement segmentation of biological features, (ii) the *in situ* determination of the structure of individual viruses is possible as they infect a cell, and (iii) novel, transient processes can be imaged with high levels of detail.

© 2016 Published by Elsevier Inc.

1. Introduction

Electron cryo tomography (cryoET) is a technique used to reconstruct 3-dimensional structures of biological samples in their native, frozen hydrated state. By taking a tilt series of images of vitrified cells (or other relevant specimens) in an electron microscope it becomes possible to visualize unique pleomorphic events, structures with short-lived and transient states, and large macromolecular organisations (e.g. lattices) that would be otherwise very difficult to reconstitute *in vitro* (Asano et al., 2015; Brandt et al., 2010; Hagen et al., 2015; Schur et al., 2015; Zeev-Ben-Mordehai et al., 2016). Furthermore, repetitive or frequently occurring molecular structures within these pleomorphic objects can be averaged together to create higher resolution maps, a technique generally referred to as sub-tomogram averaging.

Recent technical developments in electron cryo microscopy (cryoEM) have resulted in the ability to image and collect data of vitrified specimens with unprecedented signal-to-noise ratios, allowing the analysis of biological structures and features at a much higher level of detail than previously attainable. These developments include better zero-loss energy filters and direct electron detectors, both of which have vastly improved the quality of tomographic data acquisition (Koster et al., 1997; Li et al., 2013; McMullan et al., 2014), and led to the high-resolution determination of novel macromolecular complexes and viruses, as well as the structural determination of pleomorphic complexes and the *in situ* architecture of cells (Asano et al., 2015; Bartesaghi et al., 2015; Fukuda et al., 2015; Mahamid et al., 2016; Matthies et al., 2016; Schur et al., 2015; Sirohi et al., 2016; Zeev-Ben-Mordehai et al., 2016).

This move to analyze native cellular structures *in situ* has come concomitantly with a push towards the development of technologies such as Zernike phase plates, and more recently Volta phase plates (VPP) (Danev et al., 2014; Murata et al., 2010), that improve the image contrast. These improvements further include specimen thinning methods mitigating some of the detrimental impact of thick specimens – cells are typically too thick to image through standard methods, as the penetration limit of electrons through a frozen-hydrated specimen at 300 keV is around 1 μm

* Corresponding author.
E-mail address: kay@strubi.ox.ac.uk (K. Grünewald).

http://dx.doi.org/10.1016/j.jsb.2016.06.024
1047-8477/© 2016 Published by Elsevier Inc.

Please cite this article in press as: Grange, M., et al. Cellular electron cryo tomography and *in situ* sub-volume averaging reveal the context of microtubule-based processes. J. Struct. Biol. (2016), http://dx.doi.org/10.1016/j.jsb.2016.06.024

(Baumeister, 2002) – and allow us to use cryoET to image processes anywhere in the interior of cells (Al-Amoudi et al., 2004; Rigort et al., 2012). However, such techniques are still limited and challenging to implement technically.

Alternatively, it is also possible to avoid this thickness limit by focusing attention to the cell periphery. These areas of the cell are generally thin enough to be successfully imaged, and are accessible directly after plunge freezing such offering a much more widely and routinely used route of specimen preparation for many structural and cell biologists. Understanding the cell periphery is crucial to comprehending many biological mechanisms. These include, but are not limited to, cell signaling, translation, exocytosis, endocytosis, pathogen entry and egress and cytoskeletal organization and trafficking (Brandt et al., 2010; Cyrklaff et al., 2007; Dodonova et al., 2015; Ibiricu et al., 2011).

In this work, we assess what can be achieved by targeting the cellular periphery of whole intact non-thinned cells in individual tomograms, particularly through sub-volume averaging and the localization of rare events (Fig. 1A). We discuss the opportunities that novel developments offer to structural cell biologists when using direct electron detectors, especially when combined with an energy filter. Our assessment shows that the majority of information to determine usable and contextual structures is contained within the tomogram. As examples we reveal a range of regular structures that are discernible throughout the tomograms and assess their roles and interaction in the course of viral entry.

2. Materials and methods

2.1. Cell culture and plunge freezing

U87MG cells and U2OS cells were seeded and grown on poly-L-lysine-coated gold mesh carbon coated holey carbon grids (Electron microscopy sciences) in Dulbecco's modified eagle medium (DMEM) (Gibco) supplemented with 10% fetal bovine serum. The cells were grown to approximately 60–80% confluency, or until 1–2 cells per grid square. The grids were supported in 2×9-well μ-slide co-culture dishes (Ibidi). Adenovirus particles were cultured and isolated as has been described previously (Wodrich et al., 2010). For infection of U2OS cells with adenovirus, 4 μl of adenovirus was mixed in 200 μl of DMEM. 50 μl was applied to each grid and incubated with the cells for 10–20mins before plunge freezing. Grids were plunge frozen in an ethane/propane mix, cooled to liquid nitrogen temperature using a manual blotting apparatus, blotted from the backside of the grid for between 2 and 4 s.

2.2. Electron microscopy

Tomograms were acquired using a Tecnai TF30 "Polara" Microscope (FEI, Eindhoven) operating at 300 keV. The microscope was equipped with a Gatan Imaging Filter "Quantum" energy filter operated in zero-loss mode with a 20 eV wide slit, and a post energy filter mounted K2 Summit direct electron detector (Gatan, Inc.) Data were acquired in counting mode, with aligned frames produced 'on the fly', using the combined filter for image alignment in Digital Micrograph (Gatan, Inc.). Dose, pixel size, magnification and tilt angle information are provided in Table S1. Data were acquired using SerialEM (Boulder, Colorado) (Mastronarde, 2005).

2.3. Tomogram reconstruction, segmentation and subvolume averaging

Tilt series outputted from the microscope were aligned and reconstructed using the IMOD software package (Kremer et al., 1996). CTF correction, where applicable, was also performed using IMOD. A global defocus was determined for the whole tomogram, which was then used to correct individual tilts in the tilt series, taking into account the change in eucentricity across the projection images at high tilts. Phase flipping was then performed on each tilt image and the tomogram reconstructed using this phase flipped image stack. Sub-volume averaging of microtubules was performed using PEET (also part of IMOD) (Nicastro et al., 2006). Particles were picked from tomograms binned by a factor of 4, using scripts based on TEMPy (Farabella et al., 2015) that evenly sampled

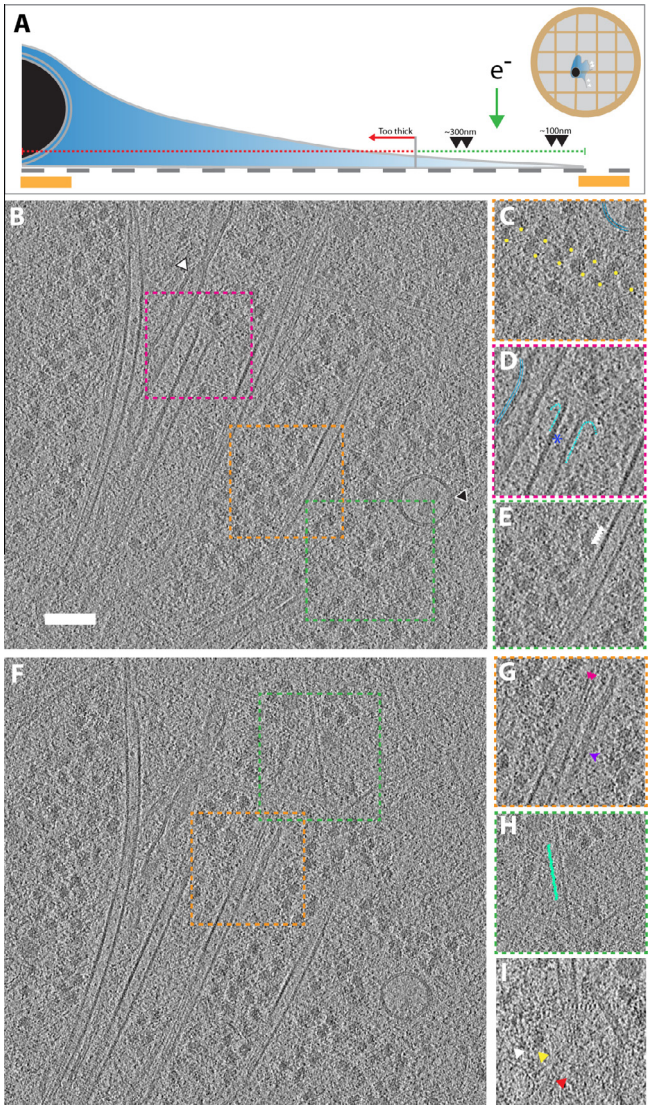

Fig. 1. CryoET of a peripheral region of an adherent U87MG neuronal cell line imaged using direct electron detection. (A) Schematic representation of an adherent cell grown on a holey carbon-coated gold grid. Red line indicates regions too thick for cryoET imaging. Area marked by green line indicates typical regions of the cell accessible to imaging by cryoET. (B) Slice through tomogram at the periphery of the U87MG cell, containing a number of cellular features such as (C) polysomes, (D) a de-polymerising microtubule in proximity to the endoplasmic reticulum with microtubule luminal bodies (blue asterisk), and (E) 4 nm tubulin spacing of the microtubule. White and black arrows in (B) represent the endoplasmic reticulum and a lysosome, respectively. (F) Another slice through the same tomogram, showing the diversity of cytoskeletal elements visible in a snapshot of the cell periphery; (G) microtubule protofilaments (pink arrows) (top-view), intermediate filaments (purple arrow) and (H) F-actin (green). (I) Vault ribonucleoprotein cage (white arrow) and a putative cytoskeletal motor, dynein (yellow arrow), engaged with a microtubule (red arrow), cf. also Fig. S2. Squares outlined by colored dashed lines in (B) and (F) indicate positions of areas in (C–E) and (G–H), respectively. Scale bar; 100 nm. Thickness of the tomographic slices is 4.22 Å for all panels.

Please cite this article in press as: Grange, M., et al. Cellular electron cryo tomography and *in situ* sub-volume averaging reveal the context of microtubule-based processes. J. Struct. Biol. (2016), http://dx.doi.org/10.1016/j.jsb.2016.06.024

at 4 nm intervals (based on the size of one tubulin monomer) through a straight line defined by the user, with each particle oriented parallel to the line. These particles were then used for iterative sub-volume refinement; with further refinement applied on factor 2 binned and unbinned tomograms. Custom scripts were used to relate reconstructions between the binning levels of the tomograms to utilize the respective Euler angles and translational information. Sub-volume averages were acquired at binning factors of 4,2 and 1 for the U87MG tomogram (final pixel size = 4.22 Å unbinned), and binning factors of 4 and 2 for the U2OS tomogram (final pixel size = 4.6 Å at binning factor 2). Symmetrisation of the microtubules was performed using custom scripts, and utilized the prior knowledge from the unsymmetrised structure that the microtubules contained 13 protofilaments, with 4 nm tubulin dimer spacing (on average).

The picked microtubule particles were split in half at random prior to sub-volume averaging and each half dataset independently averaged during refinement, including symmetrisation. Each run of sub-volume averaging at every binning level for the reconstruction was performed three times: one on the first random half dataset, the second on the second half and a third on the combined data. In the case of the U2OS tomogram, at the end of refinement, particles with a cross correlation of less than 0.2 were excluded. In the case of both tomograms, if any particles had centres within 4 nm of each other, the particle with the lower cross correlation was excluded. Resolution determination was assessed through FSC at 0.5 and 0.143 between the two half set reconstructions (the 'gold standard' criterion). Structures shown in the paper are from the combined dataset, filtered to the resolution cut-off determined by FSC0.143 between the two half sets. Curves were determined using a number of different masks, specifically: no mask, the final microtubule structure binarised at a noiseless threshold and extended with a soft edge (threshold mask), or a hard edge cylinder or soft edge cylinder of approximate microtubule diameter (Fig. 3F). FSC curves and masks for "gold-standard" FSC determination were generated using EMAN2 (Tang et al., 2007).

Refinement of the adenovirus structure was performed using PEET, utilising an option to not produce a new map after each iteration of refinement. The adenovirus reference structure (EMDB-1574) was filtered to 60 Å prior to alignment. The determined position and orientation of the picked particle was then used to symmetrize it and produce a reconstruction. We also produced a "back-plotted" tomogram, where the virus particles in the tomographic volume were substituted with the reconstruction using a custom script that utilized the translation offsets and Euler angles for each given particle position.

Segmentation and representation of tomograms (including back-plotted tomograms) was performed and viewed using the visualization software Amira (FEI, Eindhoven). Structures resulting from sub-volume averaging and backplotted coordinate models were visualized using Chimera (UCSF) (Pettersen et al., 2004).

3. Results and discussion

3.1. Whole cell electron cryo tomography of the cellular periphery using direct electron detectors

Using a 300 keV FEG electron microscope with post-energy filter mounted direct electron detector (Gatan K2 Summit), we first aimed to assess visually what information could be gained by following relatively regular and populous features within single tomograms of adherent human cells. We comparatively performed this analysis on two tomograms from two different cells lines: 1) U87MG cells and 2) U2OS cells in areas of ~80–200 nm thickness (Figs. S1 and S2).

Visual inspection of tomograms is a useful first approach in analyzing and characterizing the major components (cf. its use in some notable recent studies (Fukuda et al., 2015; Mahamid et al., 2016)). We clearly observed and easily discriminated the different components of the cytoskeleton, such as intermediate filaments, F-actin and microtubules (Fig. 1B, F) due to their characteristic structural signatures. The overall level of detail in these tomograms was very high, allowing us to clearly discern, e.g. for the cytoskeletal structures, considerable sub-structural detail. For F-actin, we could observe the zig-zag nature of F-actin (Fig. 1H, green line), a ~2.8 nm repeat feature, as well as the globular features of individual actin monomers within the filament (Fujii et al., 2010). Similarly, the intermediate filaments showed a rather smooth parallel tubular architecture slightly wider in diameter (~10 nm) than actin filaments (~7 nm), consistent with their tightly packed, cylindrical structure (Herrmann et al., 2007).

However, the greatest level of detail visible in the tomogram was found when considering the microtubules. Protofilaments were clearly visible in the top and bottom views of the microtubules. Furthermore, the tubulin lattice in the microtubule wall was evident with the 4 nm spacing of tubulin monomers being clearly distinguishable through top, bottom and middle slices of the microtubules (Fig. 1E, G), suggesting a high level of detail being contained within the tomogram. The high signal-to-noise ratio further allowed us to visualize more transient states in these filaments, such as a microtubule plus end in the process of disassembly (Fig. 1D) (Koning et al., 2008).

As well as elements of the cytoskeleton, the tomogram also showed less regular, more globular macromolecules. Ribosomes were often arranged into polysomes (Fig. 1C), as has been characterized previously (Brandt et al., 2010). The level of detail allowed us to differentiate the 50S and 40S subunits. A ribonucleoprotein "Vault" (Woodward et al., 2015) could be observed, in close proximity to a microtubule and potentially engaged with a dynein motor (Figs. 1I, S2). Putative AAA+ domains of a dynein motor complex as well as the respective stalk regions projecting onto a nearby microtubule are visible (Figs. 1I, S2) (Roberts et al., 2009). Vaults are ribonucleoprotein organelles that are thought to recruit and store mRNAs. This function has led to the suggestion that they act as a transport cages within the cytosol (Chugani et al., 1993). Our observation adds credit to the idea that Vaults are important in the transportation of mRNAs and other cargoes inside cells.

Further to macromolecules, various organelles could also be identified within the tomogram, such as the lysosome and the endoplasmic reticulum (Fig. 1B, arrows), with their 6–8-nm-thick bilayer distinctly visible.

3.2. In situ sub-volume averaging from a single tomogram

In order to assess the potential resolution achievable from this tomogram of a peripheral U87MG cell area, we performed sub-volume averaging of microtubule segments (Fig. 2). Due to the fact that the microtubules were oriented roughly perpendicular to the tilt-axis for the tomographic series, we expected that we would be able to compensate to some extent the information lost due to the CTF, as different apparent defoci of extracted volumes caused by tilting of the sample would compensate for some of the lost information. The resultant microtubule structure has 13 protofilaments, with a tubulin monomer spacing of ~4 nm, consistent with the current understanding of the microtubule structure *in vivo* (Evans et al., 1985; Kollman et al., 2010). As the sampling of the tomogram precluded the possibility of discerning the microtubule seam in these structures, we applied a 13-fold helical symmetry to the final model to produce the final structure. The gold standard Fourier Shell Correlation curve of the resultant microtubule structure (Fig. 2B) indicated a resolution of 18.5 Å at the

Please cite this article in press as: Grange, M., et al. Cellular electron cryo tomography and *in situ* sub-volume averaging reveal the context of microtubule-based processes. J. Struct. Biol. (2016), http://dx.doi.org/10.1016/j.jsb.2016.06.024

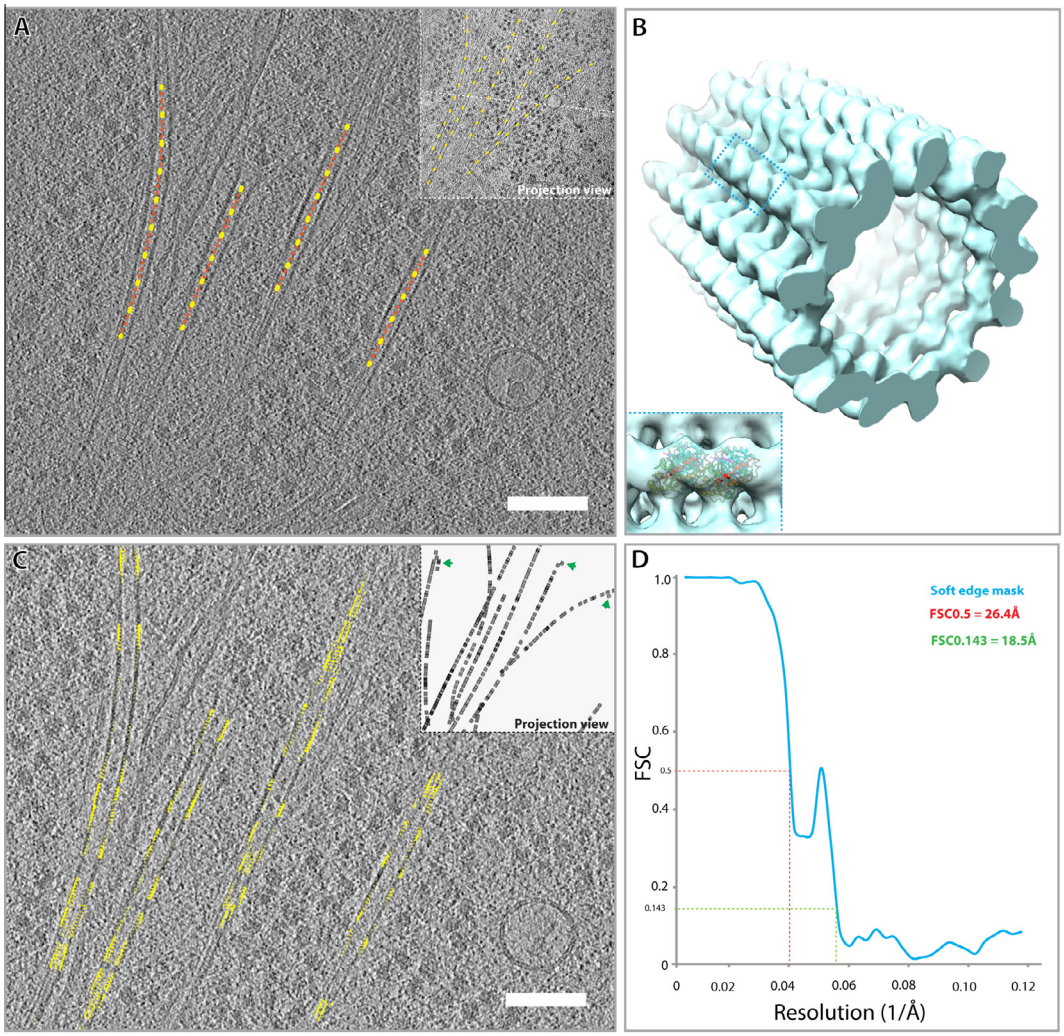

Fig. 2. Sub-volume averaging of microtubules. (A) Schematic model of how microtubules were picked for sub-volume averaging shown in the context of a single tomographic slice and as a projection of the whole tomogram (inset). (B) Resulting sub-volume average of the microtubule from this single tomogram in (A) filtered to 18.5 Å according to the calculated gold standard FSC, at threshold 0.143. Tubulin α/β dimer (PDB: 1TUB) is shown docked into the structure (inset, blue). (C) Tomographic slice overlaid with the equivalent slice in the back-plotted tomogram and projection (inset) of the microtubule average shown in (B). Green arrows in the inset indicate outlier particles. These outliers particles are found in regions of the tomogram that may be less well aligned (i.e. edge of tomogram) and are included in the final average. (D) Gold standard FSC curve for the microtubule structure determined from the tomogram. The FSC was produced using a soft-edge cylindrical mask. Scale bar for (A) and (C) is 100 nm.

0.143 threshold (Fig. 2D). A prominent local peak occurred at a spatial frequency equivalent to ~22 Å resolution (Figs. 2D and 4A). Analysis of the Fourier spectrum of the microtubule structure indicated a strong layer line at this resolution, as has been seen for other microtubule structures (Alushin et al., 2014). The calculated defocus and the nominally acquired microscope defocus differed by up to 1 μm, and accounting for inaccuracies of the defocus due to spherical aberration in the microscope, as well as the range of defoci across the tomogram, it is difficult to determine an overall single defocus. We therefore proceeded with the IMOD determined defocus (Xiong et al., 2009) as basis for comparisons.

The resulting microtubule structure is of correct size and shape to fit a crystal structure of the tubulin αβ-dimer (PDB: 1TUB) (Fig. 2B, inset). Due to the nature of tomographic data acquisition, where a range of defoci likely exist within the same dataset, the zeroes of the CTF will not be clearly visible in a sub-tomogram average if a structure that prevails throughout the field of view in a single tomogram is used for sub-volume averaging. Our analysis suggests that the sub-volume averaging performed from this single tomogram is however very likely limited in resolution by the number of particles contained within the tomogram; here 4056 overlapping sub-volumes of 25 nm × 25 nm contributed to the final average.

In the case of single particle reconstruction methods, resolution has been shown to be very sensitive to the applied electron dose (Bartesaghi et al., 2014). An element where the dose may be important in sub-tomographic averaging is when incorporating high tilts into the final sub volume average. Studies have shown that lower tilt images are the main contribution to good resolution sub-volume averages (Bartesaghi et al., 2012) and recent strategies have been developed to down weight the contribution of higher tilts (Bharat et al., 2015). However, high tilts can be very important in the reduction of back-projection artifacts from gold fiducials in tomograms, which may otherwise interfere with the interpretation of rare individual events in cellular tomograms that do not benefit from sub-volume averaging.

Sub-volume averaging of microtubules in the U2OS cellular tomogram (Fig. 3) resulted in a microtubule structure of 25 Å. This resolution was determined without a mask as use of a mask appeared to produce an FSC at 0.143 in noisy regions of the FSC curve, as shown in Fig. 4C. Due to the higher magnification, and resultant smaller field of view, only a quarter of the number of

Please cite this article in press as: Grange, M., et al. Cellular electron cryo tomography and *in situ* sub-volume averaging reveal the context of microtubule-based processes. J. Struct. Biol. (2016), http://dx.doi.org/10.1016/j.jsb.2016.06.024

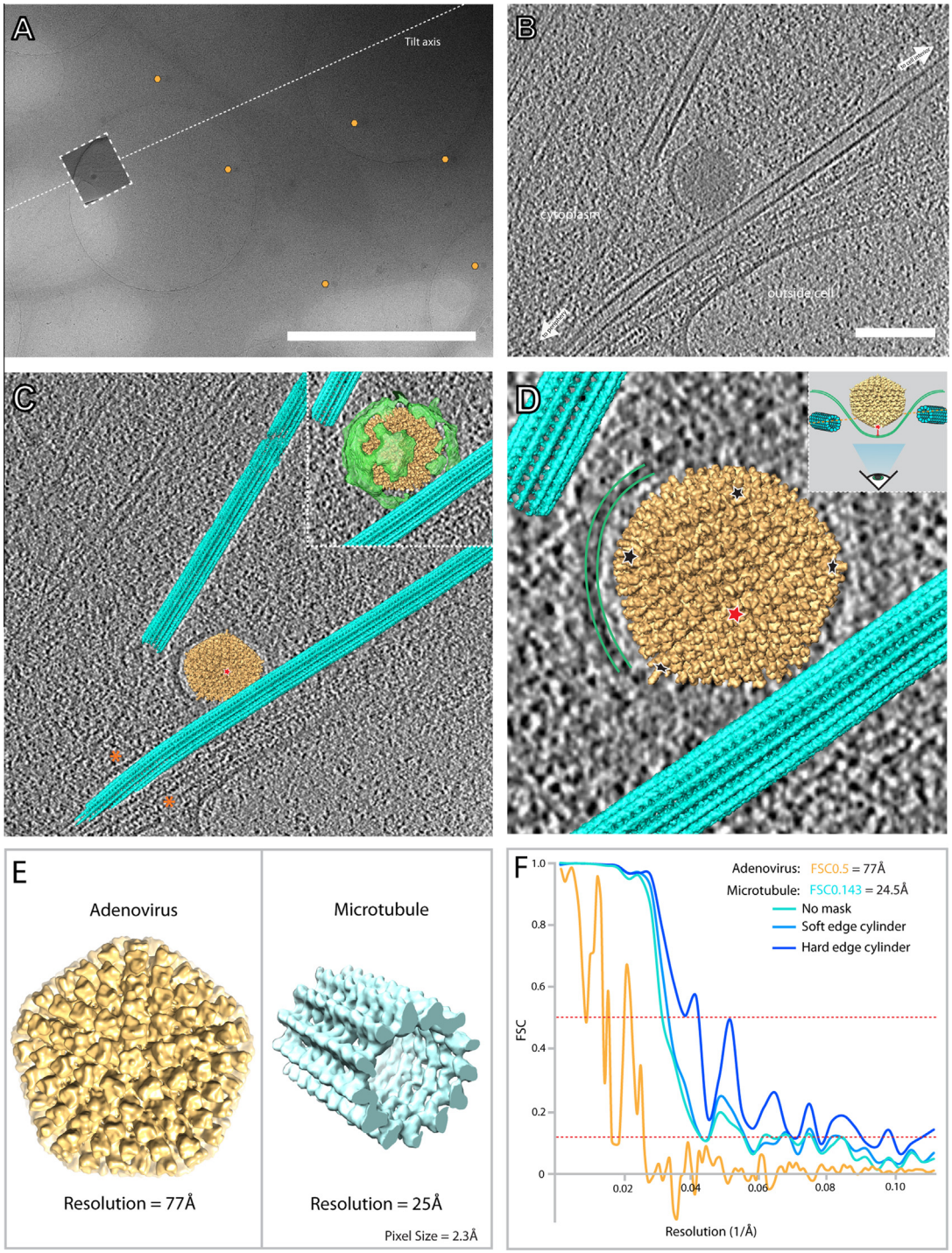

Fig. 3. Endosomal entry of Adenoviruses as a case for structure determination *in situ*. (A) Low magnification projection image (9500×, nominal) of the field of view of an U2OS cell infected with adenoviruses (marked by yellow hexagons). The tilt axis is shown as a white dotted line. (B) High magnification (95000×, nominal) slice of a tomogram taken at the position shown by the dashed-outlined box in (A) at approx. −5.2 μm defocus. (C) Tomographic slice taken at an approximately 45° angle relative to the slice shown in (B), with the microtubule (cyan) structure and an adenovirus (yellow) structure (filtered to 20 Å – EMDB-1574) back-plotted into the tomogram. Green (inset) shows a view providing also the manually segmented surrounding endosomal membrane. Orange asterisks denote the peripheral F-actin. (D) View from below the adenovirus, showing the localization of the penton bases of the adenovirus (red and black asterisks). (E) Left: Adenovirus structure (yellow) produced from the icosahedral average of the *in situ* adenovirus determined using the calculated Euler-angles of the back plotted virus and subsequent sub-tomographic averaging. Right: microtubule structure (cyan) produced from this tomogram. Adenovirus is approx. 960 Å in diameter. Microtubule is approx. 25 nm in width. (F) FSC curves of the single adenovirus (yellow) and the microtubule average (cyan – green). The colour of the curve indicates the type of mask used in the final gold standard FSC determination of the microtubule. Resolution stated is unmasked. Scale bars are 2 μm and 100 nm for (A) and (B), respectively.

particles could be picked (Table S1). Only particles with a cross-correlation coefficient (CCC) score above 0.2 after alignment were included in the final average. Removal of particles below this threshold removed the majority of the microtubule particles that were in the thicker regions of the tomograms (Fig. S4). A thickness gradient from ~90 to ~180 nm existed across this tomogram (Fig. S3). It therefore seems likely that the main contribution to the low CCC in this model is due to the increased thickness.

Please cite this article in press as: Grange, M., et al. Cellular electron cryo tomography and *in situ* sub-volume averaging reveal the context of microtubule-based processes. J. Struct. Biol. (2016), http://dx.doi.org/10.1016/j.jsb.2016.06.024

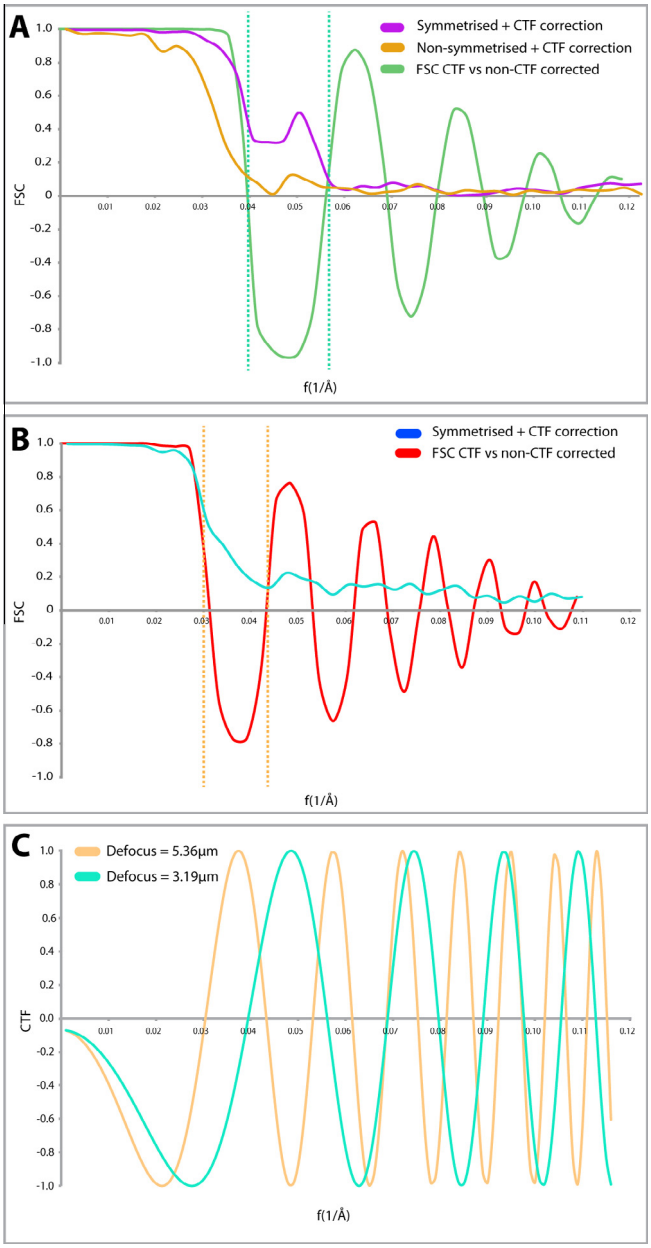

Fig. 4. Sub-volume averaging *in situ* in a single tomogram is enough to correct for the CTF, and results in a corrected sub-volume averaged structure. (A) CTF curves of sub-volume averages produced from CTF corrected sub-volume average microtubule from the tomogram of the U87MG cell before (orange) and after (magenta) symmetrisation. The green curve represents the FSC of the non-CTF corrected average when compared to the CTF-corrected structures in both cases. This produces the expected negative correlation due to the effect of the CTF (green dotted line). (B) FSC curve of the CTF-corrected U2OS cell microtubule reconstruction (blue). FSC of the equivalent non-CTF corrected when compared to the CTF-corrected structure (red). Lack of fall-off to zero of the CTF corrected structure is due to partial alignment of noise during symmetrisation of the microtubule average after alignment. (C) CTF calculation for the determined defoci for the tomograms in (A) (cyan) and (B) (brown). Phase flipping, and the range of defoci of particles within the tomograms has compensated for the inverted contrast and node of zeroes caused due to the oscillations in the CTF. This indicates that the range of defoci within a tilt series is enough to compensate for a single nominal acquisition defocus. Masks used to produce the FSC are a soft cylindrical mask in A) and no mask in B).

However, it has been shown before that filamentous objects perpendicular to the tilt axis suffer from distortions that may affect their potential to align them accurately (Mastronarde, 1997). Interestingly, these microtubules also aligned parallel to the tilt axis, suggesting the alignment may possibly be dependent on the tilt axis. The reduced signal to noise and low cross correlation, and subsequent removal of bad particles most likely contributed to the difficulty in resolution determination during masking.

In the case of this second microtubule sub-volume average structure, the fall-off in cross correlation between the two independent halves of the dataset did not fully reach zero (Fig. 3F), suggesting that there is inherent noise in this structure, possibly introduced by particles from the thicker regions of the sample. This is further validated by comparison with the non-CTF corrected FSC curve, which was generated by replacing the CTF-corrected tomogram with its non-CTF corrected equivalent, without further alignment of the particles. Since this changes the noise floor, the noise correlation disappears, as evidenced by the near zero values of the non-CTF corrected FSC curve at higher resolutions (Fig. S5B).

3.3. Backplotting of sub-volume average structure into the tomogram results in a 3-dimensional context for structural interaction

The ability to gain biological insights from cryoET data depends intrinsically on our ability to mine and detect the *in situ* context of our biological feature of interest. To allow better probing the relative localization of features in the cell, we used the refined positions and orientations of the individual particles contributing to the average. The microtubule average was back plotted (see Section 2) into the raw tomogram, which are of comparably low signal-to-noise and thus make it difficult to directly visualize a molecular interaction. In this instance, we applied two methods: a) direct back plotting of the sub-tomogram average structure using the positions and orientations determined during alignment, and b) refining the orientation of a known structural feature into the respective position in the tomogram, in this case performed for an adenovirus virus capsid.

Sub-volume averaging of the microtubule was performed as described above. For the adenovirus re-orientation, we used PEET to fit a previously determined viral structure (EMDB ID 1574, (Fabry et al., 2008)) into our tomographic viral feature. The orientation of this structure was then subsequently refined and placed into the tomogram according to the determined orientation. The fitting of the structure was then compared to the original tomogram, to verify and compare whether the adenovirus densities overlapped with features in respective slices through the back-plotted volume.

To further validate the accuracy of the alignment of the EMDB-structure to the adenovirus contained within the tomogram, we performed icosahedral averaging of the single adenovirus within the tomogram, according to the Euler angles determined during the alignment of the EMDB-map. The resultant symmetrically averaged structure yielded a structure of 77 Å, when compared to a low-pass filtered map of EMDB-map at 20 Å (Fig. 3F). The icosahedral average of the single virus before and after orientation refinement is presented in Fig. S6. The symmetrized adenovirus structure allowed for direct visualization of the trimeric hexon proteins on the virus surface, as well as of the 12 penton bases. Icosahedral symmetrisation of the virus in the absence of any refinement yielded no discernible structure (Fig. S6) indicative of a lack of symmetry axis orientation and possible position inaccuracy. This analysis shows that the information contained in our tomogram was able to produce correlative signal to 77 Å (Fig. 3E, F) from only 60 copies of an asymmetric unit, with the noisy FSC curve being indicative of particle number based limitation and even further information content. The demonstrated potential for the differential structural determination of sub-populations of virus and protein structures *in situ* provides promising and exciting possibilities for dissecting dynamic processes and subtle structural changes *in situ*.

Please cite this article in press as: Grange, M., et al. Cellular electron cryo tomography and *in situ* sub-volume averaging reveal the context of microtubule-based processes. J. Struct. Biol. (2016), http://dx.doi.org/10.1016/j.jsb.2016.06.024

The resultant "segmented" tomogram (Fig. 3C, D), allowed for directly viewing the 3-dimensional spatial organization of the microtubule network of an adenovirus undergoing viral entry. We were able to observe the topology and specific orientation of an adenovirus as it is enveloped into the periphery of a cell. Given the contextual situation of the virus, we were able to define that the virus is undergoing the process of endosomal uptake into the cell. The ability to determine the orientation of the virus with respect to the cell membrane allowed the visualization of the position of the adenovirus penton fibre as it interacts with the plasma membrane, being in this instance directly found centrally in the invaginated plasma membrane patch (Fig. 3C, D). The bilayer of the plasma membrane could clearly be followed around the virus in x, y and z, the curvature being indicative of the process of entry being fairly advanced. The immediate proximity of microtubules to the virus undergoing internalization by endocytosis suggests that the subsequent process of viral retrograde transport towards the nucleus is closely coupled to microtubules, consistent with observed speeds for incoming adenoviruses in the range of ~1 μm s^{-1} (Bremner et al., 2009), which allows the virus to quickly gain entry to the inner regions of the cell.

3.4. Evaluation of CTF correction of tomograms for in situ sub-volume averaging

Sub-volume averaging of structures from single tomograms is routine until the resolution approaches the first zero of the CTF function for the given defocus at which the tomogram was acquired. In order to achieve accurate information past the first zero, it is important that one efficiently corrects the CTF. In our instance and conditions phase flipping in IMOD was sufficient in a single tomogram to recover significant information contained across the field of view. This is the case despite a large nominal defocus range determined during the acquisition of the tomogram (Table S1). This inaccuracy in the defocus during tomogram acquisition is not uncommon, and the lack of eucentricity across the sample and non-uniformity of the defocus will make the CTF model of individual particles within the tomogram more difficult to determine.

The comparison of microtubule structures reconstructed using CTF and non-CTF corrected tomograms (Fig. 4A and B) for sub-volume averaging from each tomogram clearly shows that even in the case of one tomogram, the resolution to which we can interpret a structure is significant (Fig. 4A). The CTF corrected structure of the microtubule from the U87MG tomogram has an FSC(0.143) of 18.5 Å, and interpretable information persists in the FSC to around 17 Å. Without CTF correction, the amount of information in the structure falls off at around 25 Å (Fig. 4A). In the case of the U2OS tomogram, the non-CTF corrected structure is interpretable to 32 Å due to the CTF induced phase change, but is increased to a resolution of 25 Å after CTF correction (Fig. 4B).

Interestingly, the calculation of the defocus in IMOD of each tomogram was different to the nominal defocus of the microscope by as much as 0.5 μm (Table S1). Even accounting for inaccuracies in defocus determination of the microscope (Danev and Baumeister, 2016), this is still a large discrepancy. The calculated CTF of the calculated defoci is shown in Fig. 4C for each tomogram. To better determine the accuracy of the CTF correction, an 'ideal' microtubule structure was built by fitting atomic models of symmetrized tubulin monomers from a microtubule structure (PDB ID: 3J2U) into the sub-tomogram averages determined here. These atomic models were then Gaussian blurred in Chimera to Nyquist frequency and matched in sampling and box size to the respective sub-tomogram average. The FSCs between this 'ideal' structure and the CTF and non-CTF corrected averages are shown in Fig. 5. For both structures, CTF correction resulted in a more accurate structure, with the U87MG cell microtubule average (Fig. 4A) displaying a particularly obvious phase flip correction. However, a small dip below zero at around 25 Å in the U2OS cell microtubule average CTF-corrected FSC (Fig. 4B, purple line) may well indicate an inaccuracy in defocus determination.

We would suggest that an "all-tomogram" approach to CTF correction, especially for datasets with low particle numbers, likely results in corrections that are less accurate or not weighted correctly. Approaches that have been implemented recently (Bharat

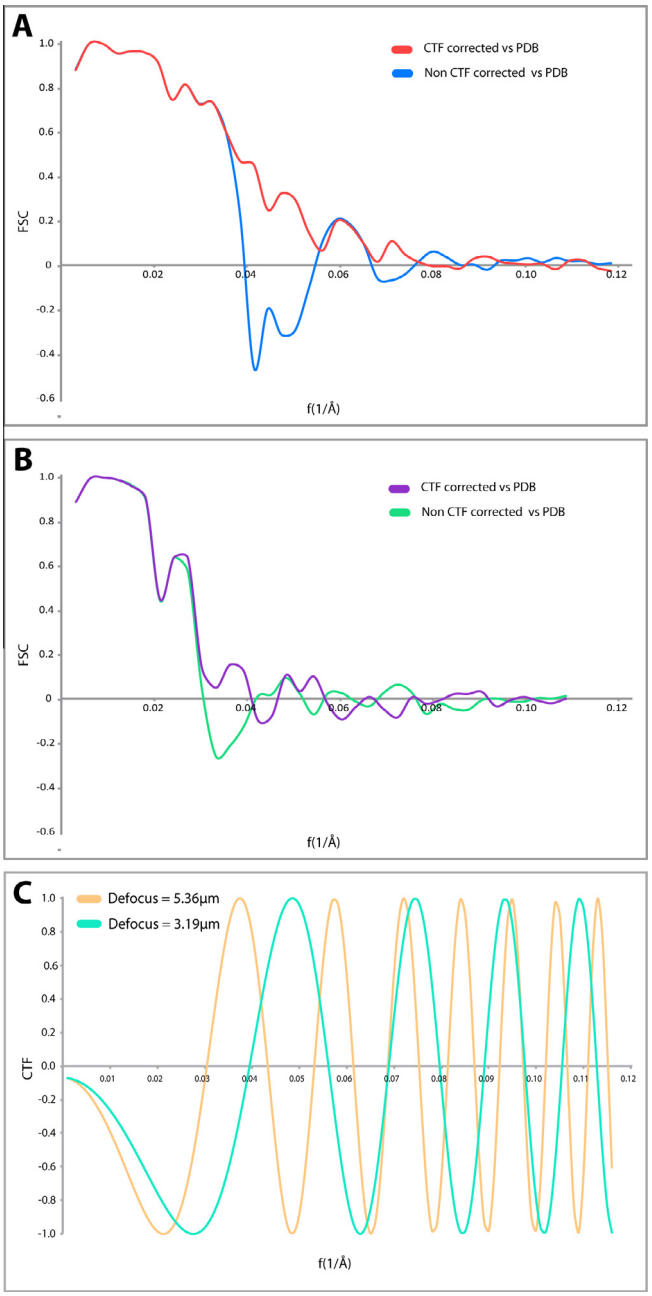

Fig. 5. Comparison of sub-volume averaged microtubule structures with a PDB-generated "ideal" 13 protofilament model highlights aberrant points in the structure. The effect of the CTF on elements of the sub-tomogram averaged microtubules structures are shown for A) U87MG and B) U2OS tomograms. A) Shows a pronounced dip below zero between 0.040 and 0.055 corresponding to the theoretical first negative oscillation of the CTF of the microscope, shown in C). An equivalent dip is also visible in B). A negative dip below 0 in the correlation of the CTF-corrected structure may indicate an inaccuracy in defocus determination (c.f. Fig. 4).

et al., 2015; Galaz-Montoya et al., 2016) whereby individual sub-volumes are tilt-dependently CTF corrected should prove to be much more accurate in determining a per-particle CTF correction. These approaches would yield a much more accurate determination of particle eucentricity across the tilt series, as a custom per-particle defocus and z-position within the tomogram can be determined. This should result in sub-volume averages that yield better results, particularly for single tomograms, or datasets with only a low number of particles.

3.5. Determination of virus structure in situ improves understanding of virus-host interactions

The current structural understanding of virus-host interactions stem mainly from studies using co-crystalized complexes, small angle scattering and sub-volume averaging of *in vitro* constituted systems, such as virus-like particles. Direct molecular imaging of the viral interactions with the host has hitherto not been a mainstay of investigation.

The increased signal-to-noise ratio in the images gained from the use of direct detection allowed us to see much greater details inside the cell, as well as to average structures to an intermediate resolution capable of bridging the gap between structural context and molecular resolution (Figs. 2 and 3). This will surely allow us to provide novel insights into the cellular biology of viral infection. The structural context of virus-cell processes in a model cell line is currently the closest one may currently come to reconstituting a disease-like state. The ability to localize structures in their cellular context (Fig. 3), and to sub-volume average different conformers of the virus as it progresses through various stages of its life cycle (Fig. 3C), will allow determining which viral proteins are lost, which cellular proteins it interacts with, and what other biological macromolecules and pathways the virus recruits or hijacks in this dynamic process. Being often easily recognizable due to their unique structural signatures viruses also constitute ideal tools to probe cellular processes. Furthermore, the structural determination of cellular factors co-localising with the virus during infection gives clues to potential novel forms of interventions to be explored.

3.6. Challenges and perspectives in the cryoET of cells

Many biological phenomena are intrinsically transient, and rare. Structural biology currently relies on approaches that can enrich for a particular biological event, state, or process of biological relevance, e.g. by overexpression of a particular protein, though this often comes with the sacrifice that the system is no longer near native. These are typified by the approaches based on purified material and can be combined with X-ray crystallography, single particle cryoEM or sub-tomographic averaging. However, these necessary and, in many cases sensible approaches, cannot always be applied due to the difficulty of producing substantial amounts of protein, DNA/RNA or other macromolecule in a structurally determinable state. Furthermore, the lack of *in situ* context for these structures means that in many cases crucial pieces of information from the overall model of how a biological process occurs are missing, such severely limiting a mechanistic understanding.

In this paper, we have discussed methods and data that allow for assessing the wealth of detail that can be mined from a single tomogram. Resolutions of 77 Å from a single symmetrized icosahedral virus and 18.5–25 Å from relatively few numbers of microtubule segments gives us a good indication that in many cases, the amount of information present even in a single tomograms is substantial, and something that, given the right biological problem and system, may lead to novel insights to complement the structural models many laboratories are building using canonical techniques.

The direct observation of biology just at the cryoET accessible periphery of a cell provides a severe limitation; as the feature of interest needs to reside in an area thin enough to image with sufficient counts. This limits the range of biological processes one can image and the number and quality of observed features. Accordingly, several approaches have been implemented addressing this shortfall by not only making localization of a biological feature of interest easier to find, but also adding to the overall interpretation of the cryoET data (Schellenberger et al., 2014; Schorb and Briggs, 2014). The recent success provided by the use of thinning methods (see below) is another promising direction.

Recent developments in phase plate technologies and in cryo-FIBSEM (Asano et al., 2015; Danev et al., 2014; Mahamid et al., 2016; Rigort et al., 2012) have given a flavor of the insights that may be gained in the future, specifically with the ability to investigate by cryoET processes and structures deeper inside a cell, and e.g. probe nuclear biology in its native context. However, these applications are currently still not routine or for higher throughput uses, and require specialist knowledge for their operation and application. These current drawbacks are significant, as they restrict the range of biological applications that may benefit from the improved insight that could be determined. Future developments need to address these, and make the technologies much easier to use and robust for routine everyday use.

A potentially powerful technique to provide further context for *in situ*-determined viral structure is the coupled use of correlative light electron microscopy (CLEM). Techniques such as light sheet fluorescence microscopy (LSFM), 3-dimensional structured illumination microscopy (3D-SIM) and localization microscopy (Chen et al., 2014; Schermelleh et al., 2008), especially when utilized in combination (Hoyer et al., 2016) offer potential for coupling the many complimentary techniques for cryoET, such as CLEM and cryoFIB/SEM, to offer a multi-scale resolution view of a molecular process *in situ* (Mahamid et al., 2015). Performing super-resolution fluorescence microscopy modalities routinely under cryo conditions and ultimately in a CLEM fashion (cryoCLEM) is the next challenge, but the few pilot studies performed demonstrate the potential and feasibility of such an approach (Wolff et al., 2016).

The examples highlighted in our study suggest that it is possible to gain valuable structural insight from only few tomograms, and a 25 Å 3D structure should be possible from fewer than 300 particles. Subsequent classification, back plotting into the tomogram, and segmentation can provide a diverse range of biological information, in the most native of contexts, over a wide range of resolutions.

The work presented in this article provide a significant and exciting frontier in cellular biology that may one day lead to the structural determination of novel structural complexes *in situ*. The multitude of classical electron microscopy applications many of which could be imaged under the much more native environment provided by cryoET, promise a rich and plentiful vein of discovery that can be judiciously mined through appropriate fluorescently tagged biological systems. This link between the high resolution imaging of cellular structure and structure determination is so far poorly explored and advancements would lead to a wealth of novel biological insight.

4. Concluding remarks

CryoET of cells offers a genuine route to the structural determination of subcellular complexes and organelles in their native state in the course of their function, and at a resolution gradually closer approaching that of single particle analysis. Improvements in microscopic hardware, software workflows, sample preparation

Please cite this article in press as: Grange, M., et al. Cellular electron cryo tomography and *in situ* sub-volume averaging reveal the context of microtubule-based processes. J. Struct. Biol. (2016), http://dx.doi.org/10.1016/j.jsb.2016.06.024

and transfer, and computational processing will require future investment if cryoET is to realize its full potential.

5. Accession codes

The microtubule sub-volume average reconstructions have been deposited in the Electron Microscopy Data Bank (EMDB) at PDBe (http://www.ebi.ac.uk/pdbe/emdb/) as EMD-4043 and EMD-4045.

Acknowledgments

We thank Harald Wodrich (Bordeaux) for providing purified adenovirus preparations, advice and discussion, Lindsay Baker for discussion and for critical reading of the manuscript, C. Alistair Siebert for technical advice and support. This work was supported by grants from the Human Frontiers Science Programme (HFSP; RGP0055/2015 to K.G.), a Wellcome Trust Senior Research Fellowship (107806/Z/15/Z to K.G.), a Wellcome Trust JIF award (060208/Z/00/Z) and a Wellcome Trust equipment grant (093305/Z/10/Z) to the Oxford Particle Imaging Centre, the Wellcome Trust core award 090532/Z/09/Z to the Wellcome Trust Centre for Human Genetics, the Leverhulme Trust (RPG-2012-519 to K.G.) and a Wellcome Trust Four-Year PhD Studentship (099683/Z/12/Z to M.G.).

Appendix A. Supplementary data

Supplementary data associated with this article can be found, in the online version, at http://dx.doi.org/10.1016/j.jsb.2016.06.024.

References

Al-Amoudi, A., Chang, J.-J., Leforestier, A., McDowall, A., Salamin, L.M., Norlén, L.P.O., Richter, K., Blanc, N.S., Studer, D., Dubochet, J., 2004. Cryo-electron microscopy of vitreous sections. EMBO J. 23, 3583–3588.

Alushin, G.M., Lander, G.C., Kellogg, E.H., Zhang, R., Baker, D., Nogales, E., 2014. High-resolution microtubule structures reveal the structural transitions in αβ-tubulin upon GTP hydrolysis. Cell 157, 1117–1129.

Asano, S., Fukuda, Y., Beck, F., Aufderheide, A., Förster, F., Danev, R., Baumeister, W., 2015. A molecular census of 26S proteasomes in intact neurons. Science 347, 439–442.

Bartesaghi, A., Lecumberry, F., Sapiro, G., Subramaniam, S., 2012. Protein secondary structure determination by constrained single-particle cryo-electron tomography. Structure 20, 2003–2013.

Bartesaghi, A., Matthies, D., Banerjee, S., Merk, A., Subramaniam, S., 2014. Structure of -galactosidase at 3.2-A resolution obtained by cryo-electron microscopy. Proc. Natl. Acad. Sci. U.S.A. 111, 11709–11714.

Bartesaghi, A., Merk, A., Banerjee, S., Matthies, D., Wu, X.W., Milne, J.L.S., Subramaniam, S., 2015. 2.2 angstrom resolution cryo-EM structure of beta-galactosidase in complex with a cell-permeant inhibitor. Science 348, 1147–1151.

Baumeister, W., 2002. Electron tomography: towards visualizing the molecular organization of the cytoplasm. Curr. Opin. Struct. Biol. 12, 679–684.

Bharat, T.A.M., Russo, C.J., Löwe, J., Passmore, L.A., Scheres, S.H.W., 2015. Advances in single-particle electron cryomicroscopy structure determination applied to sub-tomogram averaging. Structure 23, 1743–1753.

Brandt, F., Carlson, L.-A., Hartl, F.U., Baumeister, W., Grünewald, K., 2010. The three-dimensional organization of polyribosomes in intact human cells. Mol. Cell 39, 560–569.

Bremner, K.H., Scherer, J., Yi, J., Vershinin, M., Gross, S.P., Vallee, R.B., 2009. Adenovirus transport via direct interaction of cytoplasmic dynein with the viral capsid hexon subunit. Cell Host Microbe 6, 523–535.

Chen, B.-C., Legant, W.R., Wang, K., Shao, L., Milkie, D.E., Davidson, M.W., Janetopoulos, C., Wu, X.S., Hammer, J.A., Liu, Z., English, B.P., Mimori-Kiyosue, Y., Romero, D.P., Ritter, A.T., Lippincott-Schwartz, J., Fritz-Laylin, L., Mullins, R.D., Mitchell, D.M., Bembenek, J.N., Reymann, A.-C., Böhme, R., Grill, S.W., Wang, J.T., Seydoux, G., Tulu, U.S., Kiehart, D.P., Betzig, E., 2014. Lattice light-sheet microscopy: imaging molecules to embryos at high spatiotemporal resolution. Science 346, 1257998–1257998..

Chugani, D.C., Rome, L.H., Kedersha, N.L., 1993. Evidence that vault ribonucleoprotein particles localize to the nuclear pore complex. J. Cell Sci. 106 (Pt 1), 23–29.

Cyrklaff, M., Kudryashev, M., Leis, A., Leonard, K., Baumeister, W., Menard, R., Meissner, M., Frischknecht, F., 2007. Cryoelectron tomography reveals periodic material at the inner side of subpellicular microtubules in apicomplexan parasites. J. Exp. Med. 204, 1281–1287.

Danev, R., Baumeister, W., 2016. Cryo-EM single particle analysis with the Volta phase plate. eLife 5, 439.

Danev, R., Buijsse, B., Khoshouei, M., Plitzko, J.M., Baumeister, W., 2014. Volta potential phase plate for in-focus phase contrast transmission electron microscopy. Proc. Natl. Acad. Sci. U.S.A. 111, 15635–15640.

Dodonova, S.O., Diestelkoetter-Bachert, P., Appen von, A., Hagen, W.J.H., Beck, R., Beck, M., Wieland, F., Briggs, J.A.G., 2015. A structure of the COPI coat and the role of coat proteins in membrane vesicle assembly. Science 349, 195–198.

Evans, L., Mitchison, T., Kirschner, M., 1985. Influence of the centrosome on the structure of nucleated microtubules. J. Cell Biol. 100, 1185–1191.

Fabry, C.M.S., Rosa-Calatrava, M., Moriscot, C., Ruigrok, R.W.H., Boulanger, P., Schoehn, G., 2008. The C-terminal domains of adenovirus serotype 5 protein IX assemble into an antiparallel structure on the facets of the capsid. J. Virol. 83, 1135–1139.

Farabella, I., Vasishtan, D., Joseph, A.P., Pandurangan, A.P., Sahota, H., Topf, M., 2015. TEMPy: a Python library for assessment of three-dimensional electron microscopy density fits. J. Appl. Crystallogr. 48, 1314–1323.

Fujii, T., Iwane, A.H., Yanagida, T., Namba, K., 2010. Direct visualization of secondary structures of F-actin by electron cryomicroscopy. Nature 467, 724–728.

Fukuda, Y., Laugks, U., Lučić, V., Baumeister, W., Danev, R., 2015. Electron cryotomography of vitrified cells with a Volta phase plate. J. Struct. Biol. 190, 143–154.

Galaz-Montoya, J.G., Hecksel, C.W., Baldwin, P.R., Wang, E., Weaver, S.C., Schmid, M. F., Ludtke, S.J., Chiu, W., 2016. Alignment algorithms and per-particle CTF correction for single particle cryo-electron tomography. J. Struct. Biol. 194, 383–394.

Hagen, C., Dent, K.C., Zeev-Ben-Mordehai, T., Grange, M., Bosse, J.B., Whittle, C., Klupp, B.G., Siebert, C.A., Vasishtan, D., Bäuerlein, F.J.B., Cheleski, J., Werner, S., Guttmann, P., Rehbein, S., Henzler, K., Demmerle, J., Adler, B., Koszinowski, U., Schermelleh, L., Schneider, G., Enquist, L.W., Plitzko, J.M., Mettenleiter, T.C., Grünewald, K., 2015. Structural basis of vesicle formation at the inner nuclear membrane. Cell 163, 1692–1701.

Herrmann, H., Bär, H., Kreplak, L., Strelkov, S.V., Aebi, U., 2007. Intermediate filaments: from cell architecture to nanomechanics. Nat. Rev. Cell Biol. 8, 562–573.

Hoyer, P., de Medeiros, G., Balázs, B., Norlin, N., Besir, C., Hanne, J., Kräusslich, H.-G., Engelhardt, J., Sahl, S.J., Hell, S.W., Hufnagel, L., 2016. Breaking the diffraction limit of light-sheet fluorescence microscopy by RESOLFT. Proc. Natl. Acad. Sci. U. S.A. 113, 3442–3446.

Ibiricu, I., Huiskonen, J.T., Dohner, K., Bradke, F., Sodeik, B., Grünewald, K., 2011. Cryo electron tomography of herpes simplex virus during axonal transport and secondary envelopment in primary neurons. PLoS Pathog. 7, e1002406.

Kollman, J.M., Polka, J.K., Zelter, A., Davis, T.N., Agard, D.A., 2010. Microtubule nucleating gamma-TuSC assembles structures with 13-fold microtubule-like symmetry. Nature 466, 879–882.

Koning, R.I., Zovko, S., Bárcena, M., Oostergetel, G.T., Koerten, H.K., Galjart, N., Koster, A.J., Mieke Mommaas, A., 2008. Cryo electron tomography of vitrified fibroblasts: microtubule plus ends in situ. J. Struct. Biol. 161, 459–468.

Koster, A.J., Grimm, R., Typke, D., Hegerl, R., 1997. Perspectives of molecular and cellular electron tomography. J. Struct. Biol. 120, 276–308.

Kremer, J.R., Mastronarde, D.N., McIntosh, J.R., 1996. Computer visualization of three-dimensional image data using IMOD. J. Struct. Biol. 116, 1–6.

Li, X., Mooney, P., Zheng, S., Booth, C.R., Braunfeld, M.B., Gubbens, S., Agard, D.A., Cheng, Y., 2013. Electron counting and beam-induced motion correction enable near-atomic-resolution single-particle cryo-EM. Nat. Methods 10, 584–590.

Mahamid, J., Schampers, R., Persoon, H., Hyman, A.A., Baumeister, W., Plitzko, J.M., 2015. A focused ion beam milling and lift-out approach for site-specific preparation of frozen-hydrated lamellas from multicellular organisms. J. Struct. Biol. 192, 262–269.

Mahamid, J., Pfeffer, S., Schaffer, M., Villa, E., Danev, R., Cuellar, L.K., Förster, F., Hyman, A.A., Plitzko, J.M., Baumeister, W., 2016. Visualizing the molecular sociology at the HeLa cell nuclear periphery. Science 351, 969–972.

Mastronarde, D.N., 1997. Dual-axis tomography: an approach with alignment methods that preserve resolution. J. Struct. Biol. 120, 1–10.

Mastronarde, D.N., 2005. Automated electron microscope tomography using robust prediction of specimen movements. J. Struct. Biol. 152, 36–51.

Matthies, D., Dalmas, O., Borgnia, M.J., Dominik, P.K., Merk, A., Rao, P., Reddy, B.G., Islam, S., Bartesaghi, A., Perozo, E., Subramaniam, S., 2016. Cryo-EM structures of the magnesium channel CorA reveal symmetry break upon gating. Cell 164, 747–756.

McMullan, G., Faruqi, A.R., Clare, D., Henderson, R., 2014. Comparison of optimal performance at 300 keV of three direct electron detectors for use in low dose electron microscopy. Ultramicroscopy 147, 156–163.

Murata, K., Liu, X., Danev, R., Jakana, J., Schmid, M.F., King, J., Nagayama, K., Chiu, W., 2010. Zernike phase contrast cryo-electron microscopy and tomography for structure determination at nanometer and subnanometer resolutions. Struct. Fold. Des. 18, 903–912.

Nicastro, D., Schwartz, C., Pierson, J., Gaudette, R., Porter, M.E., McIntosh, J.R., 2006. The molecular architecture of axonemes revealed by cryoelectron tomography. Science 313, 944–948.

Pettersen, E.F., Goddard, T.D., Huang, C.C., Couch, G.S., Greenblatt, D.M., Meng, E.C., Ferrin, T.E., 2004. UCSF Chimera–a visualization system for exploratory research and analysis. J. Comput. Chem. 25, 1605–1612.

Rigort, A., Bauerlein, F.J.B., Villa, E., Eibauer, M., Laugks, T., Baumeister, W., Plitzko, J. M., 2012. Focused ion beam micromachining of eukaryotic cells for cryoelectron tomography. Proc. Natl. Acad. Sci. U.S.A. 109, 4449–4454.

Roberts, A.J., Numata, N., Walker, M.L., Kato, Y.S., Malkova, B., Kon, T., Ohkura, R., Arisaka, F., Knight, P.J., Sutoh, K., Burgess, S.A., 2009. AAA+ ring and linker swing mechanism in the dynein motor. Cell 136, 485–495.

Schellenberger, P., Kaufmann, R., Siebert, C.A., Hagen, C., 2014. High-precision correlative fluorescence and electron cryo microscopy using two independent alignment markers. Ultramicroscopy 143, 41–51.

Schermelleh, L., Carlton, P.M., Haase, S., Shao, L., Winoto, L., Kner, P., Burke, B., Cardoso, M.C., Agard, D.A., Gustafsson, M.G.L., Leonhardt, H., Sedat, J.W., 2008. Subdiffraction multicolor imaging of the nuclear periphery with 3D structured illumination microscopy. Science 320, 1332–1336.

Schorb, M., Briggs, J.A.G., 2014. Correlated cryo-fluorescence and cryo-electron microscopy with high spatial precision and improved sensitivity. Ultramicroscopy 143, 24–32.

Schur, F.K.M., Hagen, W.J.H., Rumlová, M., Ruml, T., Müller, B., Kräusslich, H.-G., Briggs, J.A.G., 2015. Structure of the immature HIV-1 capsid in intact virus particles at 8.8 Å resolution. Nature 517, 505–508.

Sirohi, D., Chen, Z., Sun, L., Klose, T., Pierson, T.C., Rossmann, M.G., Kuhn, R.J., 2016. The 3.8 Å resolution cryo-EM structure of Zika virus. Science 352, 467–470.

Tang, G., Peng, L., Baldwin, P.R., Mann, D.S., Jiang, W., Rees, I., Ludtke, S.J., 2007. EMAN2: an extensible image processing suite for electron microscopy. J. Struct. Biol. 157, 38–46.

Wodrich, H., Henaff, D., Jammart, B., Segura-Morales, C., Seelmeir, S., Coux, O., Ruzsics, Z., Wiethoff, C.M., Kremer, E.J., 2010. A capsid-encoded PPxY-motif facilitates adenovirus entry. PLoS Pathog. 6, e1000808.

Wolff, G., Hagen, C., Grünewald, K., Kaufmann, R., 2016. Towards correlative super-resolution fluorescence and electron cryo-microscopy. Biol. Cell (in Press).

Woodward, C.L., Mendonça, L.M., Jensen, G.J., 2015. Direct visualization of vaults within intact cells by electron cryo-tomography. Cell. Mol. Life Sci. 72, 3401–3409.

Xiong, Q., Morphew, M.K., Schwartz, C.L., Hoenger, A.H., Mastronarde, D.N., 2009. CTF determination and correction for low dose tomographic tilt series. J. Struct. Biol. 168, 378–387.

Zeev-Ben-Mordehai, T., Vasishtan, D., Hernández Durán, A., Vollmer, B., White, P., Prasad Pandurangan, A., Siebert, C.A., Topf, M., Grünewald, K., 2016. Two distinct trimeric conformations of natively membrane-anchored full-length herpes simplex virus 1 glycoprotein B. Proc. Natl. Acad. Sci. U.S.A. 113, 4176–4181.

Please cite this article in press as: Grange, M., et al. Cellular electron cryo tomography and *in situ* sub-volume averaging reveal the context of microtubule-based processes. J. Struct. Biol. (2016), http://dx.doi.org/10.1016/j.jsb.2016.06.024

Supplementary Material

Supplemental Figures

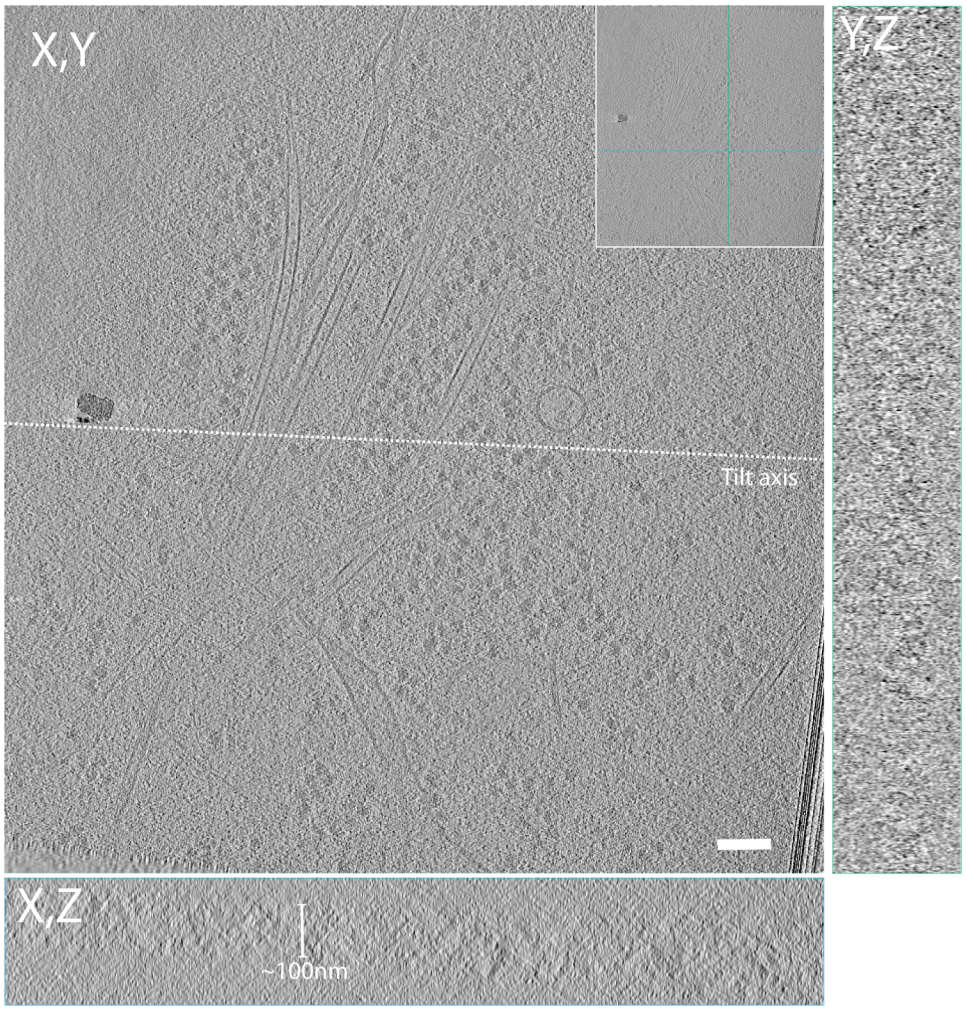

Figure S1 – Tomographic slices in 3-dimensions (XY, XZ and YZ) of U87MG tomogram used for analyses in Figure 1 and 2. Inse shows the position of XZ (blue line) and YZ (green line) in relation to the XY slice. Scale = 100nm

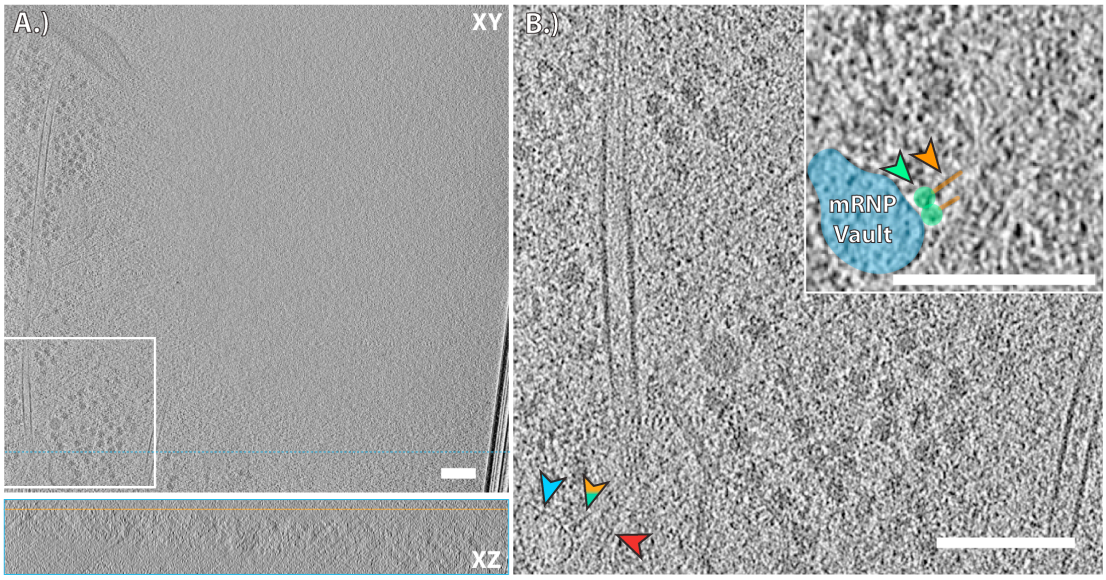

Figure S2 – Structural context of Vault protein in relation to the tomographic volume shown in Figure 1. (A) Box outlined by a dashed line in the XY slice (along the orange line in XZ; XZ sliced along the blue line XY) indicates the position of vault within the tomogram. (B) zoom into area inside the white box in (A). The blue arrow and area (inset) highlights the position of the ribonucleoprotein Vault, the green/orange arrows highlight the dynein dimer (green = AAA+ domain and orange = stalk domain) and the red arrow highlights the top of the microtubule in contact with the dynein dimer. Scale bars = 100nm.

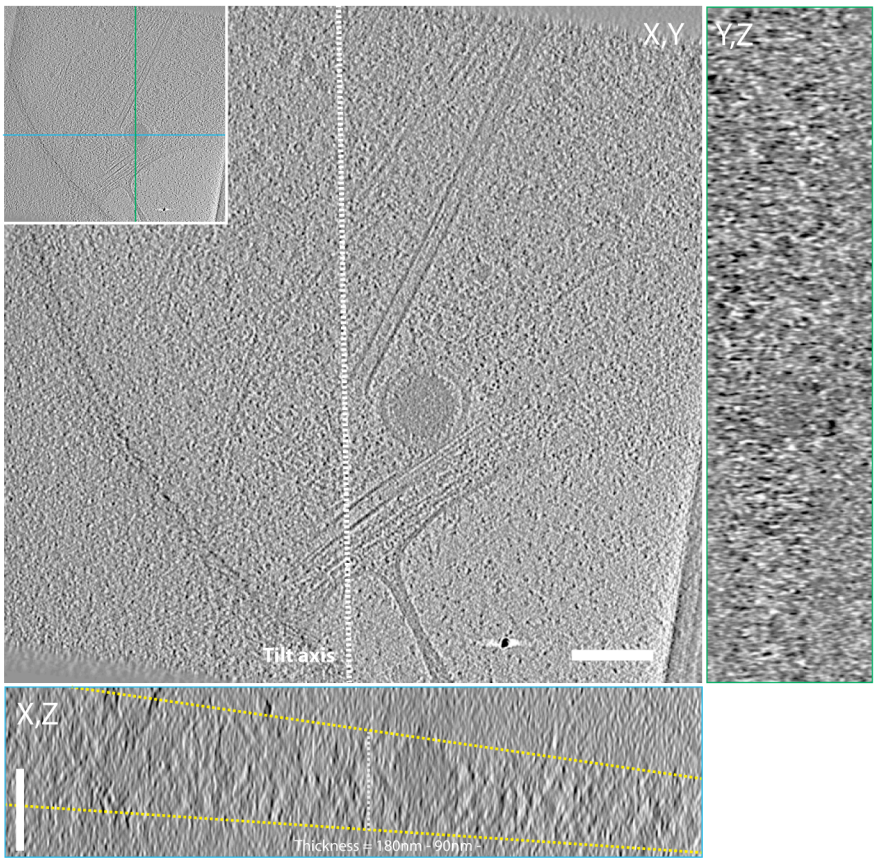

Figure S3 – Tomographic slices in 3-dimensions (XY, XZ and YZ) of U2OS tomogram used for analysis in Figure 3. Inset shows the position of XZ (blue line) and YZ (green line) in relation to the XY slice. Yellow lines indicate the thickness of the ice. Scale = 100nm.

14
15

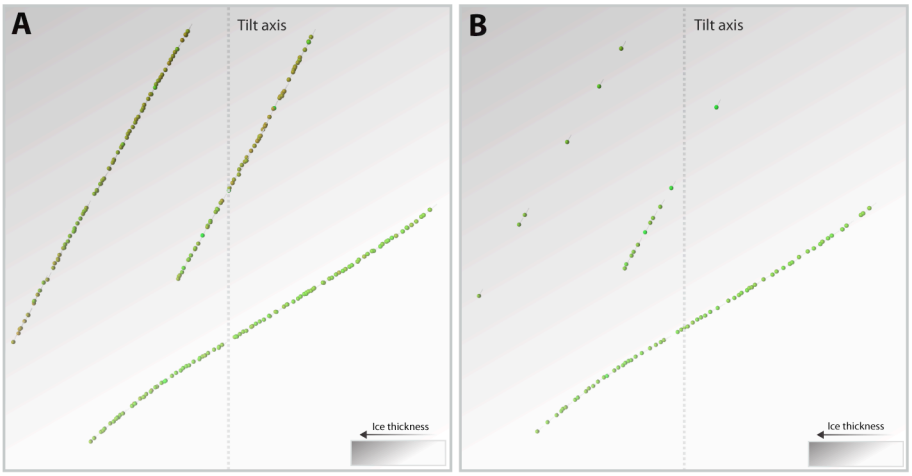

Figure S4 – Model of the linear model used to determine the microtubule structure in Figure 3. **A)** Orange/green spheres determine the position relative to the tilt axis of sub-volumes with high (green) and low (orange) cross correlation to the average. **B)** Model of sub-volumes after removal with a cross correlation of 0.2. Black and white gradient in both **A** and **B** approximated the thickness gradient across the tomogram.

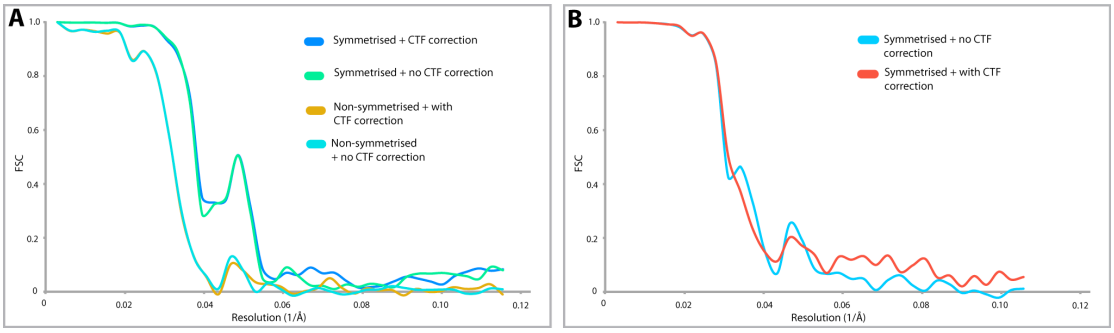

Figure S5 – Comparison of "gold standard" FSC curves for CTF and non-CTF determined structures for **A)** U87MG tomogram and **B)** U2OS tomogram.

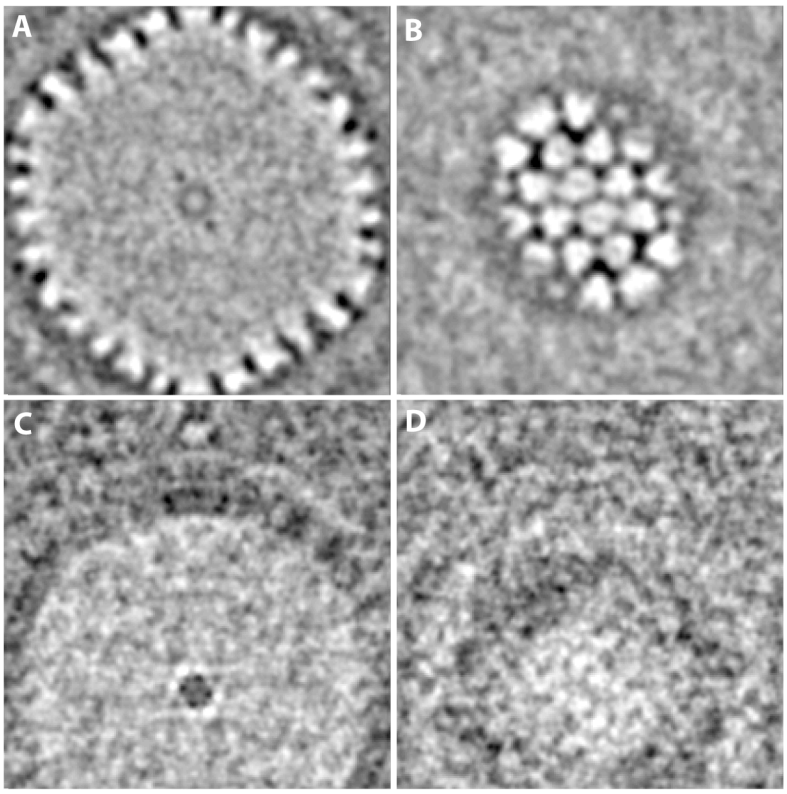

Figure S6 – Symmetrized structure of the Adenovirus in the U2OS tomogram. **A)** and **B)** shows the middle and top slice, respectively, of the adenovirus structure shown in Figure 3 after symmetrization of the virus using the refined Euler angles resulting from an orientation search for EMDB-1574 filtered to 20Å. **C)** and **D)** shows the middle and top slice, respectively, prior to any refinement, rotationally or translationally, against EMDB-1574.

16

17

Tomogram:	**U87MG Cell**	**U2OS Cell**
Nominal microscope defocus (µm)	-5.0	-4.0
Reported defocus range in acquisition (µm)	-5.13 to -4.57	-4.16 to -3.49
Calculated defocus (µm)	-3.19	-5.39
Total Dose ($eÅ^{-2}$)	72.4	75.2
No. particles before symmetrisation	312	148
No. particles after symmetrisation	4056	1924
Tilt range (degrees)	-57 to +60	-45 to +45
Tilt sampling (degrees)	3	3
Calibrated magnification	11848x	21739x
Calibrated pixel size of average (Å)	4.22	4.6 (2.3 unbinned)
Approximate ice thickness (nm)	80-100	150-180

Table S1 – Table of parameters used for acquisition and sub-volume averaging of the microtubules from the U87MG and U2OS cell lines.

Article

Cell

Structural Basis of Vesicle Formation at the Inner Nuclear Membrane

Graphical Abstract

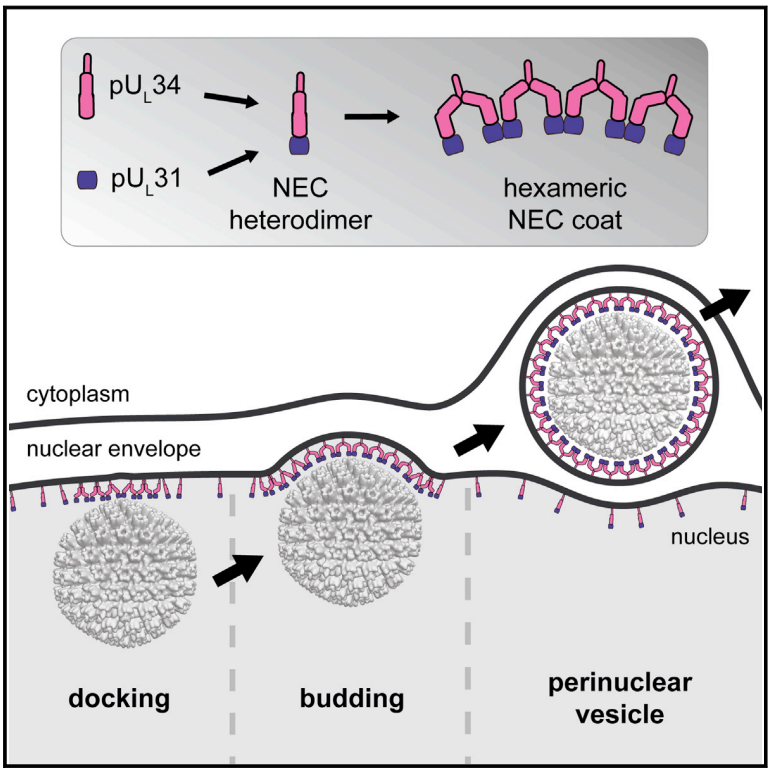

Authors

Christoph Hagen, Kyle C. Dent, Tzviya Zeev-Ben-Mordehai, ..., Jürgen M. Plitzko, Thomas C. Mettenleiter, Kay Grünewald

Correspondence

thomas.mettenleiter@fli.bund.de (T.C.M.), kay@strubi.ox.ac.uk (K.G.)

In Brief

A multi-modal live-cell and cryo-imaging approach reveals how vesicles assemble at the inner nuclear membrane for transport to the cytoplasm during herpesvirus maturation. This also suggests a functional model for counterparts in uninfected cells that mediate nuclear egress of large cargo like ribonucleoprotein particles.

Highlights

- Multimodal imaging reveals mechanism of vesicle formation at inner nuclear membrane
- Nucleo-cytoplasmic cargo vesicle coat in situ comprises two distinct lattices
- Lattices are formed by hexameric building blocks made of the nuclear egress complex
- Induction of membrane curvature based solely on heterodimeric interactions

Hagen et al., 2015, Cell *163*, 1692–1701
December 17, 2015 ©2015 The Authors
http://dx.doi.org/10.1016/j.cell.2015.11.029

CrossMark

CellPress

Cell

Article

Structural Basis of Vesicle Formation at the Inner Nuclear Membrane

Christoph Hagen,[1,9] Kyle C. Dent,[1,2,9] Tzviya Zeev-Ben-Mordehai,[1,9] Michael Grange,[1,9] Jens B. Bosse,[3,9,10] Cathy Whittle,[1] Barbara G. Klupp,[4] C. Alistair Siebert,[1] Daven Vasishtan,[1] Felix J.B. Bäuerlein,[5] Juliana Cheleski,[1] Stephan Werner,[6] Peter Guttmann,[6] Stefan Rehbein,[6] Katja Henzler,[6,11] Justin Demmerle,[7] Barbara Adler,[8] Ulrich Koszinowski,[8] Lothar Schermelleh,[7] Gerd Schneider,[6] Lynn W. Enquist,[3] Jürgen M. Plitzko,[5] Thomas C. Mettenleiter,[4,*] and Kay Grünewald[1,*]

[1]Oxford Particle Imaging Centre, Division of Structural Biology, Wellcome Trust Centre for Human Genetics, University of Oxford, Roosevelt Drive, Oxford OX3 7BN, UK

[2]Diamond Light Source Ltd., Harwell Science and Innovation Campus, Didcot OX11 0DE, UK

[3]Department of Molecular Biology, Princeton Neuroscience Institute, Princeton University, Washington Road, Princeton, NJ 08544, USA

[4]Institute of Molecular Virology and Cell Biology, Friedrich-Loeffler-Institut, 17493 Greifswald-Insel Riems, Germany

[5]Department of Molecular Structural Biology, Max Planck Institute of Biochemistry, Am Klopferspitz 18, 82152 Martinsried, Germany

[6]Helmholtz Zentrum Berlin für Materialien und Energie GmbH, Wilhelm-Conrad-Röntgen Campus, 12489 Berlin, Germany

[7]Micron Oxford, Department of Biochemistry, University of Oxford, South Parks Road, Oxford OX1 3QU, UK

[8]Max von Pettenkofer-Institut, Ludwig-Maximilians-Universität München, Pettenkoferstr. 9a, 80336 Munich, Germany

[9]Co-first author

[10]Present address: Heinrich-Pette-Institute, Leibniz-Institute of Experimental Virology, Martinistrasse 52, 20251 Hamburg, Germany

[11]Present address: Paul Scherrer Institut, Swiss Light Source, 5232 Villigen PSI, Switzerland

*Correspondence: thomas.mettenleiter@fli.bund.de (T.C.M.), kay@strubi.ox.ac.uk (K.G.)

http://dx.doi.org/10.1016/j.cell.2015.11.029

This is an open access article under the CC BY license (http://creativecommons.org/licenses/by/4.0/).

SUMMARY

Vesicular nucleo-cytoplasmic transport is becoming recognized as a general cellular mechanism for translocation of large cargoes across the nuclear envelope. Cargo is recruited, enveloped at the inner nuclear membrane (INM), and delivered by membrane fusion at the outer nuclear membrane. To understand the structural underpinning for this trafficking, we investigated nuclear egress of progeny herpesvirus capsids where capsid envelopment is mediated by two viral proteins, forming the nuclear egress complex (NEC). Using a multi-modal imaging approach, we visualized the NEC in situ forming coated vesicles of defined size. Cellular electron cryo-tomography revealed a protein layer showing two distinct hexagonal lattices at its membrane-proximal and membrane-distant faces, respectively. NEC coat architecture was determined by combining this information with integrative modeling using small-angle X-ray scattering data. The molecular arrangement of the NEC establishes the basic mechanism for budding and scission of tailored vesicles at the INM.

INTRODUCTION

Intracytoplasmic transport between compartments is primarily mediated by vesicles (Schekman and Orci, 1996). These vesicles are shaped by specific coat proteins that are recruited to the site of assembly and function to deform the membrane (McMahon and Gallop, 2005). In contrast, movement into and out of the nucleus is effected by "gated transport" via the nuclear pore complexes (NPCs). NPCs allow free diffusion of small molecules and can mediate active transport of cargo up to ~39 nm in diameter (Panté and Kann, 2002). Larger macromolecular assemblies, however, are unable to pass through the NPC. Recently, vesicular trafficking was reported to mediate nucleo-cytoplasmic transport of ribonucleoprotein particles (Speese et al., 2012). This non-canonical pathway across the nuclear double membrane involves vesicle formation at the INM and fusion at the outer nuclear membrane (ONM). Another suggested role of this pathway is in nuclear recycling, i.e., transport of nuclear protein aggregates like defective NPC assembly intermediates to the cytosolic autophagy machinery for degradation (Rose and Schlieker, 2012; Webster et al., 2014).

The ribonucleoprotein particle transport mechanism is in many respects similar to nuclear egress of herpesviruses discovered a decade earlier (Mettenleiter et al., 2013). In the latter, ~125-nm-diameter icosahedral herpesvirus capsids assemble inside the nucleus and use vesicle-mediated transport across the nuclear envelope to gain access to the cytoplasm for further maturation. The combined evidence from the cellular ribonucleoprotein particle and viral capsid transport systems makes it likely that vesicle transport represents a general mechanism for translocation of large cargo from the nucleus to the cytoplasm that herpesviruses have usurped during evolution. Whereas the overall topology of the process of herpesvirus nuclear egress resembles cellular vesicle trafficking, little is known about the nanostructural details that lead to formation, scission, and fusion of INM-derived vesicles. Studied already in great biological detail, herpesvirus nuclear egress therefore represents a unique tractable model system

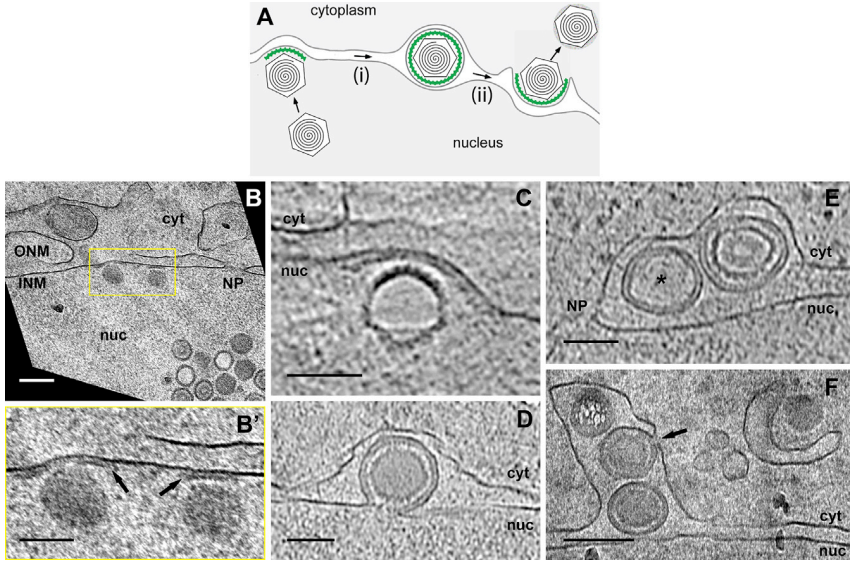

Figure 1. The NEC in the Replication Cycle of Herpesvirus

(A) Schematic of the stages of vesicle-mediated herpesvirus capsid nuclear egress, consisting of (i) primary envelopment by the NEC (green) at the INM and (ii) fusion of the vesicle with the ONM, resulting in de-envelopment to release the capsid into the cytoplasm.

(B–F) Developmental stages of the NEC coat in HSV-1-infected Vero cells (moi: 10, 16 hr p.i.) analyzed by electron cryo-microscopy of vitreous sections (CEMOVIS). (B) Projection image taken after pre-irradiation; nominal section feed: 30 nm; compression: 47%, corrected. (B′) Magnification of the yellow box marked in (B) (arrows: NEC coat). (C–E) Slices of tomographic reconstructions (C and D: nominal section feed, 100 nm; compression, 13%, 3D-corrected; E: nominal section feed, 50 nm; compression, 26%, 3D-corrected; asterisk, ILV; Movies S1 and S2). (F) Projection image taken after pre-irradiation; nominal section feed, 30 nm; compression, 47%, corrected. Scale bar, 200 nm (B and F) and 100 nm (B′–E). cyt, cytoplasm; INM, inner nuclear membrane; NP, nuclear pore; nuc, nucleus; ONM, outer nuclear membrane.

to delineate the general structural and functional basis of nucleo-cytoplasmic vesicle transport.

Studies of herpesvirus nuclear egress showed that, during infection, newly formed intranuclear capsids bud at the INM (Figure 1A) followed by membrane scission, resulting in enveloped capsids located in the perinuclear space. The envelope then fuses with the ONM to deliver the capsids to the cytoplasm. A large body of experimental studies has established that, throughout the *Herpesviridae*, two viral proteins, designated as pU_L31 and pU_L34 in the alphaherpesviruses herpes simplex virus 1 (HSV-1) and pseudorabies virus (PrV), form the heterodimeric nuclear egress complex (NEC; Figure 1A, green). The NEC is required and sufficient for vesicle formation, i.e., budding and scission, at the INM (Klupp et al., 2007; Mettenleiter et al., 2013). The C terminus of the type II membrane protein pU_L34 tethers the NEC to the INM, while pU_L31 is exposed to the nucleoplasm. pU_L31 then associates with the capsid surface in the lumen of the nascent perinuclear vesicle. After vesicle fusion with the ONM and release of the capsid, the NEC is exposed to the cytoplasm (Mettenleiter et al., 2013). NEC components are also likely to mediate cargo selection (Funk et al., 2015). Additionally, kinases recruited to the NEC are responsible for phosphorylation of lamins for local dissolution of the nuclear lamina to allow access of capsids to the INM (Hatch and Hetzer, 2014; Mettenleiter et al., 2013) and for phosphorylation of NEC components (Mou et al., 2009; Sharma et al., 2015). Whereas this prototypic budding process at the INM and its components are well characterized, the fusion process with the ONM is still under debate, including a possible role of viral fusogenic glycoproteins (Mettenleiter et al., 2013).

Recently, in vitro studies showed that partially truncated NEC components artificially membrane tethered to giant unilamellar vesicles formed a coat that can function as a minimal virus-encoded vesiculation machinery, not requiring additional viral or cellular factors (Bigalke et al., 2014). Furthermore, artificial membrane tethering of pU_L31 alone was sufficient for induction of membrane invaginations and membrane scission in giant unilamellar vesicles (Lorenz et al., 2015). However, owing in part to the reduced complexity of the models used, these studies did not provide sufficient ultrastructural detail to elucidate the architecture and functionality of the NEC coat. Thus, we here investigated the NEC in its native location, in vesicles at the periphery of the nucleus.

The size of the nucleus makes it a challenging target for visualization of intra-nuclear structures at molecular resolution in situ. Nevertheless, by applying an integrated multi-modal approach that enabled near-native imaging over variable scales and resolutions (Zeev-Ben-Mordehai et al., 2014), we were able to characterize in detail both the extent of nuclear membrane remodeling and the architecture of the NEC at the INM. We first show in cryo-sections of herpesvirus-infected cells that the NEC forms a protein coat that lines capsid-containing perinuclear vesicles during egress. We then characterize the ultrastructure of NEC-coated vesicles in non-infected cells that co-express pU_L31 and pU_L34. Further, that latter experimental system provided a higher frequency of these vesicles, allowing successful cellular electron cryo-tomography of lamellae prepared by advanced focused ion beam cryo-milling (cryoFIB). Subsequent three-dimensional averaging of the NEC coat revealed that it forms an ordered lattice with two different hexameric faces. X-ray scattering data of solubilized NEC complexes, combined with integrated modeling, allowed us to determine that these two faces represent pU_L34 anchored in the vesicle membrane and pU_L31 forming the inner layer. The unique structure and interactions between the two protein layers result in a defined membrane curvature, ensuring that viral capsids are tightly enveloped. Our data reveal how formation of correctly sized perinuclear vesicles is achieved and establish a mechanistic basis for nucleo-cytoplasmic transport of large cargoes.

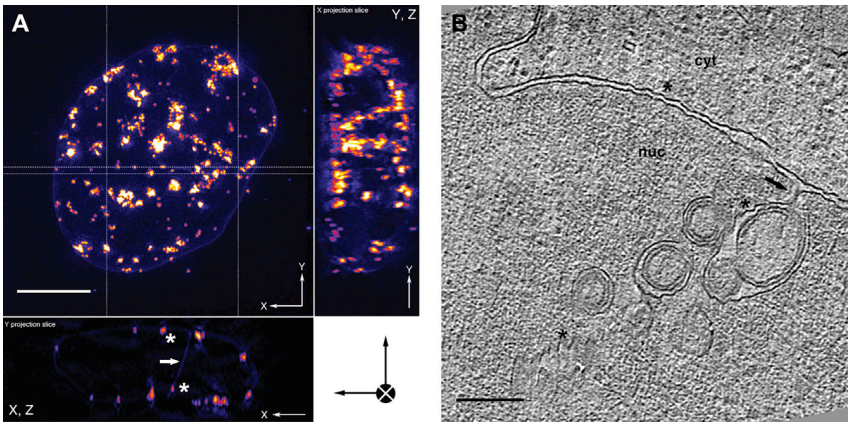

Figure 2. Nuclear Ultrastructure in PrV pU_L31/pU_L34-GFP Co-Expressing Cells

(A) Slices through a 3D volume of a porcine epithelial-like embryonic kidney cell determined by live-cell 3D-SIM at 37°C (~120 nm lateral resolution). The cell nucleus, as well as features of the nuclear envelope (arrow, tubular invagination; asterisks, vesicle clusters or "speckles"), are highlighted by stably co-expressing PrV pU_L31 and pU_L34, the latter fused to GFP. Thickness of XZ and YZ projections is indicated by dashed lines in the XY projection (for 3D volume, see Movie S3). Scale bar, 5 μm.

(B) A slice of a CEMOVIS tomographic reconstruction of the nuclear periphery of a proteinase-K-detached BK cell cryo-immobilized after 2 days standard cultivation (nominal section feed, 100 nm; compression, 13%, 3D-corrected) depicts the typical size range of ILVs in an invagination of the INM (arrow, "stalk" region; asterisks, membrane crevasses). Scale bar, 200 nm. cyt, cytoplasm; nuc, nucleus.

RESULTS AND DISCUSSION

In Situ Structural Characterization of NEC-Mediated Capsid Envelopment at the INM by CEMOVIS

To analyze the NEC coat formed in situ during viral infection in its most native environment, we used electron cryo-microscopy and tomography (cryoEM/T) (Hoenger, 2014). CryoET imaging of areas deeper inside cells typically requires vitreous sections in order to provide electron transparent specimens of <500 nm thickness (Lučić et al., 2005). In electron cryo-microscopy of vitreous sections (CEMOVIS), a method for imaging hydrated and unstained cellular ultrastructural detail (Dubochet, 2012), NECs were observed as electron-dense coats at the nucleoplasmic side of the INM and in the perinuclear space of HSV-1-infected Vero cells (Figures 1B–1F and Movies S1 and S2). When nuclear capsids were in close contact to the INM, a planar NEC coat of ~100 nm diameter, i.e., about the width of the capsid, was observed (Figure 1B′, right HSV-1 capsid). The coat curved and expanded during budding of the INM into the perinuclear space (Figure 1B′, left HSV-1 capsid). Interestingly, the electron-dense NEC coat did not extend beyond the individual sites of budding (Figures 1C and 1D and Movie S1). Ultimately, the NEC formed a tightly fitting complete coat around the capsid (Figures 1D–1F and Movies S1 and S2). In HSV-1-infected Vero cells, not only DNA-filled C-capsids underwent primary envelopment (Figures 1B, 1D, and 1F), but also empty A-capsids (Figure 1C) and scaffold-containing immature B-capsids (Figure 1E, right vesicle). Intraluminal vesicles (ILVs, defined as possessing the NEC coat but lacking capsids; Figure 1E, asterisk; Movie S2) represented 34% of all observed perinuclear vesicles in HSV-1-infected Vero cells (14 of 41 vesicles, from 21 tomograms total), with a mean inner diameter of 115 nm ± 11 nm SD (n = 12). During de-envelopment, the NEC coat was left behind at the cytoplasmic face of the outer nuclear membrane (Figure 1F, arrow), and cytoplasmic capsids, now devoid of the NEC coat, subsequently underwent virion assembly (Figure 1F, right, and Movie S2, right upper-corner). This result contradicts previous conclusions drawn on the basis of interpreting densities in heavy-metal-stained, freeze-substituted, plastic-embedded samples (Wild et al., 2015) and is in line with the absence of pU_L31 and pU_L34 in extracellular HSV-1 virions (Loret et al., 2008).

A grainy nature of the NEC coat was readily visible in computational slices through cryoET reconstructions (Figures 1C–1E and Movies S1 and S2), suggesting a modular lattice-type architecture consisting of repetitive units. To analyze the structure and function of this coat in greater detail, a multimodal imaging approach was needed, spanning several length scales and covering from the nuclear distribution of its fully assembled form down to interactions of its single constituents.

Nuclear Ultrastructure in an In Situ Cell Model for Elucidating the NEC Architecture

In HSV-1-infected cells, the number of capsid envelopment events captured at the INM was low. Therefore, we used a previously described porcine cell line that stably co-expresses pU_L31 and pU_L34 of PrV as a model frequently showing NEC-mediated vesicle formation (Klupp et al., 2007). In this BK cell line, pU_L34 is anchored to the INM by its authentic C-terminal transmembrane region, with the C-terminal GFP tag exposed on the vesicle outside, i.e., on the opposite membrane side of the NEC. Tagging allowed visualization of the NEC in vivo. By using three-dimensional structured illumination microscopy (3D-SIM) (Schermelleh et al., 2010), volumetric live-cell imaging of the nucleus at sub-diffraction resolution was achieved. This revealed clusters of fluorescent speckles of ~160–1,500 nm diameter at multiple sites around the nuclear periphery, as well as within the nuclear interior along membranous invaginations (Figures 2A and Movie S3). These clusters represent accumulations of NEC-containing vesicles in the perinuclear space (Klupp et al., 2007) and were intensely fluorescent, suggesting high local concentrations of pU_L34-GFP.

Imaging of similar regions of BK cells at higher resolution by soft X-ray cryo-microscopy/tomography, guided by correlation with GFP fluorescence (Hagen et al., 2012), provided detailed information about the spatial distribution of the NEC-containing target structures/vesicle clusters throughout the nucleus (Figure S1 and Movies S4 and S5). The ultrastructure of these

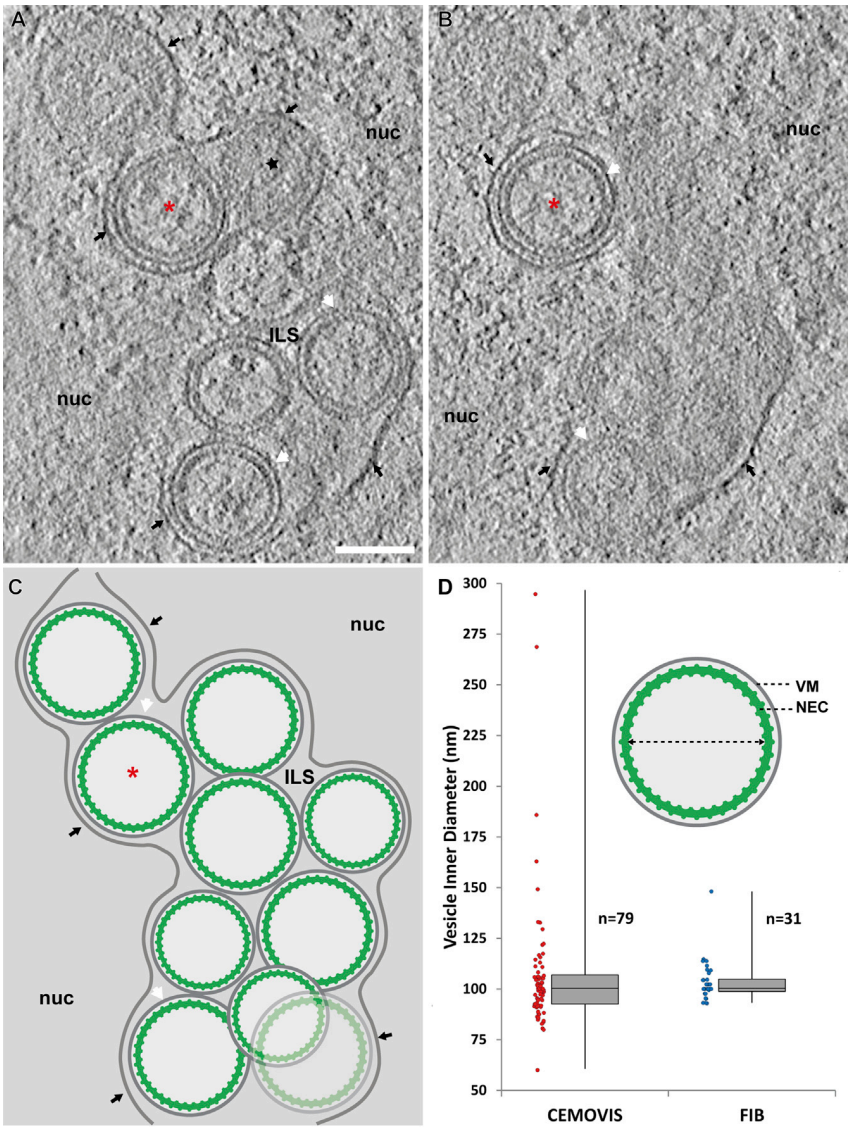

Figure 3. Ultrastructural Characterization of a Cluster of ILVs by CryoFIB/ET

(A–C) Slices through an electron cryo-tomogram of a lamella prepared by cryoFIB, interpreted schematically in (C). Vesicles not shown in the experimental map slices are depicted semi-transparently (Movie S6). ILVs are tightly surrounded by the INM (black arrows) and are closely related in size, exhibiting diffuse contents. The NEC coat (green) appears to nearly cover the entire inner surface of the vesicle membrane (white arrows). A fuzzy layer of density attributed, at least partly, to the C-terminal GFP of the type II transmembrane protein construct pU_L34-GFP, surrounds each vesicle and projects into the intraluminal/perinuclear space (ILS). Inspection of tangential slices (example: black star) suggests that imperfections in the lattice arrangement of the NEC coat do occur but that these likely represent only a small fraction of the total vesicle surface area. Red asterisks highlight a near spherical vesicle from which measurements of NEC coat parameters were taken. Scale bar, 100 nm. nuc, nucleus.

(D) Boxplot of the distribution of vesicle sizes (vesicle inner diameter: dashed line in inset vesicle) measured in 3D from BK cells prepared for tomographic electron imaging by CEMOVIS (red) and cryoFIB (blue). The distributions share a median of ~100 nm. VM, vesicle membrane.

intranuclear vesicle clusters was next characterized in 3D by CEMOVIS (Figure 2B), resulting in visualization of vesicles with a grainy inner NEC coat and a mean inner diameter of 107 ± 33 nm SD (n = 79). These vesicles were closely similar in size and structure to the capsid-less ILVs in infected cells (Figure 1E, asterisk).

Characterization of larger volumes by serial CEMOVIS sections enabled us to localize and characterize the occurrence of repetitive NEC structures/lattices suited for sub-tomogram averaging, even in rare developmental states (Figure 1). An alternative cryo-thinning technique, cryoFIB, has recently been developed to produce 100–300 nm thick lamellae from vitreous samples. This approach does not rely on physical cutting and, thereby, avoids sectioning artifacts (Marko et al., 2007; Rigort et al., 2012). CryoET data were recorded from cryoFIB-prepared lamellae of plunge-frozen BK cells. Perinuclear vesicles were typically spherical, although some exhibited a more irregular shape (Figures 3A–3C and Movie S6), possibly due to crowding. The NEC protein layer was evident as a clear lattice-like, ~10-nm-thick coat lining the entire inside of each vesicle with periodic connections to the vesicle membrane (Figures 3A and 3B). Size measurements of vesicles from three tomograms showed a peaked distribution with a mean inner diameter of 103 ± 10 nm SD (n = 31) (Figure 3D). The thickness of the coat and the size of ILVs in BK cells measured in 3D from CEMOVIS and cryoFIB-based data were in agreement (Figures 2B and 3 and Movie S6) and were similar to CEMOVIS data from HSV-1-infected Vero cells (Figure 1E). The vesicle diameters did not show a Gaussian distribution. Instead, the distribution is heavily skewed and peaked with very light tails (Figure 3D). These properties suggest that a specific mechanism inherent to NEC coat assembly is a predominant determinant of vesicle size, with positive skewness indicating a lower limit of the measured parameter.

Ultrastructure of the NEC Coat Lattice Revealed by Sub-Tomogram Averaging

The previous observations suggested a highly repetitive organization of the NEC protein layer. Taking different curvature into account, the structure of the NEC coat was therefore determined independently for each vesicle by sub-tomogram averaging from the cryoFIB/ET data (Figure 4). Each vesicle average revealed a curved hexagonal lattice composed of two

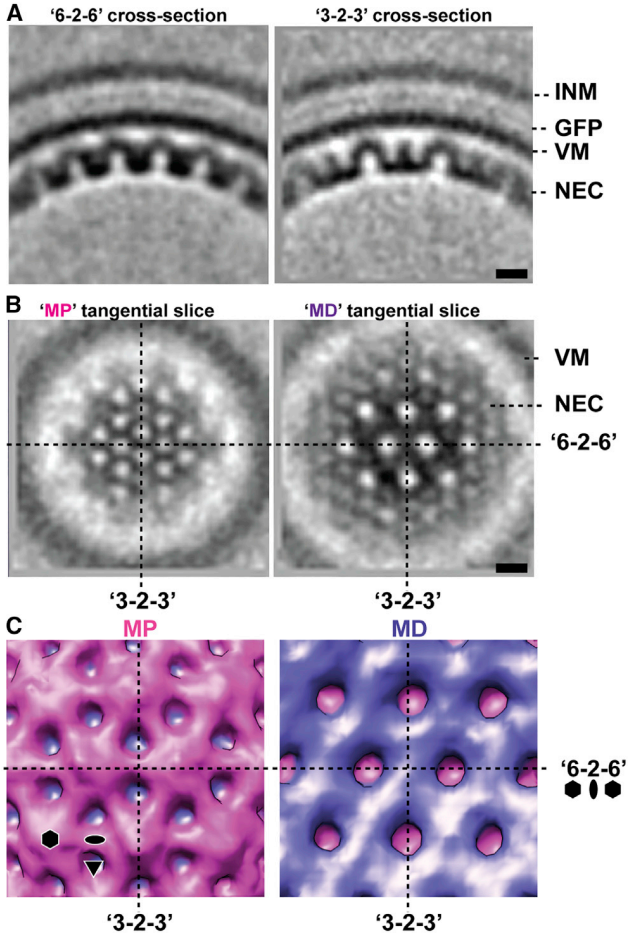

Figure 4. Sub-tomogram Averaging of the NEC Coat

(A) Sub-tomogram average (~3.5 nm resolution, Figure S2) viewed in characteristic "*6-2-6*" and "*3-2-3*" cross-section, oriented such that the slice passes through a 2-fold axis and intercepts adjacent 6-fold (Movie S7) or 3-fold axes, respectively. Scale bar, 10 nm. VM, vesicle membrane.

(B) Tangential slices through membrane proximal (MP) and membrane-distal (MD) layers (Movie S8). Each layer corresponds to *p6* symmetry with lattice spacing of ~11 nm. However, the MP layer exhibits a distinct arrangement of density that, at the available resolution, appears to correspond to a *p6* lattice with a spacing of ~6 nm and offset from the MD lattice by 30°. Scale bar, 10 nm.

(C) Surface views rendered from the vesicle exterior and the vesicle interior show characteristic features of the MP and MD layers, respectively (Movie S9). Symbols indicate symmetry axes (6-fold, 3-fold, and 2-fold).

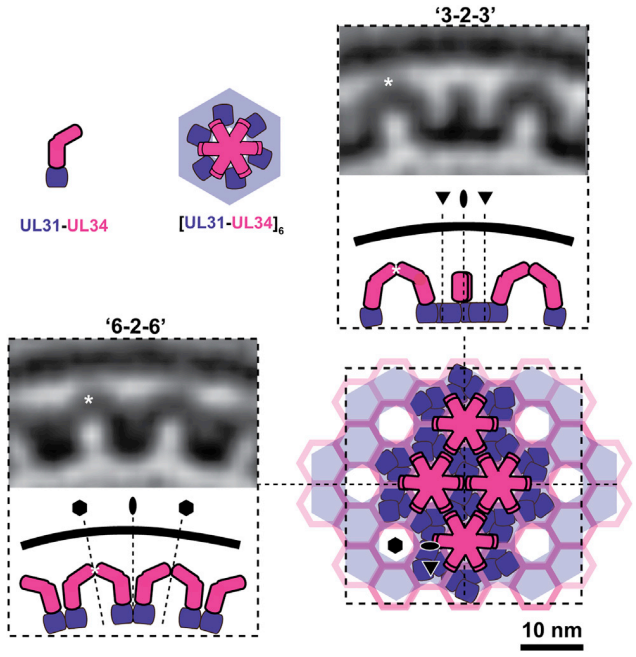

Figure 5. Interpretation of the NEC Coat Based on the Sub-tomogram Average

The initial architectural model of the NEC coat (lower-right) made from hexameric interactions of pU$_L$31/34 heterodimers (hexameric unit cell; upper-middle) is shown alongside characteristic cross-sectional views of the NEC coat average ("*6-2-6*" and "*3-2-3*" views shown in Figure 4A and "*6-2-6*" in Movie S7). An arch keystone is marked with a white asterisk. pU$_L$34 (magenta) and pU$_L$31 (purple) make up the MP and MD layers, respectively.

tightly interconnected layers of distinct appearance (Figures 4A, 4B, and S2 and Movies S7 and S8 [resolution 3.5–4 nm]). We termed the two NEC layers the membrane-proximal (MP) and membrane-distal (MD) layers. The MD layer is a ~3-nm-thick hexagonal lattice with a spacing between repeating unit centers of ~11.5 nm (purple), and the MP layer is ~7 nm thick (magenta) (Figure 4C and Movie S9). In cross-sections, the repeating unit of the NEC coat (a single hexagon) shared a characteristic "archway" motif—similar to an inverted 'U' (Figure 4A and Movie S7). The hexagonal unit could be further decomposed into a motif of angular appearance, one side of the archway, which appeared kinked at approximately two-thirds along its length. Thus, the MP layer consists of a conical arrangement of six independent densities that originate at the unit cell "keystone" extending toward the vesicle center to form an "arch" and connecting with the MD layer near the 2-fold axes. Densities connecting the arch/keystone of the unit cell to the vesicle membrane were already apparent in raw tomograms (Figure 3 and Movie S6) and became accentuated after sub-tomogram averaging (Figure 4A and Movie S7).

We assigned the MP layer to the membrane-anchored pU$_L$34 and the MD layer to pU$_L$31 (Figure 4C and Movie S9). The schematic interpretation shown in Figure 5 is based on analysis of tangential slices revealing the characteristic arrangements of protein density in each layer (Figure 4B and Movie S8). Orthogonal cross-section slices, shown adjacent to the model (Figure 5), reveal that the local curvature of the MD layer (pU$_L$31) is not isotropic. Between 3-fold axes ("*3-2-3*") the MD layer is distinctly planar, whereas between 6-fold axes ("*6-2-6*"), the curvature of MD is consistent with that of the vesicle membrane.

Integrative Modeling of the NEC Lattice Structure Using a Small-Angle X-Ray Scattering Envelope for the Soluble pU$_L$31/34 Heterodimer

The cryoFIB/ET sub-tomogram averages do not readily reveal the stoichiometry of pU$_L$31/34 heterodimers in the NEC coat. The schematic interpretation shown in Figure 5 suggests that

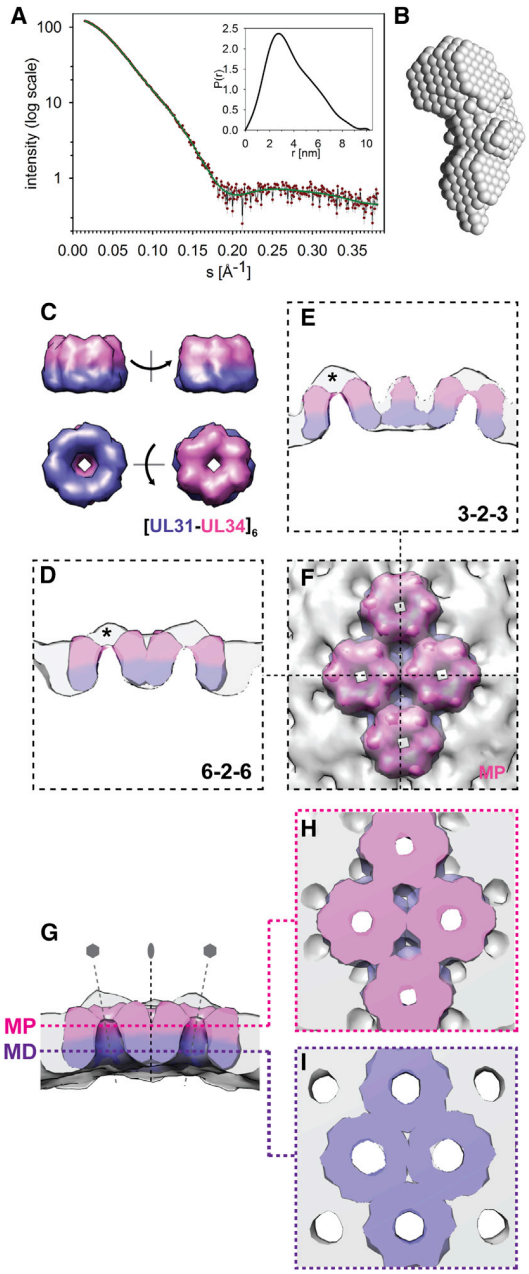

Figure 6. Stoichiometry of the pU$_L$31/34 Heterodimer within the NEC Coat, Based on SAXS Data

(A–F) (A) SAXS scattering curve for soluble PrV NEC (red circles; Figure S3) with the fit of the theoretical scattering curve calculated from the ab initio model (green line) and the respective size distribution (inset). (B) The ab initio heterodimeric model derived from the simulated annealing bead modeling of the 1D-SAXS curve. (C) Surface views of the SAXS-based hexameric model ([pU$_L$31/34]$_6$) accounting best for the cryoEM-derived density. One hexamer is rotated to show four views from different directions. (D–F) Four copies of [pU$_L$31/34]$_6$ fitted into the cryoEM map (transparent gray surface, compare Movie S10) are shown in both cross sections (D and E) as well as semi-transparent surface view from the vesicle exterior (F). Note the missing density at the center of each hexamer (the arch keystone, instances marked with a black asterisk in D and E), as the model is based on a SAXS model of a heterodimer with truncated pU$_L$34 (Figure S3B).

(G–I) The EM map of the NEC coat with four fitted hexameric SAXS-based models of soluble heterodimeric NEC is viewed from the side and sliced to remove density up to the "*6-2-6*" section passing through the map's center (G; for full hexamers, see Movie S10). The SAXS-derived model accounts for the EM density archways in all regions except the arch itself, thereby serving to validate the stoichiometry of our initial architectural model based on prediction of protein occupied volume. Tangential slices through the map at radii corresponding to MP (H) and MD (I) layers show that the "fitting search" using the SAXS-derived shape model is able to reproduce the characteristic features of the NEC coat (i.e., the two-layered arrangement) but also suggest that interactions between heterodimers occur predominantly across the 2-fold axis within both MD and MP layers, associated with pU$_L$31, and pU$_L$34, respectively.

the unit cell is composed of a hexamer of heterodimers ([pU$_L$31/34]$_6$). To independently validate the model, we characterized a soluble form of the PrV pU$_L$31/34 heterodimer (Figure S3) by small-angle X-ray scattering (SAXS) (Figure 6). We determined the shape of the soluble heterodimer by ab initio modeling from the 1D SAXS scattering curve (Figures 6A and 6B) (Franke and Svergun, 2009). The angular shape (87 nm^3 in volume, radius of gyration of 2.96 nm, and maximum dimension of 10.2 nm) was similar to that observed in the cryoEM sub-tomogram average as one side of the archway. To orient the soluble heterodimers within the cryoEM map, we carried out a fitting search using the SAXS model and sampled the full rotational range. By locally fitting multiple copies of the highest-scoring model into the cryoEM map, we were able to account for the cryoEM density as well as to reproduce its characteristic features (Figures 6C–6I and Movie S10). Together, this integrated modeling suggests that the NEC coat is composed of a ~10-nm-thick layer of interacting hexameric cores of NEC heterodimers in lateral self-association.

The densities of the MP layer leading to the membrane are not accounted for by the SAXS model (Figures 6D and 6E), consistent with it being the truncated sequence from pU$_L$34 that leads to the transmembrane domain (residues 180–240). The calculated mass from these residues (~40 kDa per hexamer) and the volume of the unaccounted density are congruent, confirming that the NEC coat consists only of pU$_L$31 and pU$_L$34, without direct contribution from any other viral or cellular factors, as was shown in vitro for HSV-1 (Bigalke et al., 2014). Previously, it has been reported that this membrane-connecting part of pU$_L$34 containing low-complexity/high-flexibility domains (Figure S3C) can be deleted and substituted by heterologous transmembrane-containing peptides (Paßvogel et al., 2014).

The NEC Structure Inherently Defines a Vesicle Size to Tightly Accommodate Viral Capsids

To unveil the architectural basis for its constrained curvature, we devised a simplified mathematical description of the NEC coat (Figure 7) and used this to produce a model of the coat that closely matches the measurements from the cryoFIB/ET average (Figure S4). The results confirm that the interplay of interactions within each layer and repeated heteromeric interactions between pU$_L$31 and pU$_L$34 define the curvature of the NEC coat.

Observation of a hexagonal NEC coat for the two alphaherpesviruses, PrV, as reported here, and HSV-1 (Bigalke et al.,

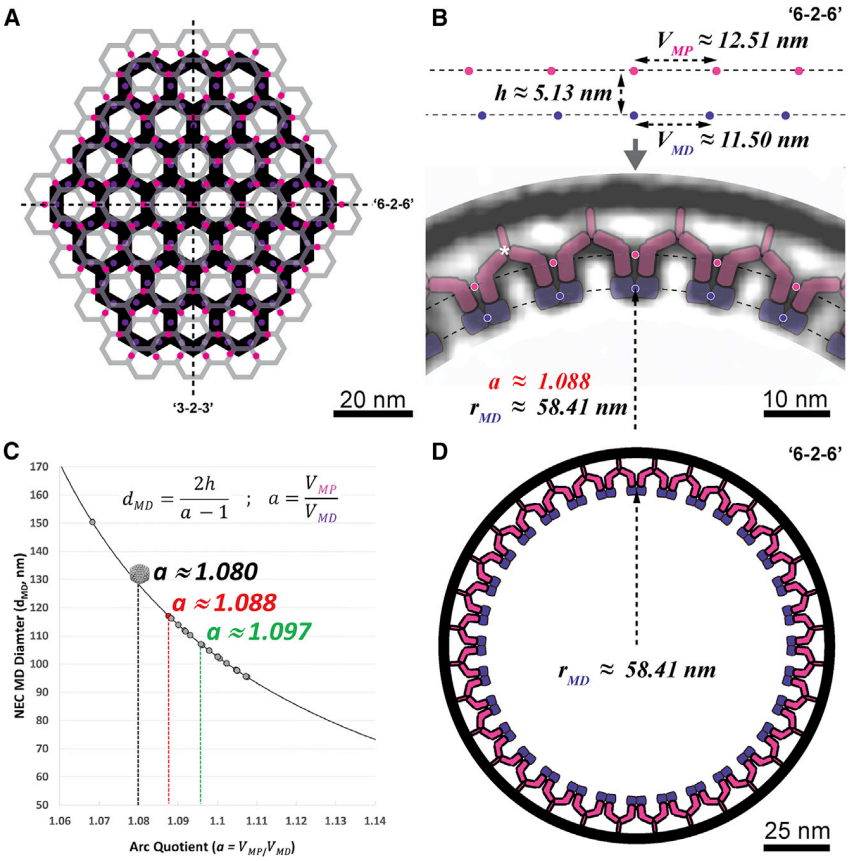

Figure 7. Architectural Basis for Constrained Curvature Formation

(A) A schematic model of the NEC where characteristic layers are represented as they appear in tangential slices (Figure 4B and Movie S8). Alignment of pink and purple points will result in formation of curvature essentially defined by the radial separation of each layer (parameter "*h*").

(B) A "*6-2-6*" cross-section view of the NEC coat average is modeled according to parameters (*h*, V_{MD}, and V_{MP}; compare Equation 1 in the Supplemental Experimental Procedures) measured from the experimental average. Magenta (MP) and purple (MD) circles highlight that hexagonal layers of characteristic repeat distances (V_{MD} and V_{MP}) interact via the $pU_L31/34$ heterodimer interface to induce a defined curvature. The basis for determination of the exact radial position of the two layers is given in Figure S4, and an arch keystone is marked with a white asterisk.

(C) The NEC coat diameter between opposite MD layers (d_{MD}) is plotted as a function of *a* (the arc quotient), and experimentally determined vesicle sizes from cryoFIB-prepared samples are shown as colored circles. The vesicle modeled in (B) is represented in red (see also red asterisk in Figures 3A–3C), while the mean vesicle size is indicated in green and a coated capsid by the respective symbol in gray, each with their respective *a* values. These values are plotted assuming that V_{MD} is constant, while V_{MP} is hypothesized to vary, owing to flexibility within coat.

(D) The resulting model in the context of an entire vesicle cross-section produced by extrapolation as described in the Supplemental Experimental Procedures. pU_L34 (magenta) and pU_L31 (purple) make up the MP and MD layers, respectively.

2014), suggests that interactions occurring at 2-fold and 3-fold axes of the MD (pU_L31) layer are likely evolutionarily conserved (lattice spacing ~11 nm in both cases). Interestingly, artificially membrane-tethered pU_L31 oligomers, i.e., in the absence of the native membrane tether pU_L34, did not show any regular/hexagonal pattern (Lorenz et al., 2015). Thus, by mutually confining the position of each of the six NEC heterodimers in space, the role of the pU_L34 membrane-connecting region is critically central in determining structural properties of the MP layer and thereby the curvature of the NEC coat. However, the distribution of vesicle sizes suggests that the NEC coat does not function as two rigidly imposed layers, i.e., it is not crystalline. While constrained in space by arch-forming interactions, the range of curvatures, vesicle sizes, and shapes observed (Figures 3D and 7C), starting from a planar NEC coat at initial budding sites (Figure 1B), is mediated by a high degree of flexibility in the membrane-connecting region of the coat.

In our experiments, we confirmed that, at artificially high local concentrations, in cells under constitutive expression (or in incubated vesicles), NECs alone can spontaneously form a coat and are able to mediate a complex process that involves induction of membrane curvature, vesicle budding, and scission. However, our observations at concentrations typical of the native situation, i.e., in infected cells, suggest that, in two-thirds of the perinuclear vesicles, the initial nucleation of $pU_L31/34$ heterodimers to form the NEC coat depended on presence of the capsid cargo (Figure 1).

In the cellular context, the NEC coat has the ability to form uniformly sized coated vesicles independent of the capsid cargo (ILVs in HSV-1-infected cells, Figures 1E and 3) (Klupp et al., 2007). A higher variability in curvature and hence size and shape has been observed in artificial model vesicles using partially truncated $pU_L31/34$ constructs without the genuine membrane anchor (Bigalke et al., 2014; Lorenz et al., 2015). The heteromeric combination of both pU_L31 and pU_L34 and their arrangement as hexamers as a result of the arch-forming interactions yield a structural environment (i.e., the inner surface of the coat) conceivably central to the task of selectively and efficiently recruiting and transporting the viral capsid. Thus, we propose that, while membrane-anchored pU_L31 is able to drive budding on its own (Lorenz et al., 2015), formation of vesicles of a curvature tailored specifically to the herpesviral capsid requires pU_L34.

Finally, we found that NEC coat assembly in situ produces vesicles of a size closely approximating but being somewhat smaller than capsids (Figures 3D and 7C). This size distribution in the absence of the capsid cargo suggests that it is most likely the capsid itself that determines the minimum diameter of an enveloped capsid (Figure 7C, gray capsid symbol), as the NEC coat appears to inherently favor a slightly higher curvature and thus

smaller vesicle size. Concomitantly, this ensures a very tight fit and interaction between the NEC coat and the capsid, leading to a cargo vesicle of the smallest possible size given the components involved.

Our current functional model of capsid envelopment at the INM can be summarized as follows: sparsely distributed NEC heterodimers form a planar layer at the INM, either spontaneously or initiated by cargo/capsid docking. At this point, the lattice already shows the ~11 nm spacing of the hexagonal MD/pU$_L$31 layer (Bigalke et al., 2014). Driven potentially by structural changes in the pU$_L$34 region during the concomitant formation of a second hexagonal layer (MP), budding of the INM into the perinuclear space is induced. New NEC heterodimers are recruited at the rim of the coat until it reaches its curvature limit through interaction of the MD/MP layers at a size to precisely envelope a herpesviral capsid.

Our insights into the molecular mechanism of remodeling the nuclear envelope for viral nuclear egress provide a molecular template by which nucleo-cytoplasmic transport can occur. The precise architecture of the NEC defines vesicles with a specific size, allowing an efficient but highly controlled method of egress. This mechanism allows the transport of cargoes with minimal disruption to the INM, a feature essential for the egress of equivalent cellular cargoes. Crucially, membrane-anchored proteins mediating a divergent process would pre-assemble with a potentially modular cargo-recruitment adaptor to form heterodimeric units capable of forming lateral, self-assembling lattices. Formation of curvature by this lattice is then a pre-requisite for envelopment of egressing cargoes, features that would be evident when investigated in vitro. High-resolution structures of NEC from different herpesvirus species have now emerged that may reveal a common structural homology to cargo recruitment at the INM (Bigalke and Heldwein, 2015; Leigh et al., 2015; Lye et al., 2015; Walzer et al., 2015). Interestingly, pU$_L$31 contains a conserved zinc-finger motif essential for vesicle formation and NEC function (Zeev-Ben-Mordehai et al., 2015). Using the curved lattice structure described here as a model for fitting the atomic structure of the NEC heterodimer (Zeev-Ben-Mordehai et al., 2015), we have defined exact interaction surfaces that could be used as a further constraint for structural and functional homology modeling of putative cellular counterparts.

Recently, it has been shown that TorsinA AAA+ ATPase is activated in a complex with type II membrane protein LAP1 at the INM (Brown et al., 2014; Sosa et al., 2014). As speculated in McCullough and Sundquist (2014), that complex might also be involved in perinuclear vesicle formation during transport of ribonucleoprotein particles in *Drosophila* cells in which TorsinA has been shown to promote INM scission (Jokhi et al., 2013). This complex and the NEC might share molecular attributes like the zinc-finger motif coming from a common ancestor when (and if) herpesvirus has hijacked this pathway in evolution (Forterre and Prangishvili, 2013). However, there are many issues in determining common ancestors for protein structures, including the increased mutation rate of viral genomes (Abroi and Gough, 2011). A next practical step to analyze that further might be to apply cryoEM also in vesicle-accumulating TorsinA-mutated cells described in Jokhi et al. (2013). This imaging technique is the sole method that can elucidate the direct presence of a (protein) coat along a membrane unequivocally as it avoids artifacts by chemical fixation and heavy metal staining and can be combined with immunostaining (Karreman et al., 2011). Finding a coat of TorsinA-LAP1 complexes, or any other players implicated in nuclear egress, might then suggest a similar mechanism of vesicle formation in a general nucleo-cytoplasmic transport pathway of large cargo, as described here for nuclear egress of herpesviral capsids.

Concluding Remarks

The described NEC coat architecture is an elegant solution for induction of membrane curvature based solely on the formation of a highly defined lattice of heterodimer interactions. This is reminiscent of virus budding at the plasma membrane, e.g., HIV (Sundquist and Kräusslich, 2012). However, the NEC targets the INM, a membrane for which no other vesicle transport has yet been mechanistically fully elucidated (Jokhi et al., 2013). Furthermore, while most cellular vesicle formation processes involve a dedicated cellular scission machinery and consume energy in form of ATP or similar, the NEC (1) appears capable of autoscission by continuing assembly of NEC units on the inside of the forming vesicle (Bigalke et al., 2014) and (2) requires at least under in vitro conditions no external energy input for both membrane budding and scission (Lorenz et al., 2015). Elucidating the unique features of the binary pU$_L$31/34 vesicle formation machinery might provide the blueprint for designing vesicles of highly defined sizes or specific volumes to be used in pharmaceutical and nanobiotechnological applications. Moreover, the characterization of the nature of the viral cargo packing system at the INM opens the search for the respective cellular counterparts and molecular determinants mediating nuclear egress of cellular large cargo, including ribonucleoprotein particles (Hatch and Hetzer, 2014; Jokhi et al., 2013).

EXPERIMENTAL PROCEDURES

Cryo-Electron Microscopy of Vitreous Sections

Sixteen hours after infection with herpes simplex virus 1 (HSV-1) strain K26GFP (Desai and Person, 1998) at a multiplicity of infection of 10, trypsinized African green monkey kidney cells (Vero cells, strain CCL-81; ATCC) or proteinase K-treated porcine epithelial-like embryonic EFN-R kidney cells stably co-expressing PrV pU$_L$31 and pU$_L$34, the latter fused with GFP (cell line designated as BK/EFN/U$_L$31/34 gfp, here abbreviated to BK, catalog No. RIE 1083 of the Collection of Cell Lines in Veterinary Medicine at the FLI, Greifswald-Insel Riems, Germany) (Hagen et al., 2012; Klupp et al., 2007), were physically fixed and analyzed. Cryo-immobilization was performed by high-pressure freezing followed by cryo-electron microscopy of vitreous sections (CEMOVIS), essentially as described in Hagen and Grünewald (2008). Further details are available in the Supplemental Experimental Procedures.

Live-Cell Three-Dimensional Structured Illumination Microscopy

BK cells were grown on high-precision 22 × 22 mm No. 1.5H glass coverslips (Marienfeld Superior) or in μ-Dish, high glass bottom 35-mm dishes (Ibidi GmbH, Martinsried, Germany) to a confluency of ~70%–80% in 10% (w/v) fetal bovine serum in Dulbecco's modified Eagle medium (DMEM; GIBCO-Invitrogen). Before imaging, the medium was replaced with pre-warmed Opti-MEM (GIBCO-Invitrogen). Three-dimensional structured illumination microscopy (3D-SIM) (Gustafsson et al., 2008) on live-cell samples was performed using an OMX V3 Blaze system (Applied Precision, GE Healthcare) (Strauss et al., 2012) equipped with a 60×/1.42 NA PlanApo oil-immersion objective (Olympus), a 488-nm diode laser with standard filter sets, and

Edge sCMOS cameras (PCO). Further details are available in the Supplemental Experimental Procedures.

CryoEM/T of Lamellae Produced by CryoFIB in a Dual-Beam Scanning Electron FIB-SEM Cryo-Microscope

Standard 3.05 mm electron microscopy 200 mesh gold grids covered with a perforated carbon foil (R2/1; Quantifoil Micro Tools GmbH, Jena, Germany) were hydrophilised in a PDC-002 plasma cleaner (Harrick Plasma, Ithaca, NY, USA). BK cells were grown on these grids in DMEM supplemented with 10% (w/v) fetal calf serum and 1% (v/v) PSN Antibiotic Mixture (GIBCO-Invitrogen), essentially as performed for 3D-SIM and soft X-ray microscopy samples. After 2 days of incubation (37°C, 5% CO_2) in plastic microscope slide growth chambers (μ-slide 2 × 9 well; Ibidi GmbH) and light microscopic screening for optimal growth, cells were cryo-immobilized by plunge freezing, as described in Hagen et al., 2012).

CryoFIB was essentially performed as recently described (Engel et al., 2015). It is detailed in the Supplemental Experimental Procedures.

For tomography of the cryoFIB lamellae, a Tecnai G2 Polara transmission electron microscope (FEI) equipped with a field emission gun operated at 300 kV, a GIF 2002 post-column energy filter (Gatan, Pleasanton, CA), and a 2048 × 2048 Gatan Multiscan CCD camera were used. Tomographic tilt-series acquisition under low-dose conditions (10 tilt series out of 14 lamellae, tilt range: −55° to 59°, cumulative dose: 110 electrons per $Å^2$) was controlled by SerialEM (Mastronarde, 2005). Tilt-series images were recorded at 3° tilt increments, with −6 μm defocus, at an object pixel size of 0.57 nm.

For alignment of the tilt-series projections, small spherical cellular features or ice contaminants were employed as tracking markers, or patch tracking following the routine in the Etomo GUI of IMOD was applied. Tomograms were reconstructed using weighted back projections, and visualization was performed with Amira 5.2 (FEI).

Sub-Tomogram Averaging and Modeling of CryoFIB/ET Data

Sub-tomogram averaging was carried out using the PEET package applying constrained cross-correlation (CCC) (Briggs, 2013; Nicastro et al., 2006). Details of data processing, integrated analysis, and model building are available in the Supplemental Experimental Procedures.

Soluble NEC Preparation

Details on the construction of a soluble NEC expression vector are provided in the Supplemental Experimental Procedures. *Escherichia coli* BL21 (DE3) transformed with pETDuet::U_L34(1–179)::U_L31-NLS was grown to saturation overnight at 25°C in LB medium containing ampicillin (100 μg ml^{-1}). An aliquot of overnight culture was diluted 1/20 in medium containing ampicillin and was grown at 37°C to an OD_{600} of 0.6, at which time expression was induced by addition of isopropyl-D- galactoside (IPTG) to a final concentration of 1 mM. Cells were incubated for a further 4.5 hr at 25°C before being harvested by centrifugation (3,500 × *g*, 10 min, 4°C), and stored at −20°C.

Cells were re-suspended in buffer A (PBS pH 7.4); supplemented with 2,500 units DNase 1, 0.2 mg ml^{-1} lysozyme, 5 mM $MgSO_4$, and 1% protease inhibitor cocktail (Sigma); and lysed by sonication. The supernatant was clarified by centrifugation (45,000 × *g*, 30 min, 4°C).

The complex was purified by metal affinity chromatography (co-sepharose 6-fast flow) followed by size-exclusion chromatography in buffer B (10 mM Tris-HCl [pH 7.4], 75 mM NaCl, 3 mM DTT). Purified proteins were analyzed by SDS-PAGE.

Small-Angle X-Ray Scattering Data Collection, Processing, and Analysis

SAXS data for soluble NEC were collected on the BM29 beamline at the ESRF synchrotron (Grenoble, France). Details are available in the Supplemental Experimental Procedures.

ACCESSION NUMBERS

The sub-tomographic reconstruction has been deposited in the Electron Microscopy Data Bank (EMDB) at PDBe (http://www.ebi.ac.uk/pdbe/emdb/) as EMD-3215.

SUPPLEMENTAL INFORMATION

Supplemental Information includes Supplemental Experimental Procedures, four figures, and ten movies and can be found with this article online at http://dx.doi.org/10.1016/j.cell.2015.11.029.

AUTHOR CONTRIBUTIONS

All authors intellectually conceived the experiments. C.H. performed CEMOVIS, cryoXM/T, and cryoFIB; K.C.D. did cryoET sub-tomogram analysis and integrated modeling; T.Z.-B.-M. provided SAXS data and models; and M.G. and J.B.B. imaged cells by live 3D-SIM. Furthermore, C.W., B.G.K., C.A.S., F.J.B.B., J.C., S.W., P.G., S.R., K.H., J.D., and B.A. performed experiments; D.V. processed and analyzed data; C.H., K.C.D., T.Z.-B.-M., M.G., J.B.B., T.C.M., and K.G. wrote the manuscript, and all authors commented on it.

ACKNOWLEDGMENTS

We thank Wolfram Antonin (Tübingen) for critical discussion and Marion Jasnin, Tim Laugks, Miroslava Schaffer, and Margarete Schüler for help with cryoFIB in Martinsried. This work was supported by a Wellcome Trust Senior Research Fellowship to K.G. (090895/Z/09/Z), German Research Council grants DFG GR1990/2 to K.G. and DFG Me 854/12-1 to T.C.M., a Leverhulme Trust grant to K.G. (RPG-2012-519), a Wellcome Trust JIF award (060208/Z/00/Z) and a Wellcome Trust equipment grant (093305/Z/10/Z) to the Oxford Particle Imaging Centre, the Wellcome Trust core award 090532/Z/09/Z to the Wellcome Trust Centre for Human Genetics, the Wellcome Trust Strategic Award 091911 supporting advanced microscopy at Micron Oxford, a Wellcome Trust PhD studentship to M.G., a São Paulo Research Foundation Fellowship to J.C. (Fapesp 2013/24972-1), and a DFG Fellowship BO 4158/1-1 to J.B.B. We acknowledge the Helmholtz-Zentrum Berlin electron storage ring BESSY II for provision of synchrotron radiation at beamline U41-FSGM. The research leading to these results has received funding from the European Community's Seventh Framework Programme (FP7/2007-2013) under BioStruct-X (Grant agreement nos. 283570 and 226716).

Received: June 1, 2015
Revised: September 11, 2015
Accepted: November 6, 2015
Published: December 17, 2015

REFERENCES

Abroi, A., and Gough, J. (2011). Are viruses a source of new protein folds for organisms? - Virosphere structure space and evolution. BioEssays *33*, 626–635.

Bigalke, J.M., and Heldwein, E.E. (2015). Structural basis of membrane budding by the nuclear egress complex of herpesviruses. EMBO J. *34*, 2921–2936.

Bigalke, J.M., Heuser, T., Nicastro, D., and Heldwein, E.E. (2014). Membrane deformation and scission by the HSV-1 nuclear egress complex. Nat. Commun. *5*, 4131.

Briggs, J.A.G. (2013). Structural biology *in situ*–the potential of subtomogram averaging. Curr. Opin. Struct. Biol. *23*, 261–267.

Brown, R.S.H., Zhao, C., Chase, A.R., Wang, J., and Schlieker, C. (2014). The mechanism of Torsin ATPase activation. Proc. Natl. Acad. Sci. USA *111*, E4822–E4831.

Desai, P., and Person, S. (1998). Incorporation of the green fluorescent protein into the herpes simplex virus type 1 capsid. J. Virol. *72*, 7563–7568.

Dubochet, J. (2012). Cryo-EM–the first thirty years. J. Microsc. *245*, 221–224.

Engel, B.D., Schaffer, M., Cuellar, L.K., Villa, E., Plitzko, J.M., and Baumeister, W. (2015). Native architecture of the *Chlamydomonas* chloroplast revealed by *in situ* cryo-electron tomography. eLife *4*, e04889.

Forterre, P., and Prangishvili, D. (2013). The major role of viruses in cellular evolution: facts and hypotheses. Curr. Opin. Virol. *3*, 558–565.

Franke, D., and Svergun, D.I. (2009). DAMMIF, a program for rapid *ab-initio* shape determination in small-angle scattering. J. Appl. Cryst. *42*, 342–346.

Funk, C., Ott, M., Raschbichler, V., Nagel, C.H., Binz, A., Sodeik, B., Bauerfeind, R., and Bailer, S.M. (2015). The herpes simplex virus protein pU_L31 escorts nucleocapsids to sites of nuclear egress, a process coordinated by its N-terminal domain. PLoS Pathog. *11*, e1004957.

Gustafsson, M.G.L., Shao, L., Carlton, P.M., Wang, C.J.R., Golubovskaya, I.N., Cande, W.Z., Agard, D.A., and Sedat, J.W. (2008). Three-dimensional resolution doubling in wide-field fluorescence microscopy by structured illumination. Biophys. J. *94*, 4957–4970.

Hagen, C., and Grünewald, K. (2008). Microcarriers for high-pressure freezing and cryosectioning of adherent cells. J. Microsc. *230*, 288–296.

Hagen, C., Guttmann, P., Klupp, B., Werner, S., Rehbein, S., Mettenleiter, T.C., Schneider, G., and Grünewald, K. (2012). Correlative VIS-fluorescence and soft X-ray cryo-microscopy/tomography of adherent cells. J. Struct. Biol. *177*, 193–201.

Hatch, E., and Hetzer, M. (2014). Breaching the nuclear envelope in development and disease. J. Cell Biol. *205*, 133–141.

Hoenger, A. (2014). High-resolution cryo-electron microscopy on macromolecular complexes and cell organelles. Protoplasma *251*, 417–427.

Jokhi, V., Ashley, J., Nunnari, J., Noma, A., Ito, N., Wakabayashi-Ito, N., Moore, M.J., and Budnik, V. (2013). Torsin mediates primary envelopment of large ribonucleoprotein granules at the nuclear envelope. Cell Rep. *3*, 988–995.

Karreman, M.A., van Donselaar, E.G., Gerritsen, H.C., Verrips, C.T., and Verkleij, A.J. (2011). VIS2FIX: a high-speed fixation method for immuno-electron microscopy. Traffic *12*, 806–814.

Klupp, B.G., Granzow, H., Fuchs, W., Keil, G.M., Finke, S., and Mettenleiter, T.C. (2007). Vesicle formation from the nuclear membrane is induced by coexpression of two conserved herpesvirus proteins. Proc. Natl. Acad. Sci. USA *104*, 7241–7246.

Leigh, K.E., Sharma, M., Mansueto, M.S., Boeszoermenyi, A., Filman, D.J., Hogle, J.M., Wagner, G., Coen, D.M., and Arthanari, H. (2015). Structure of a herpesvirus nuclear egress complex subunit reveals an interaction groove that is essential for viral replication. Proc. Natl. Acad. Sci. USA *112*, 9010–9015.

Lorenz, M., Vollmer, B., Unsay, J.D., Klupp, B.G., García-Sáez, A.J., Mettenleiter, T.C., and Antonin, W. (2015). A single herpesvirus protein can mediate vesicle formation in the nuclear envelope. J. Biol. Chem. *290*, 6962–6974.

Loret, S., Guay, G., and Lippé, R. (2008). Comprehensive characterization of extracellular herpes simplex virus type 1 virions. J. Virol. *82*, 8605–8618.

Lučić, V., Förster, F., and Baumeister, W. (2005). Structural studies by electron tomography: from cells to molecules. Annu. Rev. Biochem. *74*, 833–865.

Lye, M.F., Sharma, M., El Omari, K., Filman, D.J., Schuermann, J.P., Hogle, J.M., and Coen, D.M. (2015). Unexpected features and mechanism of heterodimer formation of a herpesvirus nuclear egress complex. EMBO J. *34*, 2937–2952.

Marko, M., Hsieh, C., Schalek, R., Frank, J., and Mannella, C. (2007). Focused-ion-beam thinning of frozen-hydrated biological specimens for cryo-electron microscopy. Nat. Methods *4*, 215–217.

Mastronarde, D.N. (2005). Automated electron microscope tomography using robust prediction of specimen movements. J. Struct. Biol. *152*, 36–51.

McCullough, J., and Sundquist, W.I. (2014). Putting a finger in the ring. Nat. Struct. Mol. Biol. *21*, 1025–1027.

McMahon, H.T., and Gallop, J.L. (2005). Membrane curvature and mechanisms of dynamic cell membrane remodelling. Nature *438*, 590–596.

Mettenleiter, T.C., Müller, F., Granzow, H., and Klupp, B.G. (2013). The way out: what we know and do not know about herpesvirus nuclear egress. Cell. Microbiol. *15*, 170–178.

Mou, F., Wills, E., and Baines, J.D. (2009). Phosphorylation of the U_L31 protein of herpes simplex virus 1 by the U_S3-encoded kinase regulates localization of the nuclear envelopment complex and egress of nucleocapsids. J. Virol. *83*, 5181–5191.

Nicastro, D., Schwartz, C., Pierson, J., Gaudette, R., Porter, M.E., and McIntosh, J.R. (2006). The molecular architecture of axonemes revealed by cryoelectron tomography. Science *313*, 944–948.

Panté, N., and Kann, M. (2002). Nuclear pore complex is able to transport macromolecules with diameters of about 39 nm. Mol. Biol. Cell *13*, 425–434.

Paßvogel, L., Janke, U., Klupp, B.G., Granzow, H., and Mettenleiter, T.C. (2014). Identification of conserved amino acids in pU_L34 which are critical for function of the pseudorabies virus nuclear egress complex. J. Virol. *88*, 6224–6231.

Rigort, A., Bäuerlein, F.J.B., Villa, E., Eibauer, M., Laugks, T., Baumeister, W., and Plitzko, J.M. (2012). Focused ion beam micromachining of eukaryotic cells for cryoelectron tomography. Proc. Natl. Acad. Sci. USA *109*, 4449–4454.

Rose, A., and Schlieker, C. (2012). Alternative nuclear transport for cellular protein quality control. Trends Cell Biol. *22*, 509–514.

Schekman, R., and Orci, L. (1996). Coat proteins and vesicle budding. Science *271*, 1526–1533.

Schermelleh, L., Heintzmann, R., and Leonhardt, H. (2010). A guide to super-resolution fluorescence microscopy. J. Cell Biol. *190*, 165–175.

Sharma, M., Bender, B.J., Kamil, J.P., Lye, M.F., Pesola, J.M., Reim, N.I., Hogle, J.M., and Coen, D.M. (2015). Human cytomegalovirus U_L97 phosphorylates the viral nuclear egress complex. J. Virol. *89*, 523–534.

Sosa, B.A., Demircioglu, F.E., Chen, J.Z., Ingram, J., Ploegh, H.L., and Schwartz, T.U. (2014). How lamina-associated polypeptide 1 (LAP1) activates Torsin. eLife *3*, e03239.

Speese, S.D., Ashley, J., Jokhi, V., Nunnari, J., Barria, R., Li, Y., Ataman, B., Koon, A., Chang, Y.T., Li, Q., et al. (2012). Nuclear envelope budding enables large ribonucleoprotein particle export during synaptic Wnt signaling. Cell *149*, 832–846.

Strauss, M.P., Liew, A.T.F., Turnbull, L., Whitchurch, C.B., Monahan, L.G., and Harry, E.J. (2012). 3D-SIM super resolution microscopy reveals a bead-like arrangement for FtsZ and the division machinery: implications for triggering cytokinesis. PLoS Biol. *10*, e1001389.

Sundquist, W.I., and Kräusslich, H.G. (2012). HIV-1 assembly, budding, and maturation. Cold Spring Harb. Perspect. Med. *2*, a006924.

Walzer, S.A., Egerer-Sieber, C., Sticht, H., Sevvana, M., Hohl, K., Milbradt, J., Muller, Y.A., and Marschall, M. (2015). Crystal structure of the human cytomegalovirus pUL50-pUL53 core nuclear egress complex provides insight into a unique assembly scaffold for virus-host protein interactions. J. Biol. Chem. *290*, 27452–27458.

Webster, B.M., Colombi, P., Jäger, J., and Lusk, C.P. (2014). Surveillance of nuclear pore complex assembly by ESCRT-III/Vps4. Cell *159*, 388–401.

Wild, P., Leisinger, S., de Oliveira, A.P., Schraner, E.M., Kaech, A., Ackermann, M., and Tobler, K. (2015). Herpes simplex virus 1 U_s3 deletion mutant is infective despite impaired capsid translocation to the cytoplasm. Viruses *7*, 52–71.

Zeev-Ben-Mordehai, T., Hagen, C., and Grünewald, K. (2014). A cool hybrid approach to the herpesvirus 'life' cycle. Curr. Opin. Virol. *5*, 42–49.

Zeev-Ben-Mordehai, T., Weberruß, M., Lorenz, M., Cheleski, J., Hellberg, T., Whittle, C., El Omari, K., Vasishtan, D., Dent, K.C., Harlos, K., et al. (2015). Crystal structure of the herpesvirus nuclear egress complex provides insights into inner nuclear membrane remodeling. Cell Rep. *13*. Published online December 17, 2015. http://dx.doi.org/10.1016/j.celrep.2015.11.008.

Cell

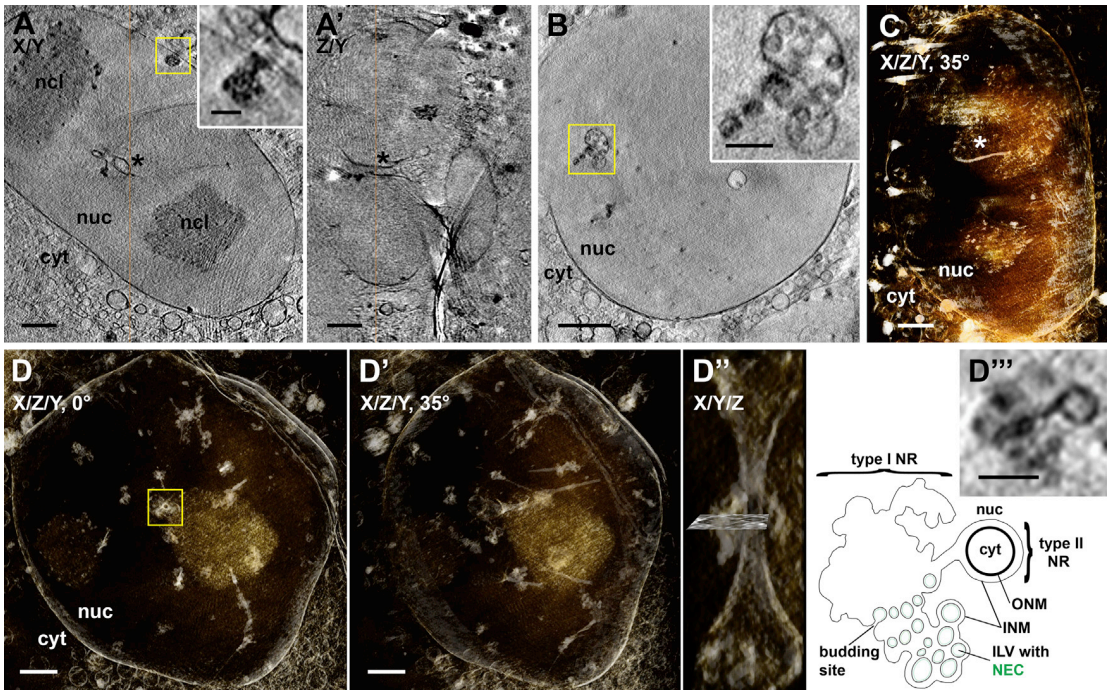

Figure S1. Nuclear Structure in PrV pU_L31/pU_L34-GFP Co-expressing Cells, Related to Figure 2

(A–D) Soft X-ray cryo-microscopy/tomography (cryoXM/T) of BK cells (A) Slice of a soft X-ray tomogram, taken with a 40 nm zone plate objective (yellow box and a magnification of a similar slice in the same area: inset). CryoXM/T directly images frozen-hydrated unstained samples and gives about five times higher resolution than 3D-SIM while still allowing the entire nucleus to be observed. Note the high absorption contrast, revealing details of nuclear substructure like nucleoli. Infoldings of the INM were clearly detectable as racemose, tree- or mushroom-shaped clusters, mostly near the nuclear envelope (yellow box and inset). These clusters correlated with fluorescent 'speckles' containing pU_L34-GFP/NEC (Hagen et al., 2012). (A') Side view of the same tomogram. Asterisks in (A) and (A') mark a tubular invagination of both nuclear envelope membranes running through the nucleus (orange lines: sectional planes). We observed such infoldings in almost all nuclei (28 out of 31; from 28 tomograms). The tubes were often the origin of INM-infoldings. Such infoldings of the INM or of both membranes of the nuclear envelope have been observed in many eukaryotic cells, and are termed nucleoplasmic reticulum (NR) type I or type II, respectively (Malhas et al., 2011). (B) Cells grown only 15 hr on grid (instead of 2 days) had less tubes but exhibited more vesicle-like infoldings of the INM. In larger vesicles, smaller spherical vesicles were detected, exhibiting the size of ILVs (yellow box and an un-binned magnification of a similar slice in the same area: inset). (C) Tubular invaginations of the nuclear membranes, here visualized with inverse contrast in a rendered volume of a tomographic reconstruction, occurred only rarely in non-transfected control cells (asterisk), suggesting induction/enhancement of their formation by co-expression of the NEC components pU_L31 and pU_L34. (D) Tubular infoldings of the entire nuclear envelope crossed the nucleus preferentially, but not invariably, along its smallest extension (D', Movie S4). The side view of these tubes revealed the interconnection of type I and type II NR (D''), as shown in detail for one sub-volume of the tomographic reconstruction (yellow box in D, slice in D'', zoom and schematic interpretation in D'''). Scale bar is 2 μm (A-D') and 500 nm (insets; D'''). cyt, cytoplasm; ILV, intraluminal vesicle; INM, inner nuclear membrane; ncl, nucleolus; NEC, nuclear egress complex; NR, nucleoplasmic reticulum; nuc, nucleus; ONM, outer nuclear membrane

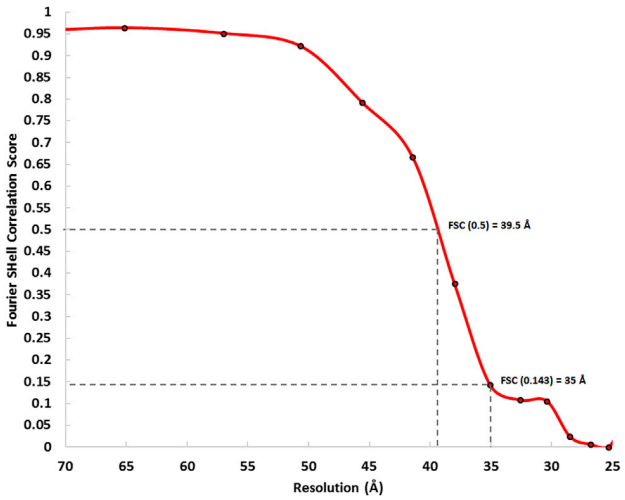

Figure S2. Resolution Assessment of the NEC Coat Map, Related to Figure 4

Fourier shell correlation calculated between two half-datasets of 150 particles each. The resolution of the map is estimated to be between 35 and 40 Å. At a nominal defocus of −6 μm the first node of the CTF is expected at 1/34 $Å^{-1}$.

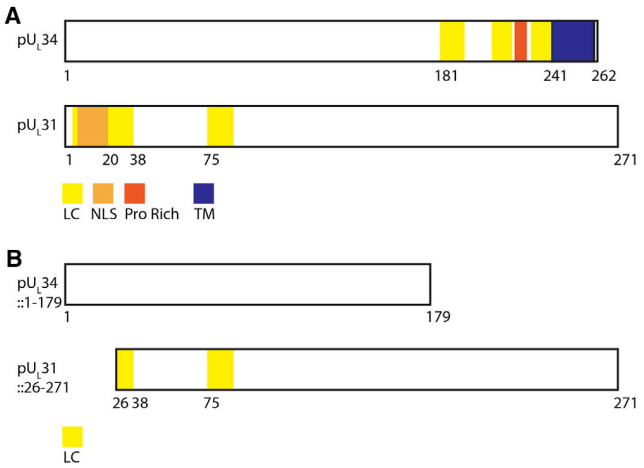

C

```
        10         20         30         40         50         60
MSGTLVQRLK LILSGGNLRC SDGETACDPE RPPTRCVFQV HGQDGSNDTF PLEYVLRLMR

        70         80         90        100        110        120
SWAHVPCDPY VRVQNTGVSV LFQGFFFRPA DAPLAAITAE HNNVILASTH STGMSLSALD

       130        140        150        160        170        180
DIKRAGGVDT RPLRAMMSVS CFVRMPRVQL SFRFMGPDDA SQTQRLLDRA EMRQRSVSRP

       190        200        210        220        230        240
GGGAGGGDDG EGPSPRAPIR PTVISPVPGH AAAAFVGQAA YPPPARFPAS LLHTLLGLRR

       250        260
LAGYAVACVT GALAIVIILN MR
```

TM: 241-260 - bold Italics
LC1: 181-192 -bold italics brown
LC2: 211-220 -bold italics red
LC3: 231-241 -bold italics orange
Pro Rich: 222-228 -bold italics blue

Figure S3. Overview of Protein Constructs, Related to Figure 6

(A) Sequence motifs for full-length pU$_L$31 (Uniprot: G3G955) and pU$_L$34 (Uniprot: G3G8X8) (PrV) are illustrated. pU$_L$31 exhibits a N-terminal nuclear localization signal (NLS, orange), while pU$_L$34 contains a C-terminal trans-membrane (TM, blue) domain (LC: low complexity domain, yellow; Pro Rich: proline rich domain, red). The NEC coat produced by co-expression and in situ assembly of the pU$_L$31/34 heterodimer (including a C-terminal GFP-tag at pU$_L$34) in porcine kidney cells was visualized by 3D-SIM, cryoXM/T, CEMOVIS and cryoFIB/ET. The GFP tag did not (substantially) affect membrane interactions/curvature as concluded from the following two lines of evidence: (i) Nuclei of HSV-1 infected host cells (native full length pU$_L$31/pU$_L$34 without any fluorescent tag) exhibited similar intraluminal vesicles (and NEC coats) as the cell model with pU$_L$34-GFP. (ii) The GFP-cryoEM densities, that topologically face the perinuclear space, were not structured regularly and did not follow the hexameric structure of the membrane-tethering/transmembrane C-terminal part of pU$_L$34 (Figure 4A, Movie S7).
(B) Truncated recombinant constructs (pU$_L$31ΔNLS and pU$_L$34t179) are illustrated as used for bacterially co-expression for SAXS experiments, as well as for the subsequent SAXS-EM fitting search. The soluble NEC expressed for SAXS measurements did not contain the C terminus of pUL34, and hence no GFP.
(C) The amino acid sequence of pU$_L$34 (PrV, Uniprot: G3G8X8) is shown and highlights five regions of interest. The transmembrane domain (TM) is colored black, and three low complexity regions (presumably highly flexible), are colored brown, red, and orange. These are in addition to a proline rich region (colored blue).

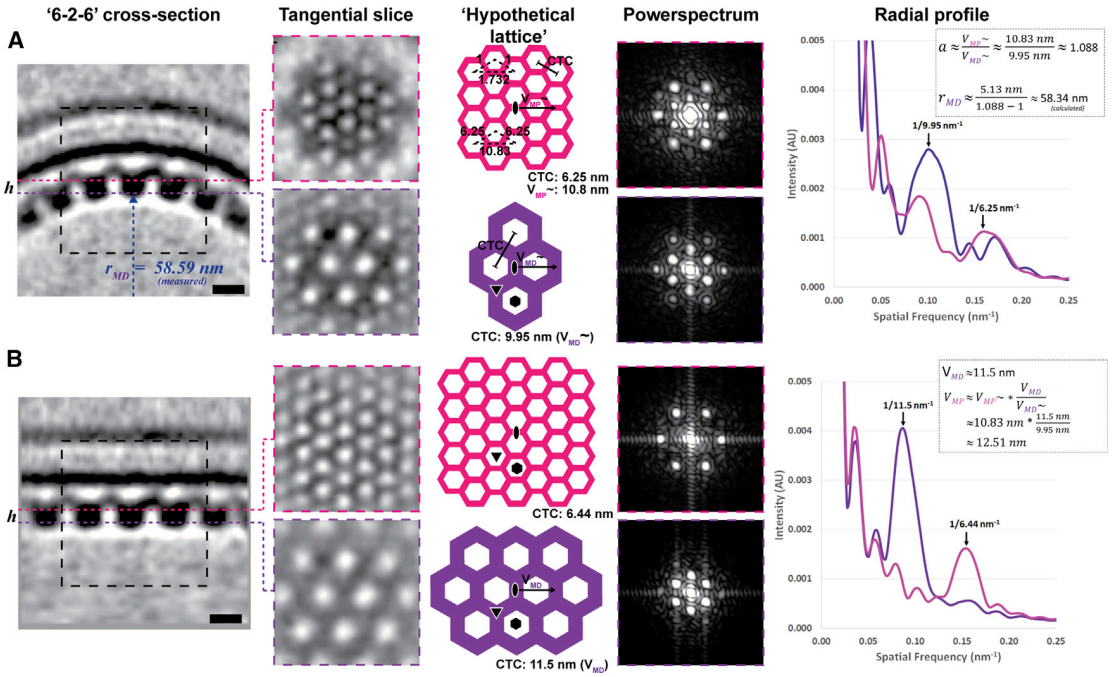

Figure S4. Characteristic Layers of the NEC CryoEM Map and Curvature Modeling, Related to Figure 7

(A and B) The 'raw' NEC coat average map (A; Movie S7), and radially projected NEC coat map (B) are centered on a 2-fold axis, and viewed along a *'6-2-6'* cross-section. Any given 2-fold axis is neighbored by only two 6-fold axes, and will therefore participate in only one *'6-2-6'* plane – the direction of curvature in the present model. For each map (A and B), tangential slices at vesicle membrane distal (MD, lower, purple) and vesicle membrane proximal (MP, upper, magenta) layers are shown. These layers are separated radially by 5.13 nm (parameter *'h'*) (Figure 7). Layers have characteristic hexagonal ('honeycomb') patterns of protein density (Movie S9). The MD layer density at 3.5 nm resolution does not reveal clearly distinct aggregates of globular domains, but instead appears as a continuous layer of protein density. The MP layer appears to be a distinct (more finely spaced) hexagonal lattice with each presumed pU_L34 unit appearing to form a vertex of the unit cell, with apparent connections to neighbors across the 2-fold axes. These layers are interpreted as 'hypothetical lattices' (colored appropriately) with characteristic center-to-center (CTC) distances (or 'spacing') as illustrated (not to scale). Observing the slices in reciprocal space as power spectra (i.e., squared amplitudes of structure factors) allowed detection of two primary reflections corresponding to ~10 nm (MD layer) and ~6 nm (MP layer, indicated by arrows), giving confirmation of the uniquely differing arrangement of densities between these layers and confirming that the MP lattice is offset by 30° in relation to the MD lattice. Radial average 'profile' curves for MD (purple) and MP (magenta) shown rightmost allow lattice parameters to be measured accurately. The relations annotated allow arc length parameters V_{MD} and V_{MP} to be approximated, and applied to estimate the vesicle radius (Figure 7C). Measurements from reflections observed from the curved NEC coat map (A) are inherently underestimated – owing to the curvature itself causing signal from multiple radial layers to contribute to the measurement, however the ratio of these is preserved and therefore used to estimate the arc quotient (*'a'*) as shown. The MD lattice is established by pU_L31 interactions (at 2-fold and 3-fold interfaces) and are used as a ruler (providing the true V_{MD}), and therefore used to scale $V_{MP}^{\sim}$ as estimated from the curved NEC coat map. Calculations are shown as inset. Slices are 0.57 nm thick.

Cell

Supplemental Information

Structural Basis of Vesicle Formation at the Inner Nuclear Membrane

Christoph Hagen, Kyle C. Dent, Tzviya Zeev-Ben-Mordehai, Michael Grange, Jens B. Bosse, Cathy Whittle, Barbara G. Klupp, C. Alistair Siebert, Daven Vasishtan, Felix J. B. Bäuerlein, Juliana Cheleski, Stephan Werner, Peter Guttmann, Stefan Rehbein, Katja Henzler, Justin Demmerle, Barbara Adler, Ulrich Koszinowski, Lothar Schermelleh, Gerd Schneider, Lynn W. Enquist, Jürgen M. Plitzko, Thomas C. Mettenleiter, and Kay Grünewald

SUPPLEMENTAL EXPERIMENTAL PROCEDURES

Electron Cryo-Microscopy of Vitreous Sections - CEMOVIS

CEMOVIS is the 'gold standard' among sectioning methods for electron microscopy (Bleck et al., 2010; Gunkel et al., 2015; Mielanczyk et al., 2014). However, structural artefacts such as inhomogeneous compression and membrane crevasses (Figure 2B, asterisks) (Al-Amoudi et al., 2005; Bouchet-Marquis and Hoenger, 2011; Pierson et al., 2011), impaired higher-resolution analysis.

Compression due to the sectioning process was estimated based on the change in aspect ratio of HSV-1 capsids. A non-linear compression dependency on the nominal section feed similar to that described in (Han et al., 2008) was observed. Projection images from vitreous sections were corrected for this thickness-dependent compression along the cutting direction (knife marks) by rescaling and interpolation, and were low-pass filtered for an improved signal to noise ratio. The projection images of tomographic tilt series were aligned using a MATLAB-implementation (provided by Matthias Eibauer, University of Zurich, Department of Biochemistry, Switzerland) of marker-free image registration algorithms described in (Sorzano et al., 2009), in combination with the global alignment correction capabilities of IMOD (Kremer et al., 1996; Mastronarde, 2008) to account for electron beam-induced movements of the vitreous section (Hsieh et al., 2006). Tomographic reconstructions were corrected for compression according to the model given in (Al-Amoudi et al., 2005), including lateral re-positioning of all X/Y-slices in the Z-direction, using MATLAB scripts provided by Lars-Anders Carlson (University of California, Department of Molecular & Cell Biology, Berkeley, CA). If not stated otherwise, CEMOVIS tomograms presented here are binned with a kernel of 2x2x2 and were, additionally, 3D-Gaussian-filtered (Amira 5.2; FEI, Eindhoven, The Netherlands). Slices are shown in the corresponding voxel size thickness.

Live Cell Three-Dimensional Structured Illumination Microscopy - 3D-SIM

Our setup was equipped with a manufacturer-supplied apparatus and objective heater to allow medium-term imaging under standard live cell conditions (37 °C and 5 % CO_2). Previous live-samples assessed by 3D-SIM have concentrated on bacterial studies at 30 ºC (Strauss et al., 2012; Turnbull et al., 2014) or for HeLa cells at 24 ºC (Shao et al., 2011). The OMX V3 Blaze system parameters were adjusted for temperature-dependent changes in immersion oil refractive index with single layers of TetraSpeck fluorescent microspheres (Life Technologies), and optical transfer functions (OTFs) were generated from individual 110 nm diameter 505/515 fluorescent microspheres (Life Technologies). Phase parameters were adjusted for optimal imaging at 488 nm, and data was acquired using an appropriately matched immersion oil. 3D-SIM data were acquired with a Z-distance of 125 nm and with 15 images per plane (five phases, three angles). The raw data was computationally reconstructed using a Wiener (high-frequency) filter setting of 0.002 and channel- and temperature-specific OTFs employing the softWoRx 6.0 software package (GE Healthcare) to obtain a super-resolution 3D image stack of 32-bit depth, with a pixel size of 40x40 nm. Typically nuclei imaged were in between 6 µm and 12 µm in height. The resolution achieved was ~120 nm in the lateral direction and ~300 nm in the axial direction. The reconstructed data was thresholded for each channel to the stack modal grey value (representing the centre of the background intensity level) and converted to 16-bit tiff-stacks.

Correlative Fluorescence and Soft X-Ray Cryo-Microscopy/Tomography - CryoXM/T - at the HZB TXM at Beamline U41-FSGM of the BESSYII Electron Storage Ring in Berlin/Germany

Incubation of the BK cells on special grids for the Helmholtz-Zentrum Berlin full-field transmission soft X-ray microscope (HZB TXM), live-cell light microscopy, cryo-immobilization by plunge-freezing and correlated fluorescence/cryoXM/T are detailed in (Hagen et al., 2012) and (Hagen et al., 2014). For methodological reviews, see (Dent et al., 2014; Schneider et al., 2012).

Focused-Ion Beam Milling – CryoFIB - in a Dual Beam Scanning Electron FIB-SEM Cryo-Microscope
Owing to the lack of three-dimensional targeting methods (Fukuda et al., 2014), successful milling depends heavily on high-densities of the target structures. In nuclei of BK cells, required density of target structures had been confirmed by CEMOVIS sectioning. Vitreous samples on grids were mounted into modified Autogrids (FEI) to increase stability. These were transferred into a dual-beam FIB-SEM microscope (Quanta 3D FEG, FEI) by means of a cryo-transfer system (PP3000T, Quorum Technologies Ltd, Laughton, UK) and a custom-built transfer shuttle/sample holder (Rigort et al., 2010). During operation, samples were kept at a constant temperature below -180 °C using a homemade 360° rotatable cryo-stage (Rigort et al., 2012). To minimize curtaining artefacts during FIB milling, the sample was coated by organometallic platinum (GIS, FEI). Thin lamellae were prepared using Ga^+ ions at 30 kV, under an effective beam to grid surface angle of 13°. Rough milling was performed with a rectangular pattern and 0.3 nA beam current, followed by sequentially lowered beam currents of 0.1 nA, 50 pA and 30 pA during the thinning and cleaning steps. Additionally, the specimen was observed by SEM at 5-10 kV and 5–50 pA.

Sub-Tomogram Averaging of CryoFIB/ET Data
The NEC units, forming a near continuous coat, did not provide clearly discernible features that might allow rational assignment of particle centres. Consequently, 31 vesicles from three tomograms were modelled as spheres to produce a series of 'particle' centres to be used for sub-tomogram averaging. The radius of each sphere was adjusted to the approximate mean radius of the NEC coat for each vesicle. Two out of three particle orientation parameters could be approximated using a 'particle axis' defined as normal to the sphere surface at each particle centre. Particle axes were then transformed to coincide with the Y-axis, and orientations around Y randomized to assist compensation of the 'missing wedge'. A spherically curved mask, 12 pixels (13.68 nm) thick, and 40 pixels wide was used to limit CCC to regions including protein signal, but not the vesicle membrane (VM). Tomograms were binned twice (to 11.4 Å/pixel), and initial averages calculated from a single vesicle of the highest quality and sphericalness over a cross-correlation box size of ~40 nm. This procedure involved a series of iterative CCC searches, in which translational search ranges were initially high, used a number of reference volumes selected from the vesicle itself as a reference template, and involved a full angular search around the particle axis (Y). For each starting reference, this approach resulted in averages showing pronounced hexagonal features with a centre-to-centre distance between unit cells (lattice spacing) of ~10 nm. Based on this observation, spherical sampling was optimized to oversample the NEC coat (nearest neighbour distance between points of ~3 nm). Sub-tomogram averaging was repeated for 9 vesicles after the initial result was centred on a 3-fold axis of symmetry and re-oriented to place the new particle axis on Y. To compensate for vesicle distortions that resulted in variable curvature of the NEC coat, a feature more pronounced for some vesicles than others, the CCC box was limited to a 26 pxl^3 box (~30 nm edge length), and an angular search range around Y of 120° was used. For each vesicle, cross-correlation searches were carried out over a number of iterations in which the angular range and step were made progressively finer, with final result being resubmitted for refinement using the same protocol until no improvements were observed. CCC was limited to a spatial frequency of 1/50 $Å^{-1}$ to ensure that alignment of noise did not significantly bias the alignment to the initial template. Duplicate particles (sharing particle centre coordinates) were removed after each iteration to produce an improved map for each vesicle from 200-350 particles. Final averages were calculated from 94 pxl^3 boxes and revealed that the NEC coat was in many cases ordered beyond the cross-correlated region. Additionally, the appearance of the VM, as well as other features in the map not involved in cross-correlation lent support to the validity of the alignment. Notably, while CCC searches were carried out about the 3-fold axes, the NEC averages exhibited 2-fold symmetry, and were consequently centred on the corresponding 2-fold axis, and the particle oriented around Y to place the *'6-2-6'* plane in coincidence with the X-axis. Owing to variability in curvature between vesicles – owing to size and shape - vesicle averages were not combined, nor was rotational symmetry applied to the vesicle maps at any stage. Resolution estimation was carried out for each vesicle

independently using the functions provided by PEET and did not follow the 'gold-standard' approach owing to the size of the vesicle particle datasets. Volumes were visualized in 3DMOD of IMOD (Kremer et al., 1996), or UCSF Chimera (Yang et al., 2012).

Construction of Soluble NEC Expression Vector

For expression of pU_L31 lacking the NLS (aa 26-271) and pU_L34 (aa 1-179) tagged with hexa-histidine (see Figure S3), the following primers were used to amplify the corresponding regions by PCR on genomic PrV strain Kaplan DNA as template:

U_L34-mpfc, CAC AGG ATC CGA CGA CCA TGA GCG GCA CC, BamHI, 31483-31502;

U_L34-mprc, CAC AAA GCT TGC GGG AGA CCG AGC GCT G, HindIII, 32027-32010;

U_L31-25F, CAC AGG TAC CGA TCG CTA CGC GCC CTA C, KpnI, 29507-29489 and

U_L31-mpr, CAC AGG TAC CCG GGC GAG GGG GGC GAA AG, KpnI, 28769-28787 with location numbers corresponding to Gene Bank Accession No. JQ809328.

Restriction enzyme sites were introduced for convenient cloning into corresponding restriction sites present in MCS1 (U_L34) and 2 (U_L31) of vector pETDuet-1 (Novagen). Correct amplification and insertion was verified by sequencing.

Small Angle X-Ray Scattering -SAXS - Data Collection, Processing, and Analysis

Data were collected from protein coming directly from a coupled size exclusion chromatography unit. The scattering patterns were measured in buffer B with 5 mM TCEP (tris(2-carboxyethyl)phosphine). The raw data were processed using PRIMUS (Konarev et al., 2003). The radii of gyration, R_g, of the particles were calculated from the Guinier approximation, as well as by use of the GNOM indirect transform package (Svergun, 1992), which calculated the distance distribution function *P*(r).

Ten independent *ab initio* models for the soluble NEC were computed with the simulated annealing *ab initio* bead modelling programs DAMMIF (Franke and Svergun, 2009). The ten models were aligned, averaged and filtered using the DAMAVER software suite (Volkov and Svergun, 2003). The model was further refined with DAMMIN (Svergun, 1999).

Architectural and SAXS-EM Integrative Model Building and Analysis

The sub-tomogram average is a 3.5-4-nm resolution representation of the NEC coat that does not unambiguously reveal the arrangement of heterodimers. The 'archway' and composing angular motifs are suggestive of a repeating feature that likely corresponded to this unit. Initially, we probed this assumption using a model of spheres corresponding to the approximate size of each component. Assuming a mass of ~30 kDa for both pU_L31 and pU_L34, each component of the NEC was initially modelled as a spherical volume ~3.5 nm in diameter. Guided by observation of lattice-type arrangements in the density, it was found that by placing these model spheres at the vertices of the lattices (Figure 4), a model could be devised which closely replicated the appearance of the experimental map for the NEC coat. The MD layer subunits were organized as clusters of 3 units (homotrimers). The placement of spheres reproduced and accounted for the 'angular' motif corresponding to a presumed heterodimer. The model subsequently served as the basis for the schematic shown in Figure 5. While this approach accounted for the 'pillars' of the 'archways', the nature of the 'arch' densities were initially difficult to reconcile, however the shared connection to the VM – also visible in raw tomograms - strongly suggests a homomeric interaction between pU_L34 in these regions with oligomerization taking place at sites distant (~3.2 nm) to the VM embedded C-terminal region (TM domain) – thereby forming the 'arch keystone'. Given the flexibility of the pU_L34 C-terminal part (Figure S3C), and that this is logically expected to be the closest part to the VM, the assertion was supported by our model. The quaternary model describes the hexagonal unit cell as consisting of a hexamer of $pU_L31/34$ heterodimers, and predicts at least three primary protein-protein interfaces contribute to assembly of the lattice in the first instance. These are the heterodimeric interface (pU_L31-pU_L34) which serves as the primary series of interfaces between the observed layers, as well as homomeric interactions of pU_L31 and pU_L34. Independently, pU_L31 was modelled initially

as a homotrimer, and these were placed on the vertices of the MD hexagonal lattice. It is equally possible that pU_L31 forms a homodimer in solution, with weaker interactions nucleating around the 3-fold axes resulting in coat formation. However, pU_L31 self-interaction in solution was not observed experimentally (Lorenz et al., 2015).

To investigate the orientation of soluble NEC within the cryoEM NEC coat unit cell – and move towards validation of the above model - we systematically cross-correlated $[pU_L31/34]_6$ SAXS models produced by varying the orientation of the heterodimer with respect to the cryoEM map. The SAXS PDB was converted to an EM density map (11.4 Å /pixel, 3 nm resolution) using the PDB2MRC program of the EMAN package (Tang et al., 2007). This map was centred on a 6-fold axis, oriented such that the NEC coat was perpendicular to Y-axis, and windowed to a 20 pxl^3 box. The SAXS map was thresholded tightly to produce an 'envelope' corresponding to a volume of ~87 nm^3. Thresholding served to approximately equalize internal densities such that these would not significantly influence the cross-correlation search against the cryoEM map (i.e. a fitting based on 'shape' alone was carried out). A series of hexameric models were created from $pU_L31/34$ envelopes using SPIDER by systematically varying six parameters (Shaikh et al., 2008). The first three parameters (phi, theta, psi) determined the orientation of the heterodimer within the unit cell, while translational parameters y, and x governed the displacement of the heterodimer from the NEC coat unit cell (particle average) centre along the Z- (unit cell radius) and Y- axis (vesicle radius), respectively. An angular step of 10° was used for the orientation search, while a step of 5.7 Å was used for the translation search. A hexameric model was created from the oriented and positioned envelope by populating heteordimers about the Y-axis according to 6-fold rotational symmetry. The final search parameter was a rotational search around the Y-axis, and was carried out over a 60° range (10° step) to identify each hexameric model best 'in-plane' orientation within the NEC coat unit cell. The SAXS-EM model supported interactions between components of the NEC coat proposed by the initial modelling (described above). Furthermore, the fit of the SAXS map allowed us to estimate the approximate number of amino acids contributing to each arch densities (C-terminal VM-connecting part of pU_L34 except the transmembrane domain) as: $pU_L34^{\text{full-length}}$-$pU_L34^{\text{construct-length}}$ (240-179) x 6 pU_L34 subunits/unit = 366 amino acids (~40.2 kDa). The sequence of pU_L34 is annotated in Figure S3C.

Modelling and Analysis of Curvature of the NEC Coat

Based on the observation of the two characteristic NEC layers (Figure 4), we hypothesized that the pattern of local interactions between components governs global properties of the vesicle by giving rise to 'well-defined' curvature when perpetuated over large surface areas; behaviour that should be amenable to modelling and analysis. The characteristic layers exhibited distinct hexagonal properties that could be represented by 'hypothetical lattices' for the MD and MP layers as shown in Figures 7A and S4. Serving as a convention for measurement, however, both layers correspond to a *p6* curved lattice. With respect to the integrative SAXS model, the MP and MD layers are positioned at either radial side of the heterodimer core ('pillar'); i.e. these coincide with locations where homomeric interactions are established and act to spatially constrain the placement of each subunit. Attempts to overlay the hypothetical lattices, i.e. as a geometric model of the NEC coat, showed these do not overlap precisely over distances larger than that of the unit of the MD lattice (Figure 7A). However, if we constrained the hexagonal unit centres of the shared unit cell to overlap (as would be carried out by multiple instances of macromolecular association), we find that precise curvature allows for radial alignment of the units (as shown in Figure 7B). The model suggested further that heteromeric association is required for curvature, and that these protein-protein interfaces are organized about the shared 2-fold axes of each layer (this was supported by SAXS-EM modelling, Figure 6). Notably, the geometric model predicts that it is this location of the heteromeric interactions that establishes the *'6-2-6'* directionality of curvature as observed in the experimental map (Figure 5 shows that the MD layer is – unexpectedly - planar between *'3-2-3'* axes), and consequently the modelling described below was carried out for the *'6-2-6'* cross-sectional plane.

To model curvature of the NEC coat, we derived an equation relating structural properties of the NEC to the radius to, or diameter between, the membrane distal layer(s) (MD) of the vesicle NEC coat (r_{MD} and d_{MD}, respectively). Equation 1 describes these in relation to the quotient ('*a*') of two arc lengths (V_{MP} and V_{MD}) between two adjacent 2-fold axes that are separated radially by a distance '*h*' (Figure 7).

$r_{MD}=h/(a-1)$, where $a=V_{MP}/V_{MD}$ (Equation 1)

The model assumes that the NEC coat achieves near complete coverage of the vesicles inner surface; an assumption supported by inspection of the tomograms. Conversely, use of the formula to successfully predict vesicle size based on local measurements from the NEC sub-tomogram average would serve to support that near complete coverage of the vesicle inner surface by the NEC coat does take place, and that the NEC coat architecture is perpetuated over most of this surface area. Sufficiently accurate measurement of these parameters should allow the appearance of the NEC coat to be modelled, as illustrated in Figure 7. *'h'* (~5.13 nm) is defined as the distance between distinct hexagonal arrangements of the MD and MP layers – coinciding with the 'pillars' of the archway, and '*a*' calculated as the quotient between arch lengths (as approximated from lattice spacing) between layers. The overall scheme for these measurements and respective calculations are described in Figure S4. To prepare for these measurements the NEC map was interpolated by a factor of two (5.7 Å/pixel), and tangential slices masked to include only well-defined unit cells, and subsequently padded by a factor of six to oversample the Fourier transform. r_{MD} (e.g. ~58.6 nm for the vesicle featured) can be measured from the experimental average in relation to the spherical model used for averaging, or as illustrated in Figures 7 and S4, calculated (predicted) from measurements taken locally from the experimental NEC coat average map. To scale arc lengths so as to construct the model overlay shown in Figure 7B, a radial projection of the NEC average was calculated using the BRADIAL program of BSOFT (Heymann et al., 2008), and this allowed the true magnitude of unit cell spacing (V_{MD}) to be measured. To produce the 2D *'6-2-6'* model overlay a hexagonal unit was created by modelling a heterodimer (the 'angular motif'), this was then displaced by half the measured V_{MD} with a reflection about the vertical axis to produce a unit cell cross-section. This unit model was then used to produce entire vesicle extrapolations by applying the angle subtended by the arc lengths measured from the sub-tomogram averages. This approach simulated the influence of the pU_L34 'arch', in spatially constraining the position of the heterodimer 'pillars'. According to this model the MD layer is thus formed by 2-fold and 3-fold interactions of pU_L31, while the MP layer varies with curvature, but is formed primarily by the 6-fold 'arch interactions', but also by interactions occurring on the 2-fold axes. The model predicts that complete coverage of the vesicle inner surface is geometrically allowed, as shown in Figure 7D, which is an extrapolation of that shown in Figure 7B.

SUPPLEMENTAL REFERENCES

Al-Amoudi, A., Studer, D., and Dubochet, J. (2005). Cutting artefacts and cutting process in vitreous sections for cryo-electron microscopy. J. Struct. Biol. *150*, 109-121.

Bleck, C.K.E., Merz, A., Gutierrez, M.G., Walther, P., Dubochet, J., Zuber, B., and Griffiths, G. (2010). Comparison of different methods for thin section EM analysis of *Mycobacterium smegmatis*. J. Microsc. *237*, 23-38.

Bouchet-Marquis, C., and Hoenger, A. (2011). Cryo-electron tomography on vitrified sections: a critical analysis of benefits and limitations for structural cell biology. Micron *42*, 152-162.

Dent, K.C., Hagen, C., and Grünewald, K. (2014). Critical step-by-step approaches toward correlative fluorescence/soft X-ray cryo-microscopy of adherent mammalian cells. In Correlative Light and Electron Microscopy II, T. Müller-Reichert, and P. Verkade, eds. (Burlington, MA: Academic Press), pp. 179-216.

Fukuda, Y., Schrod, N., Schaffer, M., Feng, L.R., Baumeister, W., and Lučić, V. (2014). Coordinate transformation based cryo-correlative methods for electron tomography and focused ion beam milling. Ultramicroscopy *143*, 15-23.

Gunkel, M., Schöneberg, J., Alkhaldi, W., Irsen, S., Noe, F., Kaupp, U.B., and Al-Amoudi, A. (2015). Higher-order architecture of rhodopsin in intact photoreceptors and its implication for phototransduction kinetics. Structure *23*, 628-638.

Hagen, C., Werner, S., Carregal-Romero, S., Malhas, A.N., Klupp, B.G., Guttmann, P., Rehbein, S., Henzler, K., Mettenleiter, T.C., Vaux, D.J.*, et al.* (2014). Multimodal nanoparticles as alignment and correlation markers in fluorescence/soft X-ray cryo-microscopy/tomography of nucleoplasmic reticulum and apoptosis in mammalian cells. Ultramicroscopy *146*, 46-54.

Han, H.M., Zuber, B., and Dubochet, J. (2008). Compression and crevasses in vitreous sections under different cutting conditions. J. Microsc. *230*, 167-171.

Heymann, J.B., Cardone, G., Winkler, D.C., and Steven, A.C. (2008). Computational resources for cryo-electron tomography in Bsoft. J. Struct. Biol. *161*, 232-242.

Hsieh, C.E., Leith, A., Mannella, C.A., Frank, J., and Marko, M. (2006). Towards high-resolution three-dimensional imaging of native mammalian tissue: electron tomography of frozen-hydrated rat liver sections. J. Struct. Biol. *153*, 1-13.

Konarev, P.V., Volkov, V.V., Sokolova, A.V., Koch, M.H.J., and Svergun, D.I. (2003). PRIMUS: a Windows PC-based system for small-angle scattering data analysis. J. Appl. Crystallogr. *36*, 1277-1282.

Kremer, J.R., Mastronarde, D.N., and McIntosh, J.R. (1996). Computer visualization of three-dimensional image data using IMOD. J. Struct. Biol. *116*, 71-76.

Malhas, A., Goulbourne, C., and Vaux, D.J. (2011). The nucleoplasmic reticulum: form and function. Trends Cell Biol. *21*, 362-373.

Mastronarde, D.N. (2008). Correction for non-perpendicularity of beam and tilt axis in tomographic reconstructions with the IMOD package. J. Microsc. *230*, 212-217.

Mielanczyk, L., Matysiak, N., Michalski, M., Buldak, R., and Wojnicz, R. (2014). Closer to the native state. Critical evaluation of cryo-techniques for Transmission Electron Microscopy: preparation of biological samples. Folia Histochem. Cytobiol. *52*, 1-17.

Pierson, J., Ziese, U., Sani, M., and Peters, P.J. (2011). Exploring vitreous cryo-section-induced compression at the macromolecular level using electron cryo-tomography; 80S yeast ribosomes appear unaffected. J. Struct. Biol. *173*, 345-349.

Rigort, A., Bäuerlein, F.J.B., Leis, A., Gruska, M., Hoffmann, C., Laugks, T., Böhm, U., Eibauer, M., Gnaegi, H., Baumeister, W.*, et al.* (2010). Micromachining tools and correlative approaches for cellular cryo-electron tomography. J. Struct. Biol. *172*, 169-179.

Schneider, G., Guttmann, P., Rehbein, S., Werner, S., and Follath, R. (2012). Cryo X-ray microscope with flat sample geometry for correlative fluorescence and nanoscale tomographic imaging. J. Struct. Biol. *177*, 212-223.

Shaikh, T.R., Gao, H.X., Baxter, W.T., Asturias, F.J., Boisset, N., Leith, A., and Frank, J. (2008). SPIDER image processing for single-particle reconstruction of biological macromolecules from electron micrographs. Nat. Protoc. *3*, 1941-1974.

Shao, L., Kner, P., Rego, E.H., and Gustafsson, M.G.L. (2011). Super-resolution 3D microscopy of live whole cells using structured illumination. Nat. Methods *8*, 1044-1046.

Sorzano, C.O.S., Messaoudi, C., Eibauer, M., Bilbao-Castro, J.R., Hegerl, R., Nickell, S., Marco, S., and Carazo, J.M. (2009). Marker-free image registration of electron tomography tilt-series. BMC Bioinformatics *10*, 124.

Svergun, D.I. (1992). Determination of the regularization parameter in indirect-transform methods using perceptual criteria. J. Appl. Crystallogr. *25*, 495-503.

Svergun, D.I. (1999). Restoring low resolution structure of biological macromolecules from solution scattering using simulated annealing. Biophys. J. *76*, 2879-2886.

Tang, G., Peng, L., Baldwin, P.R., Mann, D.S., Jiang, W., Rees, I., and Ludtke, S.J. (2007). EMAN2: An extensible image processing suite for electron microscopy. J. Struct. Biol. *157*, 38-46.

Turnbull, L., Strauss, M.P., Liew, A.T.F., Monahan, L.G., Whitchurch, C.B., and Harry, E.J. (2014). Super-resolution imaging of the cytokinetic Z ring in live bacteria using fast 3D-structured illumination microscopy (f3D-SIM). J. Vis. Exp. *91*, e51469.

Volkov, V.V., and Svergun, D.I. (2003). Uniqueness of *ab initio* shape determination in small-angle scattering. J. Appl. Crystallogr. *36*, 860-864.

Yang, Z., Lasker, K., Schneidman-Duhovny, D., Webb, B., Huang, C.C., Pettersen, E.F., Goddard, T.D., Meng, E.C., Sali, A., and Ferrin, T.E. (2012). UCSF Chimera, MODELLER, and IMP: an integrated modeling system. J. Struct. Biol. *179*, 269-278.